# Understanding Electrolyte Degradation at Alkali Metal Interfaces – Enabled by X-Ray Photoelectron Spectroscopy

Zur Erlangung des akademischen Grades eines

DOKTORS DER NATURWISSENSCHAFTEN

(Dr. rer. nat.)

von der KIT-Fakultät für Chemie und Biowissenschaften

des Karlsruher Instituts für Technologie (KIT)

genehmigte

DISSERTATION

von

M.Sc. Leonie Wildersinn

1.Referent: Prof. Dr. rer. nat Helmut Ehrenberg
2.Referent: Prof. Dr. Anass Benayad
Tag der mündlichen Prüfung: 16.07.2025

**Selbständigkeitserklärung**

Hiermit versichere ich, dass ich die vorliegende Arbeit selbstständig verfasst habe, dass ich keine anderen als die angegebenen Quellen und Hilfsmittel benutzt habe, dass ich die wörtlich oder inhaltlich übernommenen Stellen als solche gekennzeichnet habe und dass ich die Satzung des KIT zur Sicherung guter wissenschaftlicher Praxis in der jeweils gültigen Fassung beachtet habe.

Karlsruhe, den

Leonie Wildersinn

# Abstract

Lithium-ion batteries have dominated the field of energy storage for decades due to their high energy density and efficiency. However, as their performance nears theoretical limits, researchers are exploring alternative systems that utilize alkali metals, such as lithium, sodium, and potassium, as anode materials. The use of pure metal anodes is often regarded as the "Holy Grail" of battery research, as they promise a significant increase in energy density compared to conventional intercalation-based anodes. Advance sodium and potassium as metal battery electrodes is currently hindered by several significant obstacles, primarily associated with the increasing reactivity of these metals. While lithium metal anodes have been extensively studied, the reactivity of sodium and potassium introduces new challenges, particularly in terms of interfacial stability, electrolyte compatibility, and solid electrolyte interphase (SEI) formation.

Within the scope of this thesis, a systematic investigation of alkali metal surfaces in contact with various electrolyte solvents (without salt), simple electrolytes (with salt) and electrolytes with FEC (fluoroethylene carbonate) as additive was conducted. The primary objective was to gain a detailed understanding of how the increasing reactivity from Li to K affects surface chemistry, SEI formation, degradation pathways and overall the metal electrode performance in half- and symmetrical cell configurations. To achieve this, the work begins with the investigation of pristine (as received) alkali metals to assess their intial surface layer. This revealed a difference in composition of different oxide, hydroxide and carbonate species for the metals. After this groundwork these alkali metal surfaces were exposed to typical carbonate-based solvents and electrolytes under inert conditions. To address the solid and liquid/gas degradation evolution two methodes were combined: X-ray photoelectron spectroscopy and gas chromatography measurements. By comparing the interactions of the metals with pure solvents and with electrolytes containing dissolved salts, a distinction could be made between solvent-induced and salt-induced surface modifications. Both approaches showed that the introduction of $XPF_6$ (X: Li, Na, K) salts promotes the formation of mixed phosphate/fluoride metal species ($M_xPO_yF_z$/$M_xPF_y$, M: Li, Na, K) while FEC promotes metal fluoride formation. Gas chromatography confirms these trends, revealing no volatile degradation products in Li and K when FEC is present. In Na systems without FEC, liquid degradation products appear only after 48 h, while K shows immediate solvent degradation in the absence of FEC. This thesis offers valuable insights into the complex interactions between alkali metals and electrolyte components, contributing to a deeper understanding of the interfacial processes governing battery performance. The findings highlight critical challenges associated with the use of sodium and potassium metal anodes while also providing guidance for the development of improved electrolyte formulations and protective coatings. In particular, distinguishing the effects of solvents and salts on SEI formation allows for a targeted

optimization of electrolyte design for alkali metal batteries. By systematically addressing the reactivity and stability issues of alkali metal anodes, this work paves the way for the development of more reliable and efficient next-generation metal-based batteries.

# Kurzfassung

Lithium-Ionen-Batterien, dominieren seit Jahrzehnten den Bereich der Energiespeicherung aufgrund ihrer hohen Energiedichte und Effizienz. Da ihre Leistungsfähigkeit jedoch zunehmend an theoretische Grenzen stößt, rückt die Entwicklung alternativer Systeme mit Alkalimetallen wie Lithium, Natrium und Kalium als Anodenmaterialien immer stärker in den Fokus der Forschung. Der Einsatz von metallischen Anoden gilt dabei als „Heiliger Gral“ der Batterieforschung, da er eine signifikante Steigerung der Energiedichte im Vergleich zu klassischen Interkalationsanoden versprechen würde. Der Fortschritt insbesondere im Bereich von Natrium- und Kalium-Metallanoden wird jedoch durch mehrere grundlegende Herausforderungen erschwert, die hauptsächlich auf die zunehmende Reaktivität dieser Metalle zurückzuführen sind. Während Lithium-Metallanoden bereits intensiv untersucht wurden, stellen die ausgeprägte Reaktivität von Natrium und Kalium neue Anforderungen an die Stabilität der Grenzfläche, die Kompatibilität mit Elektrolyten und die Bildung der Festelektrolyt-Grenzfläche.

Im Rahmen dieser Arbeit wurde eine systematische Untersuchung der Oberflächen von Alkalimetallen in Kontakt mit verschiedenen Elektrolytsystemen durchgeführt. Ziel war es, ein detailliertes Verständnis dafür zu gewinnen, wie die zunehmende Reaktivität von Li über Na bis K die Oberflächenchemie, SEI-Bildung, Zersetzungsmechanismen und letztlich die elektrochemische Eigenschaften in Halbzellen und symmetrischen Zellen beeinflusst. Zur Untersuchung der festen sowie flüchtigen Zersetzungsprodukte kamen zwei sich ergänzende Methoden zum Einsatz: Röntgenphotoelektronenspektroskopie und Gaschromatographie-Massenspektrometrie. Durch den Vergleich der Metallwechselwirkungen mit reinen Lösungsmitteln und mit Elektrolyten, die $XPF_6$-Salze (X : Li, Na, K) enthalten, konnte zwischen lösungsmittel- und salzbedingten Oberflächen unterschieden werden. Beide Ansätze zeigten, dass die Zugabe von $XPF_6$ (X: Li, Na, K) die Bildung von gemischte phosphat-/fluorid-Metallspezies ($M_xPO_yF_z/M_xPF_y$, M: Li, Na, K) fördert, während FEC bevorzugt die Bildung von Metallfluoriden (MF) begünstigt. Gaschromatographie-Messungen bestätigten diese Trends: In Li- und K-Systemen wurden bei Zusatz von FEC keine Zersetzungsprodukte detektiert. In Na-Systemen ohne FEC traten hingegen Nebenprodukte wie DEDD, DECE und DECC nach 48 Stunden auf, während in K-Systemen die Lösungsmittelzersetzung bereits nach wenigen Minuten einsetzte. Diese Arbeit liefert damit wertvolle Einblicke in die komplexen Wechselwirkungen zwischen Alkalimetallen und Elektrolytkomponenten und trägt zu einem tieferen Verständnis der Prozesse an Grenzflächen bei, die die Leistungsfähigkeit von Batterien bestimmen. Die Ergebnisse unterstreichen die besonderen Herausforderungen bei der Verwendung von Natrium- und Kalium-Metallanoden, liefern aber zugleich wichtige Hinweise zur gezielten Weiterentwicklung von Elektrolyten und schützenden Oberflächenbeschichtungen. Insbesondere die differenzierte Betrachtung von Lösungsmittel- und Salzeinflüssen auf die SEI-Bildung eröffnet neue Ansätze zur gezielten Optimierung der

Elektrolytzusammensetzung für Alkalimetall-Batterien. Durch die systematische Auseinandersetzung mit Reaktivitäts- und Stabilitätsaspekten legt diese Arbeit einen wichtigen Grundstein für die Entwicklung zuverlässiger und leistungsfähiger metallbasierter Batterien der nächsten Generation.

# Table of Contents

# List of Abbreviations

| | |
|---|---|
| $\Delta GR$ | Gibbs free energy |
| AIMD | ab initio molecular dynamics |
| ATR-FTIR | attenuated total reflectance fourier-transform infrared spectroscopy |
| BE | binding energy |
| BP | bulk plasmon |
| cc | constant current |
| CE | coulombic efficiency |
| CMC | carboxymethyl cellulose |
| $CO_2$ | carbon dioxide |
| cp | constant potential |
| cryo-TEM | cryogenic transmission electron microscopy |
| $Cu_2O$ | copper(I) oxide |
| DEC | diethylcarbonate |
| DECC | di-(2-ethoxycarbonyloxyethyl) carbonate |
| DEDD | diethyl dioxahexane dioate |
| DFT | density functional theory |
| DMCC | di-(2-methoxycarbonyloxyethyl) carbonate |
| DMDD | dimethyl dioxahexane dioate |
| DME | dimethoxyethane |
| EC | ethylene carbonate |
| elyte | electrolyte |
| EMC | ethyl methyl carbonate |
| EMCC | 2-methoxycarbonyloxyethyl-2-ethoxycarbonyloxyethyl carbonate |
| EMDD | ethyl methyl dioxahexane dioate |
| $E_{pass}$ | pass energy |
| ESS | energy storage systems |
| FEC | fluoroethylene carbonate |
| FESEM | thermal field emission scanning electron microscope |
| FWHM | full width at half maximum |
| GC | gas chromatography |
| GCPL | galvanostatic cycling with potential limitation |
| *h* | planck's constant |

| | |
|---|---|
| HC | hard carbon |
| HF | hydrogen fluoride |
| HOMO | highest occupied molecular orbital |
| *hv* | photon energy |
| ICP-OES | inductively coupled plasma optical emission spectroscopy |
| IMFP | inelastic mean free path |
| K | potassium |
| $K^0$ | metallic potassium |
| $K_2CO_3$ | potassium carbonate |
| $K_A$ | potassium metal in ampule |
| KF | potassium fluoride |
| KHCO3 | potassium hydrogencarbonate |
| KIB | potassium-ion battery |
| $K_{MO}$ | potassium metal in mineral oil |
| KOH | potassium hydroxide |
| $KPF_6$ | potassium hexafluorophosphate |
| KTFSI | potassium bis(trifluoromethanesulfonyl)imide |
| Li | lithium |
| $Li^0$ | metallic lithium |
| $Li_2C_2$ | lithium carbide |
| $Li_2CO_3$ | lithium carbonate |
| $Li_2O$ | lithium oxide |
| LIB | lithium-ion batteries |
| $LiCoO_2$ | lithium-cobalt(III)oxid |
| LiF | lithium fluoride |
| LiFSI | lithium bis(fluorosulfonyl)imide |
| LiOH | lithium hydroxide |
| $LiPF_6$ | lithium hexafluorophosphate |
| LMO | lithium ion manganese oxide |
| LUMO | lowest unoccupied molecular orbital |
| M | molar mass |
| MS | mass spectrometry |
| Na | sodium |
| $Na^0$ | metallic sodium |

| | |
|---|---|
| $Na_2CO_3$ | sodium carbonate |
| $Na_2O$ | sodium oxide |
| $Na_2O_2$ | sodium peroxide |
| NaF | sodium fluoride |
| NaHCO3 | sodium hydrogencarbonate |
| NaOH | sodium hydroxide |
| $NaPF_6$ | sodium hexafluorophosphate |
| NaTFSI | sodium bis(trifluoromethanesulfonyl)imide |
| nm | nanometer |
| NMR | nuclear magnetic resonance |
| PC | propylene carbonate |
| PCA | principal component analysis |
| $PF_5$ | phosphorus pentafluoride |
| PO | propylene oxide |
| $POF_3$ | phosphoryl fluoride |
| ppm | parts per million |
| PVDF | polyvinylidene fluoride |
| Q | capacity |
| R&D | research and development |
| ref. | reference |
| rp | reaction products |
| RPB | Pilling–Bedworth ratio |
| SBR | styrene-butadiene rubber |
| Sc | internal standard |
| SEI | solid electrolyte interphase |
| SHE | standard hydrogen electrode |
| SIB | sodium-ion battery |
| SP | surface plasmon |
| TiS2 | titanium disulfide |
| UHV | ultrahigh vacuum |
| V | molar volume |
| v | frequency |
| VC | vinylene carbonate |
| X | alklai Metal |

| | |
|---|---|
| XANES | x-ray absorption near-edge structure |
| XPS | x-ray photoelectron spectroscopy |
| ρ | density |

# Acknowledgements

"Difficult doesn’t mean impossible." A PhD is not just a research project, it’s a marathon of perseverance, and, in my case, a lot of cake. There were moments when everything felt overwhelmingly difficult, but thanks to the incredible people around me, the impossible always became manageable.

First and foremost, I would like to express my gratitude to Prof. Dr. Helmut Ehrenberg for giving me the opportunity to work at IAM-ESS. A special thanks to Dr. Fabian Jeschull and Dr. Julia Maibach, without their patience and guidance, my PhD would have quickly turned into a chaotic experiment of its own. I deeply appreciate their time, expertise, and encouragement throughout this journey. I would also like to thank the German Research Foundation (DFG) for funding as part of the POLiS Cluster of Excellence. Wihtin POLiS I had the possibility to cooperate with other researchers, here I want to thank especially Andreas Hofmann and Daniel Stottmeister who published papers with me and underlined my ideas with there experiment in GC-MS and DFT calculation.

I owe a big thank you to Christian Njel and Vanessa Trouillet for introducing me to the world of XPS and making sure I didn’t get completely lost in it. I enjoyed our lunch breaks, endless conversations, and, of course, the legendary cakes and sweets that Udo Geckle brought along made even the toughest days bearable. I also want to acknowledge Liuda Mereacre for her invaluable technical support,without her help in setting up electrochemical measurements my experiments.

I also want to thank “Team potassium” (Timofey, Ulf, Celine, Iluri, Anna, Monika, Ferdinand) and everyone who endured the tough times at BESSY with me, long hours, frustrating experiments, but also shared struggles that somehow made things easier. A huge shout-out to Iiuri and Christopher for patiently answering all my (sometimes painfully basic) electrochemical questions. Your help was truly invaluable.

Outside the lab, I am beyond grateful for my amazing friends: Anna, Vanessa, Alex, Christian, Chris, Sabrina and Francesco—thank you for making sure I had a life beyond research. Whether it was calling me, hiking or sharing countless laughs, you made this journey so much more enjoyable.

And finally, the biggest thank you of all goes to my family—my parents, Constanze and Bernd, and my sister Jenny. Your unwavering support, patience, and love kept me going through the hardest moments. I couldn't have done this without you.

This PhD was anything but a straight path—it was chaos, trial and error, moments of frustration when nothing seemed to work, and the constant need to start over. It was also hard work, laughter, unexpected successes, and the realization that every setback was just another step forward. In the end, it was about pushing boundaries, growing beyond what I thought was possible, and proving to myself that *difficult doesn’t mean impossible.*

# List of Publications

(1) Stottmeister, D.; Wildersinn, L.; Maibach, J.; Hofmann, A.; Jeschull, F.; Groß, A. Unraveling Propylene Oxide Formation in Alkali Metal Batteries. *ChemSusChem* **2024**, 17 (3), e202300995. https://doi.org/10.1002/cssc.202300995.

(2) Wildersinn, L.; Stottmeister, D.; Jeschull, F.; Groß, A.; Hofmann, A. Decomposition of Binary Mixtures of DMC/EC, EMC/EC, and DEC/EC on Potassium Surfaces; GC, XPS, and Calculation. *ACS Appl. Mater. Interfaces* **2025**, 17 (6), 10055–10072. https://doi.org/10.1021/acsami.4c17461.

(3) Schöner S., Schmidt D., Wildersinn L., Wolf S., Speer S., Wolff B., Bokov A., Cao P., Windmüller A., Tsai C.-L., Jeschull F., Tempel H., Chen X., Yu S. and Eichel R.-A. Stable Na Deposition/Dissolution Enabled by 3D Bimetallic Carbon Fibers with Artificial Solid Electrolyte Interface. *Small Sci.* **2025**, 2400655. https://doi.org/10.1002/smsc.202400655.

## Contributions of Co-authors and Other Researchers

Parts of **Chapter 7.3** and **8.3** and the corresponding parts in the experimental section (**Section 4.5 and 4.7**) were extracted from the publications **1** and **2** and adapted with permission of the author (Leonie Wildersinn and Daniel Stottmeister). Conceiving the idea of these studies, developed methodology, organisation of the work and all included X-ray spectroscopy results were done by Leonie Wildersinn and supervised by Fabian Jeschull. Leonie Wildersinn visualized the presented data and wrote the manuscripts. Density functional theory were performed by Daniel Stottmeister. GC-MS measurements were done by Andreas Hofmann. Preparation and optical cell observation were carried out with help of Ferdinand Selbiger during his «Masterthesis». Thomas Bergfeld contributed **chapter 8.1** with ICP-OES measurements (experimental part **chapter 4.7**).

# 1 Introduction

The global demand for efficient and sustainable energy storage systems (ESS) has surged in recent years, driven by the rapid expansion of renewable energy sources and the electrification of transportation. Lithium-ion batteries (LIBs) have dominated the market since their commercialization by Sony in the 1990s due to their high energy density, long cycle life, and efficiency.[1,2] However, as LIB technology reaches its theoretical limits in energy density and cost-effectiveness, alternative battery chemistries have gained attention to meet future energy storage demands.

Among the most promising alternatives to conventional LIBs are metal-based batteries utilizing lithium (Li), sodium (Na), or potassium (K) metal as anodes. Unlike intercalation-based LIBs, metal batteries employ direct metal plating and stripping, with theoretical capacities of 3860, 1166, and 685 mAh $g^{-1}$ for Li, Na, and K, respectively. These values are based on active-material capacity, yet even when normalized to $LiC_6$, Li metal still exceeds graphite by an order of magnitude. These metal anodes eliminate the need for graphite or other intercalation host structures, enabling higher energy densities. Sodium-ion (SIB) and potassium-ion batteries (KIB) have gained interest due to their abundance and lower cost of Na and K compared to Li, because their chemistries often avoid expensive components like Ni, Co, or Cu commonly used in Li-ion systems making them attractive for large-scale ESS applications. However, the widespread commercialization of metal batteries faces substantial challenges, primarily related to the instability of the SEI, uncontrolled dendritic growth, and poor Coulombic efficiency. The higher reactivity of alkali metals with liquid electrolytes further exacerbates these issues, necessitating advanced electrolyte formulations and interface engineering strategies.

In the context of metal-anode systems, zero-access batteries have emerged as a novel concept to circumvent some of the challenges associated with metal anodes. These systems rely on the electrochemical deposition of the alkali metal onto a current collector during cycling, eliminating the need for a pre-deposited anode. This design can enhance energy density and simplify manufacturing processes. However, achieving stable cycling in anode-free configurations remains a significant challenge due to the inefficient plating/stripping process and rapid electrolyte depletion.

To understand the fundamental mechanisms governing metal batteries and their interactions with various electrolytes, advanced characterization techniques such as XPS play a crucial role. XPS enables the investigation of SEI composition, electrode surface chemistry, and interfacial stability, providing insights into degradation mechanisms and guiding the development of more stable and efficient battery systems.

# 2 Theoretical Background

The development of high-energy-density batteries has been intrinsically linked to the exploration of alkali metals, particularly lithium, sodium, and potassium. This chapter traces the evolution of alkali metal-based energy storage systems, beginning with their early inception, transitioning through the era of LIBs, and culminating in the modern resurgence of alkali metal anodes. By framing LIBs as a pivotal yet intermediate step in this progression, the discussion underscores the cyclical nature of battery innovation and refocuses on the transformative potential of alkali metal anodes in next-generation battery technologies.

## 2.1 Alkali Metals: From Origins to Revival

Developing rechargeable batteries with lithium as alkali metal anode has a long and complex history, shaped by both technological breakthroughs and practical limitations. The earliest efforts in the 1970s centered around lithium metal, whose exceptionally low electrochemical potential (−3.04 V vs. SHE) and high theoretical capacity (3861 mAh $g^{-1}$) made it an ideal anode material for high-energy-density systems.[3] Pioneering work by Whittingham et al. demonstrated the feasibility of such batteries, using lithium metal paired with titanium disulfide ($TiS_2$) cathodes.[4] These early prototypes, further developed by Exxon and Moli Energy, laid the groundwork for a new class of rechargeable batteries.[5] However, the practical use of lithium metal soon revealed serious safety concerns.[6] Dendritic growth during cycling led to short-circuiting and thermal runaway, resulting in high-profile failures and prompting a decisive shift away from metallic lithium. This transition gave rise to intercalation-based systems, most common known, the LIB, which replaced lithium metal with graphite anodes. In 1991, the commercialization of LIBs marked a turning point for high energy density electricity storage and catalyzed rapid market growth. LIBs became the foundation for a broad spectrum of applications, from portable electronics such as mobile phones and laptops to electric vehicles and grid-scale stationary storage. Their relatively high energy density (approx. 250-300 Wh $kg^{-1}$), long cycle life, and safety compared to lithium metal systems drove widespread adoption. While LIBs were a safer compromise, they imposed inherent limits. The theoretical capacity of graphite (372 mAh $g^{-1}$) is more than an order of magnitude lower than that of lithium metal (3860 mAh $g^{-1}$), and the use of intercalation hosts caps the theoretical energy density of LIBs to 350 Wh $kg^{-1}$.[3]

As performance plateaus, attention has returned to metallic alkali anodes, including lithium, but also increasingly sodium and potassium, which are far more abundant and cost-effective.

Indeed, lithium resources are limited (estimated at approx. 20 ppm in Earth's crust, or $1.6 \times 10^7$ tons) and unevenly distributed, leading to growing concerns over future supply, price volatility, and

geopolitical dependence. The cost of lithium is expected to rise further with increased global demand, particularly when lithium foil is used directly as an anode, since its price strongly depends on thickness and processing. These factors have led researchers to explore earth-abundant alternatives, such as sodium and potassium. Among these, sodium is especially promising, its crustal abundance (23000 ppm) is roughly 1150 times higher than that of lithium, while the cost of sodium metal is nearly 50 times lower than that of lithium. Potassium, too, offers advantages in cost and ionic conductivity, though its high reactivity poses distinct challenges.

The shift back to alkali metal anodes is driven by the urgent need to overcome the energy density limitations of intercalation-based batteries and the growing pressure to reduce material costs and resource dependencies. Recent advances in electrolyte formulations, interfacial engineering, and solid-state architectures now offer realistic pathways to stabilize highly reactive metal surfaces that were once considered commercially unviable. As illustrated in **Figure 1**, the number of publications related to both lithium-ion and alkali metal batteries has increased significantly in recent years, reflecting a surge in academic and industrial interest. By enabling direct metal plating and stripping, these approaches eliminate the structural burden of intercalation hosts, opening the door to significantly higher energy densities. In addition, each alkali metal brings unique advantages: potassium enables faster ion transport due to its lower desolvation energy, while sodium offers improved sustainability through its wide availability and low cost.

Nonetheless, the challenges that once hindered these systems, dendrite formation, interfacial instability, and parasitic reactions persist, especially under high current densities or extended cycling. These issues are magnified in emerging architectures such as metal-sulfur, metal-air, and all-solid-state batteries, where the reactivity of alkali metals becomes both an asset and a liability.

The following sections examine these challenges in detail and explore modern strategies to stabilize alkali metal anodes, with a particular focus on interfacial processes, electrolyte formulations, and material innovations aimed at enabling a new generation of high-performance, metal-based rechargeable batteries.

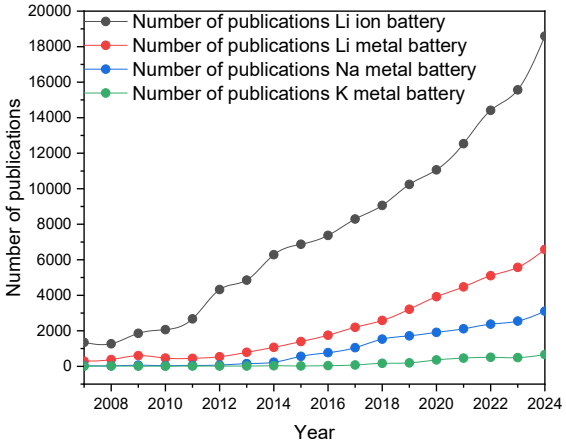


**Figure 1:** Trend in the number of publictaions on rechargeable alkali metal batteries, including lithium ion batteries (as of april 2025). The keywords used for the Scopus search were “lithium metal battery”, “lithium ion battery”, “sodium metal battery” and “potassium metal battery”.

## 2.2 Metal Anodes

Alkali metal anodes are increasingly explored as high-capacity anodes due to their ability to store charge through direct metal plating and stripping. In contrast to intercalation-based systems, where ions are inserted into the layered structure of a host material, alkali metal anodes enable energy storage by directly depositing metal cations onto the electrode surface during charging and removing them during discharge. For example, in a typical lithium metal battery with an intercalation-type cathode such as $LiCoO_2$, lithium ions ($Li^+$) are extracted from the cathode and plated as metallic lithium on the anode during charging. During discharge, these ions are stripped from the lithium metal and reinserted into the cathode. Replacing graphite with lithium metal in such cells allows for a significant increase in specific energy, reaching up to approx. 440 Wh $kg^{-1}$ with cathode materials like LMO. [7] Several large-scale R&D initiatives have been launched to accelerate this transition, including the Battery500 Consortium in the U.S. and the RISING II program in Japan. These efforts reflect a global push to reach specific energies of 500 Wh $kg^{-1}$ or more, though achieving such performance in practice remains a nontrivial task (**Figure 2**).[8]

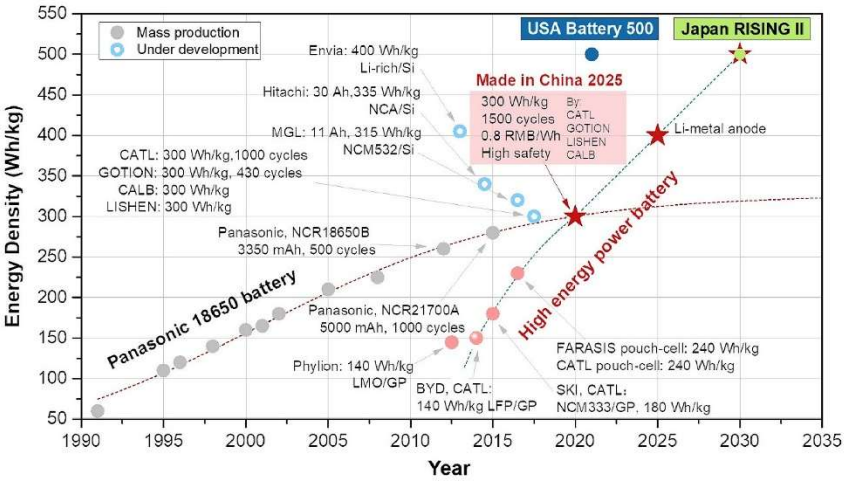


**Figure 2:** The history, current state and development of Li-ion batteries.[8]

Rising demand for rechargeable batteries, especially for electric vehicles, has raised concerns about lithium's long-term availability and supply security. Although global reserves are estimated at 89 million tons, enough to produce up to 10 billion EV batteries at current lithium usage level,s over half of today's lithium comes from Australia, and most reserves are concentrated in Bolivia, Chile, and Argentina.[9,10] In response to both these technical bottlenecks and the geopolitical concerns tied to lithium supply, sodium and potassium metal anodes have gained significant attention.

Sodium and potassium make up approximately 2.3% and 1.5% of the Earth's crust, respectively, compared to only 0.0017% for lithium.[11,12] This abundance translates into significantly lower costs and improved resource accessibility. However, the higher atomic weights of sodium (23 u) and potassium (39 u), compared to lithium (6.9 u), impose fundamental limits on the achievable energy density in Na-ion and K-ion batteries.

Sodium metal, for example, provides a theoretical capacity of 1162 mAh $g^{-1}$ and a redox potential of −2.71 V vs. SHE. Although lower in energy density than lithium, sodium offers major sustainability advantages: it is over 1000 times more abundant in Earth's crust and costs up to 50 times less than lithium. Moreover, it is compatible with aluminum current collectors, further reducing cell costs. Still, its high reactivity with carbonate-based electrolytes leads to unstable SEI layers that degrade rapidly during cycling. Ongoing research is focused on stabilizing these interphases using fluorinated solvents, engineered SEI layers, and artificial coatings.

Potassium metal, by contrast, combines a redox potential close to lithium (−2.93 V vs. SHE) with a moderate capacity of 685 mAh $g^{-1}$. Its key strength lies in fast ion transport, enabled by low desolvation energy and weak Lewis acidity. Potassium-based electrolytes also exhibit high ionic conductivity. However, potassium is extremely reactive and pyrophoric, with a large ionic radius that complicates interface stability. It tends to form fragile SEIs prone to cracking and dendrite growth, especially under

high current densities. Approaches such as ether-based solvents, ionic liquids, and functional additives are being explored to mitigate these risks.

An often-overlooked complication when using alkali metal anodes is, that even under inert storage, lithium, sodium, and potassium react with trace impurities, moisture, $CO_2$, and hydrocarbons to generate oxides, hydroxides, and carbonates on their surfaces.[13,14] These films, are chemically inhomogeneous and porous, with thicknesses ranging from several nanometers (Li) to tens of nanometers (Na), influencing how the SEI forms during battery operation. This variation in thickness and compactness can be rationalized by considering the Pilling–Bedworth ratio (RPB).[15] Pilling and Bedworth demonstrated that the ability of an oxide to form a protective, adherent film on its parent metal depends on the ratio of their molar volumes. This Pilling–Bedworth ratio is defined as:

$$R_{PB} = \frac{V_{Oxide}}{n * V_{Metal}} = \frac{M_{Oxide} * \rho_{Metal}}{n * M_{Metal} * \rho_{Oxide}}$$

With $V_x$ , $M_x$ and $\rho_x$ being the molar volume, the molar mass and density of x. While n represents the number of metal atoms in the formula of the oxide.

When the $R_{PB}$ is significantly less than one the oxide layer is too thin or porous to protect the metal. Cracking and gaps allow continued oxidation and thickening of the film. Showing a value between one and two, the oxide can form a coherent, self-limiting cover that protects the underlying metal. However, if the value is above 2, the oxide film is overly voluminous, leading to mechanical stress, cracking and the resulting layer is typically non-passivating. Such oxide layers fail to effectively block the penetration of liquid electrolytes, leading to continuous parasitic reactions between the alkali metal and the electrolyte. This persistent reactivity destabilizes the electrode–electrolyte interface and accelerates degradation phenomena during cycling.[15,16]

The $R_{PB}$ can similarly predict the protective behavior of non-oxide reaction products. Values well below 1 or well above 2 reliably indicate an ongoing metal–product reaction. Conversely, ratios that fall between 1 and 2 suggest the reaction product is capable of forming a continuous, protective layer on the metal surface. For lithium metal, calculated $R_{PB}$ for common reaction products include $Li_2CO_3$ and LiOH (each between 1 and 2), consistent with their ability to coat and partially passivate Li metal surfaces. Table 1 shows the $R_{PB}$ values selected for Li, Na and K SEI compunds on Li, Na and K metal. This values indicate that the SEI for Na and K metal might be more challenging.

**Table 1:** Pilling-Bedworth ratio for Li vs. Na vs. K SEI compounds. Ratios smaller than one indicate the formation of a porous and/or cracked film. Ratios between one and two direct the formation of a covering and protective film.[15]

| Li SEI compounds | | Na SEI compounds | | K SEI compounds | |
|---|---|---|---|---|---|
| Compound | $R_{PB}$ | Compound | $R_{PB}$ | Compound | $R_{PB}$ |
| LiF | 0.76 | NaF | 0.69 | KF | 0.52 |
| $Li_2O$ | 0.57 | $Na_2O$ | 0.58 | $K_2O$ | 0.44 |
| $Li_2O_2$ | 0.76 | $Na_2O_2$ | 0.59 | $K_2O_2$ | 0.57 |
| $Li_2CO_3$ | 1.35 | $Na_2CO_3$ | 0.88 | $K_2CO_3$ | 0.63 |
| LiOH | 1.26 | NaOH | 0.79 | KOH | 0.58 |

### 2.2.1 Challenges of Metal Anodes

To make lithium metal a viable anode material for rechargeable batteries, significant challenges must be addressed, foremost among them are safety concerns and limited cycling stability. These issues are rooted in interfacial processes between the lithium electrode and the electrolyte, particularly the inhomogeneous plating and stripping of lithium and the concurrent formation of the SEI.[17] The SEI is a passivation layer that forms spontaneously on the surface of lithium metal as a result of electrolyte decomposition at the highly reducing potential of lithium and will be discussed in detail in **chapter 2.3**. While this layer is essential to prevent continuous electrolyte degradation, it also introduces further interfacial heterogeneity, which promotes uneven nucleation and growth during lithium deposition.
Although interfacial inhomogeneities exist in commercial lithium-ion batteries as well, their impact is significantly more pronounced for lithium metal electrodes due to the extreme volume changes involved. Whereas typical intercalation anodes experience volume changes of up to 10%, while lithium metal can undergo effectively infinite volume fluctuations during cycling, since it is deposited and stripped without a host structure.[7] These drastic dimensional shifts contribute to mechanical instability and dendrite formation, that grow during plating and can pierce the separator, potentially causing internal short circuits and thermal runaway and potentially leading to fire or explosion. Inhomogeneous lithium deposition further leads to the detachment of dendrites from the bulk electrode, leaving behind electronically isolated "dead lithium," which lowers the coulombic efficiency and reduces cycle life.[18] Over time, this results in a porous, morphologically unstable electrode, accompanied by a thickening and continuously regenerating SEI. Thus, dendrite-free lithium deposition is a key requirement for advancing lithium metal battery technology. These challenges are not unique to lithium. Sodium and potassium metal anodes suffer from similar issues, magnified by their even higher reactivity. A wide range of stabilization strategies has been developed to address these challenges. These can be broadly categorized into: 1) current collector design, 2) protective layer

engineering, 3) electrolyte optimization, 4) separator modification and 5) pressure application.[19–22] These approaches aim to regulate interfacial reactions, buffer volume changes, and ensure uniform nucleation and deposition of metal. In this context, the present work primarily focuses on strategy 3, with additional consideration of separator modification (4) in the case of sodium metal anodes.

All this issues can ultimately be tracked down to two fundamental factors: the high chemical reactivity of alkali metals and its effectively infinite volume change. These characteristics make the formation of a stable interface between alkali metal and the electrolyte especially critical, particularly when using liquid electrolytes.

### 2.2.1 Dendrites

The term dendrite originates from the Greek word dendron, meaning "tree", and indeed dendrites are frequently described as tree-like structures. In the field of metallurgy, the word refers to branched morphologies that typically arise during molten metal solidification or metal electrodeposition. In the context of lithium metal batteries, however, the term is often used more broadly. As noted by Zhang et al., referring to all lithium electrodeposits as “dendrites” is somewhat ambiguous, since lithium can adopt a range of morphologies beyond just branched, tree-like forms.[17] In many cases, lithium deposits as compact particles or as slender, filamentous structures rather than classical dendrites. Despite this morphological diversity, the term "dendrite" has become ubiquitous in the battery literature and is commonly used to refer to any lithium structures formed during electrodeposition that protrude from the electrode surface.

Bai et al. categorizes lithium electrodeposits into three distinct growth modes based on current density and interfacial conditions. The three proposed growth modes are illustrated in **Figure 3** and include: Tree-like dendrites, mossy-like structures and whiskers (or needle-like deposits).[23]

Tree-like dendrites are typically observed under high current density conditions. According to Bai et al., these structures emerge when the current exceeds a critical threshold (referred to as the limiting current density) leading to salt depletion near the electrode interface at a characteristic time known as Sand's time.[24,25] This depletion destabilizes the interface and results in tip-focused growth, where lithium preferentially accumulates at the tips of protrusions, giving rise to branched morphologies.

In contrast, whisker-like growth is associated with low current densities. Under these conditions, a mechanically robust SEI can form on the lithium surface. As lithium ions are deposited underneath this rigid layer, internal pressure builds up until it is released at localized weak spots, resulting in root-based protrusions, commonly referred to as whiskers. This mechanism is termed root-induced growth and is visually and conceptually analogous to the growth of human hair. At intermediate current densities, a

more complex growth behavior is observed. Here, the rates of lithium deposition and SEI formation become comparable, leading to a hybrid growth mechanism that incorporates elements of both root- and tip-induced deposition. The resulting morphology is known as mossy lithium, characterized by globular or cauliflower-like structures with poorly defined orientation and connectivity. Bai et al. refer to this as surface growth, reflecting the interplay between SEI formation and localized lithium deposition.[24]

There are two central components that strongly influence dendrite morphology: the SEI and the electrolyte itself. These interfacial components govern ion transport, mechanical stability, and electrochemical kinetics at the electrode–electrolyte interface, and thus play a crucial role in determining the onset, shape, and propagation mode of lithium dendrites. Dendrite formation in Na and K systems has not yet been sufficiently investigated, nevertheless, studies on these metals frequently report needle-like growth behavior during electrochemical cycling. [23,24]

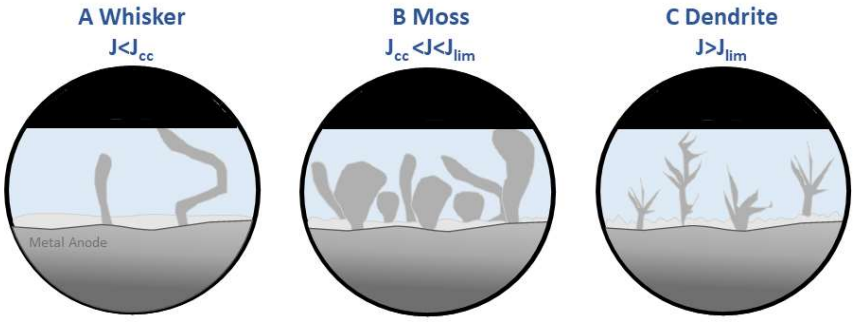


**Figure 3:** Illustration of different dendrite morphologies that can growth on a alkali metal electrode.[23,24]

## 2.3 The Electrode/Electrolyte Interphase

When an alkali metal is brought into contact with a battery electrolyte, reduction of salts, solvents, and trace impurities commences, giving rise to the SEI. [26] The SEI is a passivation layer that should exhibit the following properties: 1) high Ionic conductivity, to enable efficient ion transport with minimal energy loss, 2) electronic insulation, to prevent further electrolyte decomposition and parasitic reactions, 3) mechanical robustness, to withstand volumetric changes during cycling without fracturing, 4) chemical stability, to maintain its structure and composition over the battery's lifespan and 5) uniform coverage, to prevent localized hotspots for dendrite nucleation and growth.[27,28] The SEI forms spontaneously during the initial stages of cell operation, often during the first charging cycles but its composition and structure evolve dynamically throughout the battery's lifetime.[29] These requirements are particularly challenging for alkali metal anodes, where severe expansion and reactivity with solvents result in highly unstable SEIs. Such instability promotes dendrite growth and

increases the risk of short circuits, even under low current densities. Due to the complexity of the electrochemical reactions involved in its formation, the SEI is generally a heterogeneous, nanometer-thick structure, with a typical thickness ranging from 10 to 200 nm depending on the electrolyte composition, temperature, and the electronic conductivity of the decomposition products.[30] In most organic carbonate-based electrolytes, the SEI is conceptualized as a bilayer, composed of an inner inorganic layer and an outer organic layer.[31,32] The inner layer, located directly at the metal–SEI interface, is typically dense and composed of inorganic compounds as result of the reduction of the salt anions, such as lithium carbonate ($Li_2CO_3$), lithium fluoride (LiF), and lithium oxide ($Li_2O$).[31,32] Lithium-ion transport through this layer is theorized to occur via point defect mechanisms, such as vacancy or interstitial diffusion. In particular, the knock-off mechanism has been proposed, wherein an incoming lithium ion displaces an existing ion from its lattice site, enabling ion migration through the SEI matrix without requiring direct hopping.[31] The outer layer, situated at the interface with the bulk electrolyte, is more porous and largely organic in nature. It primarily consists of lithium alkyl carbonates such as ROLi and $ROCO_2Li$. In this region, lithium-ion transport is assumed to proceed through liquid-phase-filled pores following Fickian diffusion.[31] The structural and chemical heterogeneity of the SEI introduces spatial variability in ionic conductivity and mechanical properties across the electrode surface, contributing to non-uniform lithium deposition. This non-uniformity is a key factor in dendrite nucleation and growth, reinforcing the importance of a thorough understanding of SEI formation and evolution in the context of safe and efficient alkali metal battery operation. The SEI is a hybrid organic-inorganic passivation layer, often described by the mosaic model (**Figure 4A**), first proposed by Peled *et. al.*, where different decomposition products (e.g., carbonates, oxides, fluorides, polymers) coexist as hetero-poly-microphases.[33,34] This model points that the reduced inorganic compounds (e.g. $Li_2O$, LiF) dominate the inner layer near the metal surface while partially reduced organic species (e.g semicarbonates, polymers) form a porous outer layer.

Recent advancements in cryogenic transmission electron microscopy (cryo-TEM) have enabled direct imaging of the SEI while minimizing beam-induced damage.[35] In certain electrolyte environments, the SEI structure aligns with the mosaic model, characterized by small crystalline domains of $Li_2O$ and $Li_2CO_3$ embedded within an amorphous organic matrix, with a total thickness in the range of tens of nanometers (**Figure 4B**).[35,36] However, this structural arrangement is not universally observed. In some cases, the SEI appears entirely amorphous (**Figure 4C**), while in others, a distinct multilayered morphology has been reported (**Figure 4D**).[37–39] The physical characteristics of the SEI have significant implications for battery cycling performance, as heterogeneous mosaic-like structures have been linked to uneven lithium deposition and stripping, whereas multilayered SEIs appear to promote more uniform lithium plating and dissolution.

Beyond lithium-based systems, XPS analyses have shown that SEI compositions differ significantly across alkali metals. For example, potassium metal anodes in carbonate-based electrolytes tend to develop thick, amorphous SEIs rich in potassium carbonate ($K_2CO_3$) and organic species, whereas lithium metal in highly concentrated lithium-bis(fluorosulfonyl)imide/dimethoxyethane (LiFSI/DME) electrolytes forms relatively thin, crystalline SEIs dominated by LiF. The instability of the SEI layers on potassium electrodes presents additional challenges, leading to excessive volume expansion and high reactivity with solvents and continuous SEI breakdown and regeneration. These variations stem from the high chemical potentials of alkali metals, which provide a strong thermodynamic driving force for spontaneous reactions with both liquid and solid electrolytes. This driving force is expressed through the Gibbs free energy change ($\Delta G_R$) of the decomposition reactions, defined as the energy difference between reactants (alkali metal (am) and electrolyte molecules (elyte)) and reaction products ((rp) SEI compounds and gaseous by-products, reaction product):

$$\Delta G_R = \sum_i N_{rp}^i \mu_{rp}^i - N_{am}\mu_{am} - \sum_j N_{elyte}^i \mu_{elyte}^i$$

where μ represents the chemical potential and N the stoichiometric coefficients of each species (including SEI compounds and released gas).

Although the SEI formation is often described in terms of the difference between the alkali metal's Fermi level and the lowest unoccupied molecular orbital (LUMO) of the electrolyte, this oversimplifies the process. In reality, the kinetics are governed by a complex interplay of local free energy landscapes, interfacial reactivity, and transport limitations. These factors lead to SEI structures that are highly dependent on the metal type, electrolyte composition, and operational conditions ultimately dictating the morphological evolution of deposited alkali metal and its long-term cycling behavior.

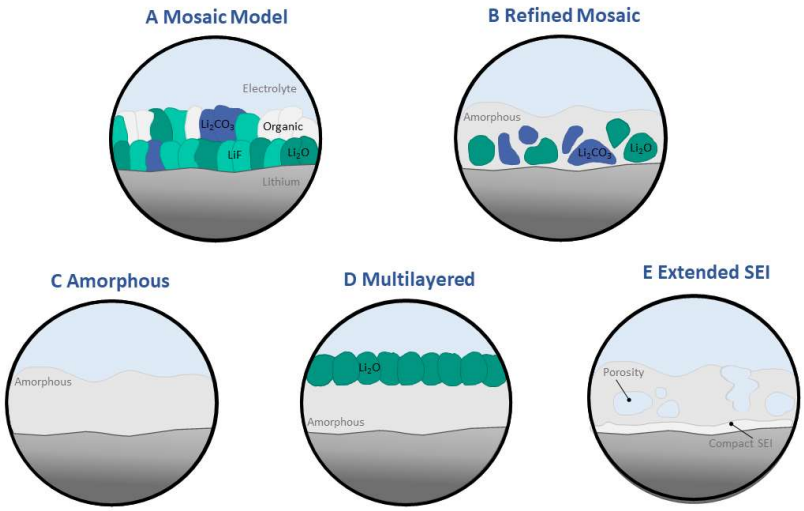


**Figure 4:** Illustration of different SEI nanostructures (A) mosaic model, (B) Refined Mosaic, (C) Amorphous, (D) Multilayered and (E) Extended SEI. [33–35,37–39]

### 2.3.1 SEI Dissolution

A key factor influencing SEI stability is the solubility of its inorganic and organic components in the electrolyte. Unlike in LIBs, where SEI dissolution is relatively limited, sodium-based SEI layers exhibit higher solubility due to the greater solubility of sodium salts such as sodium fluoride (NaF) and sodium carbonate ($Na_2CO_3$) in commonly used solvents.[40] This increased solubility can lead to continuous SEI degradation, electrolyte consumption, and capacity fade over prolonged cycling. Comparative studies have shown that SEI dissolution varies significantly depending on the electrolyte composition, including the choice of solvent, salt, and additives. For instance, electrolytes containing sodium hexafluorophosphate ($NaPF_6$) in propylene carbonate (PC) lead to higher SEI dissolution than those based on $NaPF_6$ in EC:PC (EC, ethylene carbonate) or EC:DEC (DEC, diethylcarbonate). One explanation for this behavior is that PC dissolves inorganic SEI components more readily than EC:DEC.[41] To counteract this effect, researchers have explored electrolyte formulations that mitigate SEI solubility by saturating the electrolyte with known SEI components, such as NaF and $Na_2CO_3$. By shifting the concentration equilibrium, these additives reduce the dissolution of the SEI, thereby improving its long-term stability.[42] Experimental results confirm that adding NaF to $NaPF_6$-based electrolytes effectively increases the inorganic content of the SEI, leading to improved passivation and reduced degradation.[43] In EC:DEC electrolytes, NaF addition reduced the initial SEI formation capacity by 77%, significantly lowering SEI dissolution rates and improving cycle life.[41] Conversely, in EC:PC electrolytes, NaF addition had a less pronounced effect, suggesting that the solvent environment plays a decisive role in determining the effectiveness of electrolyte additives. Additionally, while NaF is generally considered less soluble than $Na_2CO_3$ in aqueous solutions, this trend does not necessarily hold in organic electrolytes, emphasizing the need for direct solubility measurements in battery-relevant solvents.

## 2.4 Electrolytes

The electrolyte is critical to battery performance, influencing ionic conductivity, reaction kinetics, and electrochemical stability, which define the working potential range and energy density. It also affects SEI formation, composition, and stability, as well as ion storage kinetics, through solvation behavior, steric configuration, and chain length. According to molecular orbital theory, the electronic states of solvents and ion solvation (e.g., $Li^+$, $Na^+$, $K^+$) determine the electrolyte's anodic and cathodic stability.[44–46] However, the common practice of using the highest occupied molecular orbital (HOMO) and LUMO energy levels of isolated solvents to predict electrolyte stability is fundamentally flawed. These values do not accurately reflect redox reactivity in the electrochemical environment, as they ignore solvent-cation interactions and interfacial effects. Studies have shown that solvation

structure, how the cation interacts with surrounding solvent molecules, can significantly lower the oxidation onset potential, making even thermodynamically stable solvents vulnerable to early decomposition. Therefore, it is more correct to speak of potential of electrolyte reduction at negative potentials, and of potential of solvent oxidation at positive potentials.[47] Compatibility with electrodes is essential to prevent side reactions, capacity fading, and ensure high wettability, reducing polarization during battery reactions. In general, these include high ionic conductivity, wide electrochemical stability windows, thermal and chemical stability, and compatibility with cell components. In this work, the focus lies on liquid electrolytes and their ability to form stable interfaces and remain stable across the battery's operating voltage range to avoid side reactions, capacity loss, or safety hazards, as interfacial stability is central to the themes explored in this thesis.

### 2.4.1 Organic Electrolytes

Carbonate-based solvents have been the foundation of commercial lithium-ion battery electrolytes because they dissolve lithium salts effectively and offer a wide electrochemical stability window.[7,48] A group of solvents that fulfill most of these requirements is cyclic carbonate esters, such as ethylene carbonate (EC) and propylene carbonate (PC). Interest in EC and PC began in the mid-20th century, when Harris demonstrated their (electro-)chemical stability toward alkali metals.[49] Initially, a blend of lithium hexafluorophosphate ($LiPF_6$) with propylene carbonate (PC) was favored due to its high dielectric constant and chemical robustness and broad liquid temperature range (−49 to 242 °C), compared to EC (36 to 238 °C).[50] However, PC proved incompatible with lithium metal, yielding coulombic efficiencies below 85% and rapid capacity fade which drove the search for better solvents. When the focus in battery development shifted from lithium metal to graphite anodes, a significant difference between the two solvents became apparent: EC-based electrolytes clearly outperformed PC-based systems in terms of cycling stability.[51] Zhuang et al. showed via ex situ attenuated total reflectance fourier-transform infrared spectroscopy (ATR-FTIR) analysis that the SEI composition on graphite electrodes differs markedly depending on whether EC or PC is used.[52] Today, EC is widely employed as a co-solvent, due to its high dielectric constant and its ability to form a more stable SEI on graphite.[48] To reduce viscosity and improve low-temperature performance, EC is blended with linear carbonates such as DMC, DEC, or ethyl methyl carbonate (EMC). EC is essential in these mixtures as $LiPF_6$ does not dissolve in pure linear carbonates.[53] Although EC-based mixtures excel in graphite-anode cells, they generate SEI films on lithium metal that are too porous and mechanically weak to prevent dendrite growth and side reactions. EC's unique ability to form a robust SEI on graphite has made it indispensable in LIBs, but the same EC-based mixtures perform poorly with

lithium metal anodes. On lithium metal anodes, these solvents fail to produce a mechanically stable SEI, resulting in rapid dendrite growth and accumulation of “dead” lithium.[54]

In addition to solvent degradation, the chemical stability of the conducting salts themselves poses a major challenge in alkali metal systems, particularly due to their extreme sensitivity to trace moisture. Even trace amounts of water, typically specified at below 50 ppm in battery-grade electrolyte solvents and salts can significantly impact the performance and stability of batteries.[55] The water reacts with $LiPF_6$ and forms acidic species hydrogen fluoride (HF):

$$LiPF_6 + H_2O \rightarrow POF_3 + LiF + 2HF$$

$LiPF_6$ undergoes thermal decomposition even at room temperature, yielding LiF and phosphorus pentafluoride ($PF_5$).[56] The resulting $PF_5$, a strong Lewis acid, readily reacts with protic impurities such as water to generate hydrofluoric acid (HF): [56,57]

$$LiPF_6 \rightarrow LiF + PF_5$$

$$PF_5 + H_2O \rightarrow POF_3 + 2HF$$

The presence of acidic species like HF can severely impair battery performance by corroding current collectors, degrading electrode materials, and contributing to irreversible capacity loss.

A similar challenge arises with the use of $NaPF_6$ as the conducting salt in sodium based batteries. $NaPF_6$ is highly hygroscopic and prone to hydrolysis, producing NaF, HF, and phosphoryl fluoride ($POF_3$) even in electrolytes containing less than 20 ppm of water.[58,59] This pronounced sensitivity to moisture underscores the inherent instability of $NaPF_6$ and highlights the need for strict handling protocols and rigorous quality control. Notably, the extent of hydrolysis and thus the effective purity of commercial $NaPF_6$ can vary considerably depending on storage conditions and the synthetic route used for its production. The resulting hydrolysis products, particularly insoluble compounds such as NaF, can significantly reduce the effective salt concentration and negatively impact battery performance. To mitigate these issues, Menkin et al. proposed a synthesis route for high-purity $NaPF_6$ tailored for battery applications.[60]

In sodium-based battery systems, the challenges associated with carbonate ester electrolytes become even more pronounced. Mixtures of EC and PC incorporating sodium salts such as $NaPF_6$ or sodium bis(trifluoromethanesulfonyl)imide (NaTFSI) generate SEI layers enriched in sodium alkyl carbonates (RONa) and inorganic species like $Na_2CO_3$ and NaF. These SEI components are prone to dissolution in the electrolyte, leading to continuous electrolyte consumption and the accumulation of electrochemically inactive "dead sodium".[42] Additionally, carbonate-based electrolytes in contact with alkali metal producing gases such as carbon dioxide ($CO_2$), ethylene, and ethane ($C_2H_6$) through solvent decomposition. Gas generation is a critical safety issue in secondary batteries, because excessive gas buildup increases internal pressure, leading to cell swelling and potential explosions.[61,62]

Studies have shed light on the rapid degradation of carbonate ester electrolytes when exposed to alkali metals. Decomposition products, including dicarbonate compounds such as dimethyl dioxahexane dioate (DMDD), diethyl dioxahexane dioate (DEDD), and ethyl methyl dioxahexane dioate (EMDD), can be detected as early as two minutes after exposure (**Figure 5**). Their concentrations increase significantly within two hours, and additional tricarbonate species such as DMCC (di-(2-methoxycarbonyloxyethyl) carbonate), EMCC (2-methoxycarbonyloxyethyl-2-ethoxycarbonyloxyethyl carbonate), and DECC (di-(2-ethoxycarbonyloxyethyl) carbonate) form after prolonged aging of up to 14 days. These observations indicate that surface reactions begin almost immediately upon contact, rapidly altering the solvent composition through processes like transesterification, which also increases the amounts of DMC and DEC.[63] Experiments have demonstrated that metal surfaces in the presence of EMC, DMC, and DEC lead to fast transesterification reactions, significantly modifying the initial solvent composition. The formation of dialkyl dioxahexane dioate compounds, commonly referred to as dicarbonates, has been unambiguously detected using nuclear magnetic resonance (NMR) and GC–MS techniques.[63] Quantitative analyses reveal that the reaction rate for dicarbonate formation decreases in the order EC:DMC > EC:EMC > EC:DEC, while the inherent reactivity of the alkali metal surfaces follows the order potassium > sodium > lithium.[63] Furthermore, the presence of conducting salts such as potassium hexafluorophosphate ($KPF_6$) accelerates the formation of these dicarbonates, and experiments employing deuterated DMC suggest that an intermolecular reaction between cyclic and linear carbonates drives this process. When combined with performance data from coin cells, these findings suggest that an EC:DEC mixture is more advantageous in potassium-based half-cells compared to EC:DMC or EC:EMC systems. Formulations containing both linear and cyclic carbonates are widely used in lithium-ion batteries and have been adapted for sodium and potassium systems due to their synergistic effects. However, the reactivity between these two types of carbonates can lead to the formation of detrimental side products, most notably ethylene bis(alkyl carbonates), which have been linked to instantaneous capacity decay in graphite–lithium half-cells. Such degradation phenomena are particularly severe in sodium and potassium systems, raising critical questions about the transferability of degradation behavior observed in half-cell setups to full-cell configurations. This is especially relevant in the context of accelerated degradation processes observed in post-lithium storage systems like potassium-ion batteries.

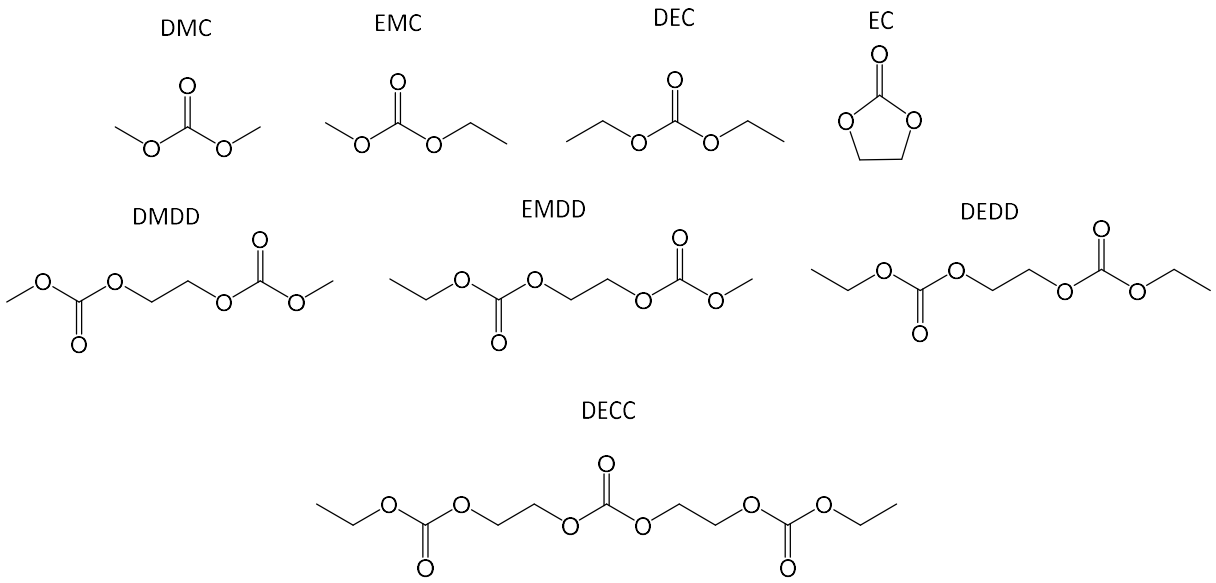


**Figure 5:** Linear organic carbonates (DMC, EMC, DEC), cyclic carbonates (EC), dicarbonates: DMDD (Ethane-1,2-diyl dimethyl biscarbonate), EMDD (Ethane-1,2-diyl ethylmethyl biscarbonate), DEDD (Ethane-1,2-diyl diethyl biscarbonate) and oligocarbonate: DECC (Di-(2-ethoxycarbonyloxyethyl)carbonate)

### 2.4.2 Additives

In addition to co-solvent blending and salt design, electrolyte additives serve as a critical strategy for stabilizing alkali metal anodes by addressing their inherent reactivity and instability in conventional electrolytes. Additives, typically introduced in small quantities (≤5 wt.% or vol.%), are engineered to modify interfacial chemistry, suppress parasitic reactions, and regulate metal deposition behavior. Their role extends beyond merely improving the SEI, they also enhance cathode electrolyte interphase stability, homogenize ion flux, and mitigate dendrite growth, all of which are pivotal for achieving high reversibility in alkali metal batteries. Film-forming additives are designed to preferentially decompose on alkali metal surfaces, creating stable SEI layers that shield the metal from continuous electrolyte degradation. Fluoroethylene carbonate (FEC), a widely used additive in Li-ion batteries, has proven effective in Li and Na metal systems.[64–67] However, in contact with potassium metal the effects of FEC are still under debate. While adding FEC to carbonate electrolytes with salts of $KPF_6$ and KFSI leads to deteriorate electrochemical performances it also showed suppressed gas evolution.[68] Vinylene carbonate (VC) is another prominent additive, particularly in lithium metal batteries. VC forms a stable polymeric SEI layer that enhances the mechanical and electrochemical stability of the interphase. This polymeric layer is highly flexible and ionically conductive, enabling dense lithium deposition and improving cycling performance.[69,70]

## 2.5 Zero-Excess Alkali Metal Batteries: Challenges and Opportunities

Anode-free alkali metal batteries, often termed “zero-excess” systems, represent a transformative leap in energy storage technology. Rather than using an insertion-type anode (e.g., graphite) or bulk metal foil, anode-free alkali metal batteries rely on operando electrochemical plating of alkali metals directly onto a bare current collector (Cu, Al, Zn) during charging. In these cells the cathode is pre-loaded with $Li^+$, $Na^+$, or $K^+$; upon charge, ions migrate through the electrolyte and deposit as metallic Li, Na, or K on the current collector, simultaneously forming a transient metal anode and its electrochemically derived SEI. During discharge the plated metal is stripped back into ions, which then reincorporate into the cathode, closing the cycle without any excess metal present. This innovative design maximizes energy density, simplifies manufacturing, and reduces material costs, positioning zero-excess alkali metal batteries as a frontier for next-generation batteries. However, the main challenge is related to plating and nterfacial instability, dendrite growth, and irreversible alkali metal loss, which must be overcome to unlock their full potential. This radical departure from conventional designs enables ultra-high theoretical energy densities by eliminating excess anode material. For instance, anode-free lithium batteries can achieve up to 60% higher energy density than graphite-based Li-ion systems.[71] The simplified architecture not only reduces manufacturing complexity and costs but also enhances safety by minimizing handling of reactive alkali metals. To prevent rapid capacity fade, with a coulombic efficiency (CE >99.9%) is required, as there is no cation reservoir of metal to compensate for losses during cycling.

The anode-free design amplifies three interrelated challenges: inhomogeneous metal deposition, SEI instability, and irreversible alkali loss. The loss of alkali inventory in anode-free alkali metal batteries is primarily caused by the production of electrochemical SEI as well as the generation and accumulation of dead alkali. Without a native metal substrate, nucleation barriers rise significantly, leading to uneven plating. Sodium and potassium, with their larger ionic radii and higher reactivity compared to lithium, exhibit pronounced tendencies toward mossy or dendritic growth.

***Optimization Strategies***. Recent advances focus on tailoring current collectors, electrolytes, and cycling protocols to mitigate these challenges. Current collector engineering plays a pivotal role: lithiophilic/sodiophilic/potassiophilic coatings (e.g., MXene, graphene, or Zn) reduce nucleation barriers. For example, graphene-coated Al (Al@G) enables dendrite-free K plating with 99.9% CE over 750 cycles, while Zn substrates outperform conventional Cu or Al in Na systems, achieving >99.9% CE due to their low nucleation overpotential.[72–75] Electrolyte design is equally critical, high-concentration salts (e.g., 4 M NaFSI/DME) are related to a stable SEIs, while additives like fluoroethylene carbonate (FEC) enrich inorganic content (LiF, KF).[76,77] Solid-state electrolytes, though nascent for Na and K, show promise in Li systems by blocking dendrite penetration. Mechanical

pressure (~1 MPa) and temperature-controlled protocols ("hot formation") further stabilize interfaces and homogenize ion flux.

***Advantages in Energy Density and Sustainability.*** Anode-free alkali metal batteries offer unparalleled energy density gains and sustainability benefits. For instance, anode-free Na configurations paired with Prussian white cathodes achieve 81% higher volumetric energy density than traditional Na-ion cells. Economically, eliminating anode production steps reduces material costs by 15–30%, while sodium's abundance (2.36% of Earth's crust) and lower carbon footprint diminish reliance on scarce resources like cobalt. Anode-free designs also align with green energy goals, reducing global warming potential (GWP) by 29% compared to Li-ion batteries.

# 3 Methodology

This chapter outlines the experimental techniques and procedures employed to investigate the surface chemistry and electrochemical behavior of alkali metal anodes. Building on the theoretical considerations presented in **chapter 2**, the methodology focuses on two key aspects: (i) X-ray photoelectron spectroscopy (XPS) for surface-sensitive chemical analysis and (ii) electrochemical characterization methods, including galvanostatic cycling and metal plating/stripping protocols. Emphasis is placed on experimental design for handling highly reactive alkali metals, including preparation strategies, sample transfer under inert conditions, and washing protocols to remove residual electrolytes. A dedicated section discusses sputter-induced effects during depth profiling and their influence on spectral interpretation, particularly regarding native oxides, carbonate decomposition, and SEI constituents.

## 3.1 X-Ray Photoelectron Spectroscopy

X-ray Photoelectron Spectroscopy is a surface-sensitive analytical technique used to determine the elemental composition, chemical state, and electronic structure of materials. It is based on the photoelectric effect, first explained by Albert Einstein in 1905, for which he received the Nobel Prize in 1921.[78] The development of high-resolution XPS, notably advanced by Kai Siegbahn, was recognized with the Nobel Prize in Physics in 1981.[79]

Understanding the basic principle of XPS requires introducing the fundamental energy balance that governs the photoemission process. This is expressed by equation:

$$h\nu = E_{binding}^{vacuum} + E_{kinetic}^{'} + V_{charge} + V_{bias}$$

$$h\nu = E_{binding}^{Fermi} + \varphi_{spectrometer} + E_{kinetic} + V_{charge} + V_{bias}$$

In this context, $h$ is Planck's constant and *v* the frequency of the incident photon (*hv* being the photon energy). The binding energy (BE) of an electron with respect to the vacuum level is denoted $E_{binding}^{vacuum}$, while $E_{kinetic}^{'}$ is the electron's kinetic energy immediately upon leaving the sample surface. The energy actually measured by the spectrometer, $E_{kinetic}$, may differ due to various external effects. Specifically, $E_{binding}^{Fermi}$ refers to the binding energy relative to the sample's Fermi level. $V_{charge}$ accounts for shifts caused by sample charging, particularly when charge compensation is insufficient. $V_{bias}$ represents any additional bias voltage applied between the sample and the analyzer, and $\varphi_{spectrometer}$ is the work function of the spectrometer used to detect the electron. When measuring XPS, the photoelectron is usually not generated from an isolated atom but from a solid. Therefore the kinetic energy and knowing the spectrometer's work function ϕ, the binding energy of photoemitted electrons can be calculated. This enables detailed identification of the elements present, their chemical

environment, and the electronic structure of the material's surface. The energy relation can be summarized more concisely by the following simplified equation:[80]

$$E_{binding} = h\nu - E_{kinetic} - \varphi_{spectrometer}$$

In this work an Al Kα source is used, as is typical, generating X-rays with hν = 1486.6 eV. The spectrometer's work function ϕ is typically just a few eV. XPS is performed under ultrahigh vacuum (UHV) conditions to prevent the emitted electrons from being scattered by gas molecules before they can reach the detector. A scheme of the XPS setup is shown in **Figure 6**, whith the main features, photon source and electron analyser with its hemispherical shape. X-rays are generated by an x-ray source and monochromatized via a single crystal, which also focuses the X-rays on the probed sample. Before entering the hemispherical energy analyzer, the emitted photoelectrons are decelerated to a defined pass energy using electron optics. The pass energy is held constant to ensure uniform energy resolution during spectral acquisition. Electrons are detected via a multichannel detector in the number of electrons for a given detection time and energy. Scanning for different energies is accomplished by applying variable electrostatic fields before the analyzer.[81]

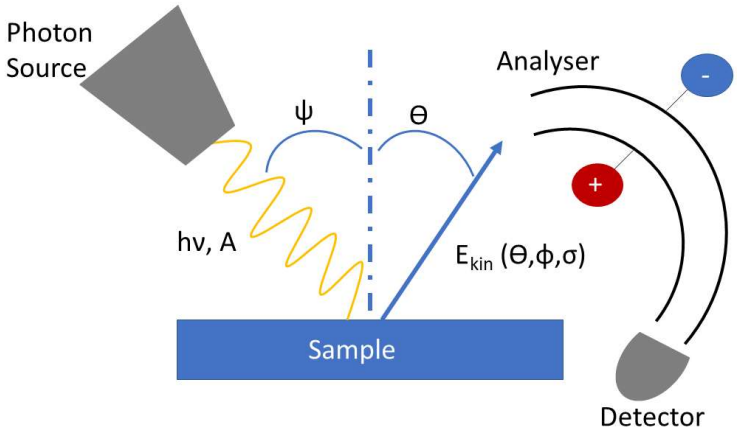


**Figure 6:** XPS experietal set up

As illustrated in **Figure 7**, a photon of energy hν excites an electron from a core level with binding energy $E_B$, promoting it above the vacuum level and allowing it to escape the sample. While the photoemission process inherently involves a many-body system, it can be approximated as a single-particle event when electron–electron correlation effects are sufficiently weak. In such cases, the photoelectric effect can be described by Fermi's golden rule, which arises from first-order time-dependent perturbation theory:

$$w_{fi} = \frac{4\pi^2}{h}\left|\langle f|\vec{eV}|i\rangle\right|^2 \delta(E_f - E_i - h\nu)$$

It describes the trasition rate $w_{fi}$ as a photo-induced excitation of a electron from a initial state $|i\rangle$ to a final state $|f\rangle$ (i.e., the electron wave function of the final state in the continuum) as a result of perturbation (i.e., photon or dipole operator: $\vec{eV}$). The $\delta(E_f - E_i - h\nu)$ corresponds to the Dirac delta

distribution and allows a transition only for $\delta(E_f - E_i - h\nu) = \delta(0) = 1$. $E_f$ is the energy state of the final state and equals the kinetic energy $E_k$ of the photoelectron and its interaction with the surrounding electrons $E_f(N-1)$, see **Eq.(1)**. Energy states of the initial state $E_i$ correspond to the interaction with the surrounding electrons $E_f(N-1)$, after photoelectron emission and the binding energy $E_B$, see **Eq.(2)**. Substituting **Eq.(1)** and **Eq.(2)** in $\delta(Ef - Ei - h\nu)$ leads to the kinetic energy of the emitted photoelectron, see **Eq.(3).**

$$E_f = (E_k - E_f(N-1) \quad (\mathbf{Eq.1})$$

$$E_i = (E_f(N-1) - E_B \quad (\mathbf{Eq.2})$$

$$E_k = h\nu - E_B \quad (\mathbf{Eq.3})$$

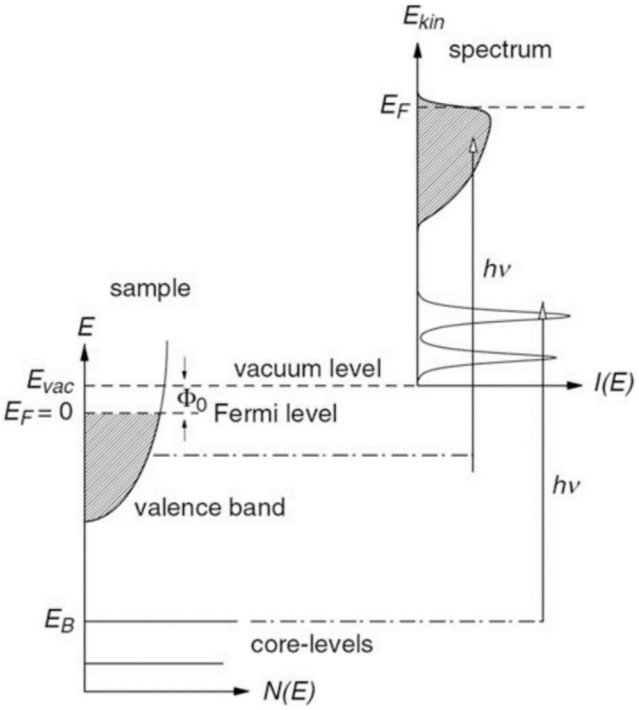


**Figure 7:** Different energy levels involved in the XPS process. [81]

When measuring XPS the initial excitation is often treated within the single-particle approximation (Koopman's theorem), final state effects such as orbital relaxation and electron correlation (e.g., shake-up or shake-off processes) must be considered for accurate interpretation, especially in solids. Additionally, Auger processes may follow photoemission, where core holes are filled by higher-energy electrons, resulting in the emission of secondary Auger electrons (**Auger electrons will be discussed in chapter 3.1.2 and 3.1.2.1**). With soilds the kinetic energy of the generated photoelectron must be complemented by a work function $\phi$ that describes the minimum energy required to remove the electron from the surface of a solid. When the sample is in Ohmic contact with the spectrometer, their Fermi levels equilibrate. In this configuration, it is not necessary to account for the sample's work function, since the reference energy scale is effectively defined by the spectrometer. The

spectrometer's work function, typically stable and well-characterized, can be experimentally calibrated using a metallic standard, where the Fermi edge is set to a binding energy of zero by convention. This allows accurate determination of binding energies without requiring prior knowledge of the sample's absolute energy levels. Moreover, spin–orbit coupling leads to characteristic splitting of p, d, and f orbitals upon ionization, resulting in subshells such as $p_{1/2}$, $p_{3/2}$, $d_{3/2}$, $d_{5/2}$, $f_{5/2}$, and $f_{7/2}$. Since each element exhibits a unique set of binding energies, XPS enables both elemental identification and quantification of surface species. Beyond elemental analysis, the binding energy also depends sensitively on the local chemical environment. For instance, in organic molecules, carbon atoms bonded to hydrogen or other carbon atoms (–C–H or –C–C) exhibit a characteristic binding energy of 285 eV. When carbon is bonded to more electronegative atoms such as oxygen, the electron density around the carbon is reduced, leading to a shift toward higher binding energies. This effect is observed in species such as –C–O (286.5 eV) and –C(=O)O (288 eV), allowing XPS to distinguish between different chemical states of the same element.

The surface sensitivity of XPS arises from the strong interaction of electrons with matter. As photoelectrons travel through a solid toward the surface, they are highly susceptible to inelastic scattering, during which they lose energy. Only those electrons that originate within a shallow region, typically just a few tens of angstroms beneath the surface can escape without energy loss and contribute to the distinct peaks observed in the XPS spectrum. In contrast, electrons that undergo inelastic collisions contribute to the continuous spectral background. The characteristic length describing the average distance an electron travels before such an energy-loss event is known as the inelastic mean free path (IMFP, denoted λ). Statistically, approximately 95% of the photoelectrons detected in an XPS measurement originate from within a depth of 3λ. The IMFP depends on the kinetic energy of the emitted electrons and the material's composition, core-level electrons in denser elements typically have shorter mean free paths. This surface sensitivity defines two fundamental requirements and consequences for XPS analysis. First, to reduce scattering by residual gas molecules and to prevent adventitious contamination of the sample surface, all XPS measurements are conducted under UHV conditions. Second, the limited escape depth implies that XPS probes only the outermost few nanometers of a material, making it particularly susceptible to the presence of atmospheric contaminants such as moisture, dust, or $CO_2$, which may mask or alter the actual surface composition. Assuming inelastic scattering is negligible, the intensity of photoelectrons escaping from a given depth can be described by the Beer–Lambert law, which models an exponential attenuation of signal with depth:

$$I = I_0 e^{-\frac{d}{\lambda cos\alpha}}$$

Here, $I_0$ denotes the initial photoelectron flux originating at a depth d, and α represents the angle between the sample surface normal and the direction toward the analyzer. The quantity λ cos(α)

defines the mean escape depth, which expresses the effective path length over which electrons can travel without undergoing inelastic scattering. Accordingly, the mean escape depth Δ can be defined as:

$$\Delta = \lambda \cos \alpha$$

This value provides an estimate of the average depth, measured along the surface normal from which electrons can escape without significant energy loss. Here, λ denotes the IMFP, and α is the electron emission angle relative to the surface normal. Empirical and theoretical values for λ have been determined for a wide range of materials.

### 3.1.1 Depth Profiling and Sputter Induced Effect

XPS depth profiling is regularly perfomed for in situ cleaning, often using gas cluster ion beams, which offer a significantly gentler alternative to conventional monoatomic argon ion sputtering. Gas cluster ion beams minimize surface damage and are especially advantageous for delicate or chemically complex samples. Nevertheless, any sputtering process inherently carries the risk of preferential sputtering, which can alter surface composition, such as the reduction of metal oxides during ion bombardment. This becomes particularly problematic for sensitive materials like spin-coated polymer films or organic layers, where sputtering can severely distort features such as the C 1s region. In such cases, avoiding sputter cleaning and tolerating some degree of adventitious carbon may be the more prudent approach.[82,83] Besides in situ cleaning, depth profiling via ion sputtering is widely employed in battery research to investigate the composition, thickness, and internal layering of the solid SEI. This method enables detailed insights into how the SEI evolves with cycling and electrolyte composition. However, ion sputtering, especially with monatomic $Ar^+$ beams can significantly alter the SEI's chemical structure, introducing artifacts that complicate quantitative interpretation. Such bombardment may induce reduction reactions in metal oxides or other inorganic SEI constituents, as observed for copper(I) oxide ($Cu_2O$) where additional features appear in XPS spectra post-sputtering. These changes obscure the native chemical state of the SEI and hinder accurate assessment of its functional role in battery performance.[83] To date, there are few systematic investigations on sputtering effects in the context of battery-related SEI analysis. One notable exception is a study by Hess et al., who examined the stability of reference compounds under $Ar^+$ sputtering. Their results showed that compounds like LiOH and $Li_2CO_3$ partially decomposed to $Li_2O$, while carbonate species disappeared entirely with prolonged sputtering. Additionally, carbide formation was observed, attributed to beam-induced decomposition of surface carbon contaminants, not as intrinsic SEI components. The emergence of metallic lithium signals after extended sputtering highlights the risk of over-interpretation and underscores the need for careful control and calibration in depth profiling experiments.[84] As part of

this thesis, a systematic investigation was carried out to assess the impact of different ion beam sources on Li metal and depth distribution. Therefore, monoatomic and cluster ion sources were compared under identical conditions. No compositional differences were observed between the two methods, however, even cluster sputtering, typically considered less damaging, resulted in an increase of $Li_2O$ signal intensity (**Figure 8**). Metallic lithium could not be detected at any point, even with a prolonged monoatomic $Ar^+$ energy of 3 keV (high), $LiO_2$ features were still observed, suggesting sputter-induced chemical modifications rather than exposure of the underlying metal.

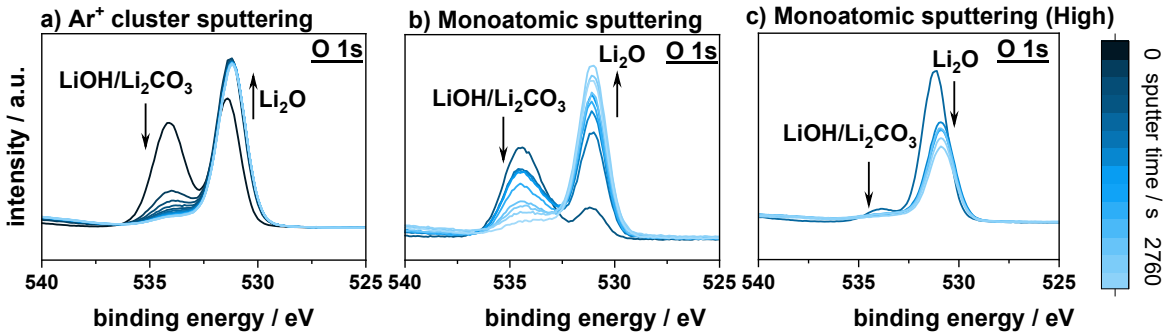


**Figure 8:** O 1s spectra for Li metal with different sputtering conditions: a) $Ar^+$ cluster ion sputtering, b) Monoatomic argon sputtering with 1keV and c) Monoatomic argon sputtering with 3keV.

In addition, sputtering effects on common electrolyte salt residues were studied, focusing on $NaPF_6$, NaF, and NaTFSI (**Figure 9**). In both $NaPF_6$ and NaTFSI systems, the F 1s signal of the parent compound decreased upon sputtering, while NaF signal intensity increased, indicating partial decomposition of the salts under ion bombardment. The same set of experiments was carried out for potassium-based salts ($KPF_6$, potassium fluoride (KF), and potassium bis(trifluoromethanesulfonyl)imide (KTFSI)), yielding analogous results. Details and comparative spectra are provided in the Supporting Information (**Figure S1**).

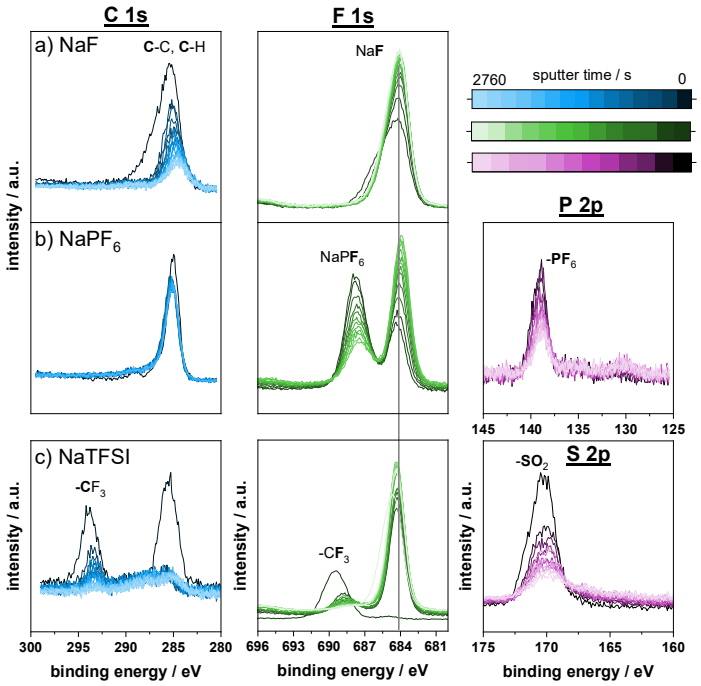


**Figure 9:** C 1s, F 1s, P 2p and S 2p spectra for the Na salts a) NaF, b) $NaPF_6$ and c) NaTFSI sputtered with monoatomic argon (1keV).

Reference measurements of sodium oxide ($Na_2O$) and sodium peroxide ($Na_2O_2$) were performed to support oxide peak assignments, however, under the applied conditions, only $Na_2CO_3$ and sodium hydroxide (NaOH) were reliably detected (**Figure 10**). Following sputtering intended to remove surface contamination or adventitious layers, only a slight increase in these oxide-related signals was observed, suggesting either limited surface coverage or rapid alteration of more reactive SEI components during the sputtering process.

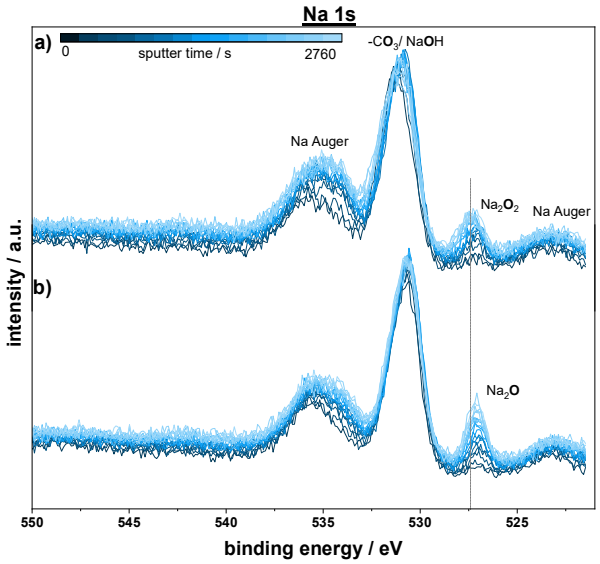


**Figure 10:** O 1s spectra for the a) peroxide $Na_2O_2$ (top) and b) oxide $Na_2O$ (bottom) sputtered with monoatomic argon (1keV).

### 3.1.2 Peak Shape

In X-ray photoelectron spectroscopy, electrons from s-orbitals (with angular momentum quantum number l = 0) produce single, unsplit peaks due to the absence of spin–orbit coupling. However, for electrons in p, d, and f orbitals (l = 1, 2, and 3), spin–orbit interaction leads to a splitting of the energy levels. This results in two distinct peaks, corresponding to the total angular momentum quantum numbers $j = l \pm ½$. The component with $j = l – ½$ appears at slightly higher binding energy compared to the $j = l + ½$ peak. The intensity ratio between the two components reflects their degeneracy (2j + 1), yielding expected ratios of 1:2 for p, 2:3 for d, and 3:4 for f orbitals. Each photoemission event leaves behind a core hole that exists for a finite duration, causing natural broadening of the emitted electron's spectral line. This broadening is Lorentzian in nature. Additional broadening introduced by the instrument and X-ray source typically follows a Gaussian distribution. The resulting peak shape is best described by a Voigt profile, which is a convolution of Lorentzian and Gaussian functions. In practice, this is often approximated by convoluted-based Gaussian–Lorentzian fitting functions for peak analysis. The width of an XPS peak, quantified as the full width at half maximum (FWHM), is governed by several factors: the natural width of the photoemission line, the energy resolution of the X-ray source, and the analyzer's performance. Prior to detection, emitted electrons are slowed to a defined pass energy ($E_{pass}$) in the hemispherical analyzer. A lower pass energy improves spectral resolution at the cost of signal intensity. In this study, a pass energy of 200 eV was used for wide-range survey scans, while 50 eV was selected for detailed core-level spectra to balance resolution and sensitivity.

When analyzing metallic systems, peak asymmetry is often observed. This arises from additional energy losses experienced by photoelectrons. One such mechanism is the excitation of electrons into empty conduction band states, while another involves the generation of plasmons, coherent oscillations of the electron gas within the material. The latter gives rise to satellite features, known as plasmon-loss peaks, at discrete energy intervals on the high binding energy side of the main signal. In highly conductive materials like lithium or sodium metal, these loss features are pronounced and must be carefully distinguished from other chemical components, especially in complex environments such as battery solid electrolyte interphases.

Finally, XPS measurements also capture Auger electrons, which originate from a non-radiative relaxation process. In this case, an electron from a higher energy level fills a core-level vacancy, while a second electron is ejected. For example, in a KLL Auger transition, an L-shell electron fills a K-shell hole, and a second L-shell electron is emitted. Unlike photoelectrons, whose binding energy is fixed by the incident photon energy, Auger electrons have constant kinetic energy, which makes their identification in spectra distinct.

#### 3.1.2.1 The XPS Signature of Pristine $Na^0$

To remove the passivation layer, the pristine Na was sputter-cleaned using a 1000 eV $Ar^+$ ion gun inside the XPS chamber for a total sputtering time of 2450 s. The removal of surface contaminants was confirmed in the survey spectrum by the disappearance of the signals in the O 1s and C 1s regions and by the metallic Fermi edge in the valence band region. **Figure 11a, b and c** shows XPS signals of the Na 1s and O 1s regions of the sputter-cleaned Na sample revealing Na metal. The Na 1s region was scanned across a wide BE range, as shown in **Figure 11b**, to capture multiple plasmon peaks**. Figure 11c** presents a narrower range view of the Na 1s region centered on the main $Na^0$ peak. **Figure 11a** displays the XPS signals in the O 1s region (between 520 and 545 eV). The region is called the O 1s region in relation to **Figure 22 (Chapter 7.1)**, however it should be noted that the peaks are primarily caused by Na metal Auger photoelectrons and their plasmon losses. In **Figure 11b**, the main $Na^0$ peak (at 1069.3 eV) is followed by a series of periodic plasmon peaks. A plasmon corresponds to a collective oscillation of valence electrons in a metallic sample.[85] The peaks appearing at higher BE relative to the main $Na^o$ peak represent photoelectrons that have lost one or multiple quanta of energy to excite plasmon resonances. Photoemission can generate both bulk and surface plasmons in metallic samples. In **Figure 11b**, bulk plasmons produce distinc peaks at integral multiples of ΔEBP = 5.9 eV from the main $Na^0$ peak. The first surface plasmon is observed at ΔESP = 4.0 eV from the main $Na^0$ peak. Despite early contributions by Barrie and Street in their 1975 XPS study of sodium metal and sodium oxide, existing literature lacks a robust fitting model for the Na 1s spectral region of metallic sodium ($Na^o$), including its inelastic background.[86] Plasmon resonances profoundly alter the background signal, distorting it

up to 50 eV below the main peak. To address this, the Tougaard background, rather than the conventional Shirley method, is essential for accurate spectral fitting.[87] The parameters for the Tougaard function were derived from broad-range XPS data (**Figure 11c**), which captures the periodic nature of bulk plasmon losses. While this function aligns well with the background intensity at BE exceeding 15 eV above the main peak, it fails to fully account for the first and second plasmon loss features. This discrepancy arises because the model incorporates only extrinsic plasmon effects, neglecting intrinsic contributions. Intrinsic plasmons originate during the initial photoemission event at the excitation site, whereas extrinsic plasmons emerge as photoelectrons traverse the material, interacting with its electron density. Consequently, the Tougaard background plateaus above the main peak but underestimates losses linked to intrinsic plasmon excitations.[88,89] **Figure 11a** shows the identification of the O 1s region with the most intense signal at 529.9 eV attributed to Na-$KL_1L_{2,3}(^1P)$ Auger peak. A critical distinction lies in the differing positions of the Auger peak between metallic sodium ($Na^o$) and sodium oxides.[86] For example in case of the pristine Na with surface contaminations of oxide species (**Figure 22, chapter 7.1**), the Na Auger peaks observed at 535.5 eV shifted by 5.6 eV. Like their photoelectron counterparts, Auger electrons can also induce plasmon excitations, generating periodic loss features. These plasmon peaks mirror the periodicity observed in the Na 1s region, with bulk and surface plasmon intervals. Notably, the peak at 523.2 eV corresponds to the second plasmon loss feature associated with the Na–$KL_1L_{2,3}(^3P)$ Auger process. To conclude this chapter, characterizing the decomposition reaction occurring at a buried interface with a technique whose depth resolution is limited to a few nanometers (such as XPS) is a challenging task.

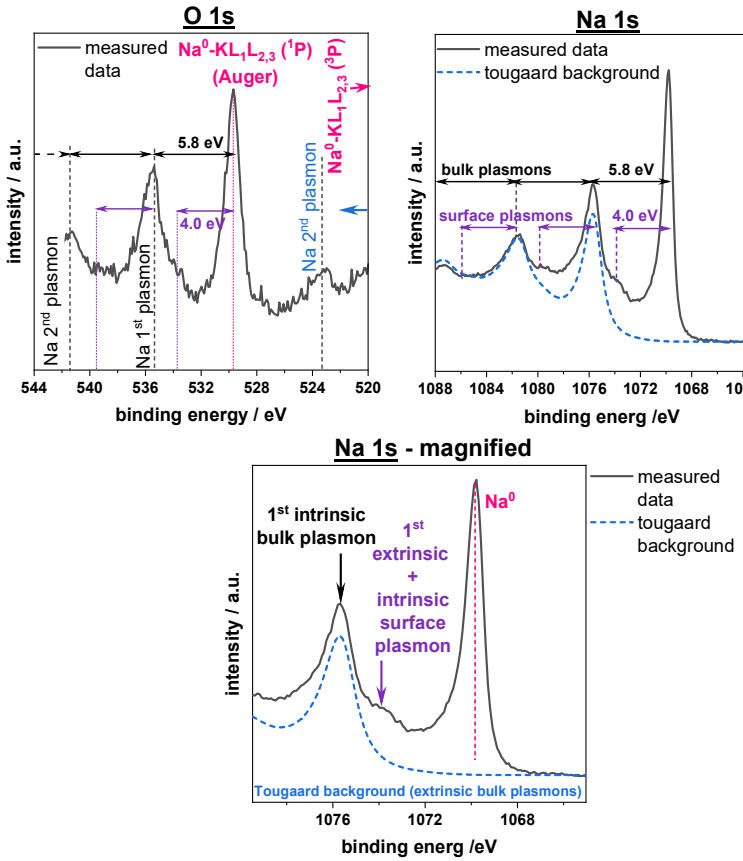


**Figure 11:** Fitting model of sputter-cleaned Na metal with tougaard background: (a) Identification of the peaks observed in the O 1s region, (b) Na 1s region measured over a wide BE range and (c) magnified region of Na 1s and corresponding fitting model.

### 3.1.3 General Procedure for XPS Data Analysis

#### 3.1.3.1 UHV

X-ray photoelectron spectroscopy is typically conducted under UHV conditions. This is primarily to prevent electron scattering by residual gases and to minimize surface contamination. While pressures around $10^{-6}$ mbar are generally sufficient to suppress scattering effects, surface adsorption of residual gas species remains significant at this level. Therefore, modern XPS systems routinely operate at even lower pressures, often below $10^{-8}$ mbar. Achieving and maintaining such vacuum levels requires a combination of advanced pumping technologies, including turbomolecular and ion pumps, supported by pressure gauges and valve systems to regulate the environment. Additionally, UHV systems regularly undergo a "bakeout" procedure in which the entire chamber is heated to approximately 100-200 °C for several days using external heating elements. This process facilitates the desorption of gas molecules and moisture trapped on the chamber walls and internal components. Despite these precautions, it is important to recognize that the UHV environment cannot be considered entirely inert or pristine, extended exposure of reactive metal surfaces, such as alkali metals, to UHV conditions

alone can still lead to measurable surface changes. **Figure 12** shows pristine potassium metal after $Ar^+$ sputtering (a), and the same surface after an additional 8 hours under UHV inside the XPS chamber (b). The comparison illustrates that even in the absence of external contaminants, the high reactivity of potassium can result in a surface alterations over time.

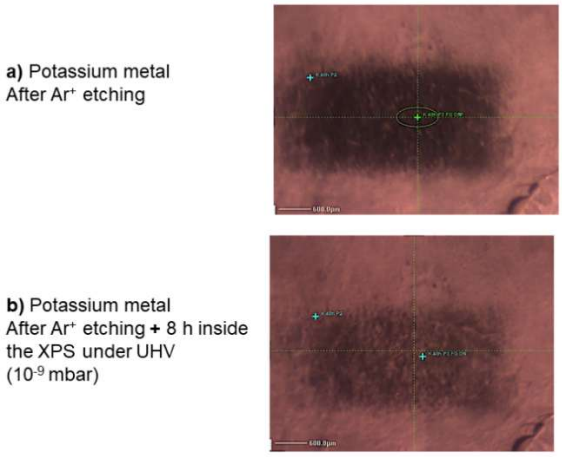


**Figure 12:** Pristine potassium metal (a) after $Ar^+$ etching and (b) after $Ar^+$ etching followed by 8 h under ultra-high vacuum (UHV) inside the XPS chamber.

### 3.1.3.2 Washing Strategies

XPS is an *ex-situ* characterization technique that requires disassembling electrochemical cells in an Ar-filled glovebox ($H_2O$ and $O_2$ < 0.1 ppm) to prevent air exposure. To remove residual electrolyte, electrodes are typically rinsed with a solvent chemically compatible with the electrolyte. However, this step risks altering the SEI composition, as highlighted in prior studies. For instance, Somerville et al. reported that washing removes fluorine-containing species like LiF, a critical SEI component.[90] To systematically evaluate the impact of washing, two protocols were compared against an unwashed control: (a) 2 min solvent immersion and (b) 10 min solvent immersion. In this work, metal electrodes were immersed in the electrolyte and subsequently rinsed with the solvent DEC. For later analyses (detailed in subsequent chapters), cycled cells will be opened under inert conditions, and the electrodes will undergo similar rinsing protocols. This approach aligns with established methods but acknowledges the inherent challenges of preserving SEI integrity during solvent exposure. **Figure 13** illustrates C1s, O1s, F1s, and P2p spectra for three Na electrodes stored in DEC:EC $NaPF_6$ electrolyte for 2 min. Each metal electrode was assigned to a distinct DEC rinsing protocol to evaluate the solvent's influence on SEI composition. While minimal differences were observed in C1s and O1s spectra across methods, significant variations emerged in F1s and P2p spectra. The unwashed sample exhibited a prominent $NaPF_6$/$Na_xPF_y$ decomposition product peak, which drastically diminished after washing for

2 min. To preserve NaF-rich layer, 2 min immersion was adopted as the standard. The same washing protocol was applied for pristine Na stored in DEC:EC NaTFSI and is shown in **Figure S2**.

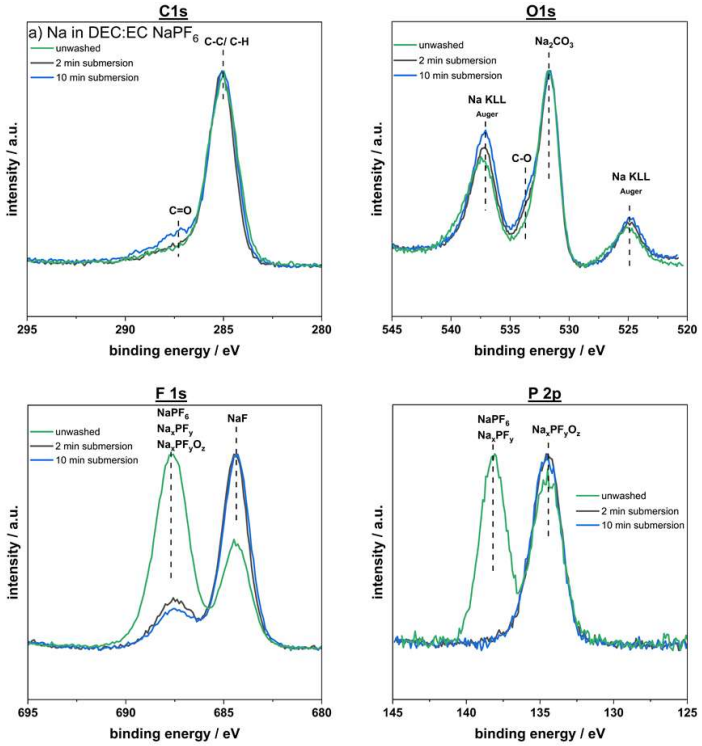


**Figure 13:** Influence of different washing procedures on the composition of the C 1s, O 1s, F 1s and P 2p spectra of pristine Na stored in DEC:EC NaPF6 for 2 min and washed through a submersion step afterwards (2 min and 10 min)

## 3.2 Electrochemical Analysis of Batteries

In this thesis, various alkali metals were investigated through electrochemical testing. Symmetrical sodium metal cells were employed to examine the influence of different electrolytes and to study the processes occurring at the electrode–electrolyte interface, including dendrite formation. In addition, potassium half-cells, comprising potassium metal as the counter electrode and hard carbon as the working electrode, were used to explore the intercalation mechanism and to evaluate how different grades of potassium metal affect the electrochemical performance during cycling.

### 3.2.1 Galvanostatic Cycling

Galvanostatic cycling is a widely applied method for investigating the performance and stability of batteries and battery prototypes under repeated charge–discharge conditions. In this thesis, galvanostatic cycling with potential limitation (GCPL) was employed as a standard technique to minimize irreversible side reactions that may occur in highly oxidative or reductive potential regions.

Battery performance is typically evaluated based on charge and discharge behavior within a defined voltage window and at a specified cycling rate. This rate, referred to as the C-rate, is commonly expressed as C/h (e.g., in A $g^{-1}$ or mA $g^{-1}$), where h denotes the number of hours required to (dis)charge the theoretical capacity of the electrode or full cell. For instance, a C-rate of C/10, as applied in this work, corresponds to a current density that charges or discharges the cell over a period of 10 hours. GCPL allows for the assessment of key electrochemical parameters, including charge ($Q_{ch}$) and discharge ($Q_{disch}$) capacities, rate capability, voltage profiles, hysteresis, and Coulombic efficiency (CE), defined as the ratio of: $CE = \frac{Q_{dis}}{Q_{ch}}$

### 3.2.2 Plating and Stripping

During electrochemical cycling, $X^+$ cations undergo reduction ($X^+ + e^- \rightarrow X$, X=Li, Na, K), depositing alkali metal onto the electrode surface. A fraction of this deposited metal can be reversibly stripped ($X \rightarrow X^+ + e^-$), with the efficiency of this process reflecting interfacial stability. The overpotential, the deviation between the equilibrium potential and the actual operating potential serves as a critical indicator of energy barriers and kinetic limitations during plating and stripping. By controlling the applied current, the overpotential reveals insights into mass transport, charge transfer, and nucleation processes. These steps govern metal deposition: (1) mass transport of ions to the electrode, (2) charge transfer at the interface, and (3) nucleation of alkali metalls, each contributing to the overall overpotential. Monitoring this parameter enables assessment of electrolyte compatibility and SEI robustness in alkali metal systems.

# 4 Experimental Part

## 4.1 Electrode Preparation

The slurry for the hard carbon (HC) electrode was prepared and provided as part of the standard material from POLiS, in an aqueous process. The conductive additive Super C65 (Imerys) and a MAC500LC (Nippon Paper) carboxymethyl cellulose (CMC) binder-solvent solution with 2 wt% were dispersed. HC (Kuranode Type II, 9 µm, Kuraray) and additional water were added. In a last mixing step, an aqueous solution of styrene-butadiene rubber (SBR, 40 wt %, Zeon Europe) was added to adjust the final solid content to 43 wt %. The electrode coating and drying was carried out under quasi-isothermal drying conditions as a discontinuous process likewise described by Klemens et al..[91,92] The slurries were applied to an aluminum current collector by a doctor blade (ZUA 2000.60, Zehntner) and dried by an impingement dryer and temperature controlled heating plates, resulting in drying rates of 0.75 $gm^{-2}$ $s^{-1}$ in both cases. After drying, the electrodes were calendered at 50 °C. The composition of 4.5 wt % polyvinylidene fluoride (PVDF) and 93 wt % HC, 1.4 wt % C65, 1.87 wt % CMC, 3.73 wt % SBR, respectively.

## 4.2 Electrolyte Preparation

The handling and preparing of all solvents and electrolytes was conducted in an argon-filled glovebox (MBraun, $O_2$<0.1 ppm, $H_2O$<0.1 ppm). The salts were dried under vacuum at 80 °C for 48 h. For the electrolyte 0.75 M lithium-/sodium-/potassium-hexafluorophosphate ($XPF_6$, X=Li, Na, K, Alfa Aesar, >99%) was dissolved in a 1:1 (by volume) mixture of EC (Sigma Aldrich, 99%) with either PC (Sigma Aldrich, 99.7%) or DEC (Gotion, >99.0%, dry). For the electrolyte with additive, 5 vol.-% FEC (Sigma Aldrich, 99%) was dissolved in the electrolyte. For further solvent test on sodium metal (**chapter 7.4**) additional 0.75 M $NaClO_4$ (Alfa Aesar, anhydrous, ACS, 98.0–102.0 %) was dissolved in 1) DEC:EC (50:50 vol.-%) and 2) PC with a third electrolyte was prepared by adding 10 % VC (Thermo Scientific Chemicals, 98 %) by volume to the 0.75 M $NaClO_4$ in PC electrolyte. In **chapter 8.1** different potassium electrolyte solvent mixtures were prepared from dimethyl carbonate (DMC, Gotion, >99.0%, dry), DEC, ethyl methyl carbonate (EMC, Merck, >99.0%, dry) and EC. Three different solvent mixtures were prepared, each containing 50 vol.% EC and 50 vol.% of a linear carbonate (DMC, DEC or EMC). The water content on the pure solvent and the electrolytes with and without additive was determined by Karl–Fischer–Titration. Each experiment was carried out three times and the values were averaged. A summary of all electrolytes can be found in **Table S1**.

## 4.3 Cell Preparation and Electrochemical Characterization

### 4.3.1 Sodium vs Sodium Symmetrical Cell and Sodium vs Copper Half Cell

Cells were assembled in an argon filled glovebox with $H_2O$ and $O_2$ with values below 1 ppm. A coin cell setup was used and consisted of sodium metal or copper foil as working and sodium as counter electrode. The sodium metal was washed with Hexane and rolled between two plastic foils. The sodium and copper foil were punched out, with a diameter of Ø = 14 mm. One glass fiber separator (GF/B, Whatman, VWR) in between two Celgard separator (3501-0660M-A) with a diameter of 16 mm were used for each cell. 150 µL of the electrolyte solution was used. The cells were sealed by a hydraulic crimping machine (MSK-110, MTI). Galvanostatic cycling was performed by the usage of either a VMP-300 or a BCS battery cycler (Bio-Logic, France) at 25 °C in a climate chamber. The coin cells were placed onto sample holders and then cycled increasing the electric current to obtain the stripping/plating profiles. All symmetric cells were cycled using 0.01 mA/ $cm^2$, 0.02 mA/ $cm^2$, 0.05 mA/ $cm^2$, 0.075 mA/ $cm^2$, 0.1 mA/ $cm^2$ and 0.5 mA/ $cm^2$ respectively. The half cells were cycled using a current of -0.5 mA/$cm^2$ for 10 h.

### 4.3.2 Potassium vs Hard Carbon Half Cell

In order to determine the electrochemical effect of different potassium grades, half cell measurements were performed. The HC electrodes, which were used as working electrodes, were punched out with a handheld precision punch tool, with a diameter of Ø = 14 mm. After drying the HC and all cell parts in a vacuum oven (Büchi, Switzerland) at 120 °C, the loading of the electrodes was determined for each cell individually. The average active material loading was found to be 5 mg/ $cm^2$. For the counter electrode, potassium metal (from different Suppliers and garde) disk were freshly prepared inside a glovebox. Potassium from, Thermo Scientific Chemicals (Supplier 1, $K_{MO}$) and STREM Catalog (Supplier 2, $K_A$) was used. Potassium was rolled between two plastic foils to a thickness of 1mm and punched out, with a diameter of Ø = 14 mm. The HC working electrode were dried at 80 °C overnight and separators were dried at 120 °C under reduced pressure over night. One glass fiber separator (GF/B, Whatman) in between two Celgard separators (3501-0660M-A) with a diameter of 16 mm were used for each cell. Electrochemical measurements were performed in a climate chamber 25 °C using a BSC potentiostat (Biologic) with EC-Lab software. The cells were cycled using a constant current (CC)-constant potential (CP) cycling protocol in the voltage range of 0.01 V to 1.7 V versus $K^+/K$ with first two cycles at C/20 followed by a rate of C/10 for 300 cycles.

## 4.4 XPS Measurements

The X-ray photoelectron spectroscopy measurements were performed using a K-alpha spectrometer (Thermo Fisher Scientific, East Grinstead, UK), applying a micro-focused, monochromatized Al Kα X-ray source (hν = 1486.6 eV) with 400 µm spot size. In case of localized surface charging, the binding energy shifts were minimized using the K-Alpha charge compensation system during analysis, using a electron flood gun with low energy-electrons of 8 eV kinetic energy. Core spectra were recorded with a 0.1 eV step, a constant 50 eV pass energy, and short-time iteration to monitor any possible sample degradation. Reproducibility was confirmed through three measurements per sample. For intense peaks and/or peaks clearly evidenced by the peak shape, the binding energy uncertainty was set around ± 0.1 eV during curve fitting. In case of weak peaks and no direct justification by the spectra, the uncertainty was set to ± 0.2 eV. Data acquisition and processing was carried out using the Thermo Avantage software (Version 5.9922, Thermo Scientific). All spectra were referenced to the hydrocarbon C 1s peak (C-C, C-H) at 285.0 eV while the overall binding energy scale was controlled by means of the well-known photoelectron peaks of metallic Cu, Ag, and Au, respectively. To provide a clear presentation and more comparable spectra, the intensity was normalized setting the maximum peak height to 1. Core peaks were utilized depending on the spectral shape, either with a linear or a nonlinear ("smart background") Shirley-type background. For peak fitting, Voigt profiles were used with a 70 % Gaussian and 30 % Lorentzian contribution and specific full width at half-maximum constraint ranges were selected to optimize areas and peak positions. The analyzer transmission function, Scofield's sensitivity factors, and effective attenuation lengths for photoelectrons were applied for quantification. Effective attenuation lengths were calculated using the standard TPP-2M formalism.

### 4.4.1 Metal Submerging Experiments

Samples were prepared in an Ar-filled glovebox ($O_2$ <0.1 ppm, $H_2O$ <0.1 ppm). The following metals where used, Li (Thermo Fisher, 99.9 %), Na (Sigma–Aldrich, 99.9 % trace metals basis), $K_{MO}$ (Thermo Fisher, 98.0 % (mineral oil)), $K_A$ (STREM, 99.0 % (ampule)). The metals which were delivered in mineral oil were first washed in hexane and then placed and rolled out using a protective PE (polyethylene) sheet to reduce sticking to the rolling pin and contaminations on a stainless-steel spacer. The Li metal was received as foil and cut into pieces. The samples were placed in high-density polyethylene vials with 1 mL of the esolvents/lectrolytes mentioned in **chapter 4.3** and stored in the electrolytes for 2 minutes, 4 min and 2 h, respectively. After storage, the electrodes were washed by immersion for 2 minutes in a glass vial containing 3 mL of DEC or PC and dried under vacuum. These conditions are

based on a pre-study investigating the washing conditions and it was found that this procedure removes almost all residual conductive salt.

#### 4.4.1.1 Reference Measurements

A detailed table for the used reference samples: NaF, NaPF6, NaTFSI, CH3CO2Na, $CH_3ONa$, $Na_2C_2O_4$, $Na_2CO_3$, $NaHCO_3$, $Na_2O$, $Na_2O_2$, KF, $KPF_6$, KTFSI, $CH_3CO_2K$, $K_2C_2O_4$, $K_2CO_3$ and $KHCO_3$ can be found in the supporting informations (**Table S2**) where the powder was mounted to the sample holder by pressing the powder into conductive double sided carbon tape.

### 4.4.2 XPS Depth Profile and Elemental Mapping

Elemental mapping was performed using a Thermo Scientific ESCALAB Xi+ XPS instrument equipped with the Fast Parallel Imaging (XPI) system. This setup enables high-resolution chemical imaging (<3 µm resolution) through parallel acquisition, which eliminates the need for serial scanning. The system incorporates a magnetic immersion lens to minimize spherical aberrations and a two-dimensional detector for simultaneous electron collection across the imaged area. A monochromatic Al Kα X-ray source (1486.6 eV) was operated at a spot size of 65 µm, with the analyzer lens axis aligned perpendicular to the sample surface. Two potassium metal surfaces ($K_{MO}$ and $K_A$) were analyzed. Prior to imaging, samples were cleaned using a scalpel. The potassium metal cube in mineral oil was first washed in n-hexane (ROTH, ≥99 %) and the surfaces that had turned black due to exposure to mineral oil was carefully removed after the washing process. Both potassium metals $K_{MO}$ and $K_A$ were carefully placed and transferred directly onto the sample holder inside a glovebox, connected to the XPS system. The sample was then immediately transferred under inert conditions to the XPS instrument and measured to prevent any exposure to air or moisture. SnapMaps of the K 2p (binding energy: 295 eV) and Na 1s (1073 eV) core levels were acquired over a 3 × 3 mm² region using a pass energy of 150 eV. Raw SnapMaps were processed using principal component analysis (PCA) to deconvolute overlapping spectral features and extract dominant chemical components.[93] The PCA algorithm identified common peak shapes (e.g., K 2p, Na 1s) across all pixels, reducing noise and enhancing contrast.[94,95] Following PCA, component scores were overlaid to generate composite chemical maps, highlighting the spatial distribution of K and Na metal in the sample. Sputter depth profiling was performed using monoatomic $Ar^+$-ion sputtering at first 500 eV following 1000eV with etch phases of 4×40 s, 7×80 s, 7×160 s, and 3×320 s on the pristine K metal samples. Elemental mapping was performed before and after each sputtering step. In **Figure 14**, it can be seen that elemental mapping was conducted directly within the sputtered area (P1). To compare the differences between the sputtered and pristine regions, mapping was also performed at P2, located at the edge between the two zones. Additionally,

to investigate potential changes induced by sputtering (e.g., migration effects or surface modifications), mappings P3 and P4 were carried out at selected positions on the sample.

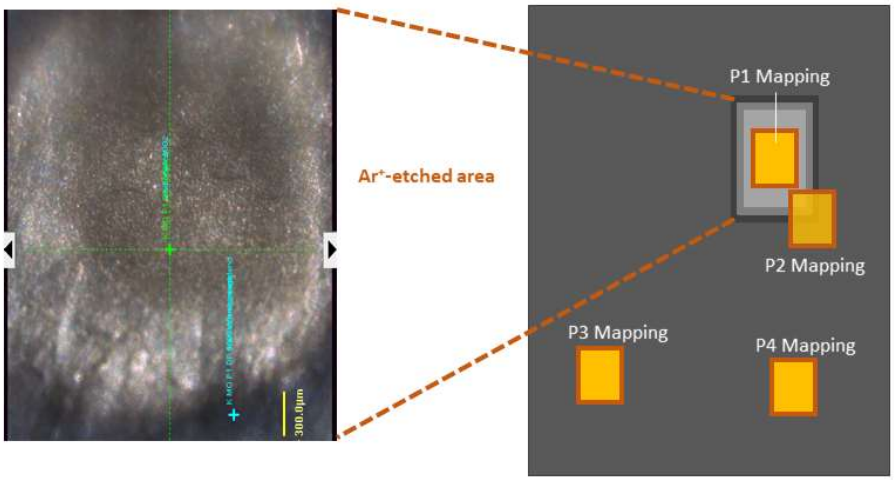


**Figure 14** left: Surface of the sample after sputtering. The bright area corresponds to the sputtered region of potassium metal, while the dark area represents the untreated, pristine surface. Right: Schematic illustration of the sputtering and mapping procedure, indicating the sputter point (marked in grey) and the locations where elemental mapping was performed (marked in orange).

## 4.5 Gas Chromatography Measurements

Gas chromatography (GC) experiments were performed in collaboration with Andreas Hofmann and followed the setup described in literature.[96] Specifically, a Clarus 690 GC device (PerkinElmer Inc., Waltham, USA) was employed, which was equipped with an autosampler, a flame ionization detector (FID), and a mass spectrometry (MS) detector (SQ 8T). After the separation, a gas split was made to be able to use both detectors, the MS and the FID. The Turbomass 6.1.2 and TotalChrom 6.3.4 software packages were utilized for both data acquisition and subsequent analysis. He 6.0 gas (Air Liquide), $H_2$ gas from a PG+160 hydrogen generator (Vici DBS) as well as Air (Air Liquide) were used as gases. The GC column utilized was an “Elite 5MS Sil” with a length of 30 m, an interior diameter of 0.25 mm, and a film thickness of 0.5 µm. Injection parameters involved a split flow of 10 ml/min, an inlet temperature of 250 °C, an injection volume of 0.5 µl, an initial pressure of 175 kPa, and a pressure-controlled mode. The oven temperature was maintained at 40 °C. Oven and pressure parameters were set as follows: an initial temperature of 40 °C for 1.5 min, followed by heating at a rate of 20 °C/min up to a final temperature of 320 °C. The initial pressure was maintained at 175 kPa for 2 min, then increased at a rate of 7.8 kPa/min up to a final pressure of 300 kPa. For the MS setup, the filament voltage was set at 70 kV, with ion source temperature of 200 °C and a transferline temperature of 200 °C. Post-

separation, the gas flow was divided using a SilFlow™ GC Capillary Column 3-port Splitter to allow signal detection in both the MS and the FID. The MS was operated in scan mode, scanning a range from 33 u to 350 u with an event time of 0.3 s and an interscan delay of 0.02 s. All samples, including electrolytes and mixtures, were compared and corrected against pure dilution solvent as well as pure electrolyte solvent. Whenever possible, impurities in the electrolyte solvents were identified based on NIST searches (using electron ionization fragmentation match), and by measuring the pure substance separately. Additionally, gas formation was investigated in an EL-CELL (PAT-Cell-Press) with a cup (polypropylene) containing the electrolyte mixture and sodium pieces. The cell was handled in an argon filled glove box and a PEEK sealing was used to close the cell tightly. The pressure was observed over a period of time and afterward the gases were extracted with a gastight syringe. The procedure is described in the reference [97] in more detail.

## 4.6 Digital Microscopy (ECC-Opto 10 assembly)

To follow the Na metal deposition, in-operando cell observation was carried out using the ECC-Opto 10 test cell (EL-CELL). A schematic illustration of the used cell can be seen in **Figure 15**.

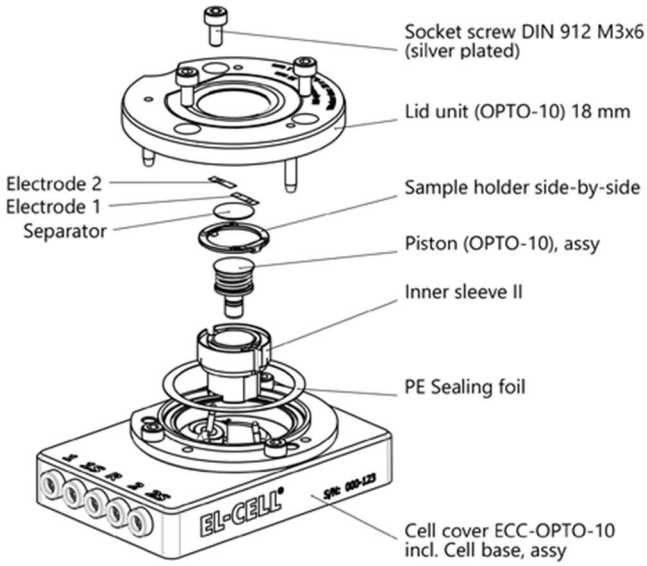


**Figure 15:** Structure of the ECC-Opto 10 test cell for in-operando optical cell observation.[98]

Before each use, the optical test cell was thoroughly cleaned using PC solvent. If visible residues remained on the glass window, it was additionally cleaned with $H_2O$, ethanol, and isopropanol. After cleaning, the cell was dried to prevent contamination before further experiments were conducted. The corresponding sealing foil was straightened during assembly to avoid leakage due to warping of the gasket. The preparation was carried out in an argon-filled glove box ($H_2O$ and $O_2$ < 0.1 ppm).

Electrodes were prepared from freshly rolled out sodium foil, which was cut into small stripes (approx. 1 mm x 0.3 mm). These were then placed on top of copper foil to cut out the finished electrode (**Figure 16**). The copper foil is essential to maintain contact with the electrodes and prevent conductivity issues.

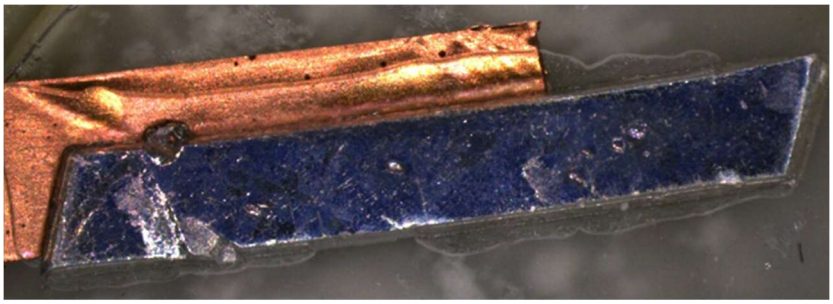

**Figure 16:** Na electrode placed on top of copper foil (CuNa, inside optical test cell).

A Whatman GF/B separator with a diameter of 10 mm was placed atop the loaded piston within the inner sleeve II (**see Figure 15**). Initially, the completed electrodes were arranged in a head-to-head orientation for the initial experiments. However, the configuration was subsequently modified to a side-by-side arrangement in later cell setups. The separator was then saturated with 50 µL of EC:PC (1:1) $NaPF_6$ electrolyte with and without FEC additive. After ensuring the precise positioning of the sealing foil, the lid unit was securely fastened in place using screws. Galvanostatic cycling was performed with a current density of 0.5 mA/ $cm^2$. Challenges arose in accurately determining the electrochemically active surface area, prompting the adjustment of the applied current to 57 µA for subsequent experiments. Throughout the cycling process, the current underwent two increments, adjusting to 114 µA and 228 µA, respectively. These variations will be explicitly documented and analyzed independently in subsequent discussions.The cycling was monitored using a ZEISS Smartzoom 5 digital microscope and pictures were taken at 34x, 70x and 100x magnification. The Autofocus feature was utilized to sharpen images and the temporal progression of the cycling process was recorded alongside each captured image.

## 4.7 ICP-OES

The elements were determined by inductively coupled plasma optical emission spectroscopy (ICP-OES, iCAP7600 DUO von Thermofisher Scientific). About 20 mg of each sample were dissolved in 5 ml Ethanol (TechniSOLV, 99,9 %, VWR Chemicals). After the solution of the metal, 10 ml nitric acid (subb. Grade; 2 %) has been add to the solution. The ethanol has been removed almost complete from the solution by evaporation in a graphite oven by 354 K for 3 h. The analysis of the elements was

accomplished with four different calibration solutions and an internal standard (Sc). The range of the calibration solutions did not exceed a decade. Two wavelengths of the elements have been used for calculation

# 5 Thesis Objectives

Alkali metal anodes offer the highest theoretical energy densities among battery technologies, making them key candidates for next-generation energy storage. However, their practical implementation remains severely limited by complex and poorly understood interfacial chemistries. While lithium metal has been extensively studied, its behavior is often used as a proxy for sodium and potassium systems, an approach that overlooks critical differences in reactivity and SEI formation. For instance, the electrolyte additive fluoroethylene carbonate, widely effective in lithium systems, fails to stabilize potassium metal anodes, underscoring the need for metal-specific interfacial insights.

A fundamental understanding of how electrolyte composition and metal reactivity shape the SEI and govern electrolyte decomposition is essential for the rational design of future electrolytes and artificial SEI architectures. Accurate characterization of both electrolyte degradation pathways and the resulting interphases will be central to overcoming current limitations.

This thesis systematically investigates SEI formation on lithium, sodium, and potassium metal. A comprehensive approach is employed, combining surface preparation protocols, time-resolved X-ray photoelectron spectroscopy (XPS), gas chromatography–mass spectrometry (GC–MS), electrochemical analysis, in situ optical microscopy, and density functional theory (DFT, by Daniel Stottmeister) modelling to disentangle the complex chemistries at play. The objectives are:

**1.Establish pristine-metal baselines**

Characterize the native oxide, hydroxide and carbonate layers on as-received Li, Na and K via XPS with and without controlled $Ar^+$ depth profiling, isolating intrinsic surface features from later SEI components.

**2.Develop non-destructive, time-resolved surface analysis**

Introduce and apply artifact-free XPS methods to directly monitor early SEI growth (2 min to 2 h) in a variety of solvent, salt (anions include $PF_6^-$, $ClO_4^-$) and additive (FEC, VC) environments, capturing the kinetics and compositional evolution of organic versus inorganic interphases.

**3.Decouple and identify soluble and gaseous by-products**

Use GC-MS on metal-exposed electrolytes and first-cycle separators to catalog liquid- and gas-phase decomposition products, ranging from dialkyl carbonates to propylene oxide and distinguish purely metal-driven pathways from electrochemical artifacts.

**4.Correlate interphase chemistry with electrochemical and morphological behavior**

Benchmark plating/stripping stability in symmetric and anode-free half-cells (Na/K) across electrolyte formulations and current densities, link overpotentials and cell lifetimes to SEI composition, and visualize dendrite/moss growth and “dead” metal formation via in-situ optical microscopy.

**5.Optimize cell components for reproducible post-mortem analysis**

Develop refined separator and stack-pressure configurations (Celgard–Whatman–Celgard sandwich) that ensure uniform metal deposition and contamination-free surfaces for subsequent XPS and GC-MS characterization.

# 6 Solid Electrolyte Interphases on Lithium

This chapter investigates the SEI formation and evolution on lithium metal anodes, with a focus on the interplay between electrolyte components, solvent, salt, and additive, and their collective impact on interfacial chemistry. To unravel the distinct behavior of the lithium metal's solid surface components, this work applies XPS for systematic characterization, while the second part focuses on GC-MS to analyze soluble decomposition products, defined as compounds that are liquid/soluble in the solvent mixture and exhibit at least minimal vapor pressure. The chapter begins with (1) a quantitative analysis of the pristine lithium metal surface, using XPS to map its elemental and chemical composition. Here, "pristine" denotes the untreated, as-received metal (exposed to the glovebox atmosphere, see Experimental Section). Sputter depth profiling is employed to probe subsurface heterogeneity, including native oxide layers and impurities. This establishes a baseline reference for the initial state of lithium metal, distinguishing intrinsic surface features from SEI-derived components. Building on this baseline, the chapter continuous with: (2) time-resolved XPS to track SEI evolution across different electrolytes and (3) time-resolved investigation of SEI components formed in contact with additive containing electrolytes. Complementing XPS, GC-MS identifies volatile and soluble and neutral byproducts formed during SEI evolution. The chapter concludes by combining XPS and GC-MS observations. The study introduces a non-destructive, time-resolved XPS method that avoids sputtering and eliminating artifacts (e.g., sputter-induced peaks or surface damage) to directly track SEI evolution. This reveals intermediates during early SEI growth (2 min – 2 h), offering artifact-free insights previously obscured by conventional techniques.

## 6.1 Surface vs. Bulk Lithium: Elemental Analysis from Initial Layer to Sputtered Metal

Lithium metal anodes for batteries are universally stored under inert conditions to mitigate their extreme reactivity. Since this "pristine" surface state reflects the lithium actually integrated into batteries, its compositional analysis is essential. In this work, I differentiate the elemental composition of as-received lithium (pristine) from its sputter-cleaned bulk metal to isolate surface modifications. Combining XPS with controlled argon sputtering enables resolution of how ambient storage alters lithium surfaces relevant to practical battery systems.

Building on the initial XPS analysis that detected lithium salts on the sample surfaces, depth profiling was employed to map their spatial distribution within the material and differentiate these surface deposits from the intrinsic spectroscopic signatures of pure lithium metal. It is important to note that for complex systems such as the SEI or even superficially formed surface layers from glovebox storage,

sputtering can significantly alter the sample composition. This occurs not only through the intended removal of surface material but also due to the preferential sputtering of certain components and the possible induction of chemical reactions, which may lead to the formation of new compounds. These effects must be carefully considered when interpreting the resulting analytical data. Sputter depth profiling was performed using monoatomic $Ar^+$-ion sputtering at 500 eV and 1000 eV with etch phases of 30 min, 1 h, 2 h, 3 h and 5 h on the pristine Li metal sample (Li foil was cut into pieces and directly transferred into the vacuum system without solvent exposure). It is critical to emphasize that the presented sputter steps exhibit a nonlinear relationship with both sputter duration and depth. These parameters were strategically selected to elucidate the qualitative depth-dependent distribution of constituent compounds. Initial sputtering parameter employed low ion energy (500 eV) and short durations (30 min) to monitor near-surface modifications within the passivation layer. Subsequently, progressively increasing ion energy (1000 eV) and prolonged sputter times (1 h – 2 h) were applied to probe subsurface regions, enabling a systematic evaluation of compositional gradients across the material. The depth profiles provide the lithium distribution across different depths, as illustrated in **Figure 17**.

***C 1s and Li 1s spectra***

The Li 1s XPS spectrum (**Figure S4**) of the pristine lithium sample exhibits two distinct peaks at binding energies of 53.8 eV and 55 eV. The peak at 53.8 eV corresponds to $Li_2O$, while the broader feature at 55 eV is attributed to a mixture of lithium-containing compounds like $Li_2CO_3$, LiOH, LiF and R-OLi that can stem from exposure to the glovebox environment. These components share overlapping binding energy signatures within this range, making individual species difficult to resolve. Following $Ar^+$-sputtering, the salt-related peak was no longer observed, and only the $Li_2O$ peak remained visible. Notably, the absence of metallic lithium ($Li^0$) signals, expected at 52.6 eV accompanied by plasmon loss features, confirms that no metallic lithium is detectable in the analyzed surface region of the sample.[99] The C 1s XPS spectra in **Figure 17** for pristine Li showed two peaks, at binding energies of 285.0 eV (C-C, C-H) and 290.0 eV (C=O, $Li_2CO_3$). All observed signals are in accordance with previous reports. After $Ar^+$ sputtering, the C 1s XPS spectra exhibit two new peaks at 283.3 eV ($Li_2C_2$) and a minor peak at 286.6 eV (C–O), indicative of carbide formation at the surface. The peak for -$CO_3$ appeaared at higher BE at 290.8 eV indicating a hydrocarbonate, $LiHCO_3$. Notably, the overall signal intensity decreases significantly post-sputtering, as evidenced by increased noise in the data.

***O 1s spectra***

In the corresponding O1s spectra of the pristine Li, carbonate was observed at 531.8 eV and a second peak at 531.1 eV indicating LiOH. The dominant peak at 529.3eV could be attributed to the $Li_2O$ species. After the initial $Ar^+$-sputtering the O 1s spectra of Li consists of two components: $Li_2CO_3$ at 531.8 eV

and $Li_2O$ at 529.3 eV. Between 3h $Ar^+$-ion sputtering and 5h of sputtering with 1000 eV, no changes in the O 1s signal are observed.

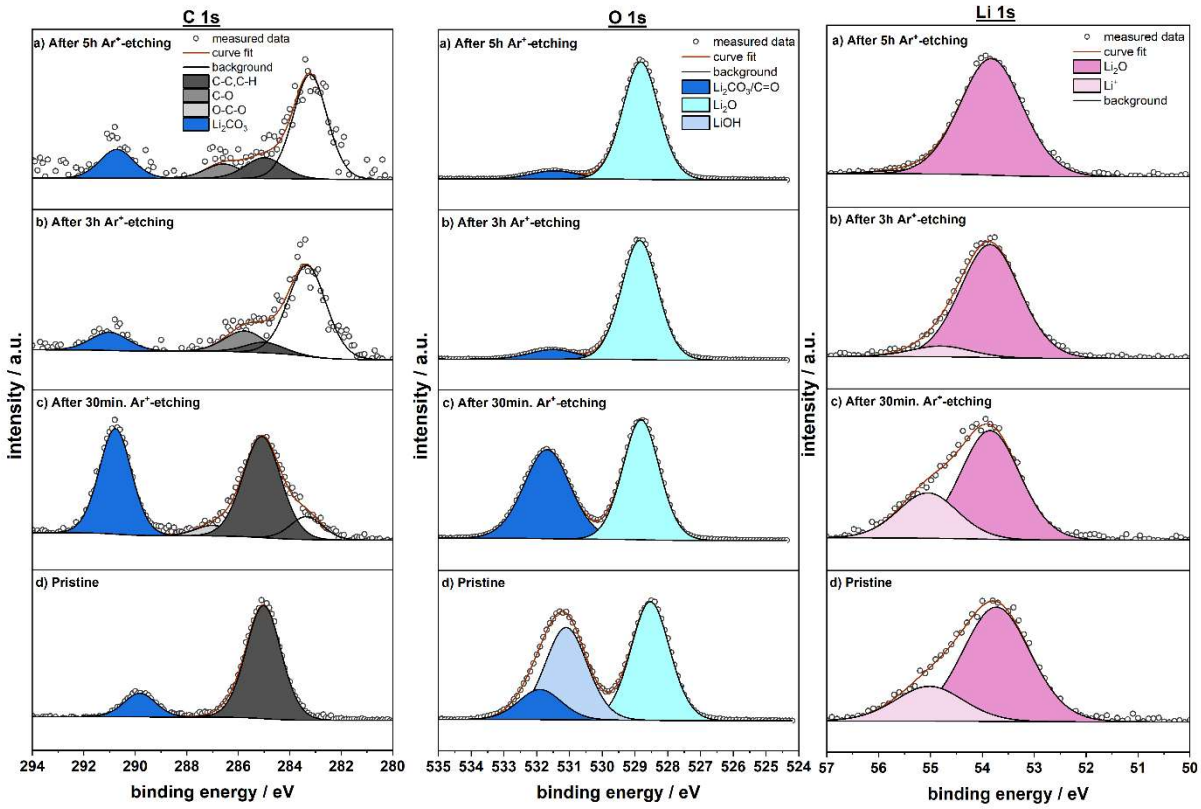


**Figure 17**: The XPS depth profile spectra of C 1s, K2p and O 1s core peaks of pristine Li after the first 30 min with 500 eV, after 3 h and 5 h with 1000 eV.

***Comparison of Surface Layer Composition***

For a quantitative analysis of the surface composition, the atomic concentrations (atom-%) for elements and specific components were derived from the peak areas of the curve fitted spectra (**Figure 18**) and on basis of the instrument specific Scofield factors. The overall elemental composition is summarized in **Table S4 .** The pristine Li sample exhibited a initial passivation layer composed primarily of C-C, C-H (≈7.3±0.1 at.%), C-O (≈0.3±0.1 at.%), $Li_2CO_3$ (≈1.4±0.1 at.%,), LiF (≈0.4±0.1 at.%), $Li_2O$ (≈16±0.1 at.%) and LiOH (≈14±0.1 at.%). During the initial 30 min sputtering step at 500 eV, significant compositional changes occurred: the LiOH peak could not be observed anymore, while $Li_2O$ (18 at.%) and $LiHCO_3$ (3.0 at.%) content increased. Concurrently, the C-C, C-H signal (3.5 at.%) diminished, consistent with the gradual removal of surface carbon contaminants. Notably, a new peak emerged at 283.3 eV, possibly attributed to lithium carbide ($Li_2C_2$, 0.7 at.%), likely formed via ion-beam-induced decomposition of residual carbon or carbonate species. Upon extending the sputtering time to 1-2h at a higher energy of 1000eV, $LiHCO_3$ (0.2 at.%) and C-C,C-H (0.12 at.%) were nearly eliminated, while $Li_2O$ (28 at.%) continued to increase and dominate the subsurface region. The $Li_2C_2$ signal

exhibited no further increase, aligning with prior studies reporting $Ar^+$-sputtering artifacts in lithium systems.[84] For instance, Henss *et. al.* observed carbide formation on sputtered $Li_2CO_3$ reference samples, underscoring its artifactual origin. These findings collectively suggest that $Li_2C_2$ arises not as a part of the native passivation layer but from beam-induced decomposition of carbon sources (e.g. adventitious carbon, carbonates). The compositional evolution of the lithium surface under $Ar^+$ sputtering reveals critical insights into both the passivation layer chemistry and analytical artifacts inherent to XPS. While $Li_2O$ dominates the subsurface region after prolonged sputtering, the detection of metallic lithium ($Li^o$) remains ambiguous due to competing spectral features and sputter-induced transformations. Notably, the absence of pronounced plasmon-loss features precludes the presence of a major metallic $Li^o$ fraction in the near-surface region. The sputter-induced decomposition of LiOH and $Li_2CO_3$ into $Li_2O$, as reported by Henss *et. al.*, further complicates the interpretation of lithium spectra. This decomposition mechanism, underscores that the observed $Li_2O$ enrichment is not solely intrinsic to the passivation layer but also a consequence of sputtering. For instance, LiOH, initially prominent on the pristine surface, is entirely depleted during sputtering, while $Li_2O$ accumulates as a stable decomposition product. This highlights the challenge of isolating metallic lithium signals in XPS, even after aggressive sputtering. The persistent overlap between decomposition products (e.g., $Li_2O$) and the weak $Li^o$ signal underscores that XPS cannot reliably resolve a "pure" lithium metal phase in such systems, as the sputtering process itself alters the near-surface chemistry.

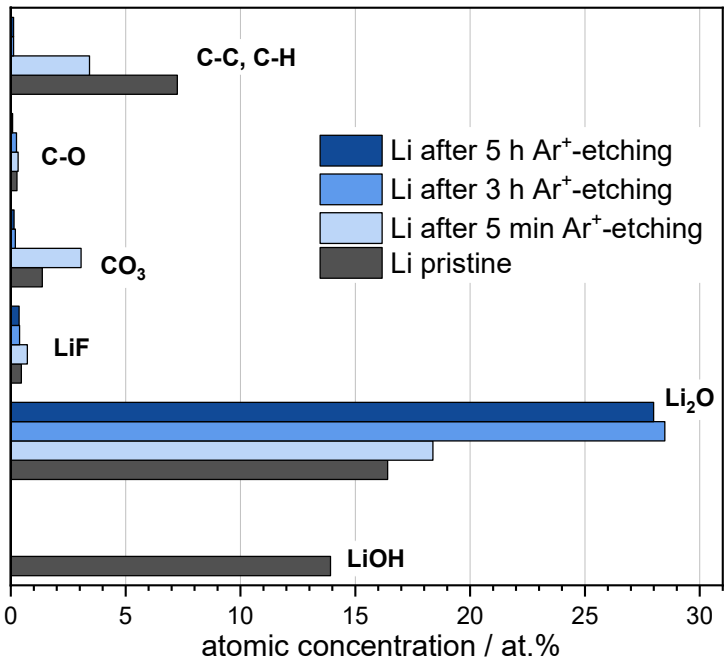


**Figure 18**: Aatomic concentration of main surface species before and after $Ar^+$ sputtering of pristine Li.

## 6.2 From Solvent to Salt to Additive: Tracking the Surface Evolution of Li

XPS measurements were carried out to investigate the surface layer composition of lithium metal after exposure to a DEC:EC (1:1 vol.%) solvent mixture for 2 minutes. Subsequently, the study was expanded to include electrolyte mixtures comprising $LiPF_6$ (0.75 M) dissolved in DEC:EC solvent as well as the addition of 5 vol.% FEC to the DEC:EC $LiPF_6$ electrolyte. To further examine the evolution of the surface composition, exposure times were extended to 4 min and 2 h. The differences in surface composition at 2 min, 4 min, and 2 h are discussed in detail and presented in **Figure 19**.

***C1s and Li1s spectra***

The C 1s in **Figure 19** and Li 1s spectra (**Figure S4**) shows the Li metal exposed to (a) the DEC:EC solvent, (b) the electrolyte containing $LiPF_6$ and (c) the electrolyte with the addition of FEC. In the Li 1s spectrum, 2 min solvent-exposure (**Figure S4**), lead to only one characteristic peak at 54.8 eV ($Li^+$), summarizes all lithium-containing species ($Li_2CO_3$, LiOH). The $Li_2O$ peak clearly visible for the pristine sample cannot be observed anymore. The absence of $Li^0$ related features (52.6eV + plasmon losses) suggests that there is no metallic lithium visible in the XPS spectra. Comparing this with the Li 1s spectra when the Li metal is exposed to electrolyte (solvent+salt) the $Li_2O$ peak appears at 53.8 eV as well as a second peak at higher BE at 56.0 eV which is assigned to all other lithium species ($Li_2CO_3$, LiOH, LiF, $Li_xPO_yF_z$, $Li_xPF_y$). The shift of this peak to higher binding energy (BE), compared to the solvent-exposed and pristine samples (54.8 eV), arises from the presence of a higher relative proportion of fluorine containing lithium species (LiF, $Li_xPO_yF_z$, $Li_xPF_y$), which contribute distinct BE signatures. In the C1s region, the samples exposed to the solvent mixture showed four C 1s peaks, at binding energies of 285.0 eV (C–C, C–H), 286.3 eV (C–O, R–OLi, R/alkyl), 288.9 eV (-$CO_2Li$) and 290.1 eV ($CO_3$, $Li_2CO_3$). In comparison to the pristine Li metal, which only shows peaks corresponding to C–C/C–H and $Li_2CO_3$ (**Figure 17**), the introduction of electrolyte solvent results in additional carbon species. However, due to the overlapping binding energies of carbonate-related signals, it is not possible to unambiguously distinguish whether the observed $CO_3$ peak originates from native $Li_2CO_3$, solvent-derived organic carbonates, or carbonate species formed upon dried in solvent. After the addition of salt ($LiPF_6$) and additive (FEC) an additional peak at 287.5eV (C=O) was observed.

***O1s spectra***

The O1s spectra of Li metal dipped in DEC:EC show two main features at binding energies 531.1 eV and 533.1 eV indicating the sepecies LiOH and C-O (**Figure 19a**). After adding salt (b) and additive (c) to the solvent two additional peak appeared in the O 1s spectra at 528.3 eV and 532.1 eV indicating $Li_2O$ and $Li_2CO_3$, C=O on the surface.

***F1s spectra***

The F1s spectra in **Figure 19a** shows Li exposed to the solvent has no impurities of fluorine species. After adding $LiPF_6$ salt to the solvent (b) there is the formation of three peaks at 685.0 eV, 686.8 eV and 688.2 eV with the main peak being LiF, followed by fluorine degradation species $Li_xPO_yF_z$ and $Li_xPF_y$. With the addition of FEC (c) as additive one additional peak appeared at 689.4 eV which results from the C-F species in FEC.

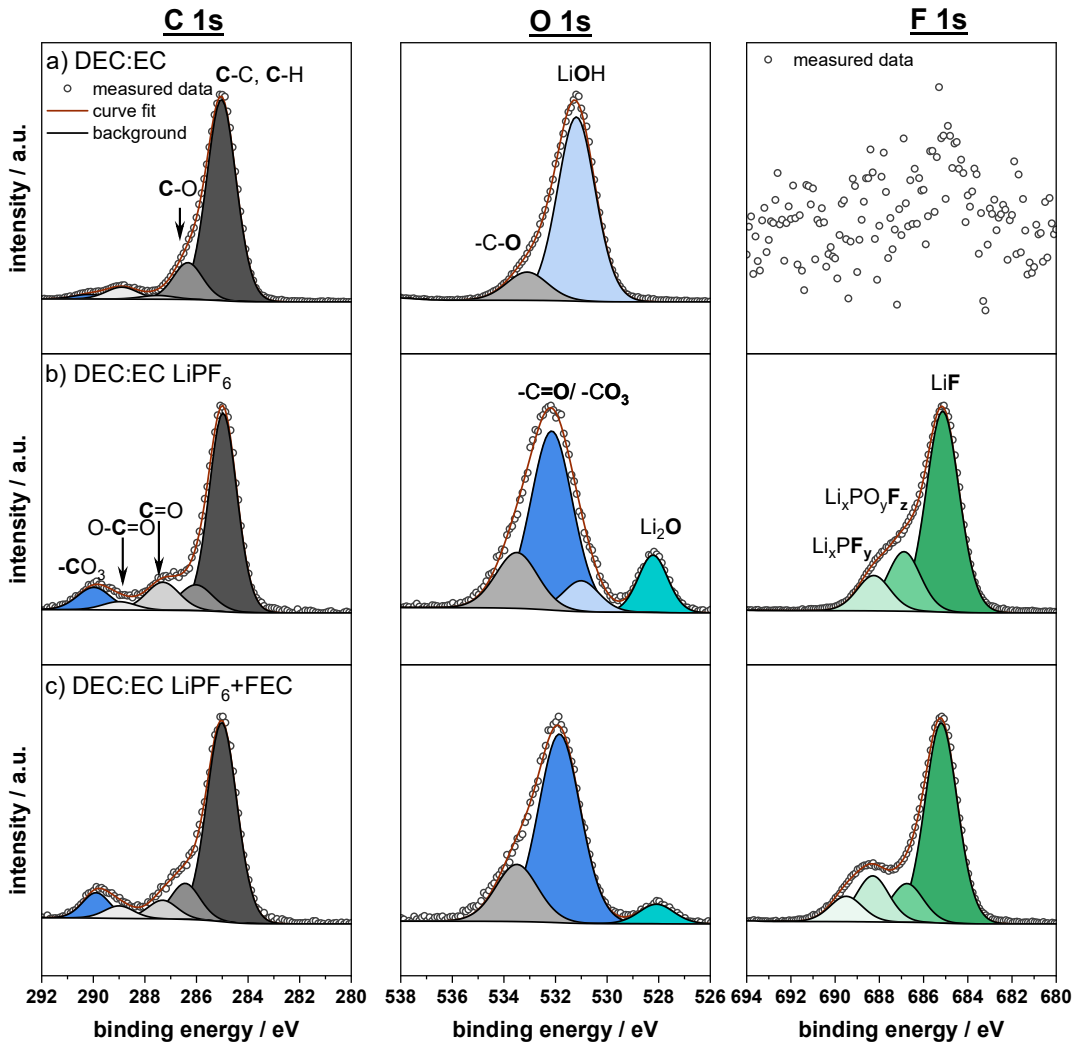


**Figure 19**: C 1s, O 1s and F 1score peaks of Li stored in (a) solvent (DEC:EC), (b) electrolyte with $LiPF_6$ and (c) electrolyte with 5% FEC for 2 min.

***Comparison of Surface Layer Composition***

As a function of progressive electrolyte exposure, the surface layer composition of lithium metal exhibits distinct compositional and structural evolution, as revealed by XPS analysis (**Figure 20**). The at.%, FWHM and BE for the samples can be found in **Table S5 and S6** .The pristine Li metal surface is dominated by $Li_2O$ (16 at.%) and LiOH (14 at.%), accompanied by minor contribution from $Li_2CO_3$, alongside residual C-C,C-H (7.3 at.%) bonding attributed to adventitious carbon. Upon exposure to the

DEC:EC (1:1 vol.%) solvent for 2 min, the surface undergoes significant alteration: $Li_2O$ disappears entirely, while LiOH increased to 26 at.% comparable to the pristine state. Concurrently, organic carbonate-derived species (C-C, C-H (≈44±0.1 at.%), C-O (≈6.6±0.1 at.%), $Li_2CO_3$ (≈1.0±0.1 at.%, $-CO_2Li$ ((≈2.3±0.1 at.%)) dominate the surface, indicating rapid decomposition of the solvent into a passivating organic-rich layer.

**Figure 20a** shows that introducing $LiPF_6$ (0.75 M) into the DEC:EC solvent further modifies the surface chemistry after 2 min of exposure. A small $Li_2O$ peak reemerges (1.5 at.%), while LiOH content decreased (1.0 at.%). Carbonate species (C=O, $CO_3$) increases compared to both pristine Li and solvent-only exposure, suggesting enhanced salt-driven decomposition. The reduction in C-C, C-H (9.6 at.%) signal may reflect either partial dissolution of organic surface layers or coverage by inorganic SEI components (e.g., $Li_2O$, LiF) as the interphase evolves. Prolonged exposure times (4 min and 2 h) reveal dynamic SEI restructuring. At short exposure time (2 min and 4 min), LiF dominates (22 at.%), likely originating from $LiPF_6$ decomposition. However, after 2 h, LiF diminishes (4.8 at.%), while phosphorus-containing $Li_xPF_y$ species (e.g., $Li_xPO_yF_z$) increase up to 38.1 at.%, indicating progressive salt degradation. Notably, both $Li_2O$ and LiOH vanish entirely after 2 h, likely due to dissolution or reaction with acidic byproducts (e.g., HF from $LiPF_6$ hydrolysis).

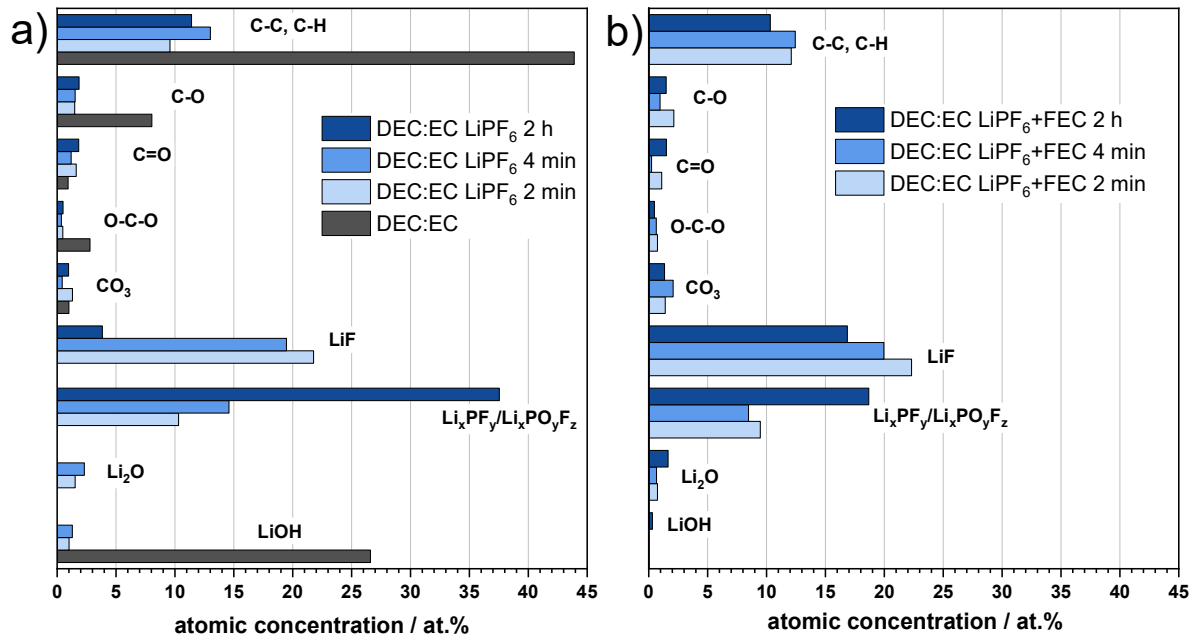


**Figure 20**: (a) A atomic concentration of main surface species of Li stored in DEC:EC and DEC:EC LiPF6 for different time scales (2 min, 4 min and 2 h) and (b) atomic concentration of main surface species of Li stored in DEC:EC $LiPF_6$+FEC for different time scales (2 min, 4 min and 2 h)

**Figure 20b** shows that introducing 5 vol.% FEC to the electrolyte leads to distinct trends when tracking the temporal evolution. After short storage times (2 min and 4 min), the SEI is dominated by inorganic

species LiF (22.3%), a small amount of $Li_2O$ (0.74%) and $Li_xPF_y$ (9.4%)), with no LiOH detected. While the overall carbonaceous matrix (C-C, C-O, C=O (~14%)) remains largely unchanged, prolonged storage time (2 h), leads to the appearance of LiOH (0.31%), likely due to slow hydrolysis reactions or residual moisture ingress. Concurrently, $Li_2O$ and $Li_xPF_y$ content increases over time up to 1.64% and 18.6%, indicating progressive inorganic layer densification, while LiF (16.8%) decreases steadily. The inverse correlation between LiF and $Li_xPF_y$ suggests potential decomposition or conversion of LiF into fluorophosphate compounds (e.g., $LiPO_xF_y$), a process hypothesized to involve reactions with $PF_5$ a common $LiPF_6$ decomposition byproduct. Such transformations are consistent with literature reports of interfacial instability under prolonged storage, where fluorinated phases may react with acidic $PF_5$ to form more complex phosphates.[100] Carbon-oxygen functionalities (C=O, C-O) initially decline after 4 min of storage, possibly due to partial dissolution or reductive cleavage of ester/carbonate groups from the DEC:EC solvent. However, after 2 h, these species rebound, potentially reflecting FEC-driven polymerization processes (e.g., cross-linked polycarbonates) or reformation of carbonate species ($Li_2CO_3$) via $CO_2$ uptake from the electrolyte or ambient environment. This dynamic reorganization highlights the SEI's self-healing capability, where FEC-derived organic fragments may stabilize the interface by replenishing dissolved or degraded components. These findings underscore FEC's dual role in SEI modulation: it suppresses undesirable LiOH formation while promoting a balanced inorganic-organic matrix that evolves dynamically over time. The gradual decline of LiF and rise of $Li_xPO_yF_z$, however, raise questions about long-term interfacial stability, as fluorophosphate species are often associated with increased impedance.

### 6.2.1 Electrolyte Decomposition Pathways Revealed by GC–MS

Soluble by-products of lithium metal interaction with common carbonate electrolytes have been extensively catalogued for EC:DEC + $LiPF_6$ systems, yet nearly all prior GC–MS studies focus on post-mortem analysis of cycled cells, where electrochemical processes and cell components (e.g. separators, current collectors) confound the identification of purely metal-driven degradation pathways. In this study, time-resolved GC–MS was applied to DEC:EC solvent and electrolyte mixtures stored with and without (reference) pristine lithium metal at 25 °C over a series of intervals (2 min, 4 min, 2 h, 48 h). By comparing chromatographic profiles as a function of exposure time, I decouple ambient induced degradation (trace $H_2O/O_2$, inherent solvent instability) from those pathways uniquely initiated by reactive lithium metal, without the influence of applied potentials or cell hardware. This kinetic perspective not only refines and extends existing GC–MS data for the EC:DEC + $LiPF_6$ system, but also uncovers early-stage intermediates and rate-limiting steps that cell-based

analyses cannot resolve, thereby deepening our mechanistic understanding of electrolyte decomposition under realistic assembly conditions.

***Time-Dependent Formation of Decomposition Products in Electrolyte***

The study investigated the degradation over time and the compounds that are formed in the initial degradation step. Therefore, the samples were analyzed after 2 min, 4 min, 2 h, and 48 h. The results for the solvent, electrolyte with and without additive are shown in **Figure 21**. It is observed that there is no degradation products detected after 2 min and 4 min. Even after 2h and 48h no decomposition liquid nor soluble products have formed. The reactans found are (1) DMC, (2) DEC and (3) EC.

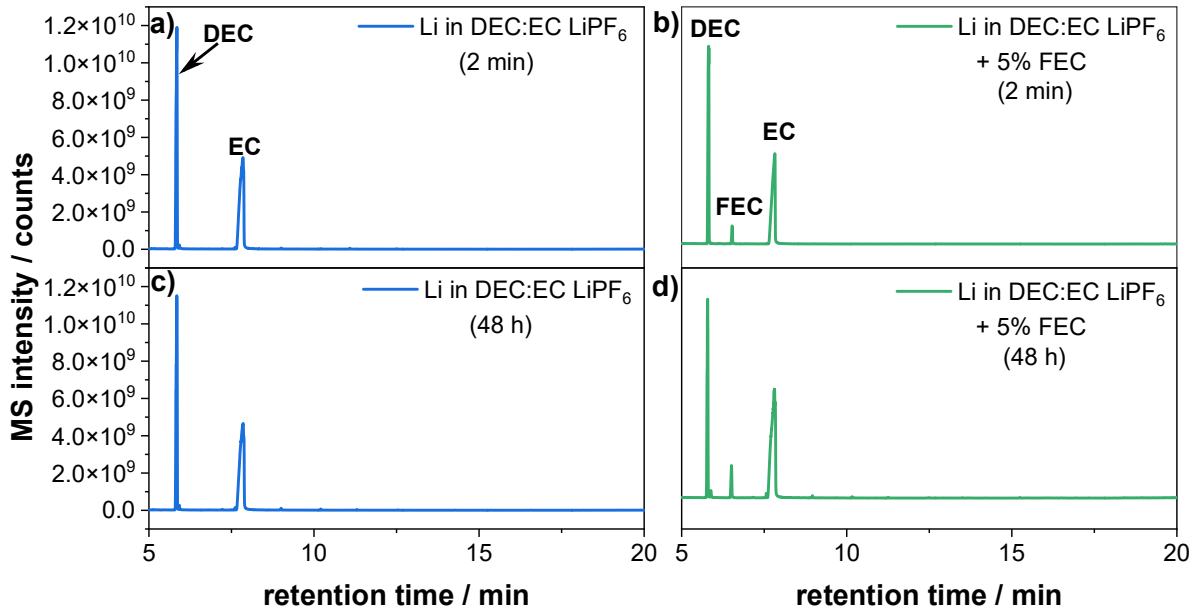


**Figure 21**: GC-MS chromatogram from the (a) DEC/EC, (b) DEC/EC LiPF6, and (c) DEC/EC LiPF6 + 5% FEC mixtures stored over lithium metal after 2 min and 2 h. The numbers and additional reference measurements are assigned in **Table S7 and Figure S5**.

### 6.2.2 Discussion

The time-dependent surface chemistry of lithium metal in carbonate-based electrolytes reveals critical insights into native interphase composition, early-stage SEI formation, and salt-additive interplay. Contrary to assumptions in many fundamental and engineering studies that Li foil is “clean” when integrated into batteries, this work demonstrates that the pristine Li foil naturally being covered with a native oxidized layer, which is mainly composed of LiOH, $Li_2O$ and $Li_2CO_3$. These contamination layers arise from unavoidable reactions during Li foil fabrication and handling, even under inert conditions (e.g., $4Li + O_2 \rightarrow 2Li_2O$; $2Li + 2H_2O \rightarrow 2LiOH + H_2$; $LiOH + CO_2 \rightarrow Li_2CO_3 + H_2O$).[101–104] In addition to these compounds, minor but detectable impurities of calcium (1 at.%) were found (**Figure S3**). XPS analysis confirms that the as-received initial Li surface is quite complex and dominated by LiOH and

$Li_2O$, consistent with prior reports of Li corrosion during gas treatment in manufacturing.[13] This complex initial layer plays a crucial role in battery performance, since this layer can considerably worsen the dendritic growth because of its poor ionic conductivity and partial dissolution.[105,106] Therefore latest research focuses on surface pretreatments, like mechanical or chemical cleaning, to remove surface contaminants and improve electrochemical performance of Li metal batteries.[107–109] When exposed to DEC:EC solvent mixture, this native layer changes within minutes, to a C-C,C-H, C-O and LiOH rich layer. With the addition of $LiPF_6$ salt into the DEC:EC mixture, $PF_6^-$ anions dissociate almost immediately upon contact with bare Li metal, as shown by AIMD simulations.[110–113] This rapid $PF_6^-$ breakdown forms an initial LiF layer, but because F atoms diffuse away from the interface, fresh lithium remains exposed and continues to reduce more $PF_6^-$ and solvent molecules. In the XPS data, this manifests as a steady increase in fluorophosphate species ($Li_xPO_yF_z$) from 11 at.% at 2 min to 38 at.% at 2 h, while LiF content declines from 22 at.% to 4.8 at.%. Such behavior mirrors DFT predictions that $PF_6^-$ undergoes autocatalytic attack on residual $Li_2CO_3$, yielding $POF_3$ and a growing fluorophosphate matrix.[100] In contrast, adding 5 vol.% FEC shifts the reaction landscape. Multiple studies, both first-principles and operando, show that FEC's low LUMO makes it the first species to be reduced at the Li surface, producing LiF and polymeric organic fragments that bind tightly to the metal.[67] In our experiments, the SEI remains LiF-rich (22.3 at.% at 2 min, declining to 16.8 at.% at 2 h) and LixPOyFz is decrease about 9 at.% over the same period. The early formation of a dense LiF layer, combined with an outer shell of FEC-derived organics, physically hinders $PF_6^-$ access and thus suppresses its continued dissociation and fluorophosphate accumulation. Taken together, these findings, and their agreement with both AIMD/DFT mechanisms and experimental reports, highlight FEC's dual role in SEI engineering: (1) chemical selectivity, whereby FEC is preferentially reduced to form stabilizing LiF before $PF_6^-$ can decompose, and (2) physical passivation, in which organic fragments from FEC create a tortuous barrier that blocks further anion attack. This synergy explains why FEC-containing electrolytes maintain a low-impedance, dendrite-resistant interface even as $PF_6^-$ would otherwise drive runaway inorganic growth in its absence.

# 7 Solid Electrolyte Interphases on Sodium

Sodium metal anodes offer an attractive route to high energy density batteries, yet their practical realization hinges on mastering the complex interfacial chemistry that unfolds even before electrochemical cycling begins. This chapter begins by addressing a seemingly simple yet critical aspect: the preparation of sodium metal for XPS analysis. Since storage of sodium in electrolytes containing $NaPF_6$ leaves salt residues on the metal surface, the resulting overlap of signals from $NaPF_6$ and other P–F-containing species complicates the interpretation of XPS data. Although this issue is introduced here due to its relevance for surface analysis, the detailed cleaning procedure, comparing untreated samples with those rinsed in pure DEC for 2 and 10 minutes is described in the experimental section, as it primarily concerns sample handling. The goal was to remove residual salt without affecting key SEI components such as NaF. Building on this, ex-situ XPS augmented by controlled $Ar^+$-sputter depth profiling maps the native passivation layers (oxides, carbonates, hydroxides) that form on pristine sodium despite rigorous inert-atmosphere handling, thereby describing the baseline surface composition.

With that foundation in place, it was possible to follow the SEI formation over time (2 min to 2 h) under three environments: pure DEC:EC solvent, DEC:EC + $NaPF_6$ salt, and DEC:EC + $NaPF_6$ + FEC additive. These measurements reveal the rapid onset of solvent-derived organics, the salt's propensity to generate inorganic fluorophosphates, and FEC's ability to enforce a NaF-analogous, mixed organic–inorganic interphase. Parallel GC–MS analyses of the surrounding electrolyte decouple purely metal-driven decomposition pathways from ambient or solvent-intrinsic processes, ensuring that all observed byproducts truly originate at the Na surface.

To link interphase chemistry with function, Na/Na symmetric cells and anode-free Na/Cu half-cells probe plating/stripping stability across EC:DEC and EC:PC electrolytes (with and without FEC), while digital microscopy visualizes dendrite and moss growth in real timeseparator composition and stack pressure were refined by replacing glass fiber with a Celgard–Whatman–Celgard configuration, enabling clean post-mortem XPS analysis of freshly plated sodium on copper. Taken together, this multi-technique approach, from sample washing through mechanistic DFT and GC–MS to electrochemical and optical characterization, paints a comprehensive, kinetic picture of sodium interfacial behavior and offers concrete strategies for engineering more robust, low-impedance SEIs in next-generation Na metal batteries.

## 7.1 Surface vs. Bulk Sodium: Elemental Analysis from Initial Layer to Sputtered Metal

Sodium metal anodes are consistently stored under inert atmospheres to prevent unwanted reactions due to their high reactivity. Earlier studies have often treated as-received alkali metals as instrinsically "clean", yet in practice even rigorously glovebox-stored sodium results in a persist surface layer. Because this "pristine" surface ultimately dictates how sodium integrates into real cells, accurately characterizing its composition is crucial. To assess the elemental composition of as-received sodium and its underlying bulk metal, the surface was analyzed using XPS combined with controlled $Ar^+$ sputter depth profiling. Residual sodium-containing surface species were first identified, followed by sequential 1 keV sputtering steps (4 × 40 s, 7 × 80 s, 7 × 160 s, 2 × 320 s) to resolve the depth-dependent distribution of surface-derived compounds relative to intrinsic metallic sodium. Because sputtering itself drives chemical changes, these nonlinear etch intervals were carefully chosen to distinguish genuine subsurface composition from artefactual transformations, thereby providing a reliable baseline for all subsequent interphase investigations.

***C 1s and Na 1s spectra***

The Na 1s XPS spectrum (**Figure 22**) of the pristine sodium sample exhibits two distinct peaks at binding energies of 1069.3 eV and 1071.0 eV. The peak at 1069.3 eV corresponds to metallic sodium, while the broad peak at 1071.0 eV is attributed to a mixture of sodium-containing compounds like $Na_2CO_3$, NaOH, NaF and R-ONa that can stem from exposure to the glovebox environment. These components share overlapping binding energy signatures within this range, making individual species difficult to resolve. Following $Ar^+$-sputtering, the intensity of the non-metallic Na peak progressively diminished and was eliminated by the final sputtering cycle. Notably, the peak of metallic sodium ($Na^o$) signal, characterized by a peak at 1069.3 eV accompanied by plasmon loss features (1075.2 eV and 1081.7 eV), confirms that metallic sodium is detectable in the analyzed surface region of the sample. The C 1s XPS spectra for pristine Na showed four peaks, at binding energies of 285.0 eV (C-C, C-H), 286.7 eV (C-O), 288 eV (C=O) and 289.8 eV ($Na_2CO_3$). All observed signals are in accordance with previous reports. After the initial $Ar^+$ sputtering steps, the C 1s XPS spectra reveal a new prominent peak at 282.9 eV, consistent with the binding energy expected for a metal carbide species (e.g., $Na_2C_2$). In the absence of a definitive sodium carbide reference, this feature is tentatively assigned by analogy to $Li_2C_2$ peaks reported by Henss et al. for sputtered lithium surfaces. Importantly, the overall C 1s signal intensity drops markedly after sputtering, visible as increased noise underscoring both removal of adventitious carbon and the challenge of distinguishing true carbide formation from beam-induced artifacts.

***O1s spectra***

In the corresponding O1s spectra of the pristine Na, carbonate was observed at 531.3 eV and a second peak at 529.7 eV indicating NaOH as well as a small peak at 533.0 eV (C-O). Beside these peaks there were additional Na Auger features visible at 523.2eV and 535.5 eV. After the initial $Ar^+$-sputtering the O 1s spectra of Na consists of two main components: $Na_2CO_3$ and $NaO_x$ at 527.5 eV. After prolonged $Ar^+$-ion sputtering with 1000eV, the carbonate species further decreased reviling only Na Auger and plamson features, which will be discussed in the following part.

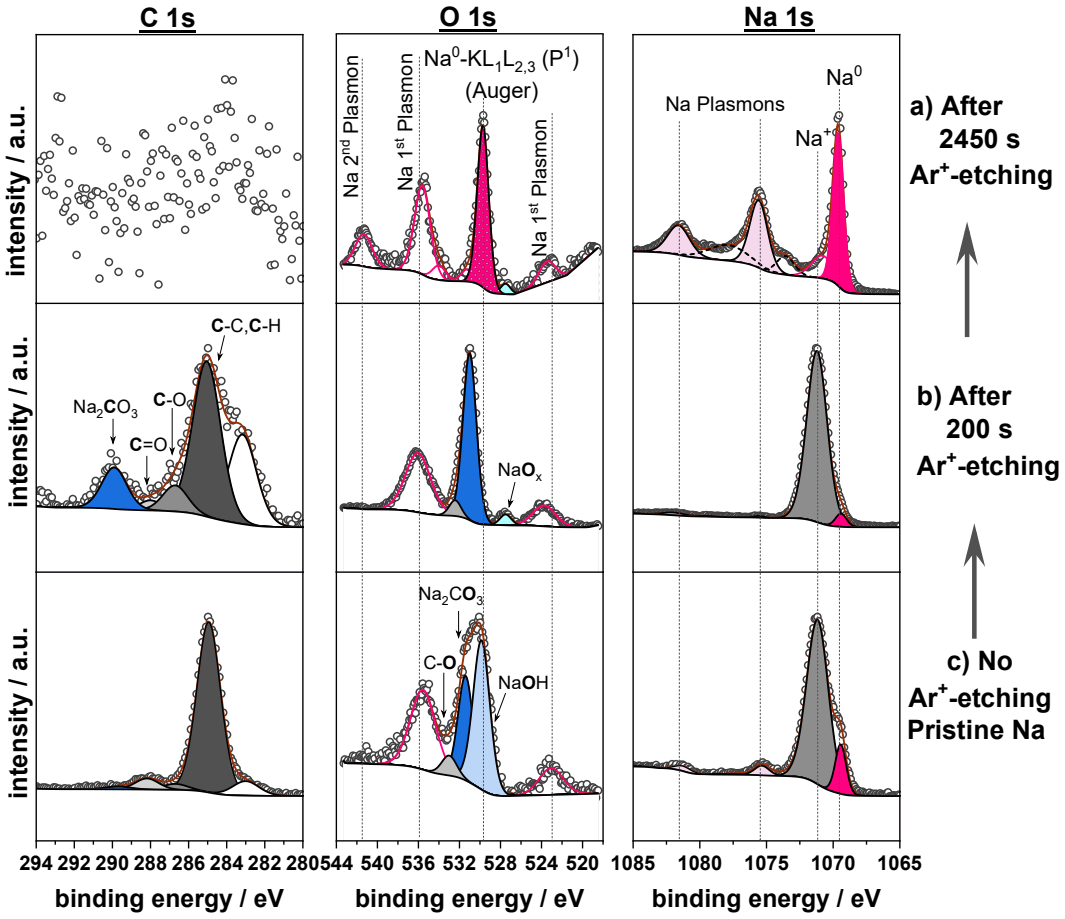


**Figure 22:** The XPS depth profile spectra of C 1s, O 1s and Na 1s core peaks after (a) 2450 s (b) the first 200 s and (c) the pristine Na without $Ar^+$-etching.

***Comparison of Surface Layer Composition***

For a quantitative analysis of the surface composition, the atomic concentrations (atom-%) for elements and specific components were derived from the peak areas of the curve fitted spectra (**Figure 23**) and on basis of the instrument specific Scofield factors. The elemental composition over

time is summarized in **Table S8**. The pristine Na sample exhibited a initial passivation layer composed primarily of carbon containing components (≈49.4±0.1 at.%), oxygen containing components (≈21.4±0.1 at.%) as well as $Na^+$ (≈20.0±0.1 at.%,) and a small fraction of metallic $Na^0$ (≈3.0±0.1 at.%). During the initial 200 s, sputtering step at 1000 eV, significant compositional changes occurred: the carbon content decreased (≈9.5±0.1 at.%), which is also reflected by **Figure 23** with an overall increase in oxygen (≈34.5±0.1 at.%) as well as $Na^+$ content (≈46.0±0.1 at.%). Upon extending the sputtering time to 2450 s, all carbonate species were eliminated (≈0.6 at.%) and the content of ionic sodium ($Na^+$) species decreased to almost zero (≈0.1 at.%), revealing metallic Na (≈98.5±0.1 at.%). The compositional evolution of the sodium surface under $Ar^+$-sputtering reveals critical insights into both the passivation layer chemistry and analytical artifacts inherent to XPS. It was possible to detect metallic sodium ($Na^0$) at the subsurface region after prolonged sputtering. But the detection remains ambiguous due to sputter-induced transformations as well as formation of Auger and Plasmon peaks that overlap with hydroxide and oxide peaks in the O1s.

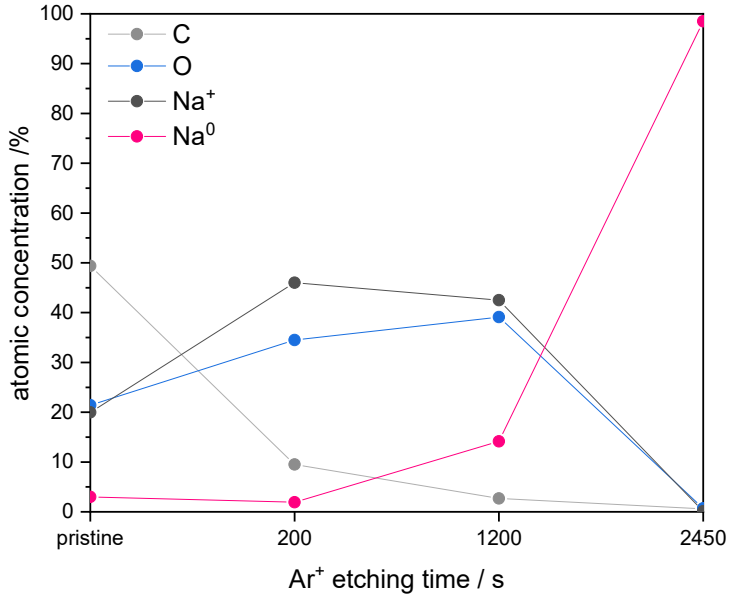


**Figure 23:** The corresponding depth profile of the atomic concentration of C, O, $Na^+$ and $Na^0$ for the $Ar^+$-sputtered pristine Na sample.

## 7.2 From Solvent to Salt to Additive: Tracking the Surface Evolution of Na Metal

To distinguish the native passivation layer from solvent- and electrolyte-induced surface films, XPS was conducted on sodium metal following controlled exposures to DEC:EC and to DEC:EC electrolytes containing 0.75 M $NaPF_6$, both with and without 5 vol.% FEC. Exposures were limited to 2 min, 4 min

and 2 h to capture early decomposition products. For clarity and direct comparison, all spectra were intensity-normalized so that their highest peaks equal unity.

***C 1s Spectra***

The C 1s spectrum for Na submerged in pure DEC:EC solvent (**Figure 24a**) shows four peaks at binding energies of 285.0 eV (C−C, C−H), 286.7 eV (C−O), 288.3 (C=O) and 290.0 eV ($CO_3$). After storing the Na metal electrode in DEC:EC for 4 min and 2 h, the same DEC:EC-attributed peaks can still be observed. However, the peak position of the $CO_3$ species shifts in BE to 289.5 eV, indicating $Na_2CO_3$ instead of $NaHCO_3$ with an increase in at.-% for the 4 min storage time, indicating further reactions between the Na surface and DEC:EC. A direct distinction between $Na_2CO_3$ and $NaHCO_3$ was achieved by performing reference XPS measurements for each species, which confirmed that their characteristic binding energies allow unambiguous differentiation (**Figure S6**). Compared to the pristine metal $CO_3$ species is detected at levels below 1 atom-%. Also, the pristine metal has a significantly higher proportion of C−C/C−H (47 atom-%). Spectra of the pristine Na metal surface is shown in the **chapter 3.1.2.1**. This indicates that the $CO_3$ species is formed on the surface after the addition of DEC:EC. The data presented in **Figure 24b** corresponds to C 1s spectra for Na metal submerged in $NaPF_6$-containing electrolyte, either without (**c**) or with (**d**) FEC as additive. For all these samples with the addition of salt, the spectra shows the same prominent peaks and intensities as the solvent exposed sample. The peak related to $CO_3$ species is shifted to a lower BE at 289.5 eV which is assigned to $Na_2CO_3$. For the sample with additive of FEC no carbonate peak is observed, while the peak at 288.7 eV is assigned to (C=O)O environment contained for example in $HCO_2Na$ or $CH_3CO_2Na$, while the peaks at lower binding energies of 286.7 eV and 285 eV indicate C−O and C−C/C−H bonds, respectively. Since all measured samples showed no DEC:EC-carbonate peak at 290.9 eV, the peak at 286.7 eV could be attributed to reacted solvent products such as carbon in −CONa indicating an alkoxide species like $CH_3ONa$ or $CH_3CH_2ONa$ while the corresponding O 1s peak was observed at 531.7 eV (see reference measurements **Figure S7**).

***O 1s Spectra***

The O 1s spectra of Na metal dipped in pure DEC:EC show three main features at binding energies 529.9 eV (NaOH), 531.9 eV (CO3, C=O) and 533.5 eV (C-O) shown in **Figure 24a**. The observed intensity ratios for carbonate species in the C 1s spectra do not match perfectly in with the O1s signal because, as discussed in the C 1s section, some $Na_2CO_3$ and other reaction products between Na and DEC:EC have formed on the surface. Generally, the O 1s region overlaps partially with the Na Auger region when using 1486.6 eV as excitation energy in XPS. Therefore, all O 1s spectra include two characteristic Auger peaks for sodium at 524 eV and 536 eV. When moving from the Na metal submerged in pure DEC:EC to Na metal in electrolytes based on $NaPF_6$ in DEC:EC without (**Figure 24b**) and with FEC (**Figure 24c**) the intensity of the O 1s species changes indicating more pronounced reactions between the metal surface and the electrolytes than between the metal surface and the pure solvent. The two

main features C-O and $CO_3$ change in relative ratio of 1:1.7 (DEC:EC), 1:6 (DEC:EC $NaPF_6$) to 1:7 (DEC:EC $NaPF_6$+FEC). The main peak centered at 531.9 eV is assigned to a carbonate species such as contained in $Na_2CO_3$ /$NaHCCO_3$ and alkyl carbonates. Because the intensity of this peak in the O 1s for carbonate is too high in relation to the − $CO_3$ peak in the C 1s, this indicates that there is likely another species contributing to this peak. As observed in the C 1s this could indicate carboxylate species like $HCO_2Na$ or $CH_3CO_2Na$, leading to an O 1s peak at 531.9 eV binding energy. After considering the carboxylate species contribution to the peak intensity at 531.1 eV, the relative amount of oxygen from the $CO_3$ peak is in good agreement with the C 1s peak for $Na_2CO_3$.

***F 1s Spectra***

The F 1s spectra for the electrolyte with and without FEC as additive show two peaks attributed to the $PO_yF_z$ species at 687.5 eV and NaF at 684.7 eV. No peak for the pure $NaPF_6$ salt was detected, showing that the applied washing procedure was effective (**Figure 10, caphter 3.1.1** ).

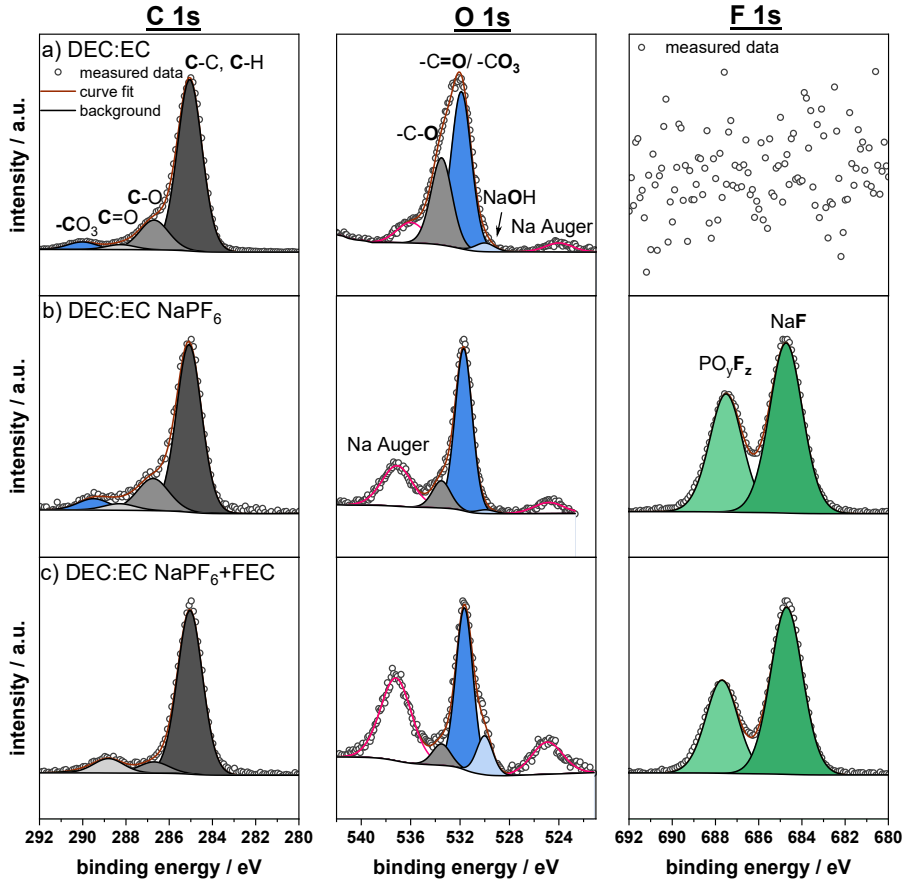


**Figure 24**: C 1s, O 1s and F1s core peaks of Na stored in (a) solvent (DEC:EC), (b) electrolyte with LiPF6 and (c) electrolyte with 5% FEC for 2min.

However, an additional experiment was performed to understand how the contact of pure FEC with Na metal effects the surface layer. The C 1s and O 1s spectra (**Figure 25**) showed the same four (C 1s) and three (O 1s) peaks as already mentioned above (**Figure 24**) The oxygen peaks showed a reduced content. Interestingly, the F1s signal only showed one prominent peak at 684.7 eV which is attributed to NaF.

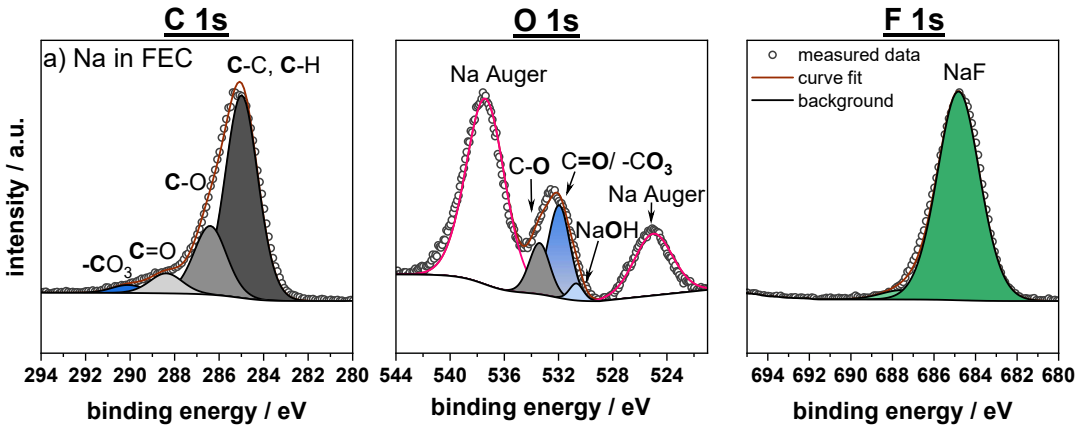


**Figure 25**: C 1s, O 1s and F 1s core peaks of Na stored in pure FEC.

***Comparison of Surface Layer Composition***

XPS analysis reveals a dynamic evolution of the sodium metal surface depending on electrolyte composition and exposure time (**Figure 26**). The elemental composition over time is summarized in **Table S9 and S10.** When sodium is stored in pure DEC:EC (1:1 vol.%) solvent, the surface is dominated by hydrocarbon species (C–C, C–H) comprising ~59 at.%, alongside minor contributions from carbonyl (C=O), ether (C–O), carbonate ($CO_3$), and NaOH species. Introducing $NaPF_6$ (0.75 M) to the solvent drastically alters the interfacial chemistry even after short exposure times. After 2 min, the surface shows significant enrichment in decomposition products, with NaF (24 at.%) and phosphorous-fluoride compounds ($Na_xPF_y$, 17 at.%) emerging as dominant species, while the hydrocarbon signal decreases to 10 at.% and NaOH becomes nearly undetectable (<2 at.%). This suggests a rapid conversion of surface-bound hydroxides and adventitious carbon into inorganic fluorinated phases. Extending the exposure time to 4 min results in further interphase transformation. $Na_xPF_y$ content increases to 29 at.%, and a decrease in NaF (up to 5 at.%) is observed, accompanied by an increase in $CO_3$ and related carbon species (~18 at.% total), indicating concurrent salt and solvent degradation pathways. Interestingly, after 2 h, the relative amount of $Na_xPF_y$ decreases to 18.7 at.%, while NaF increase again (22 at.%), suggesting either continued decomposition of $PF_6^-$ or transformation of $Na_xPF_y$ species into more stable fluorides. At this stage, most carbon-based signals (C–C, C–O, $CO_3$) drop below 8 at.%, and NaOH remains undetectable, implying the formation of a predominantly inorganic, fluoride-rich SEI. The presence of FEC significantly modifies this evolution. When sodium is exposed to DEC:EC $NaPF_6$ + 5 vol.% FEC, the SEI formed after 2 min exhibits lower $Na_xPF_y$ content (14%) compared to the additive-

free case, while NaF increases up to 26% and NaOH reappears at 4%. Carbonaceous species remain minor, with C–C (18 at.%) and all other carbon–oxygen functionalities remaining below 2%. After 4 min, NaF increases to 32%, while $Na_xPF_y$ slightly decreases to 12%, and the hydrocarbon content (C–C) rises to 23%. No NaOH is detected at this stage, and other carbon species remain low, indicating preferential formation of fluorinated inorganic layers under FEC influence. A particularly distinct surface composition is observed when sodium is stored in pure FEC without co-solvents. In this case, $Na_xPF_y$ species are nearly absent (~2%), while NaF dominates the surface (34%), accompanied by elevated hydrocarbon (24%) and ether (C–O, 8%) content. NaOH and $CO_3$ remain suppressed (<2%), suggesting a strong passivating effect of FEC that limits both salt and moisture-driven decomposition. These results point toward FEC's effectiveness in promoting a stable, predominantly inorganic SEI with reduced formation of reactive phosphorous-fluoride intermediates.

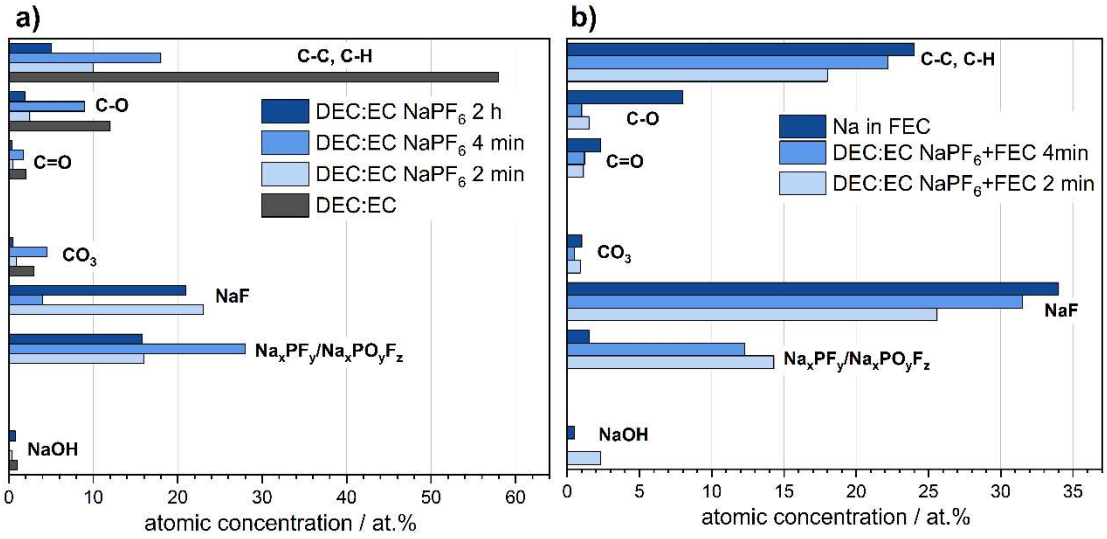


**Figure 26**: (a) Aatomic concentration of main surface species of Na stored in DEC:EC and DEC:EC $NaPF_6$ for different time scales (2 min, 4 min and 2 h) and (b) atomic concentration of main surface species of Li stored in DEC:EC $NaPF_6$+FEC for different time scales (2 min, 4 min) as well as Na stored in pure FEC.

### 7.2.1 Time-Dependent Formation of Decomposition Products in Electrolyte

Time-resolved GC–MS was applied to investigate EC:DEC solvent and electrolyte mixtures containing 0.75 M $NaPF_6$, stored with and without pristine sodium metal at 25 °C. Samples were analyzed after defined exposure intervals (2 min, 4 min, 2 h, 48 h) to differentiate degradation pathways initiated by reactive sodium metal. This method enables identification of early-stage intermediates and the kinetics of decomposition under static, electrochemically unbiased conditions. **Figure 27** shows the GC–MS results for EC:DEC electrolyte, with and without FEC additive, over time. For the storage over

DEC:EC $NaPF_6$ one decomposition product was detected already after 2 min, 4 min and 2 h of exposure to sodium metal, namely diethyl dioxahexane dioate (2, DEDD). However, after 48 h two new significant formation of liquid-phase degradation products were observed. The detected species correspond to: di-(2-ethoxycarbonyloxyethyl) carbonate (1, DECC) and diethyl-oxydiethane-2,1-diyl biscarbonate (3, DECE). With the presence of FEC no degradation products were observed.

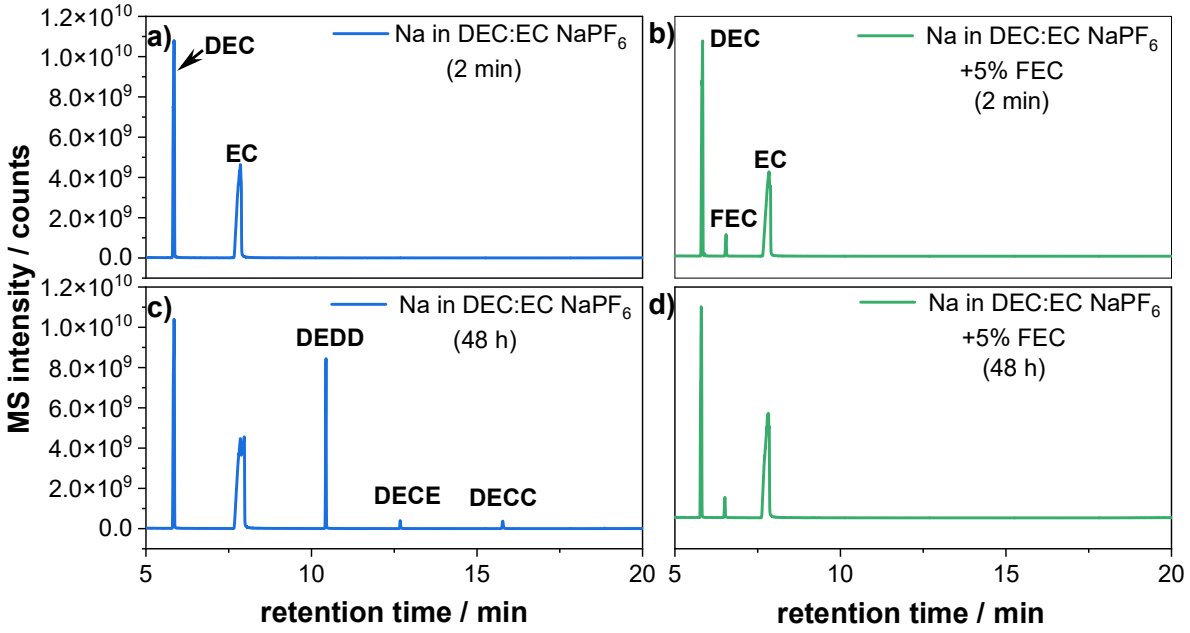


**Figure 27**: GC-MS chromatogram from the (a) DEC/EC, (b) DEC/EC $NaPF_6$, and (c) DEC/EC $NaPF_6$ + 5% FEC mixtures stored over sodium metal after 2 min, 2 h and 48 h. The numbers and additional reference measurements are assigned in **Table S7.**

### 7.2.2 Discussion

The time-dependent surface chemistry of sodium metal in carbonate-based electrolytes provides essential insights into early-stage SEI formation, salt degradation pathways, and additive effects. To avoid misinterpretations arising from sputter-induced artifacts, such as the artificial transformation of $NaPF_6$ into NaF observed during preliminary depth profiling experiments, only non-sputtered XPS measurements were used for surface analysis. The direct characterization approach revealed several key findings about the complex interfacial reactions occurring on Na metal in contact with EC:DEC-based electrolytes. A particularly striking observation is the rapid formation of an inorganic, NaF-rich interphase even after only a few minutes of exposure. In presence of $NaPF_6$, XPS showed a significant increase in NaF and phosphorous-fluoride species ($Na_xPF_y$), while GC-MS detected early liquid-phase degradation products like diethyl dioxahexane dioate (DEDD) (after 2h). After longer exposure (48 h), larger oligomeric products (DECC, DECE) were found, indicating time-dependent evolution of solvent decomposition pathways. However, when FEC was added, these liquid degradation products were

completely suppressed, and the SEI remained dominated by NaF. This highlights FEC's crucial role in stabilizing the interface. The origin of the intensified NaF signal combined with decreasing POxFy poses an important question: is the NaF truly newly generated over time, or does it result from simple growth of an already existing NaF overlayer? Given that XPS only probes the uppermost few nanometers, both scenarios are plausible. Without depth profiling or isotopic labeling, distinguishing between fresh chemical formation and overlayer thickening remains a limitation of the current methodology. Nevertheless, plausible reaction pathways suggest that NaF can form both via $PF_6^-$ reduction ($PF_6^- + Na^0 + e^- \rightarrow PF_5 + NaF$) and via FEC reduction (FEC + $Na^0 \rightarrow$ NaF + organic fragments), supported by DFT studies.[66,114] The role of $NaPF_6$ is particularly important in understanding the generation of phosphorous-fluoride intermediates. The absence of $Na_xPF_y$ species in pure-FEC exposures shows that $PF_6^-$ is the essential precursor for these degradation products. Previous studies suggest that $LiPF_6$ can partially dissociate into LiF and $PF_5$ even in the solid state, a similar equilibrium is plausible for $NaPF_6$, although likely less pronounced due to its higher cohesive energy. In the presence of trace protic impurities, $PF_5$ formed from such partial decomposition could react further to generate $POF_3$ and HF. These acidic species, especially HF, may then attack alkaline SEI components such as $Na_2CO_3$ or NaOH, softening the initially rigid inorganic interphase and promoting additional gas evolution ($CO_2$), thus impacting the long-term mechanical stability of the SEI.[115,116]

$$NaPF_6 \rightarrow NaF + PF_5$$

$$NaPF_6 + H_2O \rightarrow NaF + POF_3 + 2HF$$

$$NaPF_6 + Na_2CO_3 \rightarrow 3NaF + POF_3 + CO_2$$

$$Na_2CO_3 + 2HF \rightarrow 2NaF + CO_2 + H_2O$$

$$ROCO_2Na + 2HF \rightarrow NaF + CO_2 + H_2O + RF$$

Thus, commercial $NaPF_6$ impurities, even if low, can significantly impact SEI chemistry. Comparison with reports using ultra-pure $NaPF_6$ suggests that the observed extent of NaF and $Na_xPF_y$ formation could be partially attributed to residual salt hydrolysis and not only electrochemical breakdown, an important consideration for interpreting real-world battery behavior.[60] In terms of solvent degradation, early formation of DEDD suggests that sodium metal initiates ring-opening reactions of DEC:EC rapidly even without electrochemical cycling. The fact that larger products like DECC and DECE appear only after prolonged storage (48 h) supports a model where the initially protective SEI gradually becomes porous or chemically compromised, allowing deeper solvent attack. Again, FEC addition prevents these liquid-phase degradation processes entirely by forming a dense, crystalline NaF SEI early on. The suppression of $PF_6^-$ decomposition and solvent degradation by FEC can be rationalized by its influence on the $Na^+$ solvation structure. When FEC exceeds a coordination threshold (approx. 1.2 molecules per $Na^+$), its reduction dominates over $PF_6^-$ or solvent reduction, leading to the preferential formation of a stable inorganic SEI. This explains the much simpler and more stable surface

chemistry observed in FEC-containing electrolytes. However, limitations remain: without depth-resolved XPS or isotopic labeling, conclusions about reaction depth and kinetics must remain tentative. Furthermore, static storage conditions may not fully capture dynamic SEI evolution under real electrochemical cycling.

## 7.3 Mechanistic Insights into Electrolyte Decomposition – Propylene Oxide Formation at the Sodium Metal Interface

To further expand the understanding of electrolyte decomposition pathways in sodium-based battery systems, particularly under the influence of different electrolyte salts and solvent environments, the interaction of sodium metal with propylene carbonate (PC) and PC-based electrolytes containing sodium perchlorate ($NaClO_4$) was investigated. This study expand upon the previous work of Hofmann et al. and complements the previous findings of this thesis in DEC:EC/$NaPF_6$ systems by introducing a purely cyclic solvent and a different salt species, thereby enabling a comparative insight into SEI formation mechanisms and gas-phase decomposition products.[97] The work presented here was part of a collaborative study within POLiS (Cluster of Excelence) published in ChemSusChem. This collaborative work based on XPS, gas chromatography–mass spectrometry (GC-MS) by Andreas Hofmann and density functional theory (DFT) by Daniel Stottmeister, provides mechanistic understanding of how $NaClO_4$ and the addition of VC modifies the electrolyte decomposition pathway and enables the formation of gaseous byproducts like propylene oxide.

### 7.3.1 Theoretical Modeling (DFT Calculations)

DFT and ab initio molecular dynamics (AIMD) simulations were combined to assess the thermodynamic stability and adsorption behavior of electrolyte decomposition products on pure sodium metal, as well as on the (100) and Na-rich (111) surfaces of NaCl. These simulations reveal that perchlorate-derived chloride layers on sodium metal play a pivotal role in propylene oxide (PO) formation. In AIMD runs, Cl atoms from $[ClO_4]^-$ remain at the Na surface while O atoms penetrate below, creating a NaCl-rich overlayer absent in perchlorate-free systems. On pristine Na, ring-opening of PO is exothermic and proceeds readily. On NaCl, PO stays intact and is thermodynamically stabilized. Moreover, PO binds weakly (1 eV) to both Na and NaCl surfaces, ensuring its release into the gas phase once formed.

Mechanistic analysis indicates that PC decomposition begins via CO-induced ring opening of the carbonate moiety, yielding propanolate intermediates and CO, consistent with detected CO and absence of $CO_2$ in GC–MS. Two methyl-substituted isomers of propanolate display nearly identical formation energies, but different adsorption strengths on Na(100) influence the subsequent epoxide

step. Energetics computed on Na, NaCl(100), and NaCl(111) surfaces show that the first carbonate-forming reaction is exothermic on all but NaCl(100), whereas the final epoxide-forming step is only favorable on NaCl(100) (**Figure 28**). This suggests a sequential pathway: initial PC activation and propanolate formation occur on freshly exposed Na, followed by surface chlorination during perchlorate reduction, which then triggers ring closure to PO on the evolving NaCl overlayer. These combined theoretical insights, surface-specific adsorption, ring-opening versus ring-closing energetics, and the formation of a NaCl-rich layer explain the abrupt appearance of PO only in $NaClO_4$-containing electrolytes (**Figure 29**).

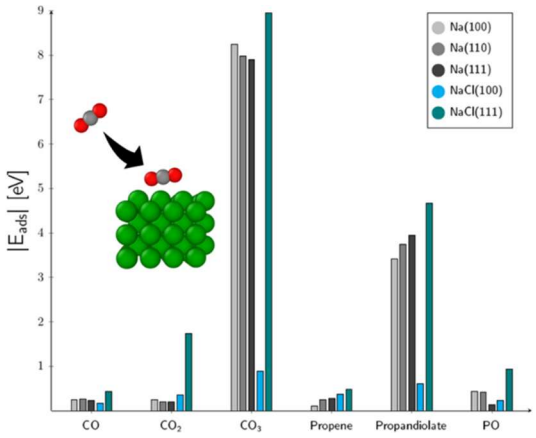


**Figure 28**: Comparison between the adsorption energies of molecules suspected to be involved in PO formation on sodium and sodium chloride surfaces.

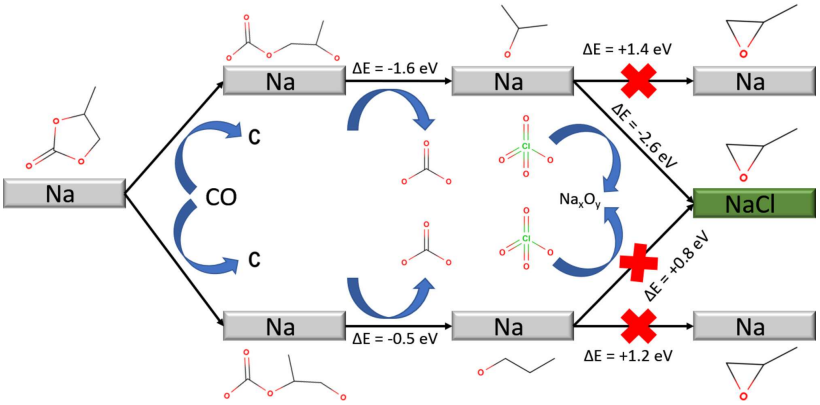


**Figure 29**: Reaction scheme for the proposed PO formation pathway, perchlorate decomposition leads to increasingly chloride-rich surfaces, which enable the ring-closing reaction for decomposition products of PC previously formed on the metal surface.

### 7.3.2 GC-MS Measurements

Gas evolution was assessed by sealing sodium metal and PC-based electrolyte (with or without $NaClO_4$) in a custom cell (**Figure 30**) and monitoring pressure and headspace composition over 800 h. In cells containing only PC and Na, no pressure increase was observed, although the PC gradually turned into

a yellow, viscous polymer, an indication of metal solvent polymerization. In contrast, cells with $NaClO_4$ exhibited a measurable pressure rise and released $H_2$, CO, propene, and trace amounts of PO as determined by GC–MS. The PO signal appeared weak on the standard system, but additional high-sensitivity GC–MS analyses (not shown) confirmed substantially higher PO intensities. Propene formation, identified with a NIST match score of 940/1000, aligns with analogous observations in EC-based electrolytes.[117]

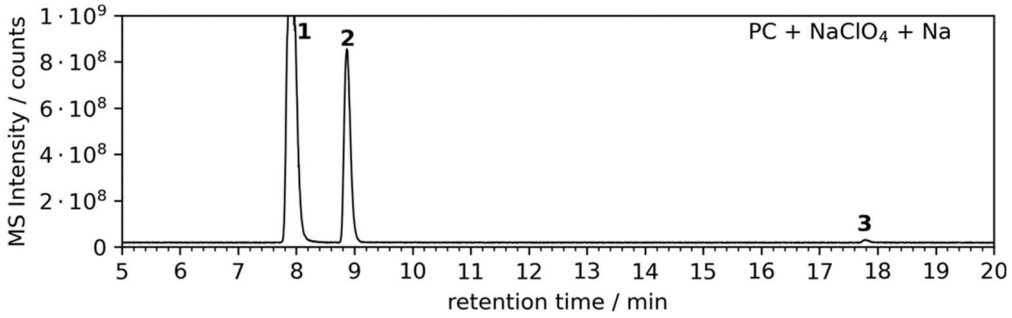


**Figure 30:** GC-MS chromatogram from the gas measurement of PC+$NaClO_4$+Na mixture after 1 week. Compound 1: air/Ar/CO, 2: propene, 3: propylene oxide.

### 7.3.3 XPS Measurements

To correlate theoretical DFT results with gas-phase products identified via GC, XPS was used to analyze solid decomposition products on sodium metal. The influence of storage time and liquid composition was examined by exposing Na metal to PC and PC-based electrolytes containing $NaClO_4$, with and without 10 % VC. Spectra of the pristine and metallic Na surface was already provided in **chapter 7.1**. Short electrolyte exposures of 2 min and 4 min showed no significant differences, therefore, only the 2 min data are shown (**Figure 31**). For better comparison, all spectra were normalized to the maximum peak height.

***C 1s Sepctra***

The C 1s spectrum of Na metal after immersion in pure PC solvent (**Figure 31a**) displays three dominant peaks at binding energies of 285.0 eV (C–C, C–H), 286.4 eV (C–O), and 290.4 eV ($CO_3$), with an intensity ratio of approximately 1.5 : 2 : 1 (for 2 min exposure). These values align well with those reported for liquid PC under near-ambient pressure XPS, suggesting either physisorbed solvent or minimal initial decomposition affecting the carbon chemical environment.[118] Additionally, a smaller signal appears at 287.7 eV, which is consistent with a carbonyl (C=O) species. In this system, two carbonate peaks can be distinguished: one at 290.4 eV from PC and another at 289.3 eV attributed to $Na_2CO_3$. After a 2 h exposure of Na to PC (**Figure 31b**), the same features remain visible, but the intensity ratios shift to 2.8 : 1.6 : 1, indicating ongoing surface reactions. In contrast to the pristine metal (**chapter 7.1, Figure 22**), where $CO_3$ signals are minimal (<1 at %), carbonate formation clearly occurs only upon PC

contact. The pristine surface also shows a higher relative contribution of C−C/C−H bonds (47 at %). The spectra in **Figure 31c–f** correspond to C 1s signals of Na samples immersed in $NaClO_4$-based electrolytes, either without (**c, d**) or with 10 % VC (**e, f**). All spectra in salt-containing environments feature pronounced peaks at 285 eV and 289.3 eV, accompanied by less intense features around 286.3 eV and 287.5 eV. The highest energy signal at 289.3 eV is assigned to $Na_2CO_3$.[119] The 287.5 eV component is attributed to carbonyl or carboxylate groups (e.g., in $HCO_2Na$), while the peaks at 286.3 eV and 285 eV represent C−O and C−C/C−H species, respectively. Notably, the PC-derived carbonate peak at 290.4 eV is absent in these samples. The 286.3 eV signal may instead indicate carbon in −CONa moieties, pointing to solvent decomposition into alkoxides such as $CH_3ONa$ or $CH_3CH_2ONa$. The associated O 1s signal was detected at 531.7 eV.

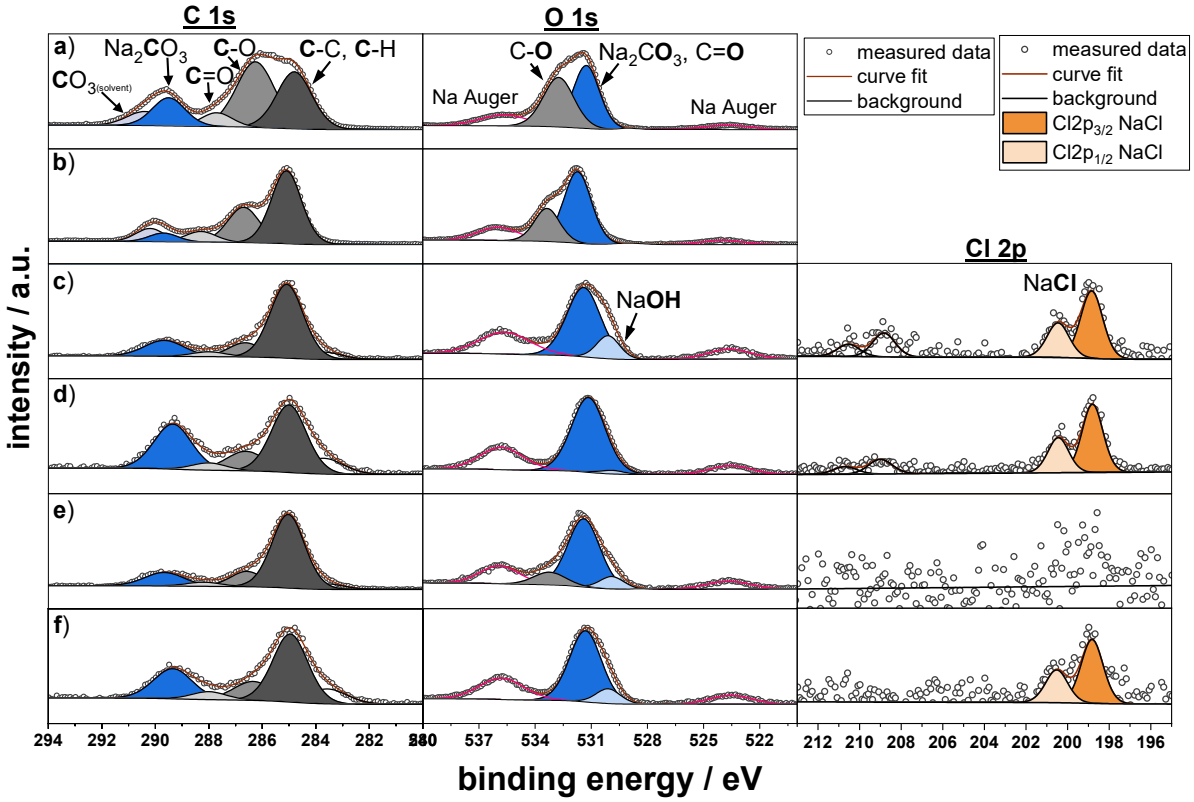


**Figure 31**: C 1s, O 1s and Cl 2p spectra of the sodium surfaces after storage in different electrolytes: pure PC solvent for 2 min (a) and 2 h (b), 0.75 M PC NaClO4 for 2 min (c) and 2 h (d), 0.75 M PC-VC NaClO4 for 2 min (e) and 2 h (f). The binding energy scale is calibrated versus the hydrocarbon peak at 285 eV.

***O 1s Spectra***

The O 1s spectra of Na metal immersed in pure PC display two main features at 531.3 eV and 532.7 eV, with a relative intensity ratio of 1 : 1 after 2 min (**Figure 31a**), shifting to 1 : 2 after 2 hours (**Figure 31b**). These signals, together with the C 1s data, align with the expected electronic environment of PC, which contains two distinct oxygen and three carbon environments. The deviation

from ideal intensity ratios suggests the formation of surface species such as $Na_2CO_3$ and other products arising from PC decomposition on Na. Due to the use of Al Kα radiation (1486.6 eV), the O 1s region partly overlaps with Na Auger signals, introducing characteristic features at approximately 524 eV and 536 eV in all O 1s spectra. Comparing samples exposed to pure PC with those in $NaClO_4$-based electrolytes (**Figure 31c–f**), substantial changes in the O 1s region are evident, pointing to more extensive surface reactions in the presence of salt and additives. In electrolyte-containing samples, three distinct O 1s contributions are resolved. For both 2 minute exposures, a low-binding energy peak at 530.0 eV is present, assigned to NaOH. A main component near 531.1 eV is attributed to carbonate species such as $Na_2CO_3$ and alkyl carbonates. However, this peak is more intense than expected based solely on the $CO_3$ signal from the C 1s spectrum, suggesting overlapping contributions—likely from alkoxide species (e.g., $CH_3ONa$), which produce an O 1s signal around 531.7 eV. Accounting for this alkoxide component brings the relative intensity of the carbonate contribution into agreement with the C 1s data.

***Cl 2p Spectra***

Chlorine 2p signals are detected in samples containing $NaClO_4$ as the electrolyte salt. Na metal immersed in 1 M $NaClO_4$ in PC for 2 min or 2 h shows Cl 2p doublets at 198.7 eV and 209.5 eV, corresponding to NaCl and residual $NaClO_4$, respectively.[120] Despite post-treatment rinsing, a small amount of salt remains at the surface. The $NaClO_4$ contribution is minor (below 0.1 at %) and is not further considered in the quantitative evaluation. For the electrolyte without VC (**Figure 31c, d**), a distinct NaCl signal is observed, indicating partial decomposition of the perchlorate salt. In contrast, when VC is included (**Figure 31e, f**), no significant NaCl is detected after 2 min. However, after 2 h, NaCl appears on the surface, suggesting that VC initially stabilizes the salt against decomposition but does not prevent it entirely over longer durations.

***SEI Composition in Different Electrolyte Mixtures***

To assess the surface composition quantitatively, atomic percentages of elements and selected species were determined from the fitted peak areas in the XPS spectra (**Figure 31**), using Scofield sensitivity factors specific to the instrument. An overview of the elemental distribution is provided in **Figure 32**. Sodium-based species commonly found in SEI layers, such as $Na_2CO_3$, NaCl, R-ONa, and NaOH, are grouped under "Na 1s" due to their overlapping binding energy range. Overall, the amount of surface-bound reaction products increases with longer storage times. A more pronounced interaction between sodium and the electrolyte is observed when salt is present, confirming that both the solvent and the salt participate in SEI formation. Elevated levels of oxygen and carbon suggest that solvent reduction is a dominant mechanism. The higher concentration of Na-containing species in salt-containing electrolytes, compared to pure solvent, further indicates the formation of additional organic and

inorganic sodium compounds. In the case of $NaClO_4$-based electrolytes without VC, the surface becomes progressively enriched in chloride species due to the formation of NaCl (**Figure 31c, d),** pointing to electrolyte salt decomposition. Although oxides formed during perchlorate reduction were not directly detected, the presence of NaOH may result from the reaction of such oxides with trace water in the electrolyte. Despite water contents between 26.5 and 31.3 ppm, these levels alone are unlikely to account for the total NaOH observed in the O 1s spectra. Notably, in the presence of 10 % VC, the initial chloride content after 2 min of soaking is significantly reduced. Although some chloride is still detected after 2 hours, its relative intensity remains lower than in VC-free electrolytes. This suggests that VC suppresses electrolyte salt degradation, thereby limiting NaCl formation on the sodium surface and indirectly mitigating propylene oxide generation.

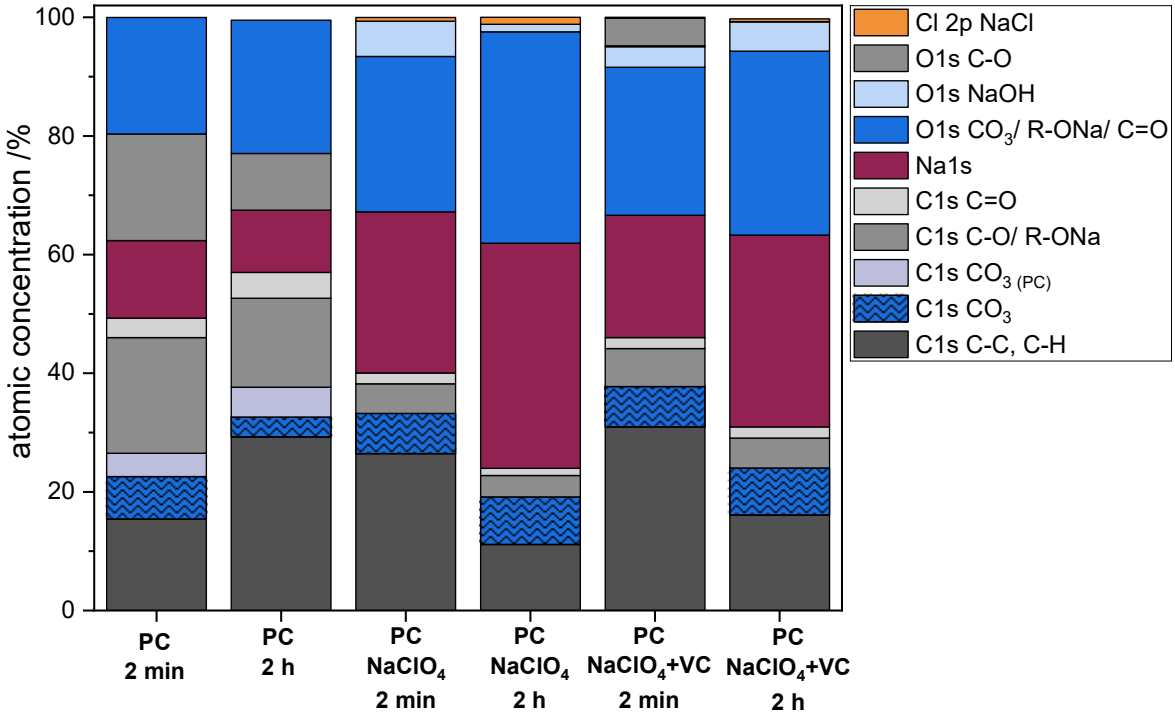


**Figure 32**: Bar plots of the atomic concentration found for the different storage conditions forming the SEI components by XPS.

### 7.3.4 Conclusion

This study integrates atomistic modeling with experimental analysis to illuminate the initial electrolyte degradation pathways that give rise to the solid electrolyte interphase in sodium metal batteries. Adsorption energies from DFT were directly correlated with GC–MS detectability, establishing why small gases (e.g., propylene oxide, CO, $CO_2$) desorb into the headspace while strongly bound intermediates (carbonates, diolates) remain buried at the interface. AIMD snapshots of perchlorate decomposition on Na surfaces revealing Cl retention in a nascent NaCl overlayer and deeper O

penetration were corroborated by XPS detection of NaCl and $Na_2CO_3$. These combined insights reveal a two-stage mechanism for PO formation: initial CO-induced ring opening of propylene carbonate on fresh Na metal produces a carbonate-bearing intermediate, and subsequent surface chlorination promotes an exothermic ring-closing step on the evolving NaCl layer. The XPS-GC-DFT triad thus not only maps species visibility across length and time scales but also proposes a coherent reaction sequence that explains PO's emergence in $NaClO_4$-containing systems. Beyond this specific electrolyte, the approach underscores how evolving inorganic films can trigger unexpected byproducts such as epoxides that have the potential to polymerize and alter SEI structure, highlighting the need for deeper investigation of secondary decomposition events and their impact on cell longevity.[121]

## 7.4 Correlating SEI Chemistry with Electrochemical Performance

### 7.4.1 Symmetrical-Cell Cycling

Following comprehensive analysis of the surface composition of sodium metal, interphase formation, and electrolyte degradation products across various electrolyte systems, the subsequent step involved investigating the correlation between these findings and electrochemical performance. To this end, all previously studied electrolytes, EC:PC and EC:DEC each containing $NaPF_6$ were tested with and without the additive FEC by assembling Na/Na symmetric cells and performing plating and stripping cycles. These experiments provided a comparative understanding of plating/stripping stability and overpotential behavior under cycling conditions. Metal plating experiments were conducted at current densities of 0.01, 0.02, 0.05, 0.075, 0.1 and 0.5 mA/ $cm^2$. As shown in **Figure 33**, when cycled at these current densities, the cell with DEC:EC, shows a small overpotential of 0.005 V which continious increase, reaching 0.22 V until failure at 200 h (at a current density of 0.5 mA/ $cm^2$). This implies the presence of polarization effects originating from higher resistance in the cell, also observed in the work of Zhang et al.[67] In contrast, after adding FEC to the electrolyte, the cell demonstrates stable cycling with a slightly higher but almost steady overpotential at the beginning of 0.02 V for 240 h without failure.

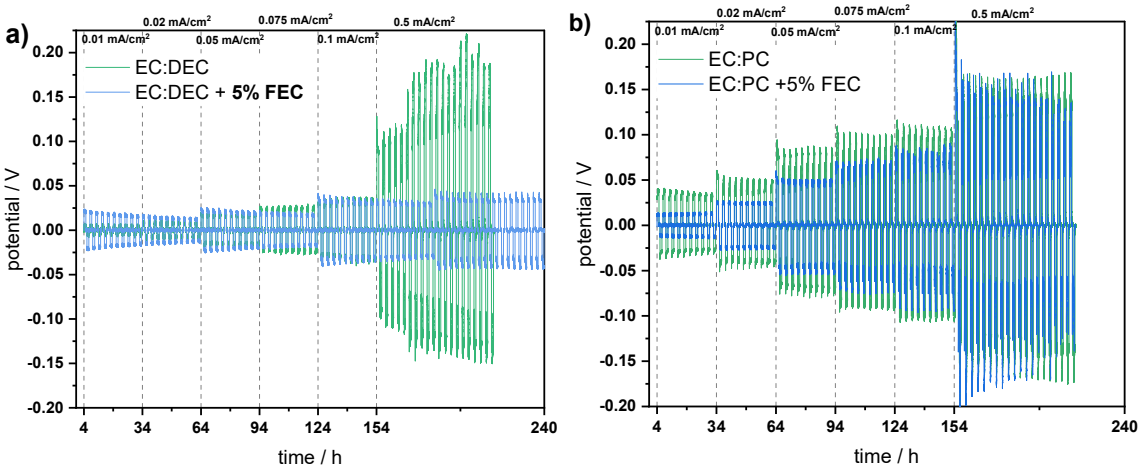


**Figure 33:** a) Voltage profiles of sodium plaiting/stripping as function of the current density for symmetrical cells in contact with organic solvent combinations (a) EC:DEC NaPF6 and (b) EC:PC NaPF6 each mixed with and without 5% FEC additive.

Comparing these, EC:PC electrolyte exhibits a higher overpotential of 0.05 V at a current density of 0.01 mA/ $cm^2$, reaching 0.15 V after 175 h. Notably, adding FEC decreases overpotential. However, overall, the cells exhibit stable plating and stripping behavior, as there are no sudden spikes in voltage. It is worth mentioning that the plating/stripping curves at 0.01 mA/ $cm^2$ and 0.05 mA/ $cm^2$ exhibit same shapes for the EC:DEC and EC:DEC+FEC electrolytes in Na/Na cells (**Figure 34a and b**). However when moving to EC:PC (**Figure 35a**) there is a different peaking behaviour visible compared to the FEC containing electrolyte. This peaking behaviour gets more prominent with increasing current density (**Figure 35b**). During the first half cycle, non-uniform sodium dissolution leads to pitting on the anode, while nucleation on the cathode introduces an additional energy barrier (peak I). Continued growth on existing nuclei lowers the overpotential, forming a voltage plateau (II). After current reversal, sodium is stripped from microstructures, and new nucleation on the anode causes peak III, followed by a deposition plateau (IV) and a second peak (V), which reflects pitting after microstructure depletion. This could be attributed to SEI instability.

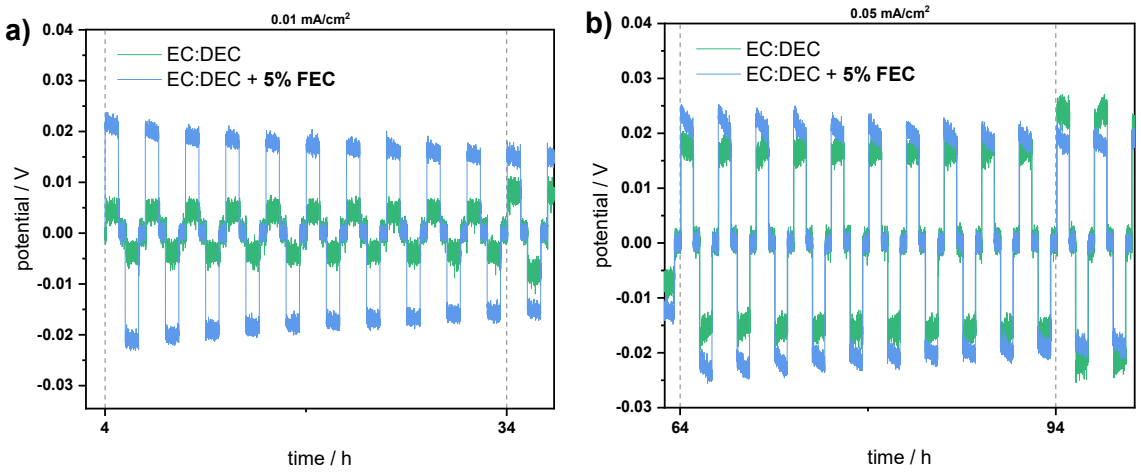


**Figure 34:** Enlarged voltage profiles of sodium plaiting/stripping as a function of the current density (a) 0.01 mA/ $cm^2$ and (b) 0.05 mA/ $cm^2$ for symmetrical cells in contact with EC:DEC $NaPF_6$ mixed with and without 5% FEC additive.

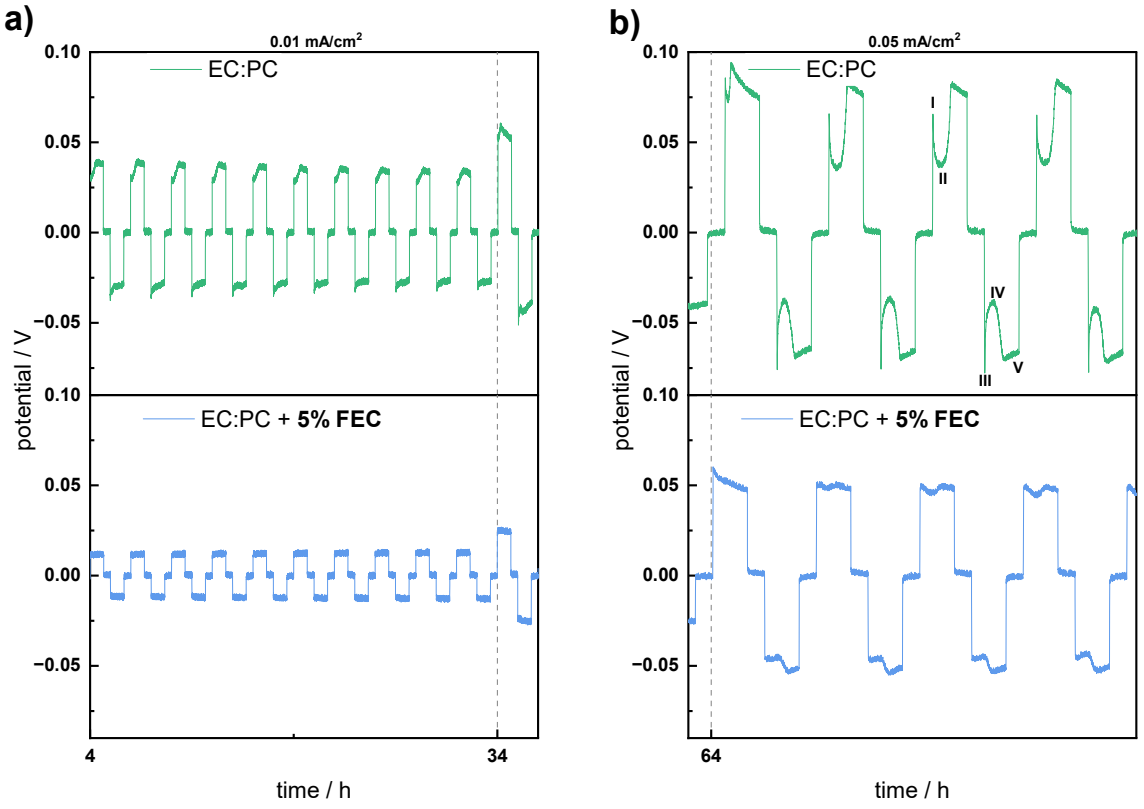


**Figure 35:** Enlarged voltage profiles of sodium plaiting/stripping as a function of the current density (a) 0.01 mA/ $cm^2$ and (b) 0.05 mA/ $cm^2$ for symmetrical cells in contact with EC:PC $NaPF_6$ mixed with and without 5% FEC additive.

### 7.4.2 First-Cycle GC-MS of Electrolyte

Previous GC–MS studies investigating sodium in various electrolytes have primarily focused on half- or full-cell configurations, where the contribution of pure sodium metal itself remains unclear. The preceding chapter demonstrated how simple immersion of the metal already leads to distinct degradation products. This chapter examines the additional impact of cycling in Na/Na symmetrical cells on the formation of soluble decomposition products. This approach is intended to serve as a baseline for future studies, helping to differentiate whether degradation products reported in the literature originate from the sodium metal itself or from other cell components typically present in full or half-cells. To gain a more detailed insight into the formation of soluble species during cycling, a Na||Na coin cell was disassembled after the first stripping/plating cycle, and the used Whatman GF/B separator was extracted and the extracted electrolyte was analyzed by GC-MS. Reference spectra of uncycled EC:DEC and EC:PC electrolytes are provided in the Supporting Information (**Figure S8** and **Table S11**).

**Table 2** summarizes the detected components of the measured electrolytes and their respective retention time. It should be noted that the peaks detected at 4.20 min retention time refer to the used solvent DMC (see experimental section) and is not related to the analyzed electrolyte formulations. All of the above listed electrolytes underwent electrochemical reactions during cycling. Additionally, pure, uncycled EC:DEC 0.75 M NaPF6 was also analyzed by GC-MS to allow determination of decomposition products formed by electrode-electrolyte reaction. The formation of soluble and oligomeric decomposition products is observed for DEC:EC $NaPF_6$ except for the electrolyte containing FEC. Notably, only DEC:EC sample contained di-(2-ethoxycarbonyloxyethyl) carbonate (1, DECC), diethyl dioxahexane dioate (2, DEDD) and diethyl-oxydiethane-2,1-diyl biscarbonate (3, DECE) as decomposition products, which was not observed in the reference sample. However, after one cycle in the FEC-containing electrolyte, no detectable degradation products were observed. This suggests that FEC is particularly effective in suppressing the formation of soluble oligomeric and polymeric species, thereby enhancing electrolyte stability and mitigating solvent decomposition. The measurement of EC:PC and EC:PC FEC revealed no additional degradation products in these measurements. Notably, the previous measured degradation product in EC:DEC could not be detected. This aligns with the reports of Eshetu et al., which reported that a linear carbonate (here: DEC) is required for the formation of DEDD.[122]

**Table 2:** GC-MS measurements of degradation products formed during the first cycle in Na/Na symmetrical cell. Additional, reference measurements on the pure solvent were conducted.

| Sample | Detected Components | Retetion time / min |
|---|---|---|
| EC:DEC $NaPF_6$ | DEC / EC / 3 / 2 / 1 | 6.65 / 8.39 / 11.15 / 13.60 / 16.82 |
| EC:DEC $NaPF_6$ + FEC | DEC / EC /FEC | 6.70 / 8.40 |
| EC:PC $NaPF_6$ | EC / PC | 8.30 / 8.67 |
| EC:PC $NaPF_6$ + FEC | EC / PC / FEC | 8.31 / 8.64 |
| EC:DEC $NaPF_6$ (ref.) | DEC / EC | 6.63 / 6.21 |
| EC:PC $NaPF_6$ (ref.) | EC / PC | 8.32 / 8.61 |

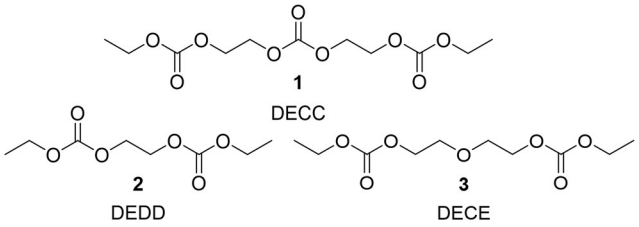


### 7.4.3 Digital Microscopy Measurements

Furthermore, Na electrode behavior during plating and stripping was observed in a symmetric cell set up employing EC:PC 0.75 M $NaPF_6$ electrolyte formulation with and without FEC (**see chapter 4.7** for experimental setup) under a digital microscope.

First, sodium electrodes were cycled in EC:PC $NaPF_6$ applying a current of 0.5 mA/ $cm^2$ for one plating/stripping cycle for 3 h respectively. The images recorded are given in **Figure 36**.

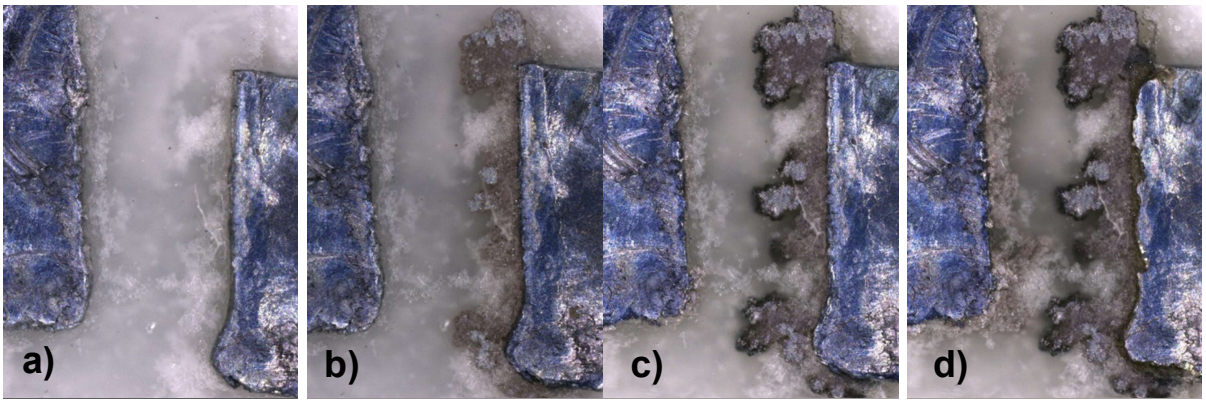


**Figure 36:** a) Image of the Na//Na in EC:PC $NaPF_6$ setup b) Image recorded after 1.5 h of plating regarding the upper electrode at a current of 0.5 mA/ $cm^2$ c) Image recorded after 3h of plating d) Image recorded after 3h of stripping regarding the upper electrode at a current of 0.5 mA/ $cm^2$.

During the performed measurements the smooth silvery sodium electrode surfaces always turned blue-violet and rough when exposed to the respective electrolytes (**Figure 36a-d**) due to degradation

processes and reaction. As can be seen in Figure **36b** and **c** for the first setup sodium dendrite growth was very uneven and followed a tree-like pattern, and the sodium was not plated as even film. In addition, when comparing image **36c** and **d**, it becomes evident that the subsequent stripping process did not take place at the formerly plated sodium structures, but at the metal electrode itself. This indicates the plaiting/stripping process to be likely irreversible and moreover, that the plated sodium was no longer reusable. After that first initial experiment, sodium electrodes were cycled in EC:PC $NaPF_6$ 5% FEC with a current density of 1.0 mA/ $cm^2$ for 2 h respectively. **Figure 37** displays the OCV of the symmetric cell.

**Figure 37:** CuNa/CuNa symmetric cell with EC:PC 0.75 M NaPF6 5% FEC electrolyte at OCV.

After coming into contact with the electrolyte solution the sodium electrode surfaces again changed color from silver to blue, indicating spontaneous reactions of metallic sodium with the electrolyte solution. The color change and roughness of the surface prior to cycling aligns with findings from Pfeifer *et al*.[123] As seen in **Figure 38a** the first sodium plating was mostly evenly distributed along the left electrode. However, there are still some visible nucleation points that display a mossy dendrite structure. Following this 2 ½ cycles later in **Figure 38b** both electrodes display mossy Na dendrite structure that seems to increase in thickness towards the center of the electrodes. The formation of mossy dendrite structures and pits, as seen in **a** and **b**, is associated with transitions between kinetically fast and slow interfacial reactions.

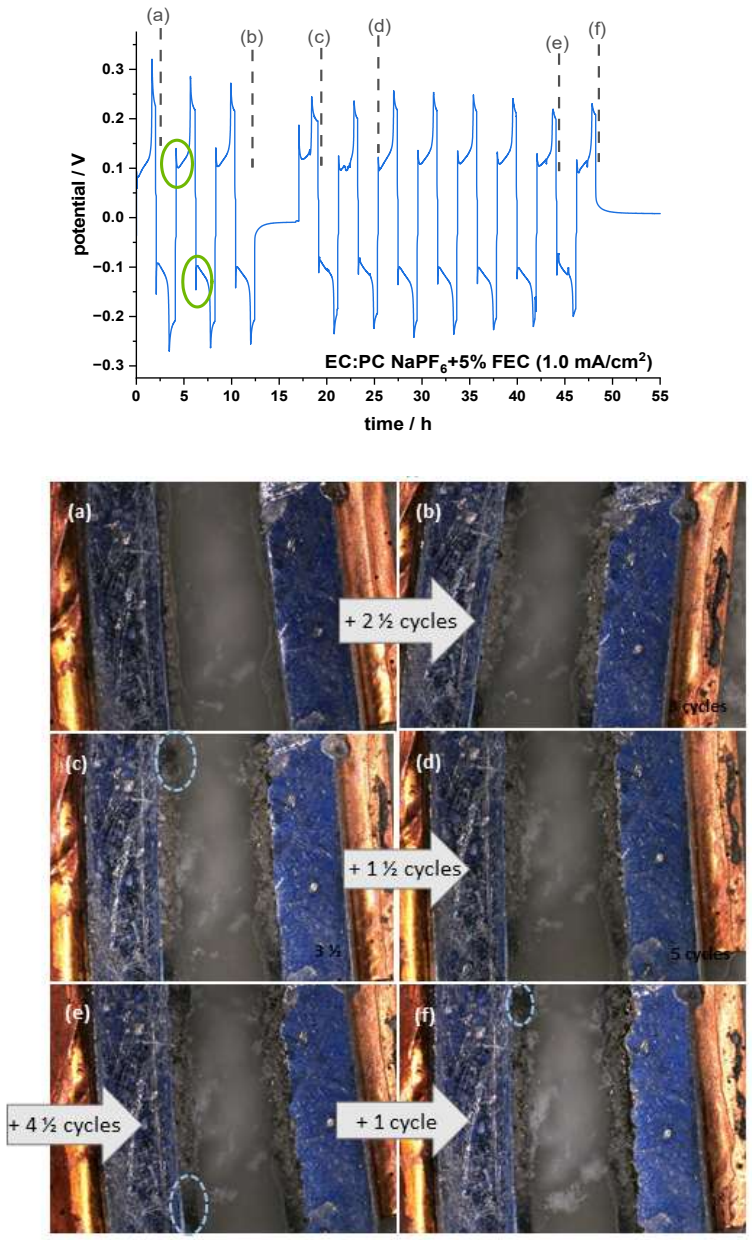


**Figure 38**: Voltage profile of sodium plating and stripping of CuNa/CuNa symmetric cell with EC:PC 0.75 M $NaPF_6$ + 5% FEC electrolyte at a current density of 1.0 mA/ $cm^2$ (57µA). (a) – (f) progressing plating and stripping of the sodium electrodes

When comparing the voltage profile in **Figure 38** to previous coin cell measurements (**Figure 35**), same features can be seen. The peaks visible during cycling (marked by green circles) can be associated with the previously described interfacial reactions (peak I and III), as described for Li by Chen *et al.*[124] It is important to note that the overpotential in the symmetric coin cell at the start of each cycle is significantly higher, indicating a greater amount of active sodium loss with each cycle compared to the symmetric optical cell. The initial overpotential peak slowly reduces with extended cycling periods, associated dendrite formations can be seen in **Figure 38c** and **d**. Notably, after several cycles the color of dendrites on the edge of the formed structure changes from silver to a dark grey indicating a

reaction of the freshly plated Na metal. Additionally, there is a noticeable growth of pits on the electrode on the right. This aligns with previous findings of Chen *et al* for Li preferentially stripping from dendrite structures that become electrically isolated, leading to subsequent stripping from the bulk metal.[124] **Figure 38e** and **f** depicts the extended cycling of the symmetric cell with 1.0 mA/ $cm^2$ current. The mossy dendrite structure keeps growing (including dark grey areas; blue circles) while the appearing pits reduce the electrode surface. Comparing **d** and **f** highlights the subsequent stripping processes at the bulk metal electrode due to the formation of electrically insulated "dead" Na. Furthermore, the measured potential for plating and stripping decreases with each cycle, as seen in the voltage profile depicted in **Figure 38**. This aligns with the findings of Chen *et al* regarding the initial cycles of Li plating and stripping. They attributed this to a reduction in maximum cell polarization from cycle to cycle, which is caused by an increase in active surface area and the formation of lower impedance interfaces. **Figure 39** provides an overview of the EL-Cell after cycling at 1.0 mA/ $cm^2$. Notably, there is an increase of white dendrite like structures visible in the separator (indicated by blue circles). These probably relate to dried sections of the glass fiber separator as electrolyte is continuously reduced by reacting with freshly plated sodium. Additionally, the plating of sodium is concentrated on previously deposited Na, aligning with the findings of Bieker *et al.* They attributed this phenomenon to a nonuniform current distribution when applying an electric field, therefore leading to locally preferred lithium deposition.[125] This leads to the cracking of the initial surface layer and protrusion of "fresh" deposited Na, which offers a stronger electrical field, higher specific surface area and therefore a higher interface area with the electrolyte. Additionally, they concluded that the incompletely formed and therefore chemically different surface film offers lower bulk and grain boundary resistance, further increasing this phenomenon.

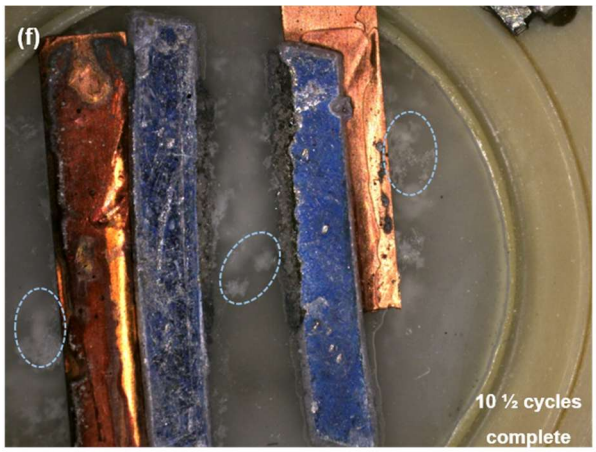


**Figure 39:** Overview of CuNa/CuNa symmetric cell with EC:PC 0.75 M $NaPF_6$ + 5% FEC electrolyte after 11 oxidations at 1.0 mA/ $cm^2$.

### 7.4.4 Separator Optimization

To enable reliable XPS analysis of cycled cells, the standard glass fiber (Whatman) separator was replaced due to its tendency to leave fibers and surface contamination on the electrode. The goal was to compare native sodium metal, as formed in storage experiments with freshly plated Na, focusing on how the initial SEI differs in both cases (**see Chapter 7.1**). In contrast, electroplated sodium is immediately exposed to the electrolyte and reflects a more reactive surface. To minimize surface contamination during XPS analysis, a Celgard separator was tested. However, the Celgard (2325-1769M) from our lab failed during cycling. To further study these different Celgard and their treatment, their surface was examined by using a thermal field emission scanning electron microscope (FESEM) (see **Figure 40**). Samples were coated with a 5 nm AuPd-layer to increase conductivity and included Celgard 3501-0660M and Celgard 2325-1760M both washed with ethanol and subsequently dried overnight at 40 °C. The images illustrate the differences between the pristine Celgard and pre-treatment method. Pristine Celgard displays known porosity, but only few pores are visible. The largest pore measures 160 nm in length, with only few of that size being visible, while the smallest measures only 100 nm. Additionally, there are many pores that allow for diffusion, but their density prohibits measurement of the corresponding width and length. Meanwhile, the Celgard 3501-0660M shows significantly lager pores. The largest pore measures 490 nm in length, while the smallest measures 360 nm in length. Furthermore the image indicates that washing the separator with EtOH and drying doesn´t increases the size number of pores.

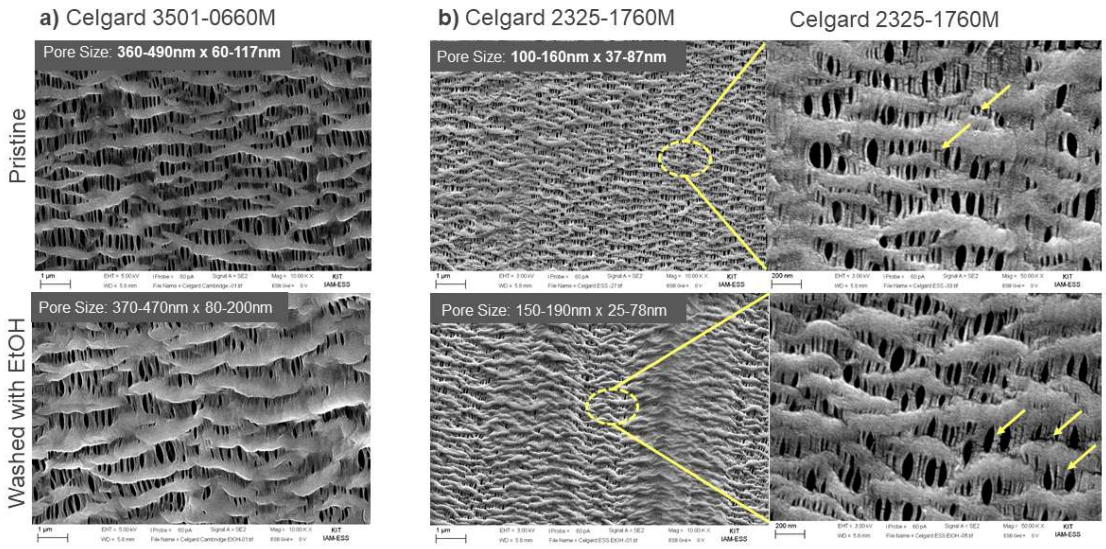


**Figure 40**: SEM imgae comparison of used Celgard within this work, pristine and washed with EtOH.

Following the optimization of the separator system, the next step was to establish a reliable method for plating sodium onto copper in a way that allows for clean post-mortem analysis. Since EC:PC had

shown favorable plating and stripping behavior in previous tests, this electrolyte formulation was chosen for all subsequent experiments. Recent studies have highlighted the critical role of stack pressure in the plating and stripping performance of Na||Cu half-cells. As demonstrated by Margadonna et al., pressures below 185 kPa result in poor performance characterized by high hysteresis and low coulombic efficiency, while moderate to high pressures (185–743 kPa) significantly enhance both efficiency and cycle life.[126] These improvements are attributed to better interfacial contact between sodium and the separator, which promotes more homogeneous plating and reduces local overpotentials. Similar trends were observed in the present investigation. **Figure 41** show initial attempts using only Celgard as the separator consistently led to poor sodium deposition. The voltage profiles were noisy and unstable, and EIS measurements revealed fluctuating, high ohmic resistance, likely due to poor wetting and limited contact between the separator and electrode. Even applying additional mechanical pressure using a spacer did not fully resolve this issue, possibly due to inherent limitations in the Celgard's wettability and mechanical properties. To improve the interfacial stability, a modified separator configuration was implemented using a Celgard–Whatman–Celgard (CWC) sandwich structure. This setup significantly improved the plating behavior: voltage traces during 10 h plating at 0.5 mA/ cm² were much smoother, and the potential response was stable over time. Additionally, impedance measurements showed a steadily decreasing ohmic resistance, indicating progressively improved ionic contact and a more homogeneous deposition process. In contrast, the resistance profile for cells with only Celgard remained erratic.

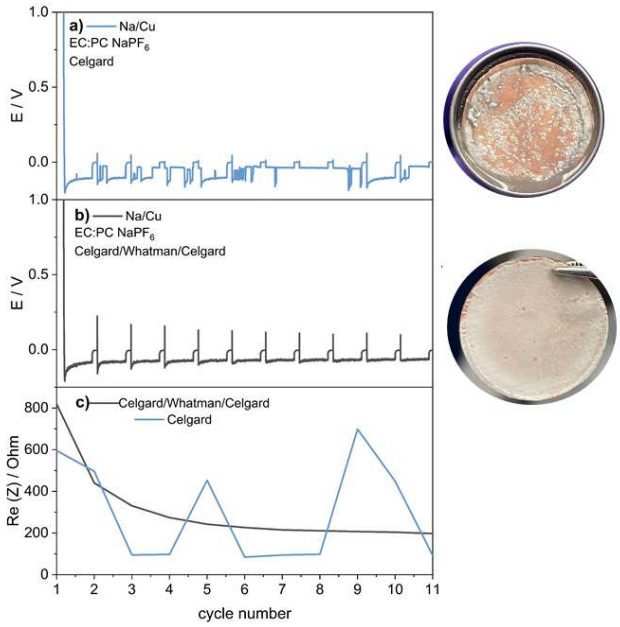


**Figure 41**: Comparison of plating behaviour on copper in Na/Cu half cell setup with (a) one celgard and (b) Celgard-Whatman-Celgard, and (c) the corresponding ohmic resistance over cycle number.

## 7.5 Comparative Surface Chemistry of Sodium Metal Under Electrochemical and Passive Conditions

In this subsection, the surface chemistry of sodium metal formed under different conditions is compared to gain deeper insight into SEI evolution and metal electrolyte interactions. Specifically, three types of sodium surfaces were analyzed: (i) native sodium that was simply soaked in EC:PC $NaPF_6$ electrolyte for 2 min, (ii) freshly plated sodium on copper obtained from Na||Cu half-cells, and (iii) residual sodium remaining on the counter electrode after cycling. This comparison allows us to distinguish between the effects of spontaneous passivation, electrochemical plating, and stripping-related surface evolution. By analyzing these samples with XPS, the influence of the nature and formation conditions of sodium metal on the composition and stability of the interphase is assessed.

***C 1s Spectra***

The C 1s spectrum for Na submerged for 2 min in EC:PC NaPF6 (**Figure 42a**) shows five peaks at binding energies of 285.0 eV (C−C, C−H), 286.7 eV (C−O), 288.3 eV (C=O) and 289.4 eV ($CO_3$) and 290 eV ($NaHCO_3$). After the applied plating conditions the Cu foil with freshly plated Na metal as well as the Na on the counter electrode showed the same peaks (**Figure 42b and c**). However, the CO3 species disappeared at the Na counter electrode .

***O 1s Spectra***

The O 1s spectra of Na metal dipped in pure EC:PC $NaPF_6$ show three main features at binding energies 529.9 eV (NaOH), 531.9 eV ($CO_3$, C=O) and 533.5 eV (C-O) shown in **Figure 13a**. However, comparing to the cycled electrodes, no NaOH is observed. Additionally, the O 1s region overlaps partially with the Na Auger region when using 1486.6 eV as excitation energy in XPS. Therefore, all O 1s spectra include two characteristic Auger peaks for sodium at 524 eV and 536 eV.

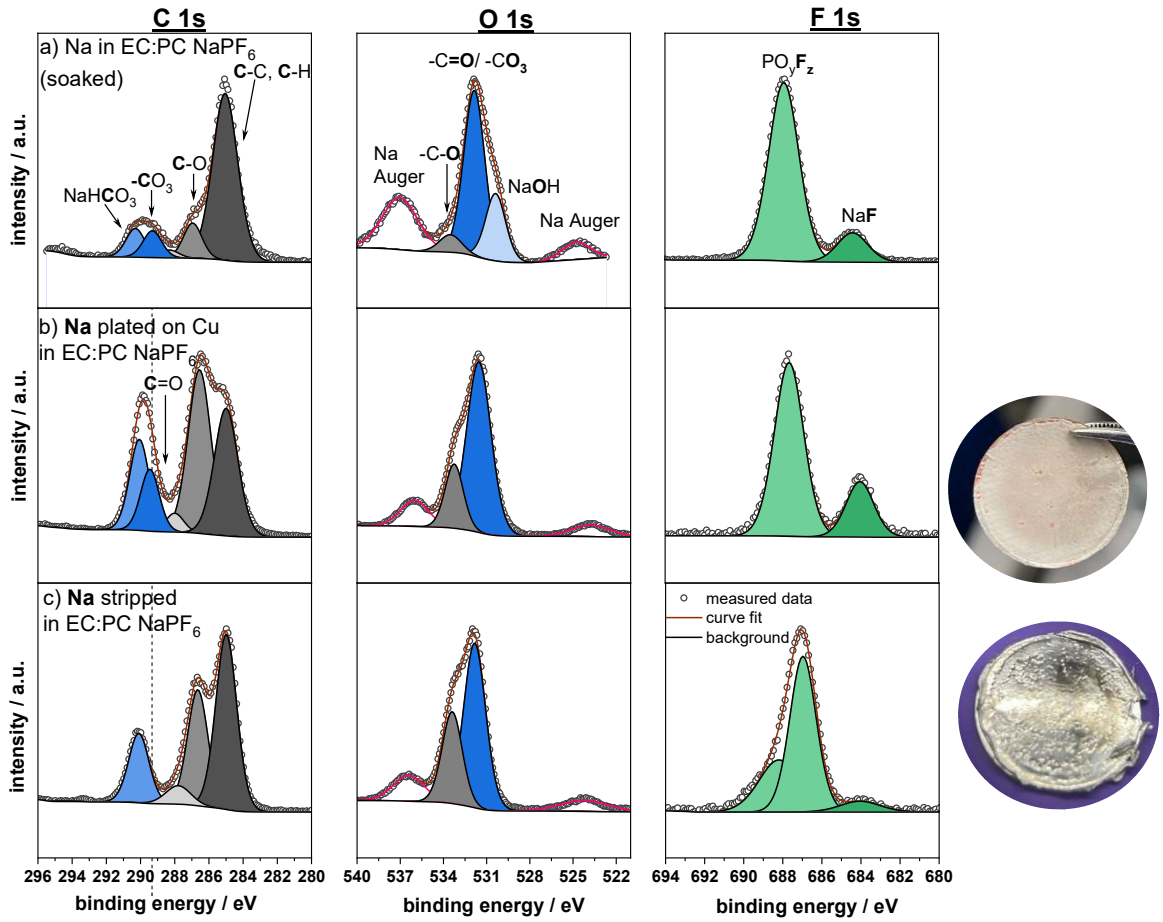


**Figure 42**: C 1s and O 1s spectra of the sodium surfaces after plating it on (a) copper side and (b) sodium side in 0.75M EC:PC $NaPF_6$ electrolyte.

***Surface Ratio Comparison***

XPS analysis reveals the evolution of the sodium metal surface under different conditions, highlighting the changes in the surface chemistry of sodium when plated onto copper and compared to a reference measurement (**Figure 42**). In the reference experiment, where pure potassium was stored under insertion conditions in EC:PC $NaPF_6$ (without electrical current), the surface was primarily composed of F and P species, with NaF at 4%, $NaPO_x$ at 24%, and C−C, C−H species at 20.7%. Additionally, NaOH was detected at 5%, and smaller amounts of $Na_2CO_3$ (2.4%) and $NaHCO_3$ (2.6%) were observed. When freshly plated sodium metal was examined, there was a noticeable increase in carbonate species, with $NaHCO_3$ at 7.1% and $Na_2CO_3$ at 3.6%. At the same time, the C−C, C−H peak decreased significantly to 11.8%, and F species were reduced, with NaF at only 1.5% and $NaPO_x$ at 5%. The C−O peak, however, saw a substantial increase, rising from 3.3% in the insertion experiment to 13.9%. In the stripped sodium side, similar trends were observed. The C−O content remained elevated at 13.8%, and the F species were further reduced to a total of 7.4%. Interestingly, no carbonate species ($Na_2CO_3$) were detected, but $NaHCO_3$ was present at 8.2%. This suggests that the freshly plated sodium metal undergoes a transformation upon exposure to the electrolyte, with an increase in carbonate species

and a reduction in the carbon hydrogen bonds, likely due to the interaction with the electrolyte. The reduced presence of fluoride species further indicates that these changes are driven by the surface interactions between the metal and the electrolyte, leading to the formation of a distinct surface layer. The changes observed in both the plated and stripped sodium parts underscore the dynamic nature of the surface chemistry in sodium metal systems.

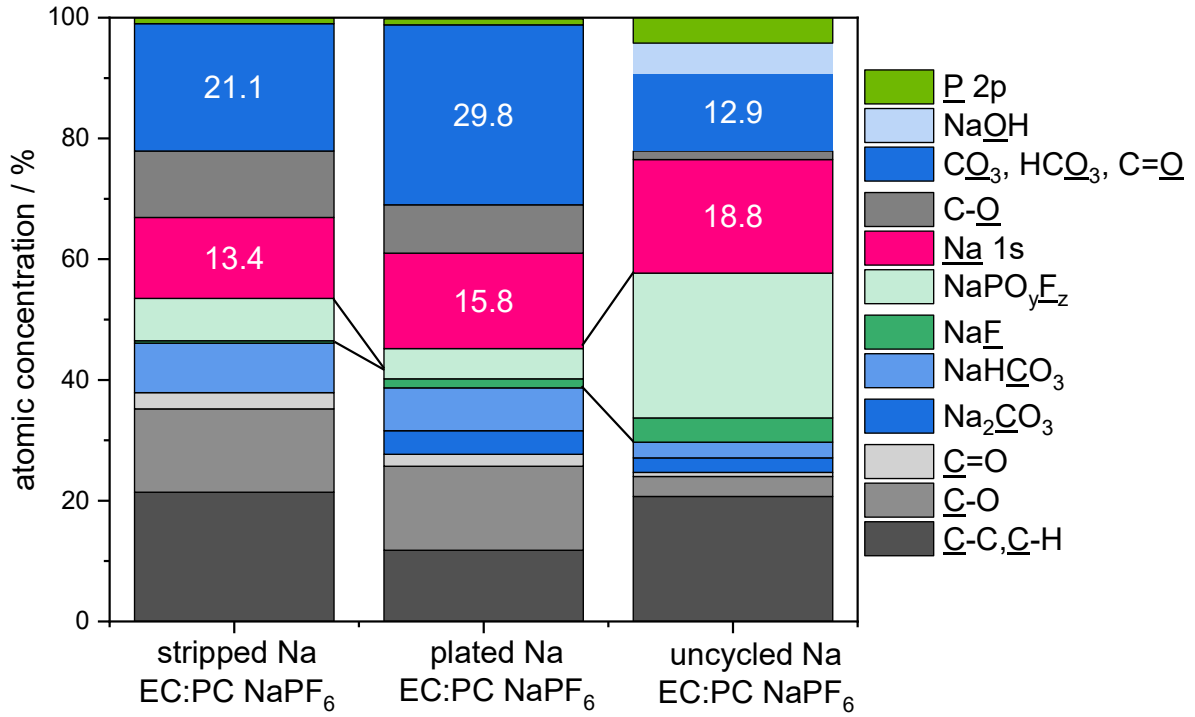


**Figure 43**: Bar plots showing the atomic concentrations of SEI components determined by XPS for three sample types in EC:PC + $NaPF_6$ electrolyte: (i) stripped sodium after cell disassembly, (ii) plated sodium on copper current collector, and (iii) sodium stored under EC:PC + $NaPF_6$ conditions as a reference for spontaneous SEI formation.

# 8 Solid Electrolyte Interphases on Potassium

## 8.1 Elemental Quantification of Pristine Potassium vs. Metal Surface and the problem with impurities

Building on the insights from **Chapters 6 and 7**, where "pristine" versus sputter-cleaned surfaces of lithium and sodium revealed distinct compositional differences, this chapter extends the same methodology to potassium metal. Two commercial potassium grades were examined to determine how supplier-specific factors, storage medium and nominal purity affect reactivity, handling, impurity levels, and half-cell performance. A complementary methodology was employed: first, galvanostatic cycling against hard carbon evaluates electrochemical behaviour, second, XPS of both pristine and $Ar^+$-sputtered surfaces maps the native passivation layer versus underlying metallic potassium; and third, GC-MS tracks volatile decomposition products emerging during electrolyte contact and cycling. This structured approach enables a holistic assessment of how subtle differences in metal purity and surface chemistry govern the stability and efficiency of potassium-based anodes.

### 8.1.1 Electrochemical Performance

Electrochemical properties of the different potassium suppliers were studied in half cells vs. hard carbon (HC) with 0.75M solution of $KPF_6$ in EC:PC (1:1 vol-%). Galvanostatic charge and discharge cycles were carried out to explore the difference in long-term cycling behavior of HC against either of the two K metal suppliers $K_A$ (potassium delivered in an ampule, 99%) and $K_{MO}$ (potassium delivered in mineral oil, 98%), respectively. During electrode preparation for the potassium half cells, noticeable differences in haptics were observed across the two potassium grades. Notably, the metal with higher purity exhibited increased softness and was more challenging to handle due to their pronounced stickiness. These physical differences translated to distinct electrochemical responses. **Figure 44a** displayed the cycling stability of $K_A$ and $K_{MO}$, where the half cell with $K_A$ as electrode showed a specific discharge capacity of 31.7 mAh/ g after 300 cycles at a current density of 38 mAh/ g. However, the capacities remained less than 4.34 mAh/ g and jumped to 73.2 mAh/ g for the initial two cycles at 19 mA/ g. In contrast, half cells with $K_{MO}$ showed higher specific capacities of 50.1 mAh/ g after 300 cycles at C/10. The $K_{MO}$ electrode shows the same decreasing trend in the initial two cycles followed by a gradually increase of the capacity, which may be related to the formation of the SEI and the penetration of the electrolyte before a stable discharge capacity is achieved. When comparing the internal resistances of $K_A$ and $K_{MO}$, the $K_{MO}$ cell demonstrates a smaller IR drop, indicative of lower internal resistance (**Figure 44d**). In both cases there is an increase of internal resistance over cycle number.

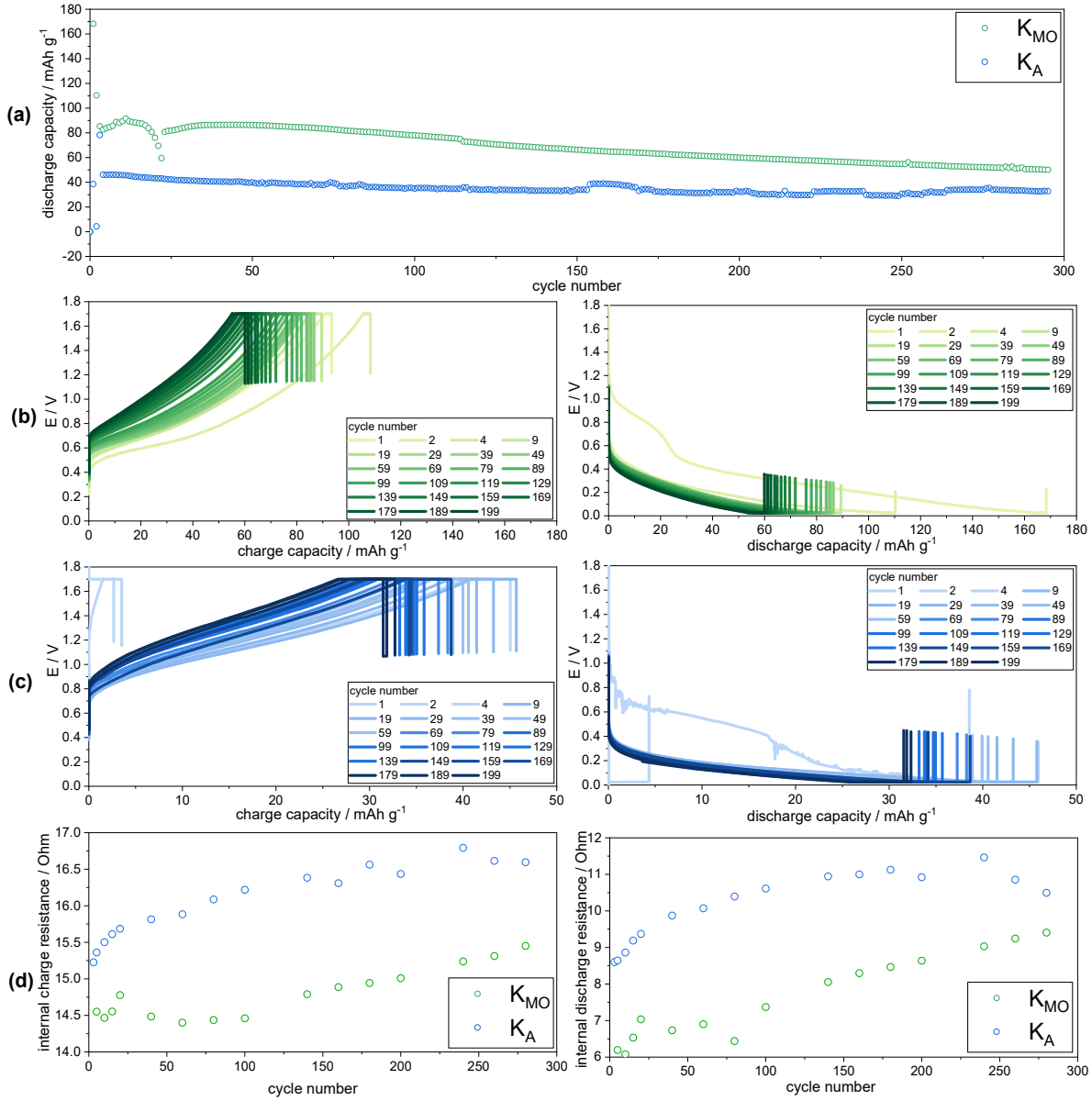


**Figure 44:** a Cycling performance at C/10 for 300 cycles, and b,c the corresponding charge-discharge curves of diverse cycles, and d variation of interanal charge (left) and discharge (right) resistance with respect to cycle numbers 0-300.

The variety of structure defects in the particles of HC offers numerous active sites for K storage. To gain more information about these side reactions, dQ/dV is plotted against the cell voltage for two cases. $K_{MO}$ (green) in EC:PC KPF6 shows two cathodic distinct peaks: a sloping region above 1 V and at a low voltage below 100mV corresponding to the intercalation of $K^+$ ions into nanovoids within the carbon matrix. There is an irreversible first cycle loss at 0.85 V that is associated with the SEI formation. In the following cycles, the peak at 0.85 V disappeared, but that at 100 mV stayed consistent. Beside this peaks there is a shoulder visible between 0.3 and 0.4 V, referred to all the surface-driven reactions. Different from the case of $K_{MO}$, $K_A$ (blue) in EC:PC KPF6 shows two cathodic peaks at 0.55 and 100 mV

in the first cycle. The cathodic peak at lower potential (0.55 V compared to 0.85V for $K_{MO}$) is noisy in the profile even in the first cycle, suggesting the presence of electrolyte decomposition. The phenomenon that the peak for depotassination with $K_{MO}$ is sharper by contrast with $K_A$ (**Figure 45**), indicates that the kinetics is faster. There is a shift in the position of the green curve with cycle number. This peak shifts from 0.65 V to 0.8 V which could be attributed to a progressive growth of a thicker SEI. To conclude this chapter, galvanostatic cycling revealed significant differences in performance between the two-electrode cells with $K_A$ and $K_{MO}$, highlighting the critical role of K-metal supplier in cell behavior. While the higher internal resistance for $K_A$ implies SEI thickening, the contributions of K metal vs HC side processes cannot be isolated. Since HC and electrolyte are unchanged, electrochemical changes could be attributed to the different behavior of potassium metals. The electrochemical disparities correlate with potassium's storage conditions and purity: $K_{MO}$ (lower purity, mineral oil-stored) delivers higher, stable capacity, whereas $K_A$ (higher purity, ampule-stored) exhibits faster capacity fade and lower Coulombic efficiency (CE). The reduced CE in $K_A$ cells signals persistent parasitic reactions (e.g., electrolyte decomposition or inhomogeneous K stripping/plating).

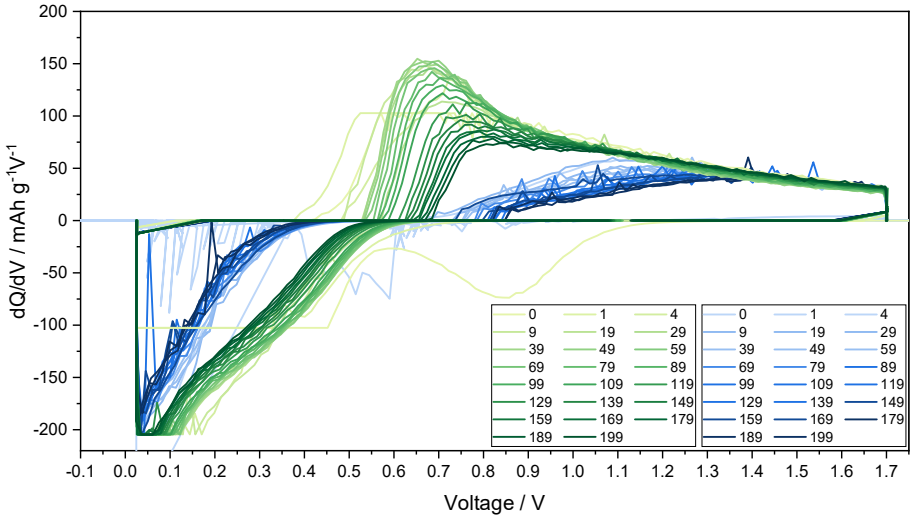


**Figure 45:** Overlayed dQ/dV plots obtained for $K_A$ (blue) and $K_{MO}$ (green) half cells against hard carbon, during the cycling at a rate of C/10 and over a voltage window from 0.001 V to 1.7 V.

### 8.1.2 XPS

To gain deeper insights into the variations in haptics, electrochemical performance, and the influence of different potassium grades, XPS analysis was conducted to characterize the chemical composition of the pristine potassium surface. Here, "pristine" refers to the untreated, as-received potassium (see experimental section). The XPS analysis is divided into three parts: 1) quantification of the surface composition of different potassium metal suppliers, 2) sputter depth profiling analysis of pristine K-metal and 3) elemental mapping.

**Figure 46** presents the XPS spectra of K 2p, C 1s, and Na 1s for pristine potassium samples from $K_{MO}$ and $K_A$. The survey spectra and a comprehensive table detailing binding energies and atomic percentages are provided in the Supporting Information (**Table S9**).

***C 1s & K 2p spectra***

The K 2p spectra of the pristine $K_{MO}$ and $K_A$ (**Figure 46a and b**) shows the characteristic doublet at 292.8 eV (K 2p3/2), in accordance with previously reported values by our group. This peak summarizes all potassium salts ($K_2CO_3$, KOH, $KHCO_3$) thus suggesting that there is no metallic potassium visible in the XPS spectra. In order to distinguish between various compounds and identify their binding energies, measurements of reference samples, namely $K_2CO_3$, $KHCO_3$ and KOH were carried out (**Figure S10).** The C 1s XPS spectra for $K_{MO}$ and $K_A$ showed four peaks, at binding energies of 285.0 eV (C-C, C-H), 286.8 eV (C-O, R-OK, R:alkyl ), 288.7 eV (C=O, $K_2CO_3$) and 289.9 eV ($KHCO_3$). The corresponding dominated O1s peak for the carbonate was observed at 530.6 eV. A second peak at 529.4 eV indicates KOH.

***Na 1s spectra***

The Na1s spectra of the pristine $K_{MO}$ (**Figure 46a**) shows no peak and therefore no appearance of sodium. In contrast, the $K_A$ (**Figure 46b**) shows a small peak centered at 1071 eV, which corresponds to the $Na^+$ species in the sample and is consistent with sodium salts. The average impurity level of Na was determined to be 4% in our samples, based on repeated experiments conducted specifically to verify this result. This also implies that a part of the $CO_3$ peak in the $K_A$ sample can be attributed to $K_2CO_3$ and $KHCO_3$.

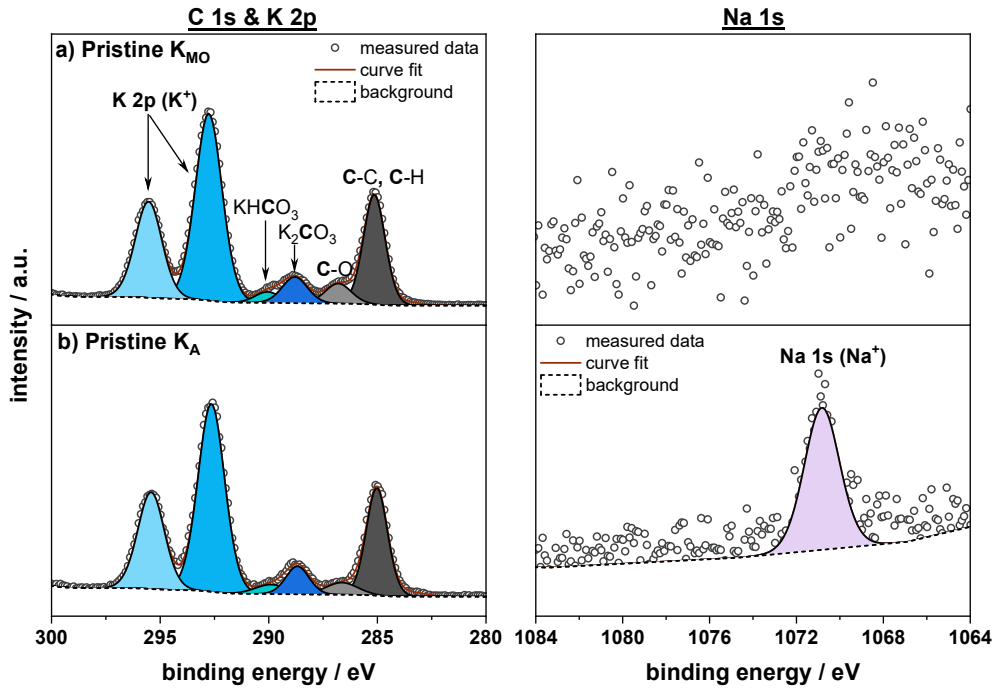


**Figure 46:** C 1s, K 2p and Na 1s spectra of the pristine $K_{MO}$ and $K_A$ surfaces. The binding energy scale is calibrated versus the hydrocarbon peak at 285 eV.

***Sputter depth profiling analysis***

Building on the initial XPS results, which identified sodium on the sample surfaces, depth profiling was conducted to assess its distribution within the material. Sputter depth profiling was performed using monoatomic $Ar^+$-ion sputtering at first 500 eV following 1000eV with etch phases of 4×40 s, 7×80 s, 7×160 s, and 3×320 s on the pristine K metal samples (cut and directly transferred into the vacuum system without solvent exposure). This approach enables a more comprehensive understanding of whether the sodium is localized at the surface or distributed throughout the bulk of the sample. The depth profiles provide qualitative information on the sodium distribution across different depths, as illustrated in **Figure 4a** ($K_{MO}$) and **4b** ($K_A$).

***C 1s & K 2p spectra***

All observed signals are in accordance with previous reports showing the C 1s XPS spectra from the $K_{MO}$ and $K_A$ in **Figure 47a and b** exhibit an adventitious carbon peak at 285.0 eV and a minor peak at 288.5 eV (C=O, $K_2CO_3$) after the initial 40 s of sputtering. A characteristic K 2p doublet at 292.3 eV (K 2p3/2) was observed, suggesting potassium salts at the surface. The shift of the K 2p peak compared to the pristine K (**Figure 46**) to lower binding energies can be attributed to a reduced amount of surface salts, which decreases the overall contribution of potassium to the signal. This shift suggests a change in the surface composition, although the absence of a metallic potassium peak indicates that the remaining surface potassium is still predominantly in oxidized or salt forms. Before $Ar^+$-ion sputtering, the outer layer of the initial K-metal surface is dominated by $K_2CO_3$ and KOH (**Figure S11),** thus highlighting the formation comparatively thick surface layers with minimal contaminants in the glovebox atmosphere. After 2700 s of $Ar^+$-ion sputtering with 500 eV, the K 2p XPS spectra showed a small additional potassium doublet feature at 291.5 eV of metallic potassium $K^0$. The presence of plasmon peaks, collective electron oscillations characteristic of metallic potassium, became increasingly pronounced after prolonged sputtering (2700 s), manifesting as broad signals above the K 2p peak up to 302 eV (**Figure 47a and b**). These features, alongside the weak $K^o$ doublet, confirm progressive exposure of metallic potassium at the sputtered surface . After 2700 s of $Ar^+$-ion sputtering with 1000 eV the $K_2CO_3$ content is completely reduced, a small fraction of KOH remains and the K 2p signal of metallic potassium becomes the main component in the spectrum (**Figure 47a**), which is characterized by a BE shift to 291.9 eV and a reduced FWHM of 1.0 eV as compared to the signals of $K^+$ species with a FWHM of 1.5 eV.

***O 1s spectra***

The O 1s spectra of $K_{MO}$ and $K_A$ in **Figure 47a and b** consists of two components after the initial 40 seconds of sputtering: $K_2CO_3$ at 530.2 eV and KOH at 529.5 eV. After 2700 s of $Ar^+$-ion sputtering with 500eV, the O 1s XPS spectra show a new sets of peaks appears. The new peak at 526.4 eV can be assigned to an sodium oxide species (**Figure 47a and b**). Additionally, characteristic Auger electrons

are observed in the O 1s spectra at 520.6 eV and 532.8 eV, indicating the presence of sodium-related species interacting with oxygen on the surface.

***Na 1s spectra***

The Na 1s XPS spectra exhibit two peaks at 1069.2 eV and 1070.5 eV that are attributed to sodium salts (NaOH, $NaO_x$, $Na_2CO_3$).

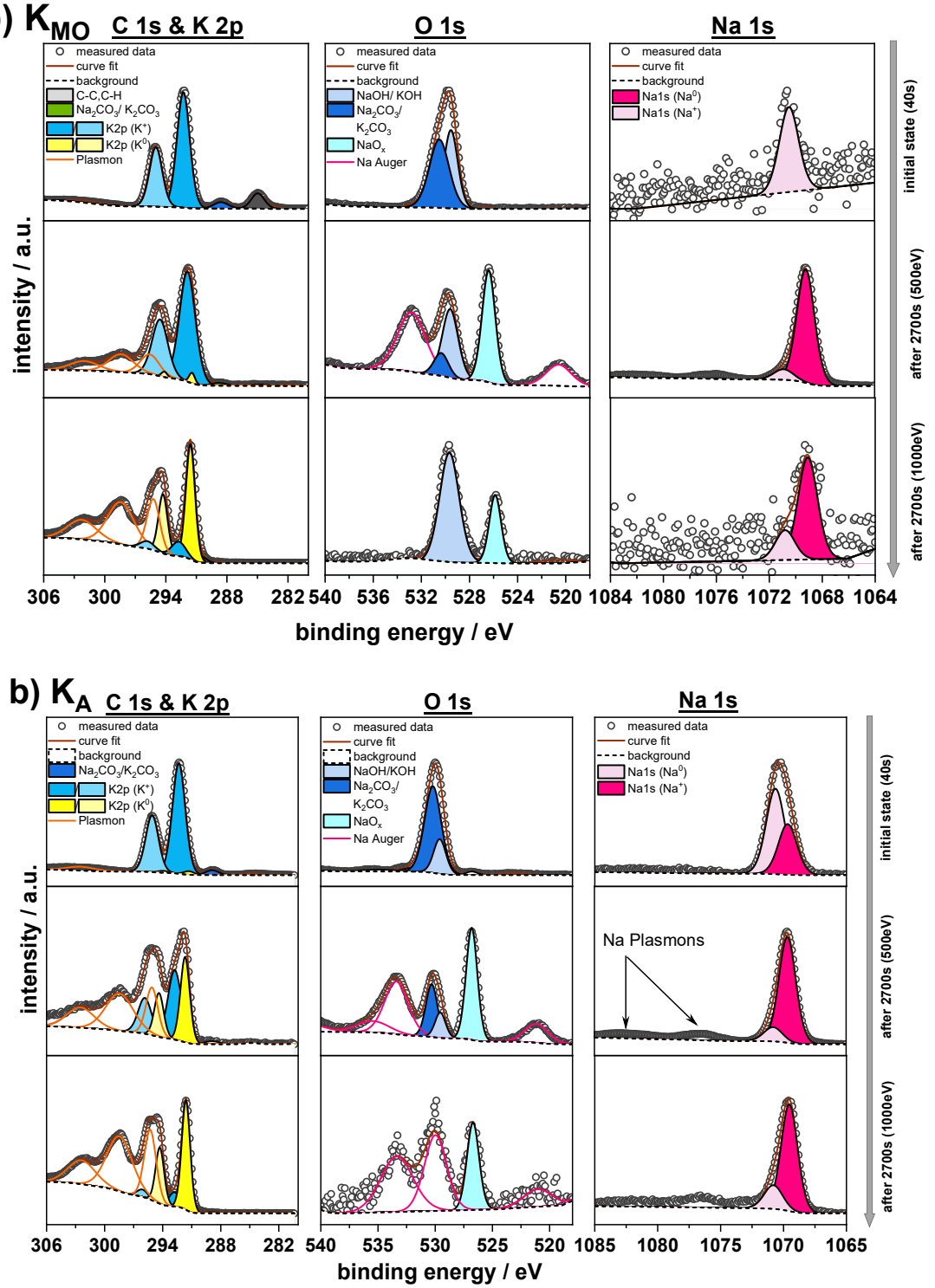


**Figure 47:** The XPS depth profile spectra of C 1s, K 2p, O 1s and Na 1s core peaks of (a) $K_{MO}$ and (b) $K_A$ after the first 40 s, after 2700 s with 500 eV and after 2700 s with 1000 eV.

***Comparison of surface layer content***

Based on the fitted spectra a quantification of the surface species was performed using relative sensitivity factors. **Figure 48** shows the relative atomic concentration of the four dominant elements, carbon, oxygen, potassium and sodium. The atomic concentrations of C (≈24±1 at.%), O (≈36±1 at.%) and K (≈36±1 at.%) is about the same for the two samples $K_{MO}$ and $K_A$ within the accuracy of the quantification (±5 at.%). In accordance, with more prominent signals of $K^0$ with increasing sputter time, the $K^+$ content strongly decreased, while the respective $K^0$ surface content increased. However, for $K_{MO}$ the $K^0$ content reached merely 0.81% and up to 3.5% for $K_A$. Surprisingly, it was found that the potassium stored in ampule and the higher purity displayed a fourteen times higher sodium content (3.5 at.%) near the interface than the potassium stored in mineral oil (0.24 at.%). It is consistent that the Na 1s intensity increased accordingly from 0.24% to 43% for $K_{MO}$ and from 3.4% to 75.8% for $K_A$, which is also seen in a noticeable increase of the Na Auger peaks in the O 1s region.

After 2700 s of $Ar^+$-ion sputtering with 1000 eV, the $K_2CO_3$ content is completely reduced, and the K 2p signal corresponding to metallic potassium becomes the dominant component in the spectrum, with potassium concentrations of approximately 75±1 at.% observed for both $K_A$ and $K_{MO}$ (**Figure 48**). In the case of $K_A$, the carbonates and hydroxides are completely reduced, leaving only a minor amount of oxide (3.24%). In contrast, for $K_{MO}$, a residual amount of KOH (14.8%) and oxide (5.60%) remains. Furthermore, while $K_A$ exhibits a gradual decrease in sodium content to 20.3%, the sodium content in $K_{MO}$ declines much more rapidly, reaching 0.8%. This is accompanied by the disappearance of sodium-related Auger features, further confirming the effective reduction of sodium species on the surface.

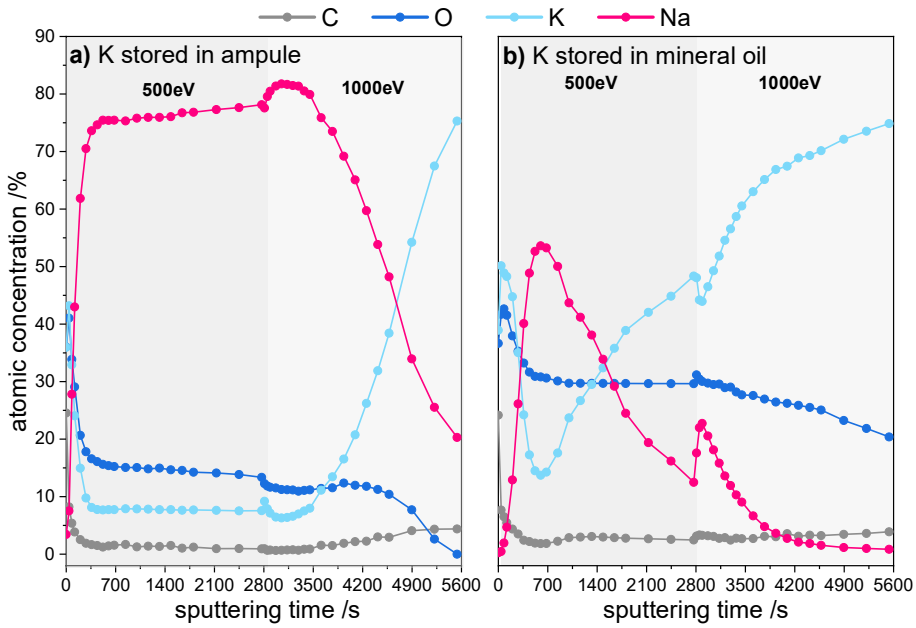


**Figure 48:** The corresponding depth profiles of the atomic concentration of C, O, K, and Na elements for the $K_A$ (a) and $K_{MO}$ (b) sample.

***Elemental Analysis***

To complement the XPS analysis, ICP-OES measurements were performed on both potassium samples in order to quantify the potassium and sodium contents. The results are in good agreement between XPS and ICP-OES results for the $K_{MO}$ sample, with Na contents of 0.079% (ICP-OES) and 0.24% (XPS). The potassium content was only 95.9 % according to the bulk analysis. In contrast, for the $K_A$ sample, ICP-OES found Na contents of 1.30%, whereas with XPS 3.5 % were measured. The potassium contents determined by ICP-OES were 95.9 % ($K_{MO}$) and 97.9 % ($K_A$) and thus significantly smaller than one would anticipate from the supplier data. Differences between XPS and ICP-OES results are attributed to the fact that XPS only captures the very surface-near regions (i.e. first 6-9 nm), as compared to a bulk analysis with (ICP-OES). Hence, the sodium content is significant in the $K_A$ sample and present in far higher concentrations than one would expect. Paradoxically, analysis of the lower purity $K_{MO}$ yielded considerably (16-fold) smaller Na contents than the high purity $K_A$.

### 8.1.3 Elemental Mapping

The comparison between XPS (surface) and ICP-OES (bulk) analysis suggests a notable surface enrichment of sodium during XPS measurements. Further investigations employed XPS elemental mapping with the primary goal to to analyze the elemental distributions of sodium (~1073 eV) and potassium (~295 eV), respectively. In addition, the study aimed to examine the origin of the observed sodium enrichment for instance by surface migration. To achieve this XPS elemental mapping was first conducted without any additional treatment, during which the X-ray gun was activated for 120 seconds (19 iterations). This step, referred to as the "wait object," was performed to assess whether the X-ray beam itself influenced the sodium distribution. Subsequently, depth profiling was performed using argon ion etching at energies of first 500 eV and following 1000 eV to explore the subsurface regions and detect potential sodium migration or surface segregation. In addition, multiple points were selected to examine how the surface outside the sputtering area behaves and to determine whether changes/migrations could also be observed in these regions. The mapping point was positioned at the edge of the sputter crater to achieve better contrast in the mapping images.

When comparing the mappings of both samples ($K_{MO}$ and $K_A$) before and after the wait object, no significant differences were observed (**Figure 49**). Sodium and potassium remained evenly distributed across the surface, with a XPS intensity (arbitrary units, a.u.) of approximately 0.05 a.u. ± 0.004 for Na and 0.09 a.u. ± 0.02 for K. However, in the samples, a higher intensity of Na and K was observed in the lower region of the mapping area (x: 0–400 µm, y: 250–450 µm). The samples exhibited surface roughness, which influenced mapping homogeneity. Details of the depth-profiling procedure and

mapping spot selection are provided in the Experimental section. Notably, measurements near the edge of the sputter crater (P2) resulted in out-of-focus regions (visible as black areas in the upper mapping zone), attributable to topographical variations at the crater boundary.

The surface intensity changes of the $K_A$ sample follow the same trend as shown in **Figure 49**, with an increase in the Na intensity during the first sputter step (at 500 eV), followed by a decay as sputtering is continued in the second step (at 1000 eV). For $K_A$, sodium began to accumulate (x: 400 µm, y: 350 µm) inside the sputtering crater, as the intensity of Na increased from 0.05 a.u. to 0.16 a.u.. This suggests that sodium is present beneath the surface layer and becomes exposed during sputtering. The sodium content in the sputtering crater decreased but maintained a higher surface intensity than initially.

In the case of $K_{MO}$, no changes were detected after the first sputtering step at 500 eV in the intensity of Na and K. In the second sputtering step at 1000 eV, sodium accumulated within the sputtered region (x: 300 µm, y: 350 µm), showing an increase from 0.05 a.u. to 0.10 a.u., while potassium remained unchanged. However, sodium appeared slightly more prominent in the bottom right corner of the mapping for both samples. This prominence shifted slightly after the “wait object” and sputtering steps, indicating minor changes in sodium distribution. To further verify these findings, additional mapping points (P3 and P4) were analyzed (see experimental part Figure 1). Across these points (P3 and P4), the intensity of Na and K remained constant and evenly distributed.

Overall, the results show that the X-ray exposure itself has minimal effect on the distribution of Na and K. However, sputtering showed changes, particularly for Na, as subsurface sodium was exposed and accumulated within the sputtering crater. These effects were more pronounced in $K_A$, which showed also a higher sodium intensity than in $K_{MO}$.

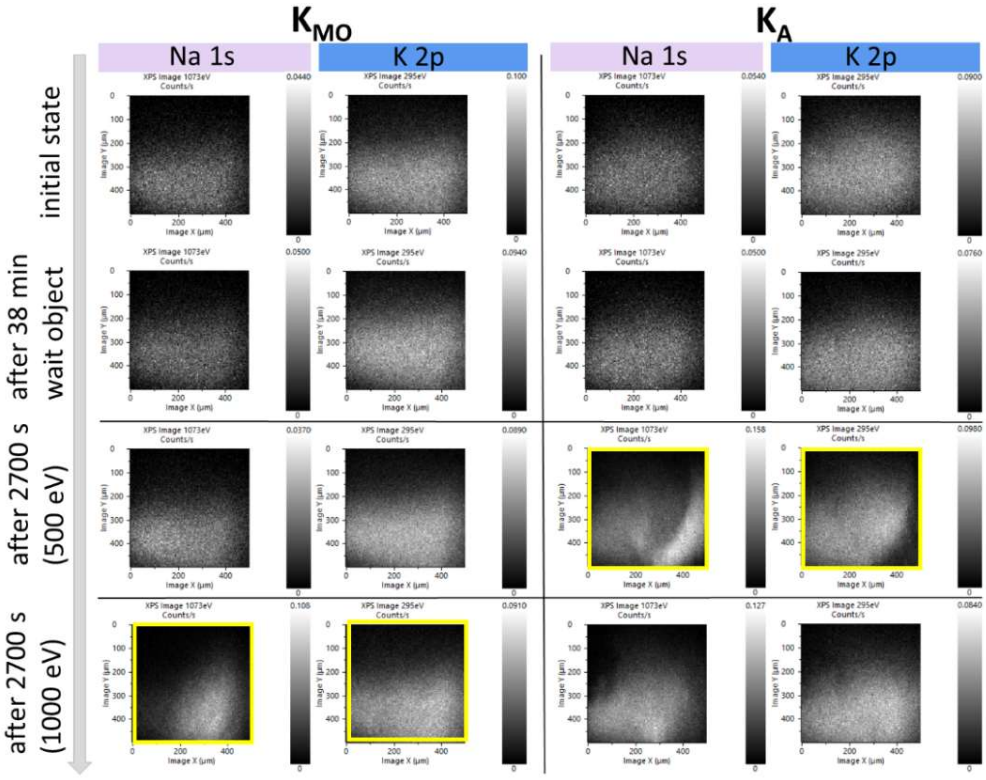


**Figure 49:** Elemental mapping of the chemical component distributions of sodium (~1073 eV) and potassium (~295 eV) for $K_{MO}$ and $K_A$ at the (a) initial state and after (b) "wait object", (c) 2700 s at 500 eV and (d) 2700 s at 1000 eV.

## 8.2 From Solvent to Salt to Additive: Tracking the Surface Evolution of K Metal

After determining that the $K_{MO}$ grade was more suitable for further analyses, it was used exclusively throughout the remainder of this work to eliminate any risk of Na contamination. To distinguish between the native surface layer and changes induced by solvent or electrolyte exposure, XPS analysis was conducted on potassium metal, analogous to the approach applied for the other alkali metals, to detect solid decomposition products. Potassium samples were immersed in EC:DEC and EC:DEC-based electrolytes containing $KPF_6$, with and without 5 % FEC, to investigate the influence of composition and short-term storage (2 and 4 min) on surface chemistry. The spectra of the pristine potassium surface are shown in the previous chapter. For clarity and comparability, all spectra were normalized to a peak intensity of 1.

***C 1s & K 2p***

The C 1s spectrum of K metal after immersion in pure DEC:EC solvent (**Figure 50a**) exhibits four prominent peaks at binding energies of 285.0 eV (C−C, C−H), 286.4 eV (C−O), 287.5 eV (C=O), and 288.5 eV ($CO_3$), with the K 2p signal appearing at 293.2 eV. A smaller, secondary K 2p signal (*) is also observed at a higher binding energy of 300 eV when FEC is added to the DEC:EC $KPF_6$ electrolyte.

***O 1s Spectra***

The O 1s spectra of K metal immersed in pure DEC:EC show four primary peaks at binding energies of 529.4 eV (KOH), 530.6 eV ($CO_3$), 531.4 eV (C=O), and 533.5 eV (C−O), as depicted in **Figure 50a**. Upon transitioning from K metal in pure DEC:EC to K metal in $KPF_6$-based electrolytes (**Figure 50b and 50c**), both with and without FEC, the intensity of the O 1s features increases. The primary peak at 531.9 eV is attributed to carbonate species, such as $K_2CO_3$/$KHCO_3$ or alkyl carbonates. However, the higher intensity of this peak in the O 1s spectrum relative to the $CO_3$ signal in the C 1s suggests the presence of another contributing species. As noted in the C 1s, carboxylate species like $HCO_2K$ may contribute to the O 1s peak at 531.9 eV. After accounting for the contribution of carboxylate species at 531.1 eV, the relative oxygen content from the $CO_3$ peak aligns well with the C 1s peak for $K_2CO_3$.

***F 1s Spectra***

The F 1s spectra for the electrolyte, with and without FEC as an additive, display three peaks attributed to the species at 687.2 eV (P-F), 684.5 eV ($K_xP_yF_z$) and 683.3 eV (KF). Additionally, a peak at 693.2 eV at higher binding energy is observed, which cannot be assigned to any known species. This peak arises due to local charging effects caused by the salt, which results in a surface charge buildup. This phenomenon leads to the observed splitting of the 684.5 eV peak, causing a shift and appearance of an additional peak at 693.2 eV. This also contributes to the splitting seen in the K 2p region. The more pronounced doublet in the FEC spectrum is attributed to this effect, and a more detailed explanation will be provided in the "Comparison of Surface Layer Composition" chapter.

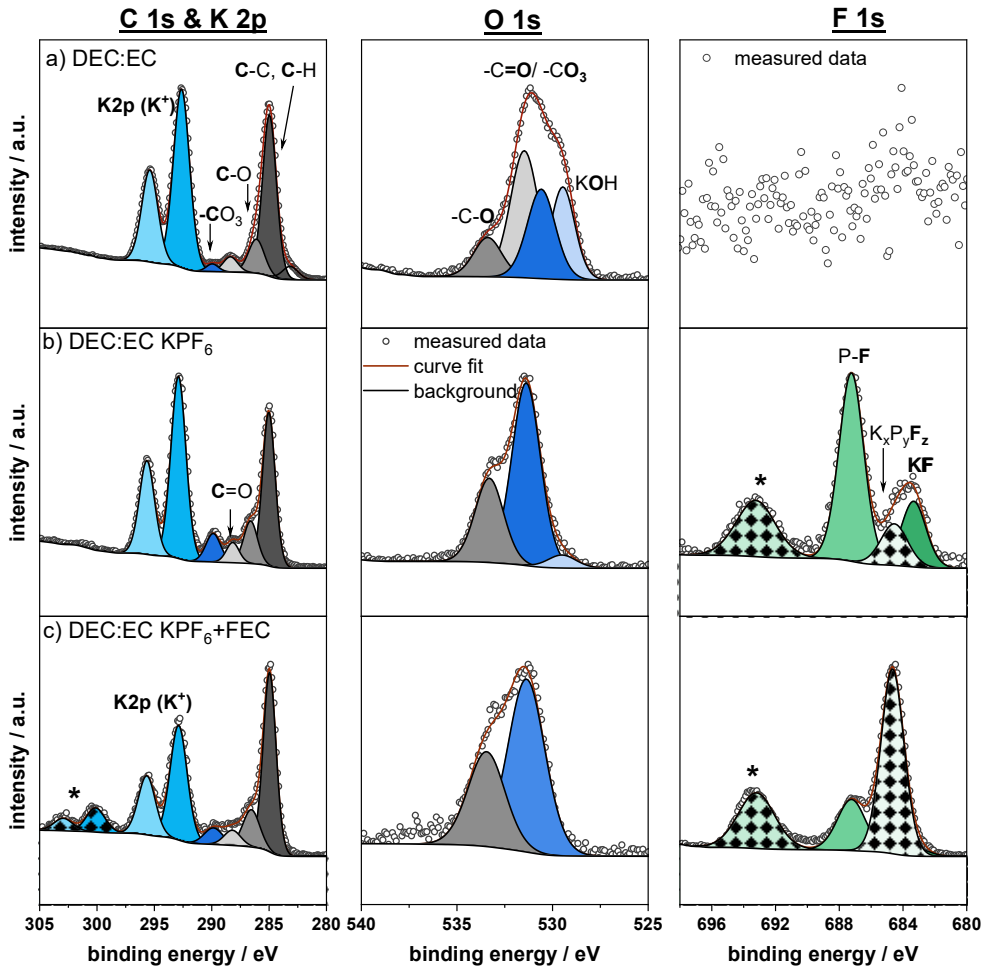


**Figure 50**: C 1s & K 2p, O 1s and F1s core peaks of K stored in (a) solvent (DEC:EC), (b) electrolyte with $KPF_6$ and (c) electrolyte with 5% FEC for 2min.

However, an additional experiment was conducted to investigate the effect of pure FEC on the surface layer of K metal. The C 1s & K 2p and O 1s spectra (**Figure 51**) displayed the same peaks, respectively, as previously discussed in the chapter above. Notably, the oxygen and carbon content was reduced in this case. Interestingly, the F 1s spectrum revealed a single prominent peak at 683.2 eV, which is attributed to KF.

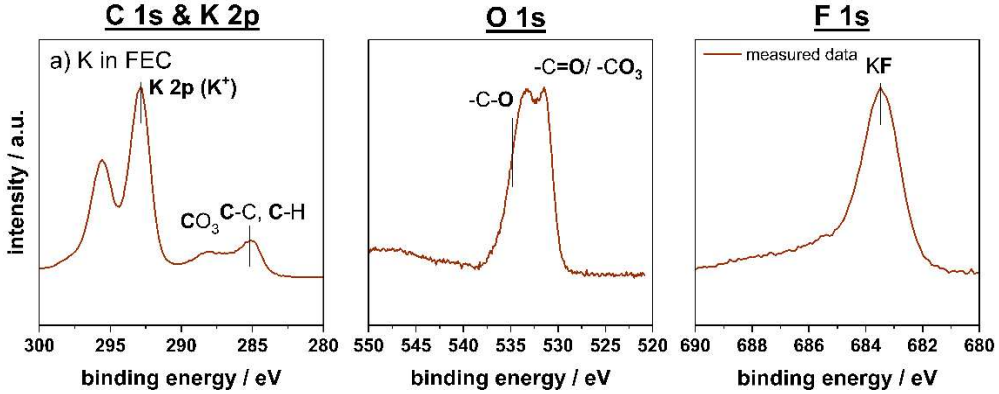


**Figure 51**: C 1s & K 2p, O 1s and F 1s core peaks of K stored pure FEC.

### 8.2.1 Time-Dependent Formation of Decomposition Products in Electrolyte

To investigate the degradation pathways of potassium metal in electrolyte systems, time-resolved GC-MS analysis was performed on EC:DEC solvent mixtures containing 0.75 M $KPF_6$, with and without pristine potassium metal, at 25 °C. Samples were analyzed after specific exposure intervals (2 min, 4 min, 2 h, 48 h) to observe the formation of degradation products and to distinguish between reactions initiated by potassium. This approach allows for the identification of early-stage intermediates and provides insights into the kinetics of decomposition under static, electrochemically unbiased conditions. As shown in **Figure 52**, degradation products were already detected after just 2 min of exposure to potassium metal in the DEC:EC $KPF_6$ electrolyte, with the primary compounds being diethyl dioxahexane dioate (2, DEDD), di-(2-ethoxycarbonyloxyethyl) carbonate (1, DECC), and diethyl-oxydiethane-2,1-diyl biscarbonate (3, DECE). These decomposition products were consistently observed at subsequent time points (4 min, 2 h, and 48 h). Notably, the presence of FEC in the electrolyte completely inhibited the formation of degradation products, confirming its stabilizing effect in the system.

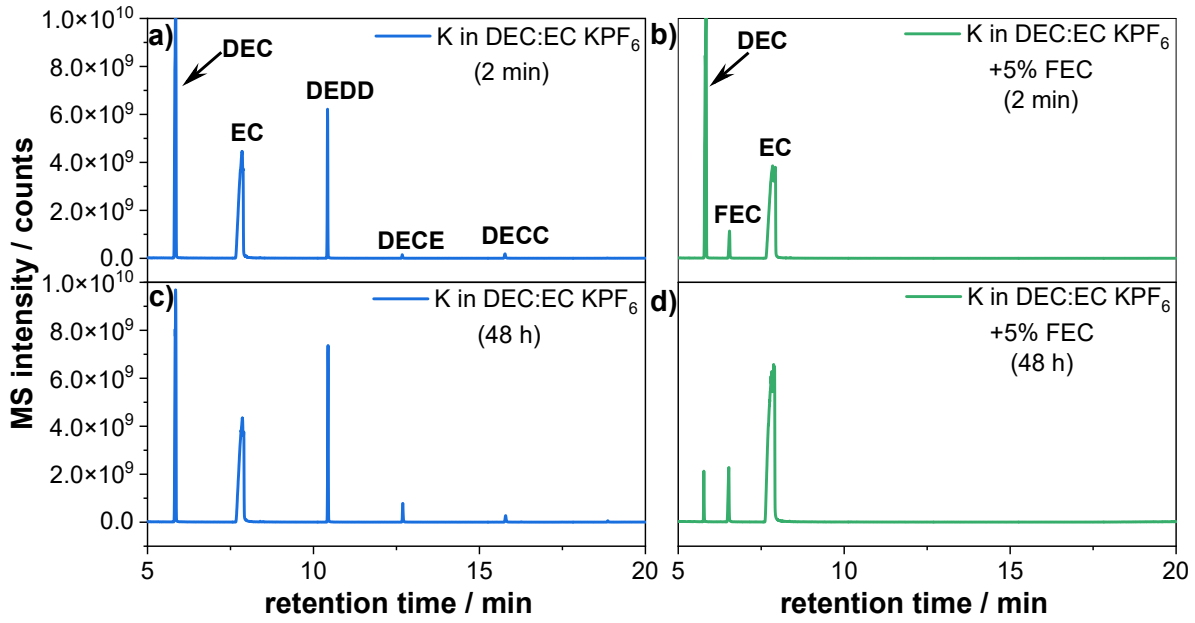


**Figure 52:** GC-MS chromatogram from the storage of K im (a and c) DEC:EC $KPF_6$ for 2 min and 48 h, (b and d) DEC:EC $KPF_6$ + 5% FEC for 2 min and 48 h. Additional reference measurements are assigned in **Table S7**.

***Comparison of Surface Layer Composition***

XPS analysis provides insight into the evolution of the potassium surface composition under different electrolyte conditions (**Figure 53**). When potassium is stored in pure DEC:EC (1:1 vol.%), the surface is mainly composed of hydrocarbon species (C–C, C–H) at around 44 at.%, accompanied by minor contributions from KOH (6 at.%) and carbonate species (~5 at.% total). Upon addition of $KPF_6$ to the

electrolyte and subsequent immersion of potassium for 2 min, a significant shift in surface chemistry is observed. KOH species disappear entirely, while small amounts of KF and additional decomposition products from the salt, such as PF species, emerge while the amount of $K_2CO_3$ stayed consistent. Extending the immersion time to 4 min and 2 h does not lead to major further changes, the atomic percentages remain relatively stable within ±3%, suggesting that the surface reaches a quasi-equilibrium state after a short exposure. The situation changes notably when FEC is added to the DEC:EC $NaPF_6$ electrolyte (**Figure 53b**). After only 2 min of exposure, a marked increase in decomposition products is observed: P–F species rise to 9 at.% (compared to 6 at.% without FEC) and the KxPyFz compounds, which were almost absent in the FEC-free electrolyte (<2%), appear at 23 at.%. After 4 min, the $K_xP_yF_z$ content further increases to 32 at.%, while $K_2CO_3$ and other surface species remain largely constant around 4 at.%. When potassium is brought into contact with pure FEC, a different interfacial composition forms. Here, the surface is dominated by KF (12 at.%) and $K_2CO_3$ (7 at.%), while only small amounts of PF species (3 at.%) are detected, and no $K_xP_yF_z$ compounds are observed. This indicates that pure FEC promotes the formation of a simpler, predominantly inorganic fluoride-carbonate interphase, whereas the combination of $NaPF_6$ and FEC drives a more complex decomposition pathway involving phosphorus-fluoride species.

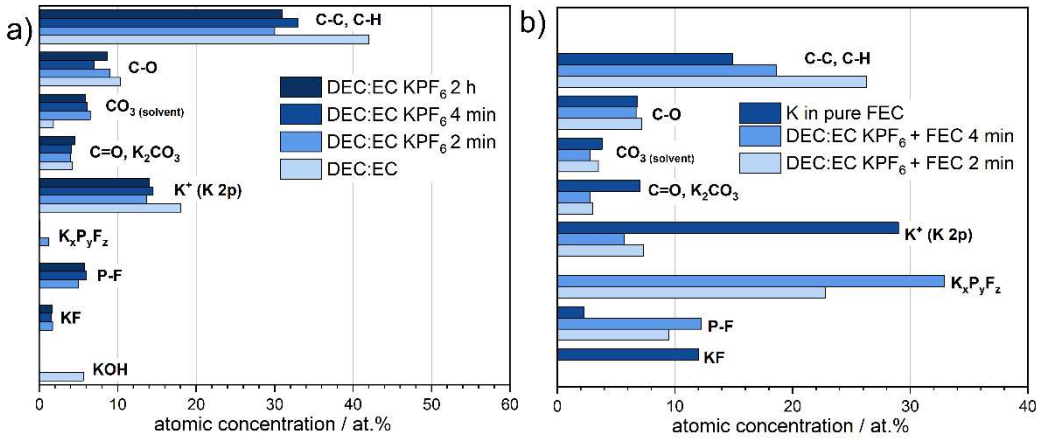


**Figure 53**: (a) Aatomic concentration of main surface species of K stored in DEC:EC and DEC:EC $KPF_6$ for different time scales (2 min, 4 min and 2 h) and (b) atomic concentration of main surface species of K stored in DEC:EC $KPF_6$+FEC for different time scales (2 min, 4 min) as well as K stored in pure FEC.

### 8.2.2 Discussion

The combined XPS and GC–MS data paint a clear picture: potassium metal immediately transforms its surface upon contact with carbonate electrolytes. Within two minutes, GC–MS detects the full suite of solvent–derived by-products (DEDD, DECC, DECE), and their concentrations remain

essentially unchanged over 33 h.[63] This instantaneous, time-invariant formation of degradation products shows that the system reaches a quasi-equilibrium SEI chemistry almost immediately. Quantitatively, XPS reveals that KxPyFz species accumulate to 23 at.% after just 2 min in $KPF_6$-containing electrolyte, rising to 32 at.% by 4 min, while carbonate- and alkoxide-derived signals ($KHCO_3$, R–OK, $CH_3CO_2K$) remain minor. The addition of FEC completely suppressed the electrolyte degradation but accelerates phosphate-fluoride formation. In this chapter, a distinct doubling of the K 2p signals was observed for potassium surfaces after electrolyte + FEC exposure for 2 min, alongside the appearance of an undefined F 1s signal at high binding energies (*). Upon closer analysis, time-dependent XPS measurements (2 min vs. 4 min acquisition) reveal a consistent shift of approximately 2.2 eV for both the K 2p and the F 1s signals (**Figure 54**). A corresponding shift is also detected in the P 2p spectra. This coordinated shift across K, F, and P strongly indicates localized charging effects, likely due to the formation of an insulating, salt-derived surface species KxPyFz. The intrinsic peak position is likely around 684 eV in the F 1s spectrum, but overlaid by this charging artefact, causing apparent signal duplication and energy shifts. Interestingly, in the EC:DEC-based $KPF_6$ electrolyte without evident K 2p doublet splitting, a shifted F 1s signal is still observed. This is explained by the significantly higher intensity of the F signal relative to the K signal, by approximately a factor of six meaning that charging effects originating from potassium species are masked by the stronger fluorine-derived signal. In XPS analysis, local charging effects can arise when poorly conductive species or multilayer structures form at the surface. If, for example, a thin inorganic salt layer overlays a less conductive bulk material, differential charging can occur. This manifests as peak splitting, peak broadening, or systematic shifts of core-level signals to higher binding energies. Interestingly, when potassium is exposed to pure FEC, all available fluoride originates from FEC ring-opening and immediately precipitates as insoluble KF. In DEC:EC + $KPF_6$ (with or without added FEC), however, the $PF_6^-$ anion is preferentially reduced at the potassium surface, releasing $F^-$ that is rapidly incorporated into mixed phosphate-fluoride networks (KxPyFz) instead of forming discrete KF. Any small amount of KF that does form is either partially solubilized in the DEC:EC solvent or buried beneath the electronically insulating KxPyFz layer, rendering its XPS signature effectively invisible.

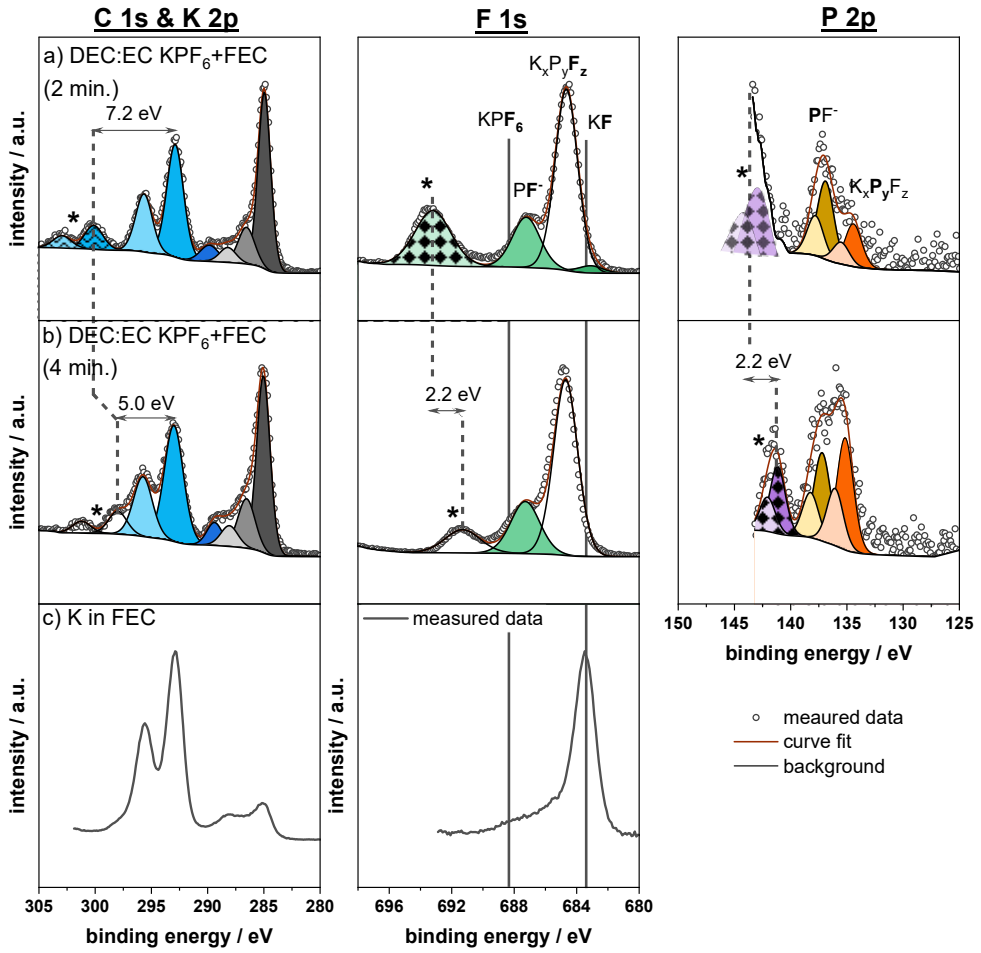


**Figure 54**: C 1s & K 2p, F 1s and P 2p core peaks of K stored in DEC:EC $KPF_6$ with FEC for (a) 2 min, (b) 4 min and (c) K stored in pure FEC for 2 min.

## 8.3 Decomposition of Binary Carbonate Mixtures on Potassium Metal- GC, XPS and DFT Insights

To place the findings of **Chapter 8.2** into a broader context, this chapter draws on results already published as part of a collaborative study within the framework of the POLiS research cluster. In this work, XPS measurements were conducted by the author, GC–MS analysis was performed by Andreas H., and Daniel Stottmeister contributed the DFT calculations. The study investigates the interfacial chemistry of three binary solvent systems — DMC:EC, EMC:EC, and DEC:EC — on potassium metal. Gas chromatography was used to identify volatile decomposition products, XPS provided insights into solid-phase species at the electrode surface, and density functional theory (DFT) calculations elucidated thermodynamic stabilities and likely reaction pathways. By comparing these three solvent pairs, both common and solvent-specific decomposition mechanisms were revealed, offering mechanistic insights that complement the findings from the DEC:EC + $KPF_6$ (+ FEC) study. Together, the results provide a more comprehensive understanding of the processes governing interphase formation and degradation

in potassium-metal batteries, informing rational electrolyte design. The first part of this chapter covers a detailed analysis of soluble components studied via GC–MS, while the second part focuses on surface layer characterization using XPS. Finally, the theoretical perspective from ab initio DFT simulations further supports the proposed reaction mechanisms at the K-metal interface.

### 8.3.1 Decomposition Products Formes in the Solvent

#### 8.3.1.1 Determination of Decomposition Products in Binary Carbonate Mixtures by GC-MS Analysis

Binary mixtures of DMC:EC, EMC:EC and DEC:EC were stored over potassium metal at 25 °C for 14 days and then analyzed by GC–MS (**Figure 55**). Peak assignments relied on authentic standards run under identical conditions, matching both EI fragmentation patterns and linear-alkane retention indices (RI; **Table S10**). Primary dialkyl carbonates (DMDD, EMDD, DEDD) appeared first but have already been extensively described in detail in literature as well in an earlier publication before and are thus not discussed again herein.[63,114,127–131] Early-eluting monoether-carbonate hybrids, MEMC and EEEC, and their mixed termini (MEEC, EEMC) were detected at RT ≈ 3–5 min. Diether (monoglyme) derivatives (MEEMC, EEEEC) and mixed-end analogues (MEEEC, EEEMC) only became visible after partial vacuum evaporation, indicating low initial abundance. Ether-bridged carbonates (DMCE, EMCE, DECE) eluted at RT ≈ 6–8 min, while trimeric alkyl carbonates (DMCC, EMCC, DECC) appeared later at RT ≈ 10–12 min. A few minor peaks (m/z 89, 103, 117) suggest the presence of higher oligocarbonate-ethers, although these were not fully characterized here.

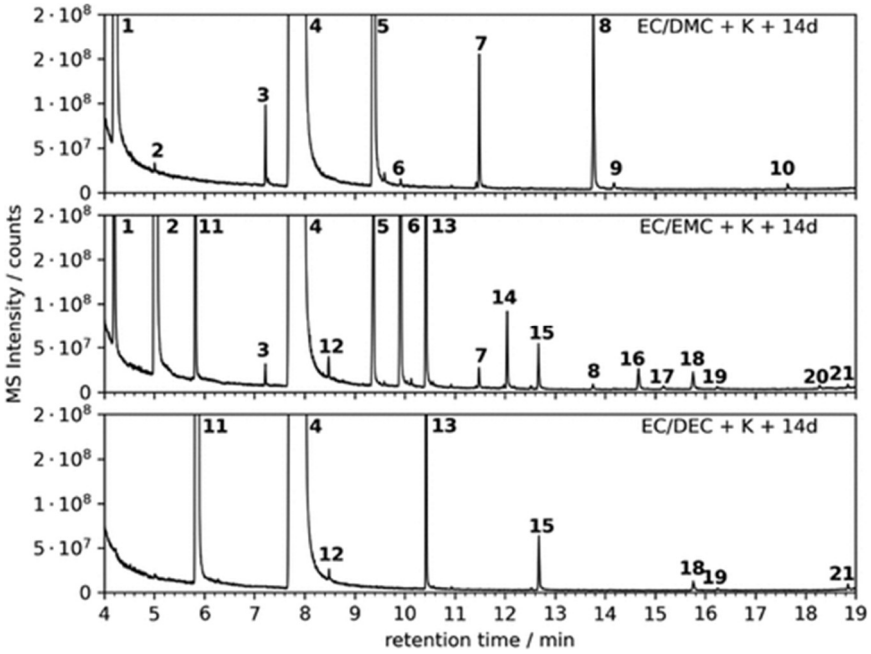


**Figure 55:** GC–MS results of DMC:EC, EMC:EC, and DEC:EC solvent mixtures after 14 days of storage over potassium metal. Compound assignments are listed in **Table 3**, peaks 9, 10, 17, 19, 20, and 21 could not be identified.

**Table 3:** Overview of all liquid degradation products formed during potassium storage for 14 days in different mixtures.

| K in | dicarbonate-substituted products | ether-bridged compounds | trimeric carbonate-substituted products | ether-like products |
|---|---|---|---|---|
| **EMC:EC** | **5** (DMDD), **6** (EMDD), **13** (DEDD) | **7** (DMCE), **14** (EMCE), **15** (DECE) | **8** (DMCC), **16** (EMCC), **18** (DECC) | **3** (MEMC), **12** (EEEC), MEEEC, EEEMC |
| **DMC:EC** | **5** (DMDD) | **7** (DMCE) | **8** (DMCC) | **3**, MEEMC |
| **DEC:EC** | **13** (DEDD) | **15** (DMCE) | **18** (DECC) | **12** (MEMC), EEEEC |

**Time-Dependent Formation of Decomposition Products in Electrolytes Including Potassium Metal**

Time-resolved analysis was carried out at 2 min, 2 h, and 14 days to capture the onset and evolution of degradation. As an illustrative case, the EC/EMC/K system (**Figure 55**) exhibits detectable degradation products within just 2 min. Semi-quantitative GC-MS data normalized to the combined EC + EMC solvent peaks reveal that the dicarbonates DMDD, EMDD and DEDD appear almost immediately and grow substantially by 2 h, consistent with prior observations. Concurrent transesterification also elevates levels of DMC and DEC. By 14 days, dicarbonate concentrations have further increased and tricarbonates (DMCC, EMCC, DECC) emerge prominently. The rapid formation of DMDD in the EC:DMC mixture highlights that metal–solvent surface reactions initiate as soon as the solvent contacts potassium, swiftly altering its composition.

**Evaluation of Reaction Products Formed by Solvent–Salt Interaction**

To further explore the influence of potassium-derived interphases on solvent stability, a series of experiments was conducted. Different potassium salts (KOH, $K_2CO_3$, $KO_2$, and KOEt) were dissolved in DEC:EC, and the mixtures were analyzed by GC–MS after one week. The detected degradation products are summarized in **Figures S9–S12** and **Table S11**. The reference measurement of pure DEC:EC showed no evidence of decomposition. As previously discussed, potassium metal induces the formation of DEDD as the main degradation product. It was found that the addition of KOH or $K_2CO_3$ to DEC:EC had little impact, with no significant degradation products observed. In contrast, the addition of $KO_2$ resulted in a pronounced formation of DEDD. Even more strikingly, the addition of KOEt led to the pronounced formation of various decomposition products, including ethanol, DEDD, DECE, and additional, unidentified species. These results emphasize the crucial role of reactive potassium species in catalyzing solvent degradation pathways.

**Evaluation of the Role of Glycol in the Formation of Oligomers on the K-Surface Using ab Initio DFT Calculations**

To understand the formation energetics of the above mentioned linear carbonates on potassium metal, DFT calculations and AIMD simulations were conducted by Daniel Stottmeister under vacuum and on K(100) surfaces. Adsorption energies and reaction energies for various fragments were evaluated, focusing on mechanisms involving ethylene glycolate ($[O–CH_2–CH_2–O]^{2-}$) species. Results suggest that nucleophilic attack of glycolate on carbonate molecules (e.g., DMC (1), DEC (11)) leads to alkoxide and oligocarbonate formation (e.g., DMDD (5)). The nucleophilic substitution pathway was nearly thermoneutral, while alternative routes involving methylcarbonate anions were more exothermic but less likely due to instability (**Figure 56**). Direct polymerization of glycol fragments and ether bond cleavage were found to be energetically unfavorable. Although certain longer chain products like DMCE (7) were observed experimentally, their exact formation mechanism remains unresolved. Overall, surface interactions strongly influence reaction pathways, highlighting the necessity to include metallic surfaces in reaction modeling.

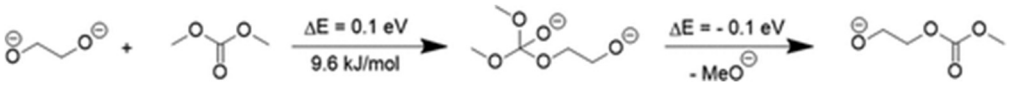


**Figure 56:** Proposed reaction mechanism for the nucleophilic substitution reaction forming alkoxides on the potassium surface; all reactants are adsorbed on the K-surface. Reaction energies are given in both eV and in kJ/mol.

**8.3.1.2 Surface Analysis using XPS**

Complementing the GC–MS results, XPS was employed to probe the solid interphase formed on potassium metal after 2 min immersion in EC:DMC, EC:EMC, and EC:DEC mixtures. Identical experiments at 2 h showed negligible changes, while 14 day exposures produced excessively thick films (see Supporting Information, **Figure S13** and **Table S12**). The XPS investigation comprises: (1) spectra of solvent-exposed surfaces; (2) charge state analysis; and (3) quantitative surface composition.

***C 1s & K 2p Spectra***

The K 2p spectra of pristine potassium (**Figure 57d**) and the solvent-exposed samples after 2 min (Figure 14a–c and Table 3) all display the characteristic K $2p_{3}/_{2}$ peak at 292.7 eV, in agreement with previous work from our group.[132] This signal encompasses all potassium salts, including $K_2CO_3$, KOH, and potassium alkoxides (K–OR), indicating the absence of metallic potassium at the surface **(see chapter 8.1).** To support spectral assignment and further extend the potassium SEI reference database, core-level spectra of relevant inorganic salts, $K_2CO_3$, $K_2C_2O_4$, $CH_3CO_2K$, and $KHCO_3$ were recorded and

are shown in **Figure S9**. The corresponding binding energy shifts for O 1s and C 1s–K 2p regions are listed in **Table S12**. In the C 1s region, four distinct peaks were detected in the solvent-treated samples: 285.0 eV (C–C, C–H), 286.3 eV (C–O, R–OK, R/alkyl), 288.4 eV (C═O, $K_2CO_3$), and 289.9 eV ($CO_3$). The feature at 286.3 eV is attributed to alkoxide species (e.g., $CH_3OK$ or $CH_3CH_2OK$), with a corresponding O 1s signal at 531.4 eV.

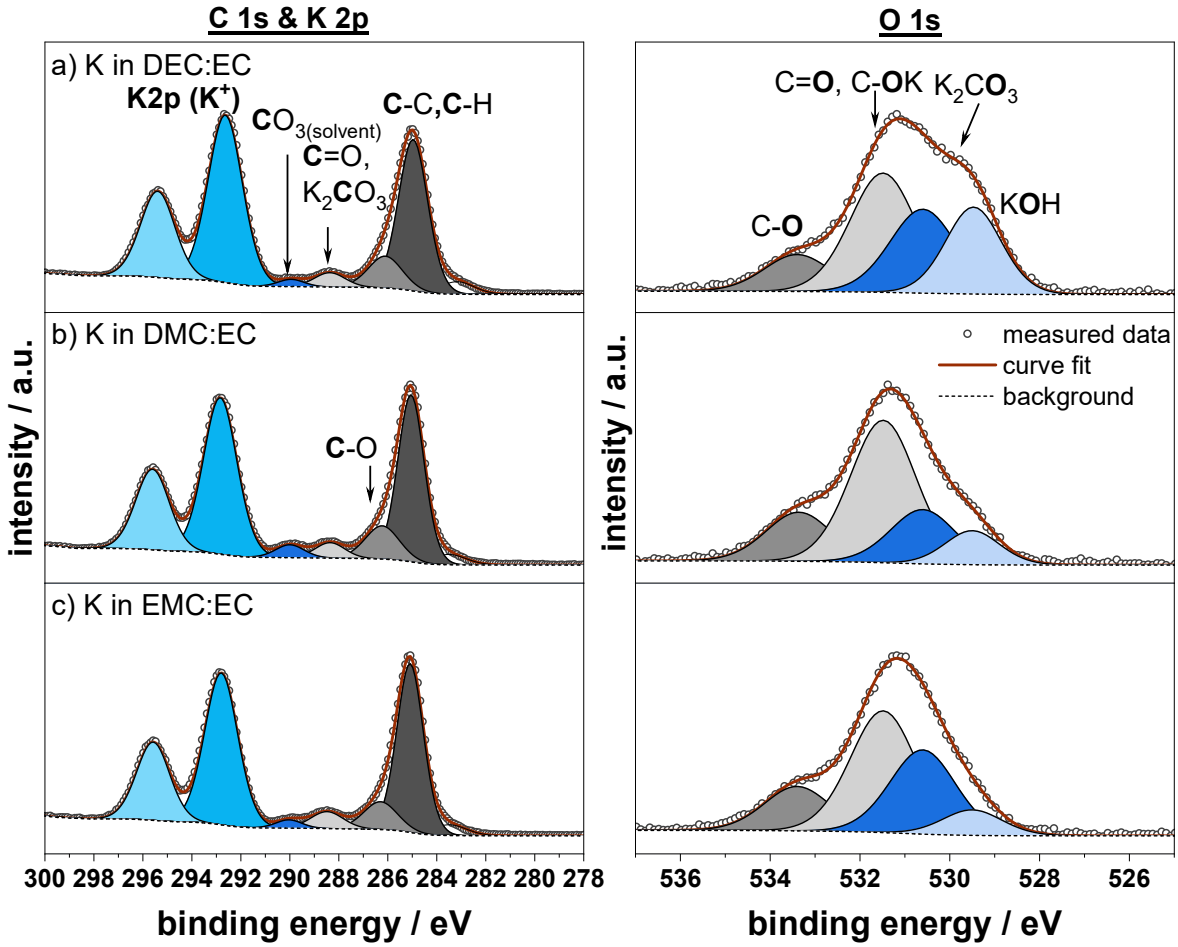


**Figure 57:** C 1s & K 2p and O 1s spectra of the potassium surfaces after a storage time of 2 min in different solvent mixtures: DEC:EC (a) DMC:EC (b), and EMC:EC (c). The BE scale is calibrated versus the hydrocarbon peak at 285 eV.

Based on previous literature assignments and the reference measurements, the peak at 286.3 eV can be attributed to a mixture of two species: C–O (typically observed slightly higher, around 286.5 eV) and alkoxide species, which shift the peak to lower binding energies. Similarly, the peak at 288.4 eV likely results from a superposition of carbonyl (C═O; expected near 287.9 eV) and carbonate ($K_2CO_3$; expected at 288.6 eV) species. The BE at 289.9 eV is assigned to carbonate species as well. At even higher binding energies, organic carbonates appear at the surface—likely originating from trapped solvent residues or degradation products, as discussed in the GC–MS section. These degradation products are assumed to be the corresponding carbonate salts formed after losing their terminal

groups. In comparison, the pristine K metal only shows the C═O/$K_2CO_3$ peak (see **Figure 57d**), indicating that a distinction between $K_2CO_3$ and organic carbonates is indeed possible.

***O 1s Spectra***

The O 1s spectra of the solvent-exposed potassium samples (**Figure 57a–c**) show four components. Alongside the characteristic KOH peak at 529.8 eV and the carbonate/carbonyl signal at 531.1 eV, additional features corresponding to alkoxide and alcoholate (C–O) species appear at 531.5 and 533.4 eV, respectively.

### 8.3.1.3 Charge Analysis

Andersson et al. recently showed that Bader charge analysis can be effectively applied without the need for X-ray absorption near-edge structure (XANES) calculations.[133] Using the theoretical results in this work, an attempt was made to correlate the BE differences in the fitted O 1s and C 1s peaks with calculated atomic charges. This approach yields a series of spectra corresponding to the previously identified decomposition products. The charges are plotted in units of electron charge/e (1.602176634 × $10^{-19}$ C), which directly correlate with binding energy shifts in the photoemission spectra (**Figure 58**).

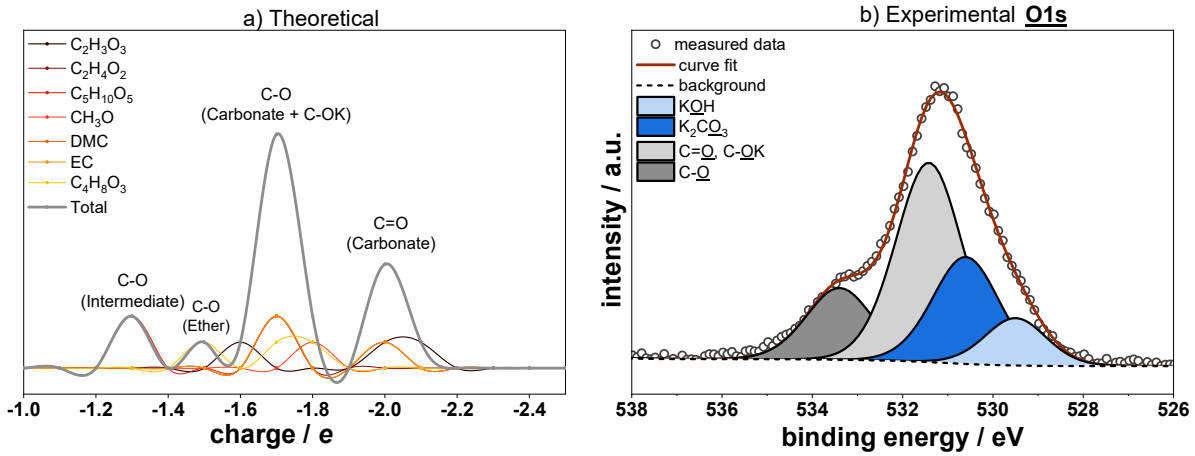


**Figure 58:** Comparison of charge analysis results for carbon and measured XPS O 1s spectra for potassium stored in the DMC/EC mixture. The results are plotted in units of electron charge/e (1.602176634 × $10^{-19}$ C), which directly correlates to units of eV in the photoemission spectra.

***O 1s Spectra***

The O 1s spectra from the potassium/DMC/EC storage experiment reveal four main peaks: C–O at 533.4 eV, C═O/C–O–K at 531.5 eV, carbonates ($K_2CO_3$) at 530.6 eV, and hydroxides (KOH) at 529.5 eV. The measured spectra align well with the theoretical oxygen charge hierarchy shown in **Figure 58**. While the calculated intensities carry no physical meaning, the relative shifts in oxygen charge are reflected in the experimental spectra (**see Figure 58b**). The dominant peak stems from C–O (alkoxide) species with a charge of −1.7e, followed by C═O/carbonate oxygen at −2e, and C–O (intermediate) at

−1.3e. The latter likely overlaps with the ether-related peak but may not be detectable due to the instability of the intermediate. Notably, ether oxygen species at −1.5e are also presumed to contribute to this signal.

#### 8.3.1.4 Surface Layer Composition

Based on the fitted XPS spectra, quantification of the surface species was performed using relative sensitivity factors. **Figure 59a** displays the atomic concentrations of the three dominant elements: carbon, oxygen, and potassium. Across all three solvent mixtures, the concentrations of C (≈59 ± 1 at.%), O (≈24 ± 1 at.%), and K (≈17 ± 1 at.%) remained comparable within the accuracy of quantification (±5 at.%). Notably, the pristine potassium foil exhibited a similar potassium concentration as the solvent-exposed samples but a higher carbon content (69 at.%) and a lower oxygen content (15 at.%). The distribution of the main chemical compounds KOH, $K_2CO_3$, and R–OK (potassium alkoxides), is detailed in **Figure 59b**. For the pristine K sample, only KOH and $K_2CO_3$ were detected in roughly similar amounts. Upon exposure to carbonate solvents, the KOH content markedly decreased in favor of alkoxide species. As discussed earlier, the formation of ethylene glycolate from EC is a key intermediate in the broader degradation cascade of soluble decomposition products. In EC:DMC mixtures, alkoxide formation appears particularly pronounced, aligning with previous GC–MS results showing a faster formation of DMDD compared to DEDD.[63] Interestingly, the DEC:EC sample retained about twice the amount of KOH compared to the DMC:EC and EMC:EC samples. Moreover, the EMC:EC system exhibited the highest proportion of $K_2CO_3$ (≈35 at.%). These findings hint at different degrees of surface interaction and reactivity depending on the linear carbonate solvent used.

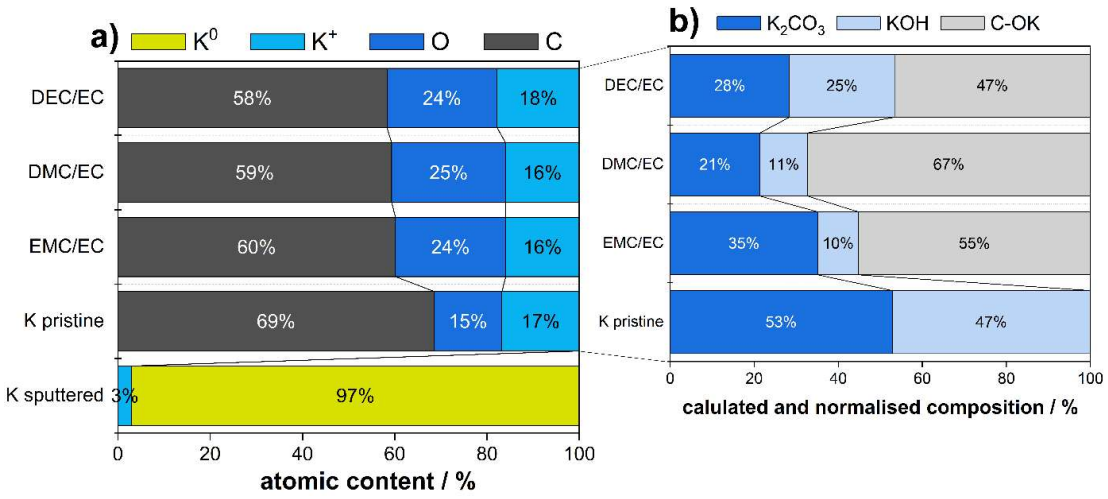


**Figure 59:** Bar plots showing the calculated atomic concentrations (in percent) of (a) the main surface elements, carbon, oxygen, and potassium and (b) the dominant surface species, carbonates, hydroxides, and alkoxides on potassium metal. Values were normalized to 1.

### 8.3.2 Conclusion

This study combines theoretical simulations and experimental analysis to elucidate the early degradation processes leading to the formation of the initial interphase on potassium metal in contact with various carbonate-based solvent mixtures. Correlating the adsorption behavior of decomposition products, as identified by GC–MS and XPS, with insights from DFT calculations enables a bridging of the distinct length and timescales of these techniques, from the Ångström/nanometer and femto/picosecond regime of DFT to the minute-to-day range of laboratory experiments. Surface analysis of pristine potassium revealed that even under glovebox and UHV conditions, the surface layer undergoes early changes due to the adsorption of residual moisture and contaminants. Exposure to different solvent mixtures altered the surface composition significantly, leading to the formation of potassium alkoxides. Concurrently, solvent degradation products such as di- and tricarbonate-functionalized oligomers, ether-bridged carbonates, and ether-like structures were identified. To facilitate broader detection and identification, retention time indices for these compounds were established, making the results transferable across different GC-MS setups. By integrating experimental findings and theoretical modeling, a mechanistic pathway for solvent decomposition was proposed, highlighting the central role of EC degradation. Specifically, ethylene glycolate generated from EC is suggested to link carbonate groups from DMC and DEC, forming $C_4H_7O_4$ intermediates via methoxycarbonylation, with alkoxide species as byproducts, a conclusion strongly supported by the pronounced potassium alkoxide signals in XPS. This work represents an important step toward understanding solvent decomposition mechanisms and provides detailed insights that are likely applicable to more complex electrolyte systems involving conducting salts. Nevertheless, further studies are necessary to clarify whether longer-chain (poly)ethylene glycol structures can form without EC, thereby confirming the pivotal role of EC decomposition in oligomer formation.

# 9 Electrolyte Comparison

In this thesis, each alkali metal, lithium, sodium, and potassium was systematically studied using a consistent set of electrolyte conditions. For each metal, one solvent system (a mixture of DEC:EC) and two electrolyte formulations were applied: (i) DEC:EC with 0.75 M $XPF_6$ (X = Li, Na, K), and (ii) the same electrolyte with FEC as an additive. This standardized approach enables a direct comparison of how different alkali metals interact with the same electrolyte environment. Because all experiments were conducted under identical conditions, including sample handling, washing protocols, and XPS/GC-MS analysis, observed differences in both solid (SEI) and volatile (liquid-phase) decomposition products can be attributed to the intrinsic reactivity of each metal with the respective electrolyte. The surface property of electrodes significantly affects the electrochemical behavior of the electrode-electrolyte interface. Therefore, the initial surface nature of alkali metal (pristine) was investigated first. According to the Pilling–Bedworth (P–B) ratio theory, the morphology of species formed on metal surfaces varies with the P–B ratio. As illustrated in **Figure 60**, the surface layer shrinks when P-B ratio < 1, maintains integrity when 1 > P-B ratio > 2, and flaking when the P-B ratio > 2. XPS analysis of pristine lithium metal showed an approximately 1:1 ratio of $Li_2O$ and LiOH, with only a minor contribution from $Li_2CO_3$. In contrast, sodium and potassium surfaces were dominated by hydroxide, carbonate and hydrocarbonates. These findings reflect each metal's unique reactivity and the nature of spontaneous passivation under inert gas environment. $Li_2O$ has a P-B ratio below 1, favoring porous films that provide limited passivation, while the observed LiOH with values between one and two allowing a denser and more uniform passivation film. In contrast, the observed hydroxides and carbonates for Na and K show decreasing values below 1. These trends help explain why lithium often forms a more stable native layer than sodium or potassium, which remain more reactive and prone to further corrosion.

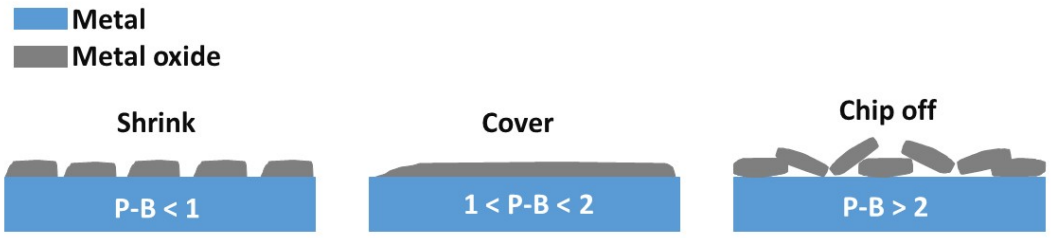


**Figure 60:** Surface properties of alkali metal, illustration of the P-B ratio theory.

Despite the thermodynamic preference for $Li_2CO_3$ over $Na_2CO_3$ and $K_2CO_3$ (as reflected in its more negative Gibbs free energy of formation (**Table 4**)), carbonate formation was more pronounced on sodium and potassium. This discrepancy can be attributed to kinetic factors: Na and K react more rapidly with trace $CO_2$ due to their higher chemical reactivity and lower activation barriers.

Consequently, even minimal atmospheric exposure or residual $CO_2$ in glovebox atmospheres is sufficient to form detectable carbonate layers on pristine Na and K, while carbonate formation on Li is comparatively suppressed under the same conditions.

**Table 4:** Standard Gibbs energy of formation of SEI components on alkali metals.[134]

| Li SEI compounds | | Na SEI compounds | | K SEI compounds | |
|---|---|---|---|---|---|
| Compound | $G^0_f$ /kJ mol$^{-1}$ | Compound | $G^0_f$ /kJ mol$^{-1}$ | Compound | $G^0_f$ /kJ mol$^{-1}$ |
| LiF | -588.7 | NaF | -545.2 | KF | -538.9 |
| $Li_2O$ | -561.9 | $Na_2O$ | -367.6 | $K_2O$ | -322.2 |
| | | $NaHO_3$ | -851.9 | | |
| $Li_2CO_3$ | -1132.2 | $Na_2CO_3$ | -1047.7 | $K_2CO_3$ | -1064.4 |
| LiOH | -438.9 | NaOH | -379.1 | KOH | -379.1 |

Upon exposure to a standard electrolyte (DEC:EC with $XPF_6$), the evolution of surface species highlights both the chemical similarities and kinetic differences among lithium, sodium, and potassium. For lithium metal, XPS analysis revealed a progressive increase in $Li_xPF_y$-type decomposition products with time, accompanied by a decrease in LiF content. This trend suggests a dynamic restructuring of the SEI, where initially formed inorganic LiF becomes increasingly overlaid or replaced by more complex phosphorus-containing species. A similar temporal evolution was observed for sodium, indicating comparable reactivity and SEI instability. In both cases, the partial passivation by native surface, due to low P–B ratios, appears insufficient to fully suppress ongoing electrolyte decomposition.

In contrast, potassium displays markedly different kinetics. Its SEI composition remains largely unchanged over time, with minimal fluorine content and no significant accumulation of new surface species. This static behavior is further supported by GC–MS data: while sodium continues to evolve volatile degradation products over extended contact times, potassium produces nearly the entire spectrum of detectable liquid-phase decomposition products within just 2 minutes (**Table 5**). These findings suggest that although potassium is highly reactive, the majority of electrolyte decomposition reactions occur rapidly upon initial contact, leading to the immediate formation of a relatively stable SEI that does not significantly evolve thereafter.

**Table 5:** Summary of degradation products DEDD, DECE and DECC found over different storage times in DEC:EC $XPF_6$ without FEC additive.

| Degradation Product | Li | | | Na | | | K | | |
|---|---|---|---|---|---|---|---|---|---|
| | 2 min | 2 h | 48 h | 2 min | 2 h | 48 h | 2 min | 2 h | 48 h |
| DEDD 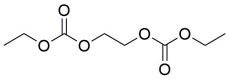 | ○ | ○ | ○ | ● | ● | ● | ● | ● | ● |
| DECE 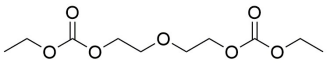 | ○ | ○ | ○ | ○ | ○ | ● | ● | ● | ● |
| DECC 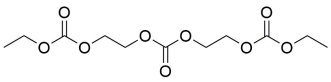 | ○ | ○ | ○ | ○ | ○ | ● | ● | ● | ● |

The interplay between electrolyte salt and additive plays a critical role in defining the composition and stability of the solid electrolyte interphase (SEI). XPS analysis revealed that when $XPF_6$ salts (X = Li, Na, K) were combined with FEC, both alkali metal fluorides (XF) and fluorophosphate species were formed, while FEC alone primarily yields XF species. Thus, $PF_6^-$ not only contributes additional inorganic content to the SEI (**Figure 61**).

Interestingly, the inclusion of FEC in the electrolyte appears to suppress the formation of volatile or soluble decomposition products altogether—this was consistently observed across all alkali metals (Li, Na, K) by GC–MS, where no gaseous degradation products were detected in FEC-containing electrolytes. This suggests that FEC facilitates the rapid formation of a passivating SEI, possibly dominated by metal fluorides and stabilized fluorophosphate species, which effectively inhibit further solvent breakdown. The ability of FEC to preferentially decompose and form robust inorganic layers may "outcompete" the solvent and salt decomposition pathways, thereby stabilizing the interphase at an early stage.

However, the long-term persistence of such protective SEI components is also determined by their solubility in the electrolyte. A clear trend was observed for the metal fluorides in EC:DEC their solubility increases from LiF to NaF to KF. This suggests that even if KF forms during early SEI development on potassium, its higher solubility may lead to gradual dissolution, resulting in a weaker XPS signal and a potentially less stable, fluorine-rich SEI. This dissolution pathway likely explains the consistently low KF intensity observed for potassium surfaces, despite its high initial reactivity.

Taken together, these results highlight that FEC plays a dual role: it enhances early passivation by forming stable inorganic SEI components and simultaneously suppresses ongoing electrolyte

degradation (**Figure 61**). However, the stability and retention of these SEI species, particularly in the case of potassium depend critically on their solubility in the electrolyte medium, which must be considered when designing stable interfaces for alkali metal batteries.

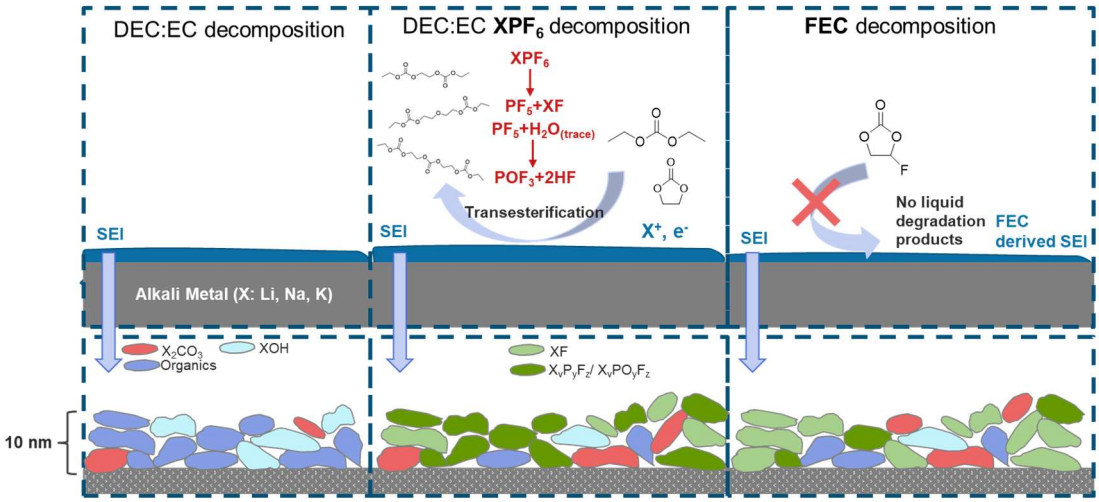


**Figure 61:** Overview of tested solvent DEC:EC and electrolyte ($XPF_6$) with and without additive (FEC) and side reactions on the alkali metals.

# 10 Conclusion and Outlook

In conclusion, this thesis has highlighted the critical role that the initial surface layer of alkali metals plays in determining interfacial reactions, SEI formation, and ultimately battery performance. Alkali metals such as lithium, sodium, and potassium are not only used as reference electrodes in half-cells and analytical zero-excess configurations but are also essential components in the development of next-generation high-energy batteries. A thorough understanding of their surface reactivity is therefore a prerequisite for advancing both fundamental electrochemical knowledge and practical cell design.

The investigations presented in this work emphasize that the SEI, an inherently dynamic and complex interphase, is highly sensitive to the metal's intrinsic reactivity and the applied electrolyte formulation. The electrolyte composition critically influences both initial SEI formation and its evolution over time and during cell operation, thereby affecting cycling stability, efficiency, and safety. However, rational electrolyte design remains hindered by a limited understanding of how electrolyte chemistry, transport properties, and SEI structure are interrelated, particularly in the context of highly reactive alkali metal surfaces.

This thesis contributes to bridging this knowledge gap. First, a comprehensive baseline analysis of pristine and cleaned metal surfaces was performed using XPS. The results revealed significant differences in the initial surface compositions of Li, Na, and K. Importantly, the limitations of XPS sputter depth profiling and fitting (for sodium metal) were demonstrated: sputtering led to partial reduction of oxidized species and misinterpretation of SEI composition, especially on highly reactive metals like potassium. These findings underscore the necessity of careful surface analysis strategies when characterizing alkali metal SEIs.

To monitor interphase evolution over time, a time-resolved storage experiment was developed, combining XPS and GC-MS analysis. The results demonstrated a much higher chemical reactivity of potassium compared to lithium and sodium. While Li and Na showed gradual increases in degradation products, K exhibited immediate and extensive solvent degradation, detectable via GC-MS within minutes. This rapid formation of volatile degradation products suggests a fast process. The addition of FEC was found to suppress these reactions by stabilizing the SEI. These findings provide direct evidence that additives like FEC can fundamentally alter interfacial chemistry and mitigate electrolyte breakdown.

In addition, this work uncovered that the choice of metal supplier significantly influences initial surface chemistry. Variations in impurity levels can affect SEI formation and electrochemical performance. These results call for stricter quality control and deeper characterization of starting materials when comparing studies or designing cells.

While this thesis provides fundamental insights into the surface chemistry and electrolyte reactivity of alkali metals, several open questions remain that should be addressed in future studies. First and foremost, density functional theory (DFT) calculations were only applied selectively within the scope of this work. A more comprehensive theoretical approach could help elucidate general trends across the alkali metal group and their interaction with solvents and electrolyte components, thereby contributing to a periodic understanding of surface reactivity, SEI thermodynamics, and degradation pathways.

Moreover, many of the limitations observed in this work stem from the constraints of conventional surface characterization techniques. In particular, XPS depth profiling via sputtering introduces artifacts due to partial reduction of the SEI and damage to sensitive species, especially on highly reactive alkali metal surfaces. To overcome this, synchrotron-based, non-destructive methods such as hard X-ray photoelectron spectroscopy (HAXPES), near-ambient pressure XPS (NAP-XPS), or X-ray absorption spectroscopy (XAS) should be employed in future studies. These techniques would allow for more accurate and depth-resolved insights into the SEI structure without the need for sputtering, thus preserving chemical integrity.

Altogether, addressing these aspects, integrating advanced theoretical modeling, analytical solution-phase techniques, and high-resolution non-destructive surface characterization, will be essential for developing a comprehensive understanding of SEI formation and stability on alkali metal anodes. These efforts are crucial for advancing both the fundamental science and the practical application of next-generation high-energy metal batteries.

# References


[1] M. Li, J. Lu, Z. Chen, K. Amine, 30 Years of Lithium-Ion Batteries, Adv. Mater. 30 (2018). https://doi.org/10.1002/adma.201800561.

[2] A. Yoshino, K. Sanechika, T. Nakajima, Secondary battery, US4668595A, 1987. https://patents.google.com/patent/US4668595A/en (accessed May 2, 2025).

[3] X.-B. Cheng, R. Zhang, C.-Z. Zhao, Q. Zhang, Toward Safe Lithium Metal Anode in Rechargeable Batteries: A Review, Chem. Rev. 117 (2017) 10403–10473. https://doi.org/10.1021/acs.chemrev.7b00115.

[4] M.S. Whittingham, Electrical Energy Storage and Intercalation Chemistry, Science 192 (1976) 1126–1127. https://doi.org/10.1126/science.192.4244.1126.

[5] Whittingham, M. S., Exxon and Moli Energy, Patent US 4009052A, n.d.

[6] B. Scrosati, Lithium Batteries: from early stages to the future, in: Lithium Batter., John Wiley & Sons, Ltd, 2013: pp. 21–38. https://doi.org/10.1002/9781118615515.ch2.

[7] D. Lin, Y. Liu, Y. Cui, Reviving the lithium metal anode for high-energy batteries, Nat. Nanotechnol. 12 (2017) 194–206. https://doi.org/10.1038/nnano.2017.16.

[8] Y. Lu, X. Rong, Y.-S. Hu, L. Chen, H. Li, Research and development of advanced battery materials in China, Energy Storage Mater. 23 (2019) 144–153. https://doi.org/10.1016/j.ensm.2019.05.019.

[9] U.S.G. Survey, Mineral commodity summaries 2022, U.S. Geological Survey, 2022. https://doi.org/10.3133/mcs2022.

[10] The Role of Critical Minerals in Clean Energy Transitions – Analysis, IEA (2021). https://www.iea.org/reports/the-role-of-critical-minerals-in-clean-energy-transitions (accessed May 2, 2025).

[11] H. Wang, E. Matios, J. Luo, W. Li, Combining theories and experiments to understand the sodium nucleation behavior towards safe sodium metal batteries, Chem. Soc. Rev. 49 (2020) 3783–3805. https://doi.org/10.1039/D0CS00033G.

[12] W. Zhang, J. Yin, W. Wang, Z. Bayhan, H.N. Alshareef, Status of rechargeable potassium batteries, Nano Energy 83 (2021) 105792. https://doi.org/10.1016/j.nanoen.2021.105792.

[13] S.-K. Otto, T. Fuchs, Y. Moryson, C. Lerch, B. Mogwitz, J. Sann, J. Janek, A. Henss, Storage of Lithium Metal: The Role of the Native Passivation Layer for the Anode Interface Resistance in Solid State Batteries, ACS Appl. Energy Mater. 4 (2021) 12798–12807. https://doi.org/10.1021/acsaem.1c02481.

[14] A. Thomas, B. Pohle, J. Schultz, M. Hantusch, D. Mikhailova, NaOH protective layer for a stable sodium metal anode in liquid electrolytes, J. Energy Storage 77 (2024) 109900. https://doi.org/10.1016/j.est.2023.109900.

[15] N. Philling, R.J. Bedworth, The Oxidation of Metals at High Temperatures, Inst. Metals 29 (1923) 529.

[16] C.A. Hart, C.H. Skinner, A.M. Capece, B.E. Koel, Sorption of atmospheric gases by bulk lithium metal, J. Nucl. Mater. 468 (2016) 71–77. https://doi.org/10.1016/j.jnucmat.2015.11.006.

[17] J.-G. Zhang, W. Xu, W.A. Henderson, Lithium Metal Anodes and Rechargeable Lithium Metal Batteries, Springer International Publishing, Cham, 2017. https://doi.org/10.1007/978-3-319-44054-5.

[18] J. Steiger, D. Kramer, R. Mönig, Microscopic observations of the formation, growth and shrinkage of lithium moss during electrodeposition and dissolution, Electrochimica Acta 136 (2014) 529–536. https://doi.org/10.1016/j.electacta.2014.05.120.

[19] S. Daskeviciute-Geguziene, Y. Zhang, K. Rakstys, C. Xiao, J. Xia, Z. Qiu, M. Daskeviciene, T. Paskevicius, V. Jankauskas, A.M. Asiri, V. Getautis, M.K. Nazeeruddin, Passivating Defects of Perovskite Solar Cells with Functional Donor-Acceptor–Donor Type Hole Transporting Materials, Adv. Funct. Mater. 33 (2023) 2208317. https://doi.org/10.1002/adfm.202208317.

[20] T. Zhu, J. Huang, B. Huang, N. Zhang, S. Liu, Q. Yao, S.-C. Haw, Y.-C. Chang, C.-W. Pao, J.-M. Chen, Q. Shao, Z. Hu, Y. Ma, X. Huang, High-Index Faceted RuCo Nanoscrews for Water Electrosplitting, Adv. Energy Mater. 10 (2020) 2002860. https://doi.org/10.1002/aenm.202002860.

[21] X. Li, X. Yue, Y. Wang, T. Chen, Y. Zhou, D. Liu, H. Xiang, S. Zhang, H. Zeng, Z. Xiang, Electron donor–acceptor (D-A) tuning to achieve soluble covalent organic polymers for optoelectronic devices, EScience 3 (2023) 100084. https://doi.org/10.1016/j.esci.2022.10.009.

[22] X. Shen, K. Kang, Z. Yu, W.H. Jeong, H. Choi, S.H. Park, S.D. Stranks, H.J. Snaith, R.H. Friend, B.R. Lee, Passivation strategies for mitigating defect challenges in halide perovskite light-emitting diodes, Joule 7 (2023) 272–308. https://doi.org/10.1016/j.joule.2023.01.008.

[23] P. Bai, J. Guo, M. Wang, A. Kushima, L. Su, J. Li, F.R. Brushett, M.Z. Bazant, Interactions between Lithium Growths and Nanoporous Ceramic Separators, Joule 2 (2018) 2434–2449. https://doi.org/10.1016/j.joule.2018.08.018.

[24] P. Bai, J. Li, F. R. Brushett, M. Z. Bazant, Transition of lithium growth mechanisms in liquid electrolytes, Energy Environ. Sci. 9 (2016) 3221–3229. https://doi.org/10.1039/C6EE01674J.

[25] Electrochemical Methods: Fundamentals and Applications, 2nd Edition | Wiley, Wiley.Com (n.d.). https://www.wiley.com/en-us/Electrochemical+Methods%3A+Fundamentals+and+Applications%2C+2nd+Edition-p-9780471043720 (accessed May 2, 2025).

[26] E. Peled, The Electrochemical Behavior of Alkali and Alkaline Earth Metals in Nonaqueous Battery Systems—The Solid Electrolyte Interphase Model, J. Electrochem. Soc. 126 (1979) 2047. https://doi.org/10.1149/1.2128859.

[27] H. Wu, H. Jia, C. Wang, J.-G. Zhang, W. Xu, Recent Progress in Understanding Solid Electrolyte Interphase on Lithium Metal Anodes, Adv. Energy Mater. 11 (2021) 2003092. https://doi.org/10.1002/aenm.202003092.

[28] F. Hao, A. Verma, P.P. Mukherjee, Mechanistic insight into dendrite–SEI interactions for lithium metal electrodes, J. Mater. Chem. A 6 (2018) 19664–19671. https://doi.org/10.1039/C8TA07997H.

[29] H. Wang, D. Yu, C. Kuang, L. Cheng, W. Li, X. Feng, Z. Zhang, X. Zhang, Y. Zhang, Alkali Metal Anodes for Rechargeable Batteries, Chem 5 (2019) 313–338. https://doi.org/10.1016/j.chempr.2018.11.005.

[30] G. Liu, W. Lu, A Model of Concurrent Lithium Dendrite Growth, SEI Growth, SEI Penetration and Regrowth, J. Electrochem. Soc. 164 (2017) A1826. https://doi.org/10.1149/2.0381709jes.

[31] S. Shi, P. Lu, Z. Liu, Y. Qi, L.G.Jr. Hector, H. Li, S.J. Harris, Direct Calculation of Li-Ion Transport in the Solid Electrolyte Interphase, J. Am. Chem. Soc. 134 (2012) 15476–15487. https://doi.org/10.1021/ja305366r.

[32] E. Peled, S. Menkin, Review—SEI: Past, Present and Future, J. Electrochem. Soc. 164 (2017) A1703–A1719. https://doi.org/10.1149/2.1441707jes.

[33] E. Peled, D. Golodnitsky, G. Ardel, Advanced Model for Solid Electrolyte Interphase Electrodes in Liquid and Polymer Electrolytes, J. Electrochem. Soc. 144 (1997) L208. https://doi.org/10.1149/1.1837858.

[34] B. Jagger, M. Pasta, Solid electrolyte interphases in lithium metal batteries, Joule 7 (2023) 2228–2244. https://doi.org/10.1016/j.joule.2023.08.007.

[35] Y. Li, Y. Li, A. Pei, K. Yan, Y. Sun, C.-L. Wu, L.-M. Joubert, R. Chin, A.L. Koh, Y. Yu, J. Perrino, B. Butz, S. Chu, Y. Cui, Atomic structure of sensitive battery materials and interfaces revealed by cryo–electron microscopy, Science 358 (2017) 506–510. https://doi.org/10.1126/science.aam6014.

[36] C. Fang, B. Lu, G. Pawar, M. Zhang, D. Cheng, S. Chen, M. Ceja, J.-M. Doux, H. Musrock, M. Cai, B. Liaw, Y.S. Meng, Pressure-tailored lithium deposition and dissolution in lithium metal batteries, Nat. Energy 6 (2021) 987–994. https://doi.org/10.1038/s41560-021-00917-3.

[37] X. Cao, X. Ren, L. Zou, M.H. Engelhard, W. Huang, H. Wang, B.E. Matthews, H. Lee, C. Niu, B.W. Arey, Y. Cui, C. Wang, J. Xiao, J. Liu, W. Xu, J.-G. Zhang, Monolithic solid–electrolyte interphases formed in fluorinated orthoformate-based electrolytes minimize Li depletion and pulverization, Nat. Energy 4 (2019) 796–805. https://doi.org/10.1038/s41560-019-0464-5.

[38] Z. Yu, H. Wang, X. Kong, W. Huang, Y. Tsao, D.G. Mackanic, K. Wang, X. Wang, W. Huang, S. Choudhury, Y. Zheng, C.V. Amanchukwu, S.T. Hung, Y. Ma, E.G. Lomeli, J. Qin, Y. Cui, Z. Bao, Molecular design for electrolyte solvents enabling energy-dense and long-cycling lithium metal batteries, Nat. Energy 5 (2020) 526–533. https://doi.org/10.1038/s41560-020-0634-5.

[39] B. Han, Z. Zhang, Y. Zou, K. Xu, G. Xu, H. Wang, H. Meng, Y. Deng, J. Li, M. Gu, Poor Stability of Li2CO3 in the Solid Electrolyte Interphase of a Lithium-Metal Anode Revealed by Cryo-Electron Microscopy, Adv. Mater. 33 (2021) 2100404. https://doi.org/10.1002/adma.202100404.

[40] M. Moshkovich, Y. Gofer, D. Aurbach, Investigation of the Electrochemical Windows of Aprotic Alkali Metal (Li, Na, K) Salt Solutions, J. Electrochem. Soc. 148 (2001) E155. https://doi.org/10.1149/1.1357316.

[41] A. Le Ma, A.J. Naylor, L. Nyholm, R. Younesi, Strategies for Mitigating Dissolution of Solid Electrolyte Interphases in Sodium-Ion Batteries, Angew. Chem. 133 (2021) 4905–4913. https://doi.org/10.1002/ange.202013803.

[42] R. Mogensen, D. Brandell, R. Younesi, Solubility of the Solid Electrolyte Interphase (SEI) in Sodium Ion Batteries, ACS Energy Lett. 1 (2016) 1173–1178. https://doi.org/10.1021/acsenergylett.6b00491.

[43] S. Komaba, T. Ishikawa, N. Yabuuchi, W. Murata, A. Ito, Y. Ohsawa, Fluorinated Ethylene Carbonate as Electrolyte Additive for Rechargeable Na Batteries, ACS Appl. Mater. Interfaces 3 (2011) 4165–4168. https://doi.org/10.1021/am200973k.

[44] T.A. Pham, K.E. Kweon, A. Samanta, V. Lordi, J.E. Pask, Solvation and Dynamics of Sodium and Potassium in Ethylene Carbonate from ab Initio Molecular Dynamics Simulations, J. Phys. Chem. C 121 (2017) 21913–21920. https://doi.org/10.1021/acs.jpcc.7b06457.

[45] M. Shakourian-Fard, G. Kamath, K. Smith, H. Xiong, S.K.R.S. Sankaranarayanan, Trends in Na-Ion Solvation with Alkyl-Carbonate Electrolytes for Sodium-Ion Batteries: Insights from First-Principles Calculations, J. Phys. Chem. C 119 (2015) 22747–22759. https://doi.org/10.1021/acs.jpcc.5b04706.

[46] G. Kamath, R.W. Cutler, S.A. Deshmukh, M. Shakourian-Fard, R. Parrish, J. Huether, D.P. Butt, H. Xiong, S.K.R.S. Sankaranarayanan, In Silico Based Rank-Order Determination and Experiments on Nonaqueous Electrolytes for Sodium Ion Battery Applications, J. Phys. Chem. C 118 (2014) 13406–13416. https://doi.org/10.1021/jp502319p.

[47] P. Peljo, H.H. Girault, Electrochemical potential window of battery electrolytes: the HOMO–LUMO misconception, Energy Environ. Sci. 11 (2018) 2306–2309. https://doi.org/10.1039/C8EE01286E.

[48] K. Xu, Nonaqueous Liquid Electrolytes for Lithium-Based Rechargeable Batteries, Chem. Rev. 104 (2004) 4303–417. https://doi.org/10.1002/chin.200450271.

[49] W.S. Harris, Electrochemical Studies in Cyclic Esters, University of California Radiation Laboratory, 1958.

[50] K. Xu, Electrolytes and Interphases in Li-Ion Batteries and Beyond, Chem. Rev. 114 (2014) 11503–11618. https://doi.org/10.1021/cr500003w.

[51] R. Fong, U. von Sacken, J.R. Dahn, Studies of Lithium Intercalation into Carbons Using Nonaqueous Electrochemical Cells, J. Electrochem. Soc. 137 (1990) 2009. https://doi.org/10.1149/1.2086855.

[52] G.V. Zhuang, H. Yang, B. Blizanac, P.N. Ross, A Study of Electrochemical Reduction of Ethylene and Propylene Carbonate Electrolytes on Graphite Using ATR-FTIR Spectroscopy, Electrochem. Solid-State Lett. 8 (2005) A441. https://doi.org/10.1149/1.1979327.

[53] N. Xin, Y. Sun, M. He, C.J. Radke, J.M. Prausnitz, Solubilities of six lithium salts in five non-aqueous solvents and in a few of their binary mixtures, Fluid Phase Equilibria 461 (2018) 1–7. https://doi.org/10.1016/j.fluid.2017.12.034.

[54] J. Liu, Z. Bao, Y. Cui, E.J. Dufek, J.B. Goodenough, P. Khalifah, Q. Li, B.Y. Liaw, P. Liu, A. Manthiram, Y.S. Meng, V.R. Subramanian, M.F. Toney, V.V. Viswanathan, M.S. Whittingham, J. Xiao, W. Xu, J. Yang, X.-Q. Yang, J.-G. Zhang, Pathways for practical high-energy long-cycling lithium metal batteries, Nat. Energy 4 (2019) 180–186. https://doi.org/10.1038/s41560-019-0338-x.

[55] Z. Chen, N. Xu, W. Li, R. Zhao, Y. Dong, J. Liu, C. Su, J. Wang, C. Zhang, Effect of trace hydrofluoric acid in a LiPF6 electrolyte on the performance of a Li–organic battery with an N-heterocycle based conjugated microporous polymer as the cathode, J. Mater. Chem. A 7 (2019) 16347–16355. https://doi.org/10.1039/C9TA01810G.

[56] M. Stich, M. Göttlinger, M. Kurniawan, U. Schmidt, A. Bund, Hydrolysis of LiPF6 in Carbonate-Based Electrolytes for Lithium-Ion Batteries and in Aqueous Media, J. Phys. Chem. C 122 (2018) 8836–8842. https://doi.org/10.1021/acs.jpcc.8b02080.

[57] T. Kawamura, S. Okada, J. Yamaki, Decomposition reaction of LiPF6-based electrolytes for lithium ion cells, J. Power Sources 156 (2006) 547–554. https://doi.org/10.1016/j.jpowsour.2005.05.084.

[58] P. Barnes, K. Smith, R. Parrish, C. Jones, P. Skinner, E. Storch, Q. White, C. Deng, D. Karsann, M.L. Lau, J.J. Dumais, E.J. Dufek, H. Xiong, A non-aqueous sodium hexafluorophosphate-based electrolyte degradation study: Formation and mitigation of hydrofluoric acid, J. Power Sources 447 (2020) 227363. https://doi.org/10.1016/j.jpowsour.2019.227363.

[59] L. Terborg, S. Nowak, S. Passerini, M. Winter, U. Karst, P.R. Haddad, P.N. Nesterenko, Ion chromatographic determination of hydrolysis products of hexafluorophosphate salts in aqueous solution, Anal. Chim. Acta 714 (2012) 121–126. https://doi.org/10.1016/j.aca.2011.11.056.

[60] D.M.C. Ould, S. Menkin, C.A. O'Keefe, F. Coowar, J. Barker, C.P. Grey, D.S. Wright, New Route to Battery Grade NaPF6 for Na-Ion Batteries: Expanding the Accessible Concentration, Angew. Chem. Int. Ed. 60 (2021) 24882–24887. https://doi.org/10.1002/anie.202111215.

[61] H. Zhao, J. Wang, H. Shao, K. Xu, Y. Deng, Gas Generation Mechanism in Li-Metal Batteries, ENERGY Environ. Mater. 5 (2022) 327–336. https://doi.org/10.1002/eem2.12180.

[62] Gas Generation in Anode-Free Li-Metal Batteries with Localized High-Concentration Electrolytes, (n.d.). https://sioc-journal.cn/Jwk_hxxb/EN/10.6023/A24050167 (accessed May 3, 2025).

[63] A. Hofmann, F. Müller, S. Schöner, F. Jeschull, Revealing the Formation of Dialkyl Dioxahexane Dioate Products from Ethylene Carbonate based Electrolytes on Lithium and Potassium Surfaces, Batter. Supercaps 6 (2023) e202300325. https://doi.org/10.1002/batt.202300325.

[64] Z. Wang, A. Hofmann, NaDFOB and FEC as Electrolyte Additives Enabling Improved Cyclability of Sodium Metal Batteries and Sodium Ion Batteries, ChemElectroChem 12 (2025) e202400597. https://doi.org/10.1002/celc.202400597.

[65] J. Ma, X. Feng, Y. Wu, Y. Wang, P. Liu, K. Shang, H. Jiang, X. Hou, D. Mitlin, H. Xiang, Stable sodium anodes for sodium metal batteries (SMBs) enabled by in-situ formed quasi solid-state polymer electrolyte, J. Energy Chem. 77 (2023) 290–299. https://doi.org/10.1016/j.jechem.2022.09.040.

[66] J. Chen, T. Liu, M. Chu, K. Yu, X. Xie, K. Lin, Y. Cheng, X. Zhang, J. Li, Z. Shi, Insight into the interfacial reaction mechanism of FEC and NaF on Na for high performance sodium metal batteries, J. Mater. Chem. A 12 (2024) 25222–25232. https://doi.org/10.1039/D4TA03266G.

[67] X.-Q. Zhang, X.-B. Cheng, C. Xiang, Y. Chong, Q. Zhang, Fluoroethylene Carbonate Additives to Render Uniform Li Deposits in Lithium Metal Batteries, Adv. Funct. Mater. 27 (2017) 1605989. https://doi.org/10.1002/adfm.201605989.

[68] S. Baek, S. Jie, B. Lee, Effects of fluoroethylene carbonate additive on potassium metal anode, J. Mech. Sci. Technol. 37 (2023) 3657–3665. https://doi.org/10.1007/s12206-023-0630-3.

[69] F. Fasulo, A.B. Muñoz-García, A. Massaro, O. Crescenzi, C. Huang, M. Pavone, Vinylene carbonate reactivity at lithium metal surface: first-principles insights into the early steps of SEI formation, J. Mater. Chem. A 11 (2023) 5660–5669. https://doi.org/10.1039/D2TA08772C.

[70] N. Dautain, J.-F. Martin, D. Sotta, P. Azais, D. Peralta, The tremendous challenge of suitable KPF6-based electrolytes for 4 V-class K-metal cells, J. Power Sources 614 (2024) 234993. https://doi.org/10.1016/j.jpowsour.2024.234993.

[71] A.J. Louli, A. Eldesoky, J. deGooyer, M. Coon, C.P. Aiken, Z. Simunovic, M. Metzger, J.R. Dahn, Different Positive Electrodes for Anode-Free Lithium Metal Cells, J. Electrochem. Soc. 169 (2022) 040517. https://doi.org/10.1149/1945-7111/ac62c4.

[72] P. He, N.F. Xavier Jr, M.J. Golomb, Y. Han, Y. Du, Q. Cai, Y. Xu, Toward Zero-Excess Alkali Metal Batteries: Bridging Experimental and Computational Insights, Adv. Mater. n/a (n.d.) 2502052. https://doi.org/10.1002/adma.202502052.

[73] P. Liu, Y. Wang, Q. Gu, J. Nanda, J. Watt, D. Mitlin, Dendrite-Free Potassium Metal Anodes in a Carbonate Electrolyte, Adv. Mater. 32 (2020) 1906735. https://doi.org/10.1002/adma.201906735.

[74] C. Xie, H. Wu, K. Liang, Z. Ding, J. Dai, R. Zhang, Q. Zhang, D. Sun, Y. Ren, Y. Li, Y. Tang, H. Wang, Microalloying induced stable welded interfaces for highly reversible zero-excess sodium metal batteries, Energy Environ. Sci. 17 (2024) 4228–4237. https://doi.org/10.1039/D4EE00136B.

[75] J. Wang, Y. Zhou, Y. Zhuo, K. Fang, S. Wang, B. Zhao, J. Zhou, H. Wang, The challenges and strategies towards high-performance anode-free post-lithium metal batteries, Chem. Sci. 16 (2025) 552–574. https://doi.org/10.1039/D4SC06630H.

[76] K. Tang, L. Tian, Y. Zhang, Z. J. Xu, Anode-free lithium metal batteries: a promising flexible energy storage system, J. Mater. Chem. A 12 (2024) 16268–16292. https://doi.org/10.1039/D4TA02003K.

[77] Z. Lu, H. Yang, Q.-H. Yang, P. He, H. Zhou, Building a Beyond Concentrated Electrolyte for High-Voltage Anode-Free Rechargeable Sodium Batteries, Angew. Chem. Int. Ed. 61 (2022) e202200410. https://doi.org/10.1002/anie.202200410.

[78] A. Einstein, Über einen die Erzeugung und Verwandlung des Lichtes betreffenden heuristischen Gesichtspunkt, Ann. Phys. 322 (1905) 132–148. https://doi.org/10.1002/andp.19053220607.

[79] ESCA : atomic, molecular and solid state structure studied by means of electron spectroscopy /, (1967).

[80] Handbook of X Ray Photoelectron Spectroscopy: A Reference Book of Standard Spectra for Identification and Interpretation of Xps Data - Moulder, John F.; Stickle, William F.; Sobol, Peter E.; Bomben, Kenneth D.: 9780964812413 - AbeBooks, (n.d.). https://www.abebooks.com/9780964812413/Handbook-Ray-Photoelectron-Spectroscopy-Reference-096481241X/plp (accessed April 29, 2025).

[81] J. Kumar, Photoelectron Spectroscopy: Fundamental Principles and Applications, in: S.K. Sharma (Ed.), Handb. Mater. Charact., Springer International Publishing, Cham, 2018: pp. 435–495. https://doi.org/10.1007/978-3-319-92955-2_12.

[82] J.W. Pinder, G.H. Major, D.R. Baer, J. Terry, J.E. Whitten, J. Čechal, J.D. Crossman, A.J. Lizarbe, S. Jafari, C.D. Easton, J. Baltrusaitis, M.A. van Spronsen, M.R. Linford, Avoiding common errors in X-ray photoelectron spectroscopy data collection and analysis, and properly reporting instrument parameters, Appl. Surf. Sci. Adv. 19 (2024) 100534. https://doi.org/10.1016/j.apsadv.2023.100534.

[83] S. Hashimoto, A. Tanaka, A. Murata, T. Sakurada, Formulation for XPS spectral change of oxides by ion bombardment as a function of sputtering time, Surf. Sci. 556 (2004) 22–32. https://doi.org/10.1016/j.susc.2004.03.002.

[84] S.-K. Otto, Y. Moryson, T. Krauskopf, K. Peppler, J. Sann, J. Janek, A. Henss, In-Depth Characterization of Lithium-Metal Surfaces with XPS and ToF-SIMS: Toward Better Understanding of

the Passivation Layer, Chem. Mater. 33 (2021) 859–867. https://doi.org/10.1021/acs.chemmater.0c03518.

[85] Charles Kittel-8th Edition, Introduction to Solid State Physics, n.d. http://archive.org/details/IntroductionToSolidStatePhysics (accessed May 15, 2025).

[86] A. Barrie, F.J. Street, An Auger and X-ray photoelectron spectroscopic study of sodium metal and sodium oxide, J. Electron Spectrosc. Relat. Phenom. 7 (1975) 1–31. https://doi.org/10.1016/0368-2048(75)80052-1.

[87] S. Tougaard, Quantitative analysis of the inelastic background in surface electron spectroscopy, Surf. Interface Anal. 11 (1988) 453–472. https://doi.org/10.1002/sia.740110902.

[88] S. Tougaard, Practical algorithm for background subtraction, Surf. Sci. 216 (1989) 343–360. https://doi.org/10.1016/0039-6028(89)90380-4.

[89] S. Tougaard, Energy loss in XPS: Fundamental processes and applications for quantification, non-destructive depth profiling and 3D imaging, J. Electron Spectrosc. Relat. Phenom. 178–179 (2010) 128–153. https://doi.org/10.1016/j.elspec.2009.08.005.

[90] L. Somerville, J. Bareño, P. Jennings, A. McGordon, C. Lyness, I. Bloom, The Effect of Pre-Analysis Washing on the Surface Film of Graphite Electrodes, Electrochimica Acta 206 (2016) 70–76. https://doi.org/10.1016/j.electacta.2016.04.133.

[91] J. Klemens, L. Schneider, D. Burger, N. Zimmerer, M. Müller, W. Bauer, H. Ehrenberg, P. Scharfer, W. Schabel, Process and Drying Behavior Toward Higher Drying Rates of Hard Carbon Anodes for Sodium-Ion Batteries with Different Particle Sizes: An Experimental Study in Comparison to Graphite for Lithium-Ion-Batteries, Energy Technol. 11 (2023) 2300338. https://doi.org/10.1002/ente.202300338.

[92] P. Stüble, C. Müller, J. Klemens, P. Scharfer, W. Schabel, M. Häringer, J.R. Binder, A. Hofmann, A. Smith, Enabling Long-term Cycling Stability of Na3V2(PO4)3/C vs. Hard Carbon Full-cells, Batter. Supercaps 7 (2024) e202300375. https://doi.org/10.1002/batt.202300375.

[93] R. Simpson, Rapid XPS Image Acquisition Using SnapMap, (n.d.).

[94] R. Bro, A.K. Smilde, Principal component analysis, Anal. Methods 6 (2014) 2812–2831. https://doi.org/10.1039/C3AY41907J.

[95] B. Moeini, T.G. Avval, N. Gallagher, M.R. Linford, Surface analysis insight note. Principal component analysis (PCA) of an X-ray photoelectron spectroscopy image. The importance of preprocessing, Surf. Interface Anal. 55 (2023) 798–807. https://doi.org/10.1002/sia.7252.

[96] L. Wildersinn, D. Stottmeister, F. Jeschull, A. Groß, A. Hofmann, Decomposition of Binary Mixtures of DMC/EC, EMC/EC, and DEC/EC on Potassium Surfaces; GC, XPS, and Calculation, ACS Appl. Mater. Interfaces 17 (2025) 10055–10072. https://doi.org/10.1021/acsami.4c17461.

[97] A. Hofmann, Z. Wang, S.P. Bautista, M. Weil, F. Müller, R. Löwe, L. Schneider, I.U. Mohsin, T. Hanemann, Comprehensive characterization of propylene carbonate based liquid electrolyte mixtures for sodium-ion cells, Electrochimica Acta 403 (2022) 139670. https://doi.org/10.1016/j.electacta.2021.139670.

[98] EL-Cell GmbH, EL-CELL Manual ECC-Opto-10, (2024).

[99] K.N. Wood, G. Teeter, XPS on Li-Battery-Related Compounds: Analysis of Inorganic SEI Phases and a Methodology for Charge Correction, ACS Appl. Energy Mater. 1 (2018) 4493–4504. https://doi.org/10.1021/acsaem.8b00406.

[100] E.W.C. Spotte-Smith, T.B. Petrocelli, H.D. Patel, S.M. Blau, K.A. Persson, Elementary Decomposition Mechanisms of Lithium Hexafluorophosphate in Battery Electrolytes and Interphases, ACS Energy Lett. 8 (2023) 347–355. https://doi.org/10.1021/acsenergylett.2c02351.

[101] M.M. Markowitz, D.A. Boryta, Lithium Metal-Gas Reactions., J. Chem. Eng. Data 7 (1962) 586–591. https://doi.org/10.1021/je60015a047.

[102] Y. Li, Y. Li, Y. Sun, B. Butz, K. Yan, A.L. Koh, J. Zhao, A. Pei, Y. Cui, Revealing Nanoscale Passivation and Corrosion Mechanisms of Reactive Battery Materials in Gas Environments, Nano Lett. 17 (2017) 5171–5178. https://doi.org/10.1021/acs.nanolett.7b02630.

[103] M. Klanchar, B.D. Wintrode, J.A. Phillips, Lithium-Water Reaction Chemistry at Elevated Temperature, (n.d.).

[104] W.R. Irvine, J.A. Lund, The Reaction of Lithium with Water Vapor, J. Electrochem. Soc. 110 (1963) 141. https://doi.org/10.1149/1.2425691.

[105] C.-F. Lin, A.C. Kozen, M. Noked, C. Liu, G.W. Rubloff, ALD Protection of Li-Metal Anode Surfaces – Quantifying and Preventing Chemical and Electrochemical Corrosion in Organic Solvent, Adv. Mater. Interfaces 3 (2016). https://doi.org/10.1002/admi.201600426.

[106] H.R. Grady, Lithium metal for the battery industry, J. Power Sources 5 (1980) 127–135. https://doi.org/10.1016/0378-7753(80)80101-7.

[107] N. Delaporte, Y. Wang, K. Zaghib, Pre-treatments of Lithium Foil Surface for Improving the Cycling Life of Li Metal Batteries, Front. Mater. 6 (2019). https://doi.org/10.3389/fmats.2019.00267.

[108] M. Ishikawa, H. Kawasaki, N. Yoshimoto, M. Morita, Pretreatment of Li metal anode with electrolyte additive for enhancing Li cycleability, J. Power Sources 146 (2005) 199–203. https://doi.org/10.1016/j.jpowsour.2005.03.007.

[109] J.S. Sakamoto, F. Wudl, B. Dunn, Passivating lithium electrodes with trimethylsilylacetylene, Solid State Ion. 144 (2001) 295–299. https://doi.org/10.1016/S0167-2738(01)00902-X.

[110] K. Adair, Y. Zhao, Y. Sun, C. Wang, X. Sun, Stabilizing the Li Metal Interface: Molecular Layer Deposition for Advanced Next-Generation Energy Storage Systems, ECS Meet. Abstr. MA2020-01 (2020) 281. https://doi.org/10.1149/MA2020-012281mtgabs.

[111] A. Wang, S. Kadam, H. Li, S. Shi, Y. Qi, Review on modeling of the anode solid electrolyte interphase (SEI) for lithium-ion batteries, Npj Comput. Mater. 4 (2018) 1–26. https://doi.org/10.1038/s41524-018-0064-0.

[112] D.E. Galvez-Aranda, J.M. Seminario, Li-Metal Anode in a Conventional Li-Ion Battery Electrolyte: Solid Electrolyte Interphase Formation using Ab Initio Molecular Dynamics, J. Electrochem. Soc. 169 (2022) 030502. https://doi.org/10.1149/1945-7111/ac55c8.

[113] Z. Wang, Z. Sun, Y. Shi, F. Qi, X. Gao, H. Yang, H.-M. Cheng, F. Li, Ion-Dipole Chemistry Drives Rapid Evolution of Li Ions Solvation Sheath in Low-Temperature Li Batteries, Adv. Energy Mater. 11 (2021). https://doi.org/10.1002/aenm.202100935.

[114] G. Gachot, S. Grugeon, M. Armand, S. Pilard, P. Guenot, J.-M. Tarascon, S. Laruelle, Deciphering the multi-step degradation mechanisms of carbonate-based electrolyte in Li batteries, J. Power Sources 178 (2008) 409–421. https://doi.org/10.1016/j.jpowsour.2007.11.110.

[115] G.G. Eshetu, T. Diemant, M. Hekmatfar, S. Grugeon, R.J. Behm, S. Laruelle, M. Armand, S. Passerini, Impact of the electrolyte salt anion on the solid electrolyte interphase formation in sodium ion batteries, Nano Energy 55 (2019) 327–340. https://doi.org/10.1016/j.nanoen.2018.10.040.

[116] S.E. Sloop, J.K. Pugh, S. Wang, J.B. Kerr, K. Kinoshita, Chemical Reactivity of PF5 and LiPF6 in Ethylene CarbonateÕDimethyl Carbonate Solutions, (n.d.).

[117] Q. Liu, D. Mu, B. Wu, L. Wang, L. Gai, F. Wu, Density Functional Theory Research into the Reduction Mechanism for the Solvent/Additive in a Sodium-Ion Battery, ChemSusChem 10 (2017) 786–796. https://doi.org/10.1002/cssc.201601356.

[118] J. Maibach, I. Källquist, M. Andersson, S. Urpelainen, K. Edström, H. Rensmo, H. Siegbahn, M. Hahlin, Probing a battery electrolyte drop with ambient pressure photoelectron spectroscopy, Nat. Commun. 10 (2019) 3080. https://doi.org/10.1038/s41467-019-10803-y.

[119] L. Caracciolo, L. Madec, H. Martinez, XPS Analysis of K-based Reference Compounds to Allow Reliable Studies of Solid Electrolyte Interphase in K-ion Batteries, ACS Appl. Energy Mater. 4 (2021) 11693–11699. https://doi.org/10.1021/acsaem.1c02400.

[120] Y.-C. Lin, Y.-Y. Chen, B.-Y. Yu, W.-C. Lin, C.-H. Kuo, J.-J. Shyue, Sputter-induced chemical transformation in oxoanions by combination of C60+ and Ar+ ion beams analyzed with X-ray photoelectron spectrometry, Analyst 134 (2009) 945–951. https://doi.org/10.1039/B814729A.

[121] Z. Liu, J. Huang, S. Chen, Y. Huang, F. Ding, W. Guo, D. Lei, L. Yang, F.-L. Qing, Z. You, CO2-based poly (propylene carbonate) with various carbonate linkage content for reactive hot-melt polyurethane adhesives, Int. J. Adhes. Adhes. 96 (2020) 102456. https://doi.org/10.1016/j.ijadhadh.2019.102456.

[122] G.G. Eshetu, S. Grugeon, H. Kim, S. Jeong, L. Wu, G. Gachot, S. Laruelle, M. Armand, S. Passerini, Comprehensive Insights into the Reactivity of Electrolytes Based on Sodium Ions, ChemSusChem 9 (2016) 462–471. https://doi.org/10.1002/cssc.201501605.

[123] K. Pfeifer, S. Arnold, J. Becherer, C. Das, J. Maibach, H. Ehrenberg, S. Dsoke, Can Metallic Sodium Electrodes Affect the Electrochemistry of Sodium-Ion Batteries? Reactivity Issues and Perspectives, ChemSusChem 12 (2019) 3312–3319. https://doi.org/10.1002/cssc.201901056.

[124] K.-H. Chen, K.N. Wood, E. Kazyak, W.S. LePage, A.L. Davis, A.J. Sanchez, N.P. Dasgupta, Dead lithium: mass transport effects on voltage, capacity, and failure of lithium metal anodes, J. Mater. Chem. A 5 (2017) 11671–11681. https://doi.org/10.1039/C7TA00371D.

[125] G. Bieker, M. Winter, P. Bieker, Electrochemical in situ investigations of SEI and dendrite formation on the lithium metal anode, Phys. Chem. Chem. Phys. 17 (2015) 8670–8679. https://doi.org/10.1039/c4cp05865h.

[126] A. Willow, H.E.M. Hussein, S. Vajirakaphan, A. Chasri, S. Margadonna, Improving In-Situ Sodium Metal Plating on Copper Foil Through Optimization of Mechanical Pressure: Towards High-Performance Anode-Free Sodium Ion Batteries, Front. Energy Res. 10 (2022). https://doi.org/10.3389/fenrg.2022.888321.

[127] X. Mönnighoff, P. Murmann, W. Weber, M. Winter, S. Nowak, Post-Mortem Investigations of Fluorinated Flame Retardants for Lithium Ion Battery Electrolytes by Gas Chromatography with Chemical Ionization, Electrochimica Acta 246 (2017) 1042–1051. https://doi.org/10.1016/j.electacta.2017.06.125.

[128] T. Sasaki, T. Abe, Y. Iriyama, M. Inaba, Z. Ogumi, Formation mechanism of alkyl dicarbonates in Li-ion cells, J. Power Sources 150 (2005) 208–215. https://doi.org/10.1016/j.jpowsour.2005.02.021.

[129] T. Sasaki, S.-K. Jeong, T. Abe, Y. Iriyama, M. Inaba, Z. Ogumi, Effect of an Alkyl Dicarbonate on Li-Ion Cell Performance, J. Electrochem. Soc. 152 (2005) A1963. https://doi.org/10.1149/1.2008987.

[130] C. Schultz, V. Kraft, M. Pyschik, S. Weber, F. Schappacher, M. Winter, S. Nowak, Separation and Quantification of Organic Electrolyte Components in Lithium-Ion Batteries via a Developed HPLC Method, J. Electrochem. Soc. 162 (2015) A629. https://doi.org/10.1149/2.0401504jes.

[131] S. Takeda, W. Morimura, Y.-H. Liu, T. Sakai, Y. Saito, Identification and formation mechanism of individual degradation products in lithium-ion batteries studied by liquid chromatography/electrospray ionization mass spectrometry and atmospheric solid analysis probe mass spectrometry, Rapid Commun. Mass Spectrom. 30 (2016) 1754–1762. https://doi.org/10.1002/rcm.7652.

[132] F. Allgayer, J. Maibach, F. Jeschull, Comparing the Solid Electrolyte Interphases on Graphite Electrodes in K and Li Half Cells, ACS Appl. Energy Mater. 5 (2022) 1136–1148. https://doi.org/10.1021/acsaem.1c03491.

[133] E.K.W. Andersson, L.-T. Wu, L. Bertoli, Y.-C. Weng, D. Friesen, K. Elbouazzaoui, S. Bloch, R. Ovsyannikov, E. Giangrisostomi, D. Brandell, J. Mindemark, J.-C. Jiang, M. Hahlin, Initial SEI formation

in LiBOB-, LiDFOB- and LiBF4-containing PEO electrolytes, J. Mater. Chem. A 12 (2024) 9184–9199. https://doi.org/10.1039/D3TA07175H.

[134] J. Dean, Lange´s Handbook of Chemistry, 12th ed., McGraw-Hill Inc, New York, 1979.

[135] L. Wildersinn, D. Stottmeister, F. Jeschull, A. Groß, A. Hofmann, Decomposition of Binary Mixtures of DMC/EC, EMC/EC, and DEC/EC on Potassium Surfaces; GC, XPS, and Calculation, ACS Appl. Mater. Interfaces 17 (2025) 10055–10072. https://doi.org/10.1021/acsami.4c17461.

# Appendix

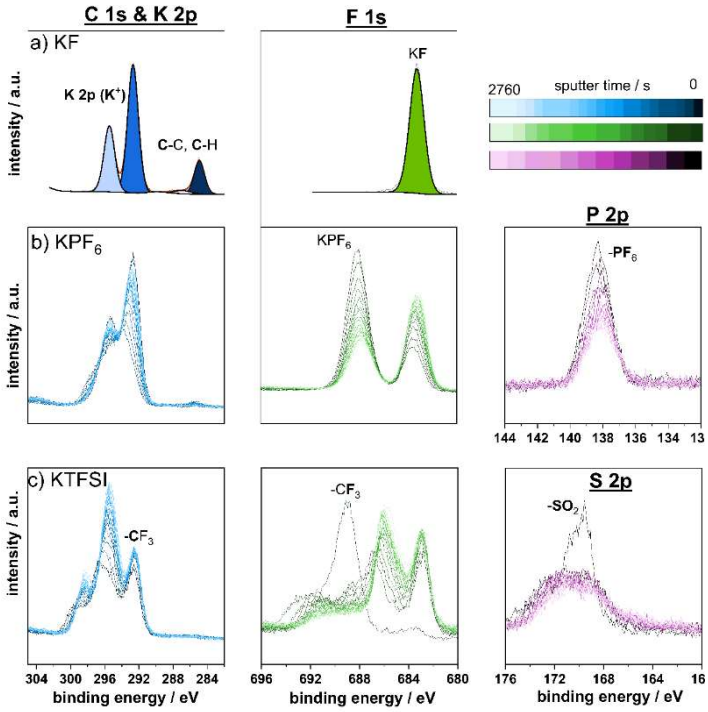


**Figure S1:** C 1s, F 1s, P 2p and S 2p spectra for the components a) KF, b) $KPF_6$ and c) KTFSI sputtered with monoatomic argon (1keV).

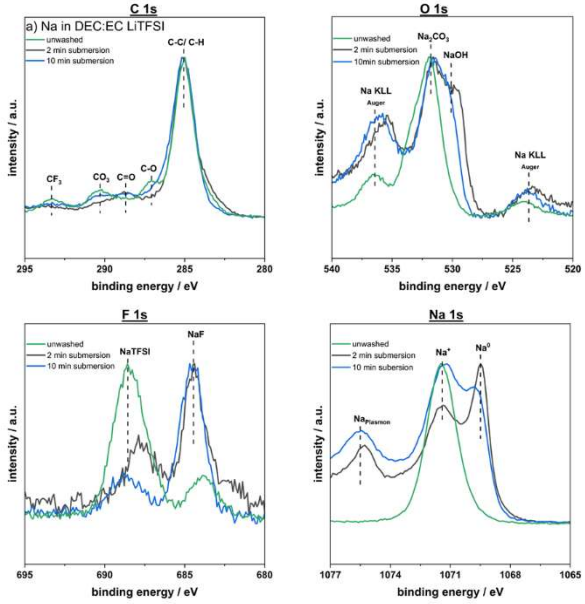


**Figure S2:** Influence of different washing procedures on the composition of the C 1s, O 1s, F 1s and P 2p spectra of pristine Na stored in DEC:EC NaTFSI for 2min. and washed through a submersion step afterwards (2min. and 10min.

**Table S1:** Titration of different electrolytes with corresponding salt and with additive.

| Sample | Mean water content / ppm |
|---|---|
| DEC:EC $LiPF_6$ | 3.86 |
| DEC:EC $NaPF_6$ | 11.2 |
| DEC:EC $KPF_6$ | 14.0 |
| DEC:EC $LiPF_6$ + 5 vol.-% FEC | 2.92 |
| DEC:EC $NaPF_6$ + 5 vol.-% FEC | 12.3 |
| DEC:EC $KPF_6$ + 5 vol.-% FEC | 15.2 |
| DEC:EC LiTFSI | 12.6 |
| DEC:EC NaTFSI | 13.2 |
| DEC:EC KTFSI | 13.9 |
| PC | 26.5 |
| EC:PC $NaClO_4$ | 26.1 |
| EC:PC $NaClO_4$ + 10 vol.% VC | 31.3 |

**Table S2:** List of all measured reference samples with supplier and purity.

| Reference sample | Supplier and Purity / % |
|---|---|
| NaF | Alfa Aesar, 99.99 % |
| $NaPF_6$ | Sigma Aldrich, 99.0 % |
| NaTFSI | Solvionic, 99.5 % |
| $CH_3CO_2Na$ | Sigma Aldrich, 99.0 % |
| $CH_3CONa$ | Thermo Fisher, 99.0 % |
| $Na_2C_2O_4$ | Thermo Fisher, 99.0 % |
| $Na_2CO_3$ | Merck, 99.9 % |
| $NaHCO_3$ | Thermo Fisher, 99.7 % |
| $Na_2O$ | Sigma Aldrich, 80.0 % |
| $Na_2O_2$ | Merck, 97 % |
| NaCl | Alfa Aesar, anhydrous, ACS, 98.0–102.0 % |
| KF | Merck, 99.9 % |
| $KPF_6$ | Sigma Aldrich 99.0 % |
| KTFSI | Solvionic, 99.5 % |
| $CH_3CO_2K$ | Thermo Fisher, 99.0 % |
| $K_2C_2O_4$ / $K_2CO_3$ | VWR, 99.0 % |
| $KHCO_3$ | Mercl, 99.5 % |

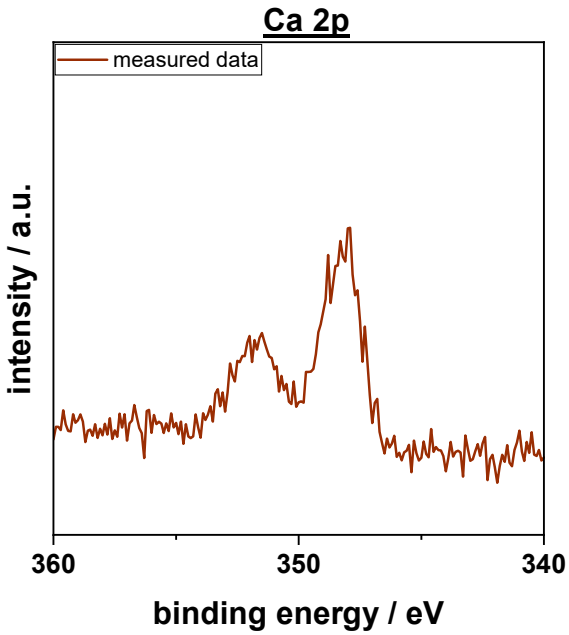


**Figure S3**: The XPS spectra of Ca 2p core peaks of pristine Li, showing Ca impurities of approx. 1 at.%..

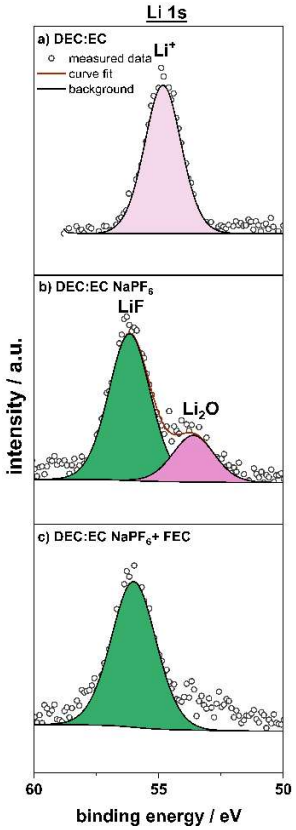


**Figure S4**: The XPS depth profile spectra of Li 1s core peaks of pristine Li in contact with solvent, electrolyte and electrolyte+FEC.

**Table S4:** Peak position and normalized peak areas in the C 1s, F 1s, Li 1s and O 1s BE region of pristine and metallic Li (after $Ar^+$ etching).

| | Li Pristine | | | Li metal after $Ar^+$etching | | |
|---|---|---|---|---|---|---|
| Component | Peak BE eV | FWHM eV | Atomic % | Peak BE | FWHM eV | Atomic % |
| C1s C-C,C-H | 285.02 | 1.6 | 7.25 | 284.99 | 1.73 | 0.12 |
| C1s C-O | 286.3 | 1.54 | 0.27 | 286.58 | 1.65 | 0.08 |
| C1s $CO_3$ | 289.82 | 1.44 | 1.37 | 290.72 | 1.56 | 0.14 |
| F1s LiF | 684.91 | 1.83 | 0.46 | 685.9 | 1.83 | 0.36 |
| Li1s Li-X | 55.02 | 1.54 | 12.99 | 56.3 | 1.62 | 1.98 |
| Li1s Li-Y | 53.73 | 1.54 | 42.73 | 54.37 | 1.62 | 66.32 |
| O1s -$CO_3$, C=O | 531.9 | 1.54 | 4.59 | 532.14 | 1.83 | 2.5 |
| O1s $Li_2O$ | 528.53 | 1.4 | 16.41 | 529.26 | 1.42 | 27.99 |
| O1s LiOH | 531.1 | 1.52 | 13.92 | | | |

**Table S5:** Peak position and normalized peak areas in the C 1s, F 1s, Li 1s, P 2p and O 1s BE region of pristine Li stored in solvent and electrolyte for 2 min, 4 min and 2 h.

| | Li in DEC:EC | | | Li in DEC: EC $LiPF_6$ (2 min) | | | Li in DEC: EC $LiPF_6$ (4 min) | | | Li in DEC: EC LiPF6 (2 h) | | |
|---|---|---|---|---|---|---|---|---|---|---|---|---|
| Element and Component | Peak BE | FWHM eV | Atomic % | Peak BE | FWHM eV | Atomic % | Peak BE | FWHM eV | Atomic % | Peak BE | FWHM eV | Atomic % |
| C1s C-C, C-H | 285.03 | 1.35 | 43.9 | 284.97 | 1.27 | 9.58 | 285.03 | 1.3 | 13.01 | 285.1 | 1.28 | 11.41 |
| C1s -C-O | 286.33 | 1.35 | 8.04 | 286.02 | 1.52 | 1.49 | 286.1 | 1.31 | 1.53 | 286.17 | 1.41 | 1.86 |
| C1s -C=O | 287.5 | 1.54 | 0.93 | 287.3 | 1.52 | 1.62 | 287.3 | 1.31 | 1.19 | 287.32 | 1.41 | 1.83 |
| C1s -$CO_2$ | 288.9 | 1.44 | 2.79 | 289 | 1.52 | 0.48 | 289 | 1.31 | 0.36 | 289 | 1.41 | 0.5 |
| C1s -$CO_3$ | 290.17 | 1.44 | 1.06 | 289.98 | 1.52 | 1.3 | 289.87 | 1.31 | 0.43 | 289.89 | 1.41 | 0.97 |
| F1s LiF | 685.03 | 1.76 | 0 | 685.13 | 1.76 | 21.77 | 685.3 | 1.71 | 19.47 | 685.2 | 1.83 | 3.84 |
| F1s $Li_xPF_y$ | 688.13 | 1.76 | 0 | 688.25 | 1.76 | 3.84 | 688.4 | 1.71 | 6.51 | 688.3 | 1.92 | 13.01 |
| F1s $Li_xPO_yF_z$ | 686.76 | 1.76 | 0 | 686.88 | 1.76 | 6.47 | 686.8 | 1.71 | 8.08 | 686.3 | 1.86 | 24.53 |
| Li1s Li-X | 56.07 | 1.96 | 9.31 | 56.17 | 1.96 | 30.05 | 56.19 | 1.79 | 24.48 | 56.5 | 1.73 | 21.76 |
| Li1s Li-Y | 53.5 | 1.96 | 0 | 53.6 | 1.96 | 9.53 | 53.81 | 1.79 | 11.76 | 53.2 | 1.73 | 4.55 |
| O1s -C-O | 533.45 | 1.92 | 4.20 | 533.5 | 1.92 | 2.14 | 533.1 | 2.12 | 4.61 | 532.9 | 1.73 | 8.62 |
| O1s -$CO_3$, -C=O | 532 | 1.92 | 3.15 | 532.15 | 1.92 | 6.87 | 532.2 | 2.12 | 2.44 | 531.9 | 1.83 | 0.7 |
| O1s $Li_2O$ | 528.12 | 1.34 | 0 | 528.22 | 1.35 | 1.53 | 538.4 | 1.35 | 2.31 | 528.03 | 1.74 | 0 |
| O1s LiOH | 531 | 1.83 | 26.6 | 531 | 1.64 | 1.01 | 531 | 1.92 | 1.29 | 531.1 | 1.74 | 0 |
| P2p1 ScanA | | | | 136.4 | 1.68 | 0 | 136.5 | 1.64 | 0 | 136.6 | 1.68 | 0 |
| P2p1 Scan B | | | | 138.2 | 1.49 | 0 | 138.1 | 1.38 | 0 | 138.3 | 1.88 | 0 |
| P2p3 Scan A | | | | 135.5 | 1.68 | 1.63 | 135.6 | 1.64 | 1.31 | 135.7 | 1.68 | 2.94 |
| P2p3 Scan B | | | | 137.1 | 1.49 | 0.47 | 137 | 1.83 | 1.03 | 137.2 | 1.88 | 1.52 |

**Table S6:** Peak position and normalized peak areas in the C 1s, F 1s, Li 1s, P 2p and O 1s BE region of pristine Li stored in electrolyte with FEC additivw for 2 min, 4 min and 2 h.

| | Li in DEC: EC $LiPF_6$ (2 min) + 5% FEC | | | Li in DEC: EC $LiPF_6$ (4 min) + 5% FEC | | | Li in DEC: EC $LiPF_6$ (2 h) + 5% FEC | | |
|---|---|---|---|---|---|---|---|---|---|
| Element and Component | Peak BE | FWHM eV | Atomic % | Peak BE | FWHM eV | Atomic % | Peak BE | FWHM eV | Atomic % |
| C1s C-C, C-H | 285.02 | 1.38 | 21.1 | 285.1 | 1.3 | 12.44 | 285.03 | 1.29 | 10.32 |
| C1s -C-O | 286.44 | 1.35 | 2.13 | 286.79 | 1.37 | 0.96 | 286.16 | 1.54 | 1.48 |
| C1s -C=O | 287.31 | 1.35 | 1.1 | 287.88 | 1.37 | 0.24 | 287.3 | 1.54 | 1.5 |
| C1s $-CO_2$ | 289.0 | 1.35 | 0.74 | 289.2 | 1.17 | 0.64 | 289 | 1.54 | 0.48 |
| C1s $-CO_3$ | 289.89 | 1.35 | 1.4 | 290.17 | 1.27 | 2.07 | 289.87 | 1.54 | 01.34 |
| F1s C-F | 689.5 | 1.73 | 2.84 | 689.5 | 1.73 | 2.54 | 689.41 | 1.68 | 1.09 |
| F1s LiF | 685.2 | 1.73 | 22.31 | 685.2 | 1.73 | 19.69 | 685.3 | 1.68 | 16.86 |
| F1s $Li_xPF_x$ | 688.3 | 1.73 | 5.15 | 688.3 | 1.73 | 4.61 | 688.16 | 1.68 | 6.75 |
| F1s $Li_xPO_xF_z$ | 686.75 | 1.73 | 4.32 | 686.75 | 1.73 | 3.86 | 686.6 | 1.68 | 11.93 |
| Li1s Li-X | 56.0 | 1.73 | 33.14 | 56.07 | 1.96 | 30.22 | 56.27 | 1.87 | 24.91 |
| Li1s Li-Y | 53.0 | 1.73 | 0 | 53.5 | 1.96 | 9.59 | 53.63 | 1.87 | 11.25 |
| O1s -C-O | 533.5 | 1.92 | 2.61 | 533.5 | 1.92 | 2.33 | 533.1 | 1.92 | 4.78 |
| O1s $-CO_3$, -C=O | 531.85 | 1.92 | 8.59 | 531.85 | 1.92 | 7.69 | 532.0 | 1.92 | 1.97 |
| O1s $Li_2O$ | 528.09 | 1.59 | 0.74 | 528.1 | 1.59 | 0.66 | 528.4 | 1.27 | 1.64 |
| O1s LiOH | 531.29 | 1.9 | 0 | | | | 531 | 1.83 | 0.31 |
| P2p1 ScanA | 136.25 | 2.12 | 0 | 136.4 | 2.12 | 0 | 136.9 | 2.08 | 0 |
| P2p1 Scan B | 137.86 | 2.12 | 0 | 137.4 | 2.12 | 0 | 139.4 | 2.08 | 0 |
| P2p3 Scan A | 135.35 | 2.12 | 2.03 | 135.5 | 2.12 | 1.47 | 135.8 | 2.08 | 2.3 |
| P2p3 Scan B | 136.96 | 2.12 | 0.51 | 136.5 | 2.12 | 0.26 | 138.5 | 2.08 | 0.36 |

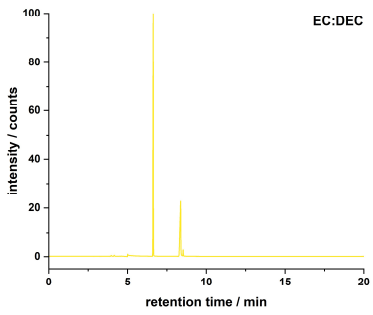


**Figure S5**: Gas chromatogram of uncycled EC:DEC, stored for 2h in a vial.

**Table S7:** Detected components and their respective retention time for a 2h storage in vials of a) DEC:EC and b) DEC:EC with conducting salt.

| Sample | Detected Components | R.T. |
|---|---|---|
| **EC:DEC** | **DEC** | **6.63** |
| | **EC** | **6.20** |
| | **DEC** | **6.63** |
| **EC:DEC $XPF_6$ (X: Li, Na, K)** | **EC** | **6.21** |

**Table S8:** Peak position and normalized peak areas in the C 1s, F 1s, Na 1s and O 1s BE region of pristine and metallic Na (after $Ar^+$ etching).

| | Na Pristine | | | Na metal after $Ar^+$etching | | |
|---|---|---|---|---|---|---|
| **Component** | **Peak BE eV** | **FWHM eV** | **Atomic %** | **Peak BE** | **FWHM eV** | **Atomic %** |
| **C1s C-C,C-H** | **284.94** | **1.46** | **44.15** | | | |
| **C1s C-O** | **286.7** | **1.54** | **1.62** | | | |
| **C1s C=O** | **288.18** | **1.44** | **2.84** | | | |
| **C1s $CO_3$** | **289.7** | **1.54** | **0.78** | | | |
| **F1s NaF** | **684.02** | **1.79** | **6.0** | **684.2** | | **1.6** |
| **Na1s Na-X** | **1069.4** | **0.96** | **3.01** | **1069.8** | **0.94** | **80.4** |
| **Na1s Na-Y** | **1071.2** | **1.92** | **19.97** | **1071.0** | **1.92** | **18** |
| **O1s -C-O** | **533.0** | **1.73** | **1.47** | | | |
| **O1s -$CO_3$, -C=O** | **531.4** | **1.73** | **7.73** | | | |
| **O1s NaO** | **529.85** | **1.92** | **12.23** | | | |

**Table S9:** Peak position and normalized peak areas in the C 1s, F 1s, Na 1s, P 2p and O 1s BE region of pristine Na stored in solvent and electrolyte over a time of 2 min, 4 min, 2 h.

| | Na in DEC:EC | | | Na in DEC: EC $NaPF_6$ (2 min) | | | Li in DEC: EC $LiPF_6$ (4 min) | | | Li in DEC: EC LiPF6 (2 h) | | |
|---|---|---|---|---|---|---|---|---|---|---|---|---|
| Element and Component | Peak BE | FWHM eV | Atomic % | Peak BE | FWHM eV | Atomic % | Peak BE | FWHM eV | Atomic % | Peak BE | FWHM eV | Atomic % |
| C1s C-C, C-H | 285.05 | 1.34 | 58.0 | 285.08 | 1.37 | 10.17 | 284.94 | 1.27 | 18.24 | 285.0 | 1.73 | 5.02 |
| C1s -C-O | 286.7 | 1.6 | 12.0 | 286.7 | 1.73 | 2.46 | 286.88 | 1.39 | 8.98 | 286.7 | 1.73 | 1.84 |
| C1s -C=O | 288.3 | 1.6 | 2.0 | 288.3 | 1.73 | 0.5 | 288.53 | 1.39 | 1.74 | 287.97 | 1.73 | 0.43 |
| C1s $-CO_3$ | 290.0 | 1.6 | 3.0 | 289.5 | 1.73 | 0.87 | 290.3 | 1.39 | 4.35 | 289.5 | 1.73 | 0.51 |
| F1s NaF | | | | 684.73 | 1.8 | 22.99 | 684.2 | 1.74 | 3.6 | 684.49 | 2.0 | 20.75 |
| F1s NaPFO | | | | 687.51 | 1.8 | 16.01 | 687.45 | 1.47 | 27.79 | 687.39 | 2.0 | 15.82 |
| Na1s | 1071.48 | 1.76 | 4.43 | 1071.79 | 2.0 | 17.69 | 1071.9 | 1.94 | 11.43 | 1071.57 | 2.1 | 26.47 |
| O1s -C-O | 533.5 | 2.0 | 7.26 | 533.5 | 1.73 | 3.12 | 533.5 | 2.12 | 8.11 | 533.5 | 2.0 | 4.98 |
| O1s $-CO_3$, -C=O | 531.9 | 1.92 | 12.59 | 531.7 | 1.64 | 17.55 | 531.8 | 2.12 | 10.92 | 531.8 | 1.92 | 15.35 |
| O1s NaOH | 530.0 | 1.83 | 0.67 | 529.9 | 1.73 | 0.44 | | | | 530 | 2.0 | 0.78 |
| Na Auger 1 | 536 | 2.63 | 0 | 537.0 | 2.91 | 0 | | | | | | |
| Na Auger 2 | 524 | 2.63 | 0 | 524.8 | 2.91 | 0 | | | | | | |
| P2p1 ScanA | | | | 138.3 | 1.44 | 0 | 138.28 | 1.35 | 0 | 138.2 | 1.92 | 0 |
| P2p1 Scan B | | | | 135.21 | 1.44 | 0 | | | | 135.23 | 1.92 | 0 |
| P2p3 Scan A | | | | 137.34 | 1.44 | 1.62 | 137.38 | 1.35 | 4.83 | 137.3 | 1.92 | 1 |
| P2p3 Scan B | | | | 134.11 | 1.44 | 6.59 | | | | 134.13 | 1.92 | 7.04 |

**Table S10:** Peak position and normalized peak areas in the C 1s, F 1s, Na 1s, P 2p and O 1s BE region of pristine Na stored in electrolyte with FEC additive over a time of 2 min, 4 min, 2 h.

| | Na in DEC: EC $NaPF_6$ (2 min) + 5% FEC | | | Na in DEC: EC $NaPF_6$ (4 min) + 5% FEC | | | Na in pure FEC (2 min) | | |
|---|---|---|---|---|---|---|---|---|---|
| Element and Component | Peak BE | FWHM eV | Atomic % | Peak BE | FWHM eV | Atomic % | Peak BE | FWHM eV | Atomic % |
| C1s C-C, C-H | 285.04 | 1.37 | 16.22 | 285.06 | 1.64 | 22.06 | 284.99 | 1.73 | 23.62 |
| C1s -C-O | 286.7 | 1.65 | 1.34 | 286.89 | 1.51 | 1.01 | 286.4 | 1.73 | 8.02 |
| C1s -C=O | 288.81 | 1.65 | 1.72 | 288.5 | 1.51 | 1.21 | 288.38 | 1.73 | 2.33 |
| C1s $-CO_3$ | 290.1 | 1.65 | 0.24 | 289.3 | 1.51 | 0.49 | 290.1 | 1.73 | 0.93 |
| F1s NaF | 684.2 | 1.74 | 3.78 | 684.9 | 1.87 | 31.35 | 684.82 | 2.4 | 33.38 |
| F1s NaPFO | 687.45 | 1.74 | 29.15 | 687.7 | 1.87 | 12.26 | 687.55 | 2.4 | 1.49 |
| Na1s | 1071.48 | 1.94 | 11.99 | 1071.81 | 2.02 | 12.92 | 1071.8 | 2.5 | 24.08 |
| O1s -C-O | 533.5 | 1.83 | 8.51 | 533.5 | 1.76 | 1.43 | 533.4 | 1.8 | 1.97 |
| O1s $-CO_3$, -C=O | 531.85 | 1.73 | 11.45 | 531.64 | 1.67 | 10.11 | 531.9 | 1.89 | 3.75 |
| O1s NaOH | 532.58 | 1.9 | 0.35 | 530 | 1.57 | 2.23 | | | |
| Na Auger 1 | 537.25 | 3.0 | 0 | 537.18 | 2.89 | 0 | 537.4 | 3.37 | 0 |
| Na Auger 2 | 524.90 | 3.0 | 0 | 525 | 2.89 | 0 | 525 | 3.37 | 0 |
| P2p1 ScanA | 138.28 | 1.28 | 0 | 138.53 | 1.44 | 0 | | | |
| P2p1 Scan B | 135.28 | 1.9 | 0 | 135.34 | 1.44 | 0 | | | |
| P2p3 Scan A | 137.38 | 1.28 | 5.02 | 137.43 | 1.44 | 1.65 | | | |
| P2p3 Scan B | 124.28 | 1.9 | 10.22 | 134.24 | 1.44 | 3.29 | | | |

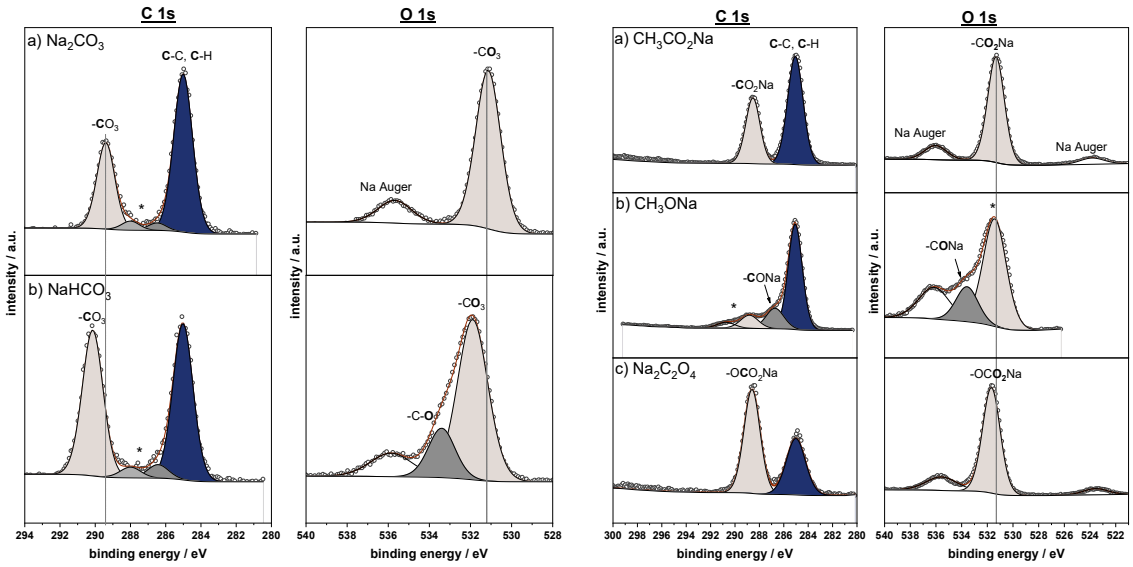


**Figure S6 (left):** Reference measurements of $Na_2CO_3$ and $NaHCO_3$. **Figure S7 (right):** Reference measurements of $CH_3CO_2Na$, $CH_3ONa$ and $Na_2C_2O_4$.

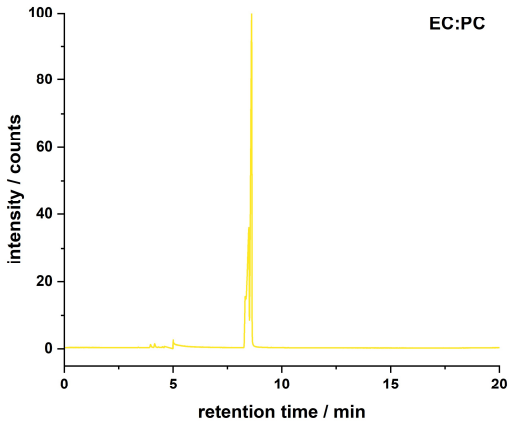


**Figure S8**: Gas chromatogram of uncycled EC:DEC, stored for 2h in a vial.

**Table S11:** Detected components and their respective retention time for a 2h storage in vials of EC:PC

| Sample | Detected Components | R.T. |
|---|---|---|
| **EC:PC** | **EC** | **8.32** |
| | **PC** | **8.61** |

**Table S12:** Peak position and normalized peak areas in the C 1s, K2, F 1s, P 2p and O 1s BE region of pristine K stored in electrolyte over a time of 2 min, 4 min, 2 h.

| | K in DEC: EC | | | K in DEC: EC $KPF_6$ (2 min) | | | K in DEC: EC $KPF_6$ (4 min) | | | K in DEC: EC $KPF_6$ (2 h) | | |
|---|---|---|---|---|---|---|---|---|---|---|---|---|
| Element and Component | Peak BE | FWHM eV | Atomic % | Peak BE | FWHM eV | Atomic % | Peak BE | FWHM eV | Atomic % | Peak BE | FWHM eV | Atomic % |
| C1s C-C, C-H | 284.97 | 1.41 | 42.02 | 285.02 | 1.30 | 29.08 | 284.96 | 1.29 | 32.56 | 285.05 | 1.31 | 30.97 |
| C1s -C-O, -COK | 286.1 | 1.64 | 10.28 | 286.61 | 1.41 | 8.8 | 286.57 | 1.26 | 6.67 | 286.67 | 1.35 | 8.67 |
| C1s -C=O, $CO_{3(K2CO3/KHCO3)}$ | 288.36 | 1.49 | 4.21 | 288.17<br>289.87 | 1.39<br>1.5 | 3.9<br>6.3 | 288.16<br>289.81 | 1.26<br>1.26 | 3.97<br>5.86 | 288.17<br>289.9 | 1.35<br>1.35 | 4.54<br>5.93 |
| C1s -$CO_{3(solvent)}$ | 289.95 | 1.40 | 1.8 | | | | | | | | | |
| F1s (*) | | | | 693.24 | 2.88 | 2.31 | 692.22 | 2.85 | 4.15 | 693.0 | 3.0 | 0 |
| F1s KF | | | | 683.33 | 1.83 | 1.69 | 683.1 | 1.54 | 1.7 | 683.25 | 1.83 | 1.59 |
| F1s P-F | | | | 687.23 | 1.83 | 4.88 | 687.28 | 1.83 | 5.8 | 687.41 | 1.83 | 5.79 |
| F1s $K_xP_yF_z$ | | | | 684.54 | 2.0 | 1.18 | 684.7 | 1.26 | 0.19 | 684.7 | 2.0 | 0.98 |
| K2p | 292.63 | 1.66 | 17.81 | 292.9 | 1.54 | 13.34 | 295.59 | 1.53 | 13.92 | 292.9 | 1.63 | 13.65 |
| O1s -C-O | 533.4 | 1.73 | 2.81 | 533.3 | 1.76 | 8.14 | 533.16 | 1.64 | 6.47 | 533.4 | 2.06 | 8.02 |
| O1s -$CO_3$, -C=O, -COK | 531.49 | 1.73 | 9.07 | 531.37 | 1.76 | 17.61 | 531.26 | 1.64 | 16.32 | 531.4 | 2.06 | 18.43 |
| O1s -$CO_{3(K2CO3)}$ | 530.6 | 1.73 | 6.38 | | | | | | | | | |
| O1s KOH | 529.47 | 1.50 | 5.61 | 529.5 | 1.76 | 1.25 | 529.3 | 1.16 | 1.11 | | | |
| P2p1 ScanA | | | | 137.8 | 1.73 | 0 | 137.95 | 1.46 | 0 | 137.98 | 1.68 | 0 |
| P2p1 Scan B | | | | 134.9 | 1.73 | 0 | 134.7 | 1.46 | 0 | 134.83 | 1.68 | 0 |
| P2p3 Scan A | | | | 136.9 | 1.73 | 0.87 | 137.05 | 1.46 | 1.08 | 137.08 | 1.68 | 1.13 |
| P2p3 Scan B | | | | 133.8 | 1.73 | 0.66 | 133.8 | 1.46 | 0.22 | 133.8 | 1.68 | 0.3 |

**Table S13:** Peak position and normalized peak areas in the C 1s, F 1s, K 2p, P 2p and O 1s BE region of pristine K stored in electrolyte with FEC additive over a time of 2 min and 4 min.

| | K in DEC: EC $KPF_6$ (2 min) + 5% FEC | | | K in DEC: EC $KPF_6$ (4 min) + 5% FEC | | |
|---|---|---|---|---|---|---|
| Element and Component | Peak BE | FWHM eV | Atomic % | Peak BE | FWHM eV | Atomic % |
| C1s C-C, C-H | 284.95 | 1.32 | 27.16 | 285.04 | 1.5 | 24.24 |
| C1s -C-O | 286.54 | 1.72 | 7.41 | 286.54 | 1.8 | 8.74 |
| C1s -C=O | 288.2 | 1.72 | 3.02 | 288.07 | 1.8 | 3.68 |
| C1s -$CO_3$ | 289.85 | 1.8 | 3.65 | 289.39 | 1.61 | 3.63 |
| F1s (*) | 692.9 | 2.5 | 5.54 | 692.22 | 2.8 | 5.71 |
| F1s KF | 682.9 | 1.54 | 2.27 | 683.1 | 1.54 | 2.33 |
| F1s P-F | 687.08 | 1.8 | 7.74 | 687.2 | 1.8 | 7.97 |
| F1s $K_xP_yF_z$ | 684.08 | 1.26 | 0.25 | 684.7 | 1.26 | 0.26 |
| K2p<br>K2p (*) | 292.88<br>300.12 | 1.8<br>1.8 | 7.54<br>1.76 | 293.0<br>297.99 | 1.9<br>1.9 | 7.39<br>1.41 |
| O1s -C-O | 533.0 | 1.64 | 8.65 | 533.16 | 1.64 | 8.9 |
| O1s -$CO_3$, -C=O | 531.06 | 1.64 | 21.8 | 531.26 | 1.64 | 22.44 |
| O1s KOH | 529.1 | 1.16 | 1.48 | 529.2 | 1.16 | 1.53 |
| P2p1 ScanA | 137.75 | 1.46 | 0 | 137.95 | 1.46 | 0 |
| P2p1 Scan B | 134.5 | 1.46 | 0 | 134.7 | 1.46 | 0 |
| P2p1 Scan C | 125.76 | 1.64 | 0 | 125.96 | 1.46 | 0 |
| P2p3 Scan A | 136.85 | 1.46 | 1.45 | 137.0 | 1.46 | 1.49 |

**Table S14:** Overview of solvents and decomposition products. (All compounds were measured as pure substances, supplier-reported purities >95%.) This table provides gas chromatography (GC) data, including retention indices (RI) and mass fragmentation patterns. RI values refer to the onset of each peak, using the peak maximum yields comparable values (variation within ±2). Values in brackets represent estimated data from the NIST database. A detailed discussion of each compound can be found in the corresponding publication.[135]

| **Abbreviations** | **Compound** | **RI** | **RI NIST** | **m/z (descending intensity)** | **No in Figure X** |
|---|---|---|---|---|---|
| **DMC** | dimethyl carbonate | 619 | 620 | 45 59 90 60 62 | **1** |

| | | | | | |
|---|---|---|---|---|---|
| **DEC** | diethyl carbonate | 782 | 767 | 45 91 63 44 75 | **11** |
| **EMC** | ethyl methyl carbonate | 702 | (662) | 45 77 59 44 60 | **2** |
| **EC** | ethylene carbonate | 960 | (814) | 43 88 44 58 73 | **4** |
| **DMDD** | dimethyl 2,5-dioxahexanedioate | 1177 | | 59 45 58 91 74 | **5** |
| **DEDD** | diethyl 2,5-dioxahexanedioate | 1323 | (1303) | 45 44 91 63 89 | **13** |
| **EMDD** | ethyl methyl 2,5-dioxahexanedioate | 1251 | | 59 45 77 44 58 | **6** |
| **DMCE** | di-(2-methoxycarbonyloxyethyl) ether | 1471 | (19) | 103 59 45 104 70 | **7** |
| **DECE** | di-(2-ethoxycarbonyloxyethyl) ether | 1613 | | 89 117 45 44 70 | **15** |
| **EMCE** | 2-ethoxycarbonyloxyethyl-2-methoxycarbonyloxy ethyl ether | 1541 | | 103 89 45 117 59 | **14** |
| **DMCC** | di-(2-methoxycarbonyloxyethyl) carbonate | 1714 | | 59 103 58 45 91 | **8** |
| **DECC** | di-(2-ethoxycarbonyloxyethyl) carbonate | 1856 | | 44 45 89 117 102 | **18** |
| **EMCC** | 2-methoxycarbonyloxyethyl-2-ethoxycarbonyloxyethyl carbonate | 1782 | | 44 45 59 103 89 | **16** |
| **MEMC** | 2-methoxyethyl methyl carbonate | 926 | | 45 58 59 43 77 | **3** |
| **EEMC** | 2-ethoxyethyl methyl carbonate | 1004/ 1011 | | | |
| **MEEC** | 2-methoxyethyl ethyl carbonate | 1004/ 1011 | | | |
| **EEEC** | 2-ethoxyethyl ethyl carbonate | 1070 | | 72 59 45 89 91 | **12** |
| **MEEMC** | 2-(2-methoxyethoxy)ethyl methyl carbonate | 1211 | | 103 59 58 45 43 | |

| | | | | |
|---|---|---|---|---|
| **EEEMC** | 2-(2-ethoxyethoxy)ethyl carbonate | methyl | 1274/ 1288 | |
| **MEEEC** | 2-(2-methoxyethoxy)ethyl carbonate | ethyl | 1274/ 1288 | |
| **EEEEC** | 2-(2-ethoxyethoxy)ethyl carbonate | ethyl | 1345 | 45 89 59 72 73 |

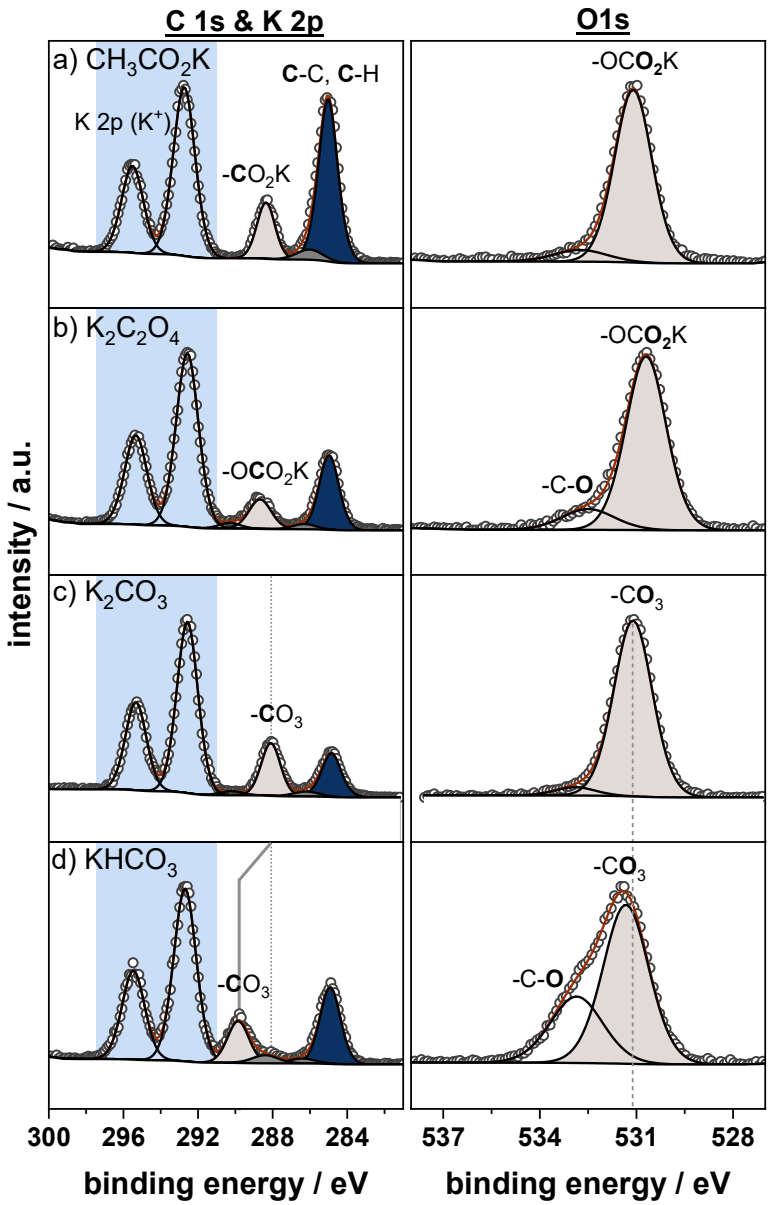


**Figure S9:** Reference measurements of $CH_3CO_2K$, $K_2C_2O_4$, $K_2CO_3$ and $KHCO_3$

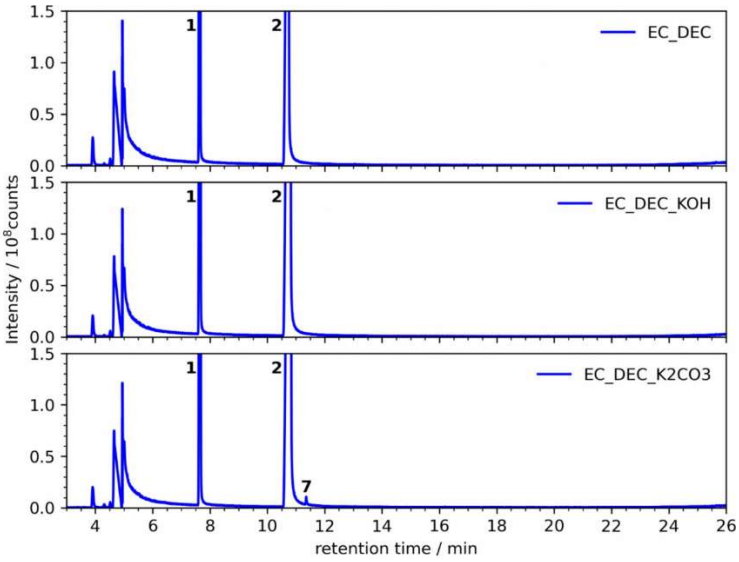


**Figure S10:** Degradation after one week of EC:DEC solvent and EC:DEC when KOH or $K_2CO_3$ is present

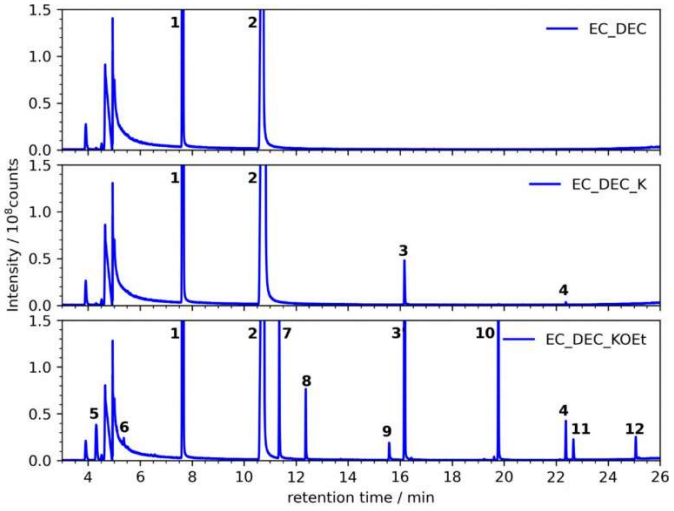


**Figure S11:** Degradation after one week of EC:DEC solvent when potassium metal or KOEt is present.

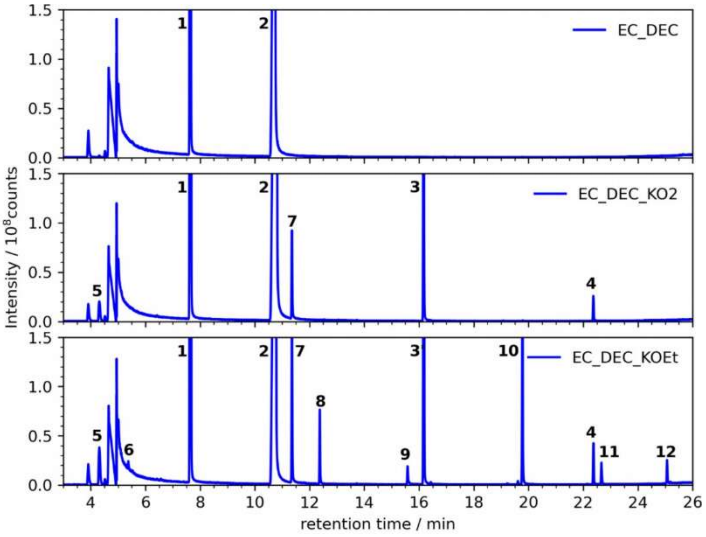


**Figure S12:** Degradation after one week of EC:DEC solvent when potassium oxidel or KOEt is present.

**Table S15:** GC-MS results of the solvent mixture DEC:EC in contact with several potassium salts after one week including the assigned decomposition products.

| | Retention time /min. | Product |
|---|---|---|
| 1 | 7,65 | DEC |
| 2 | 10,74 | EC |
| 3 | 16,17 | DEDD, ethane-1,2-diyl diethyl dicarbonate |
| 4 | 22,37 | |
| 5 | 4,31 | Ethanol |
| 6 | 5,37 | Ethylacetat |
| 7 | 11,36 | |
| 8 | 12,37 | EEEC, 2-ethoxyethoxy ethyl carbonate |
| 9 | 15,58 | |
| 10 | 19,78 | Di-(2-ethoxycarbonyloxyethyl)ether |
| 11 | 22,67 | DECC |
| 12 | 25,07 | |

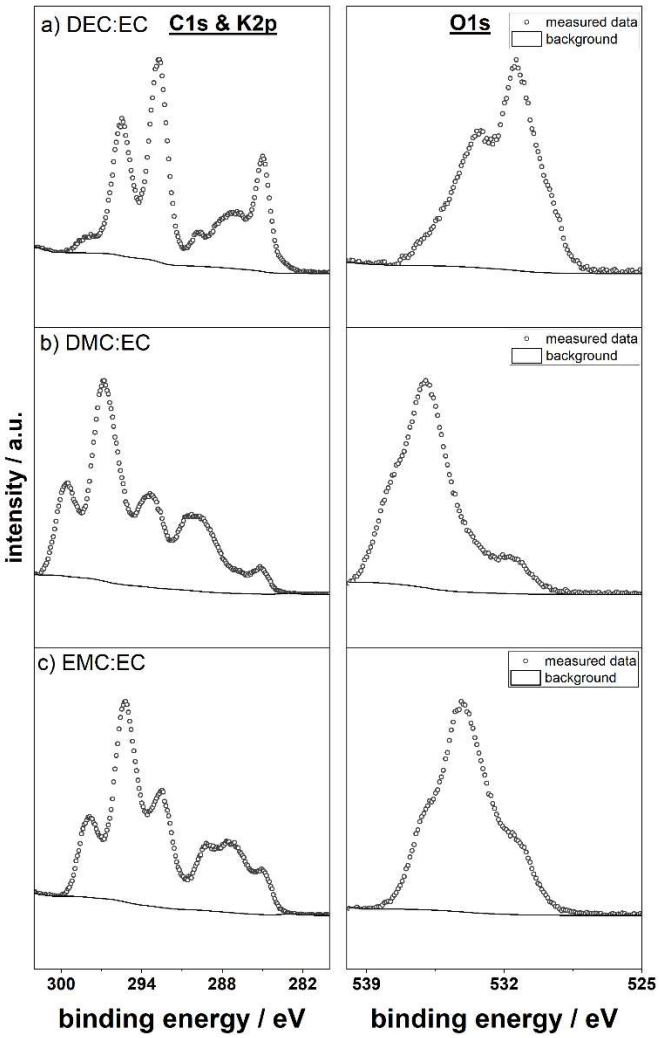


**Figure S13:** C 1s and K 2p and O 1s spectra of the potassium surface after a storage time of 14 days in different solvent mixtures: DEC:EC (a), DMC:EC (b), EMC:EC (c). No calibration possible.

**Table S16:** XPS measurements on stored potassium in various solvent compositions for 2 h with the corresponding peak position and at.%.

| Storage time **2 h** | Samples binding energy/ eV (atomic concentration/ atom.-%) | | | | | | | | |
|---|---|---|---|---|---|---|---|---|---|
| K in | **C1s** **C**-C, **C**-H | **C1s** -**C**-O-, -**C**-OK | **C1s** -**C**=O- $K_2$**C**$O_3$ | **C1s** -(**C**$O_3$)- | **K2p** | **O1s** K**O**H | **O1s** $K_2C$**O**$_3$ | **O1s** C=**O**, -C-**O**K | **O1s** C-**O** |
| EMC/EC | 285 (43.2) | 286.3 (10.4) | 288.4 (5.5) | 289.9 (2.1) | 292.8 (15.3) | 529.5 (2.4) | 530.6 (6.0) | 531.5 (11.1) | 533.4 (4.0) |
| DMC/EC | 285 (41.6) | 286.3 (10.0) | 288.4 (5.4) | 290.0 (2.8) | 292.8 (15.4) | 529.4 (1.3) | 530.5 (5.2) | 531.4 (13.4) | 533.3 (4.9) |
| DEC/EC | 285 (41.9) | 286.3 (7.0) | 288.5 (4.0) | 290.0 (1.5) | 292.7 (20.8) | 529.5 (6.7) | 530.4 (6.3) | 531.3 (9.2) | 533.3 (2.5) |

**Table S17:** LiF, $Li_2CO_3$, NaF, $Na_2CO_3$ and KF solubilities in PC and DEC:EC measured with ICP-OES. Measurements conducted within this work are **marked**. (literature values from Ref. ([41])

| | **Solubility** | | | |
|---|---|---|---|---|
| | In PC /mg $L^{-1}$ | | In DEC:EC /mg $L^{-1}$ | |
| | Literature/ | in-house | Literature/ | in-house |
| LiF | 0.16 | 0.25 | 0.06 | n.d. |
| $Li_2CO_3$ | 0.16 | - | 0.14 | - |
| NaF | 8.6 | n.d. | 3.06 | n.d. |
| $Na_2CO3$ | 6.6 | - | 3.65 | - |
| KF | - | **13.6** | - | **22.0** |

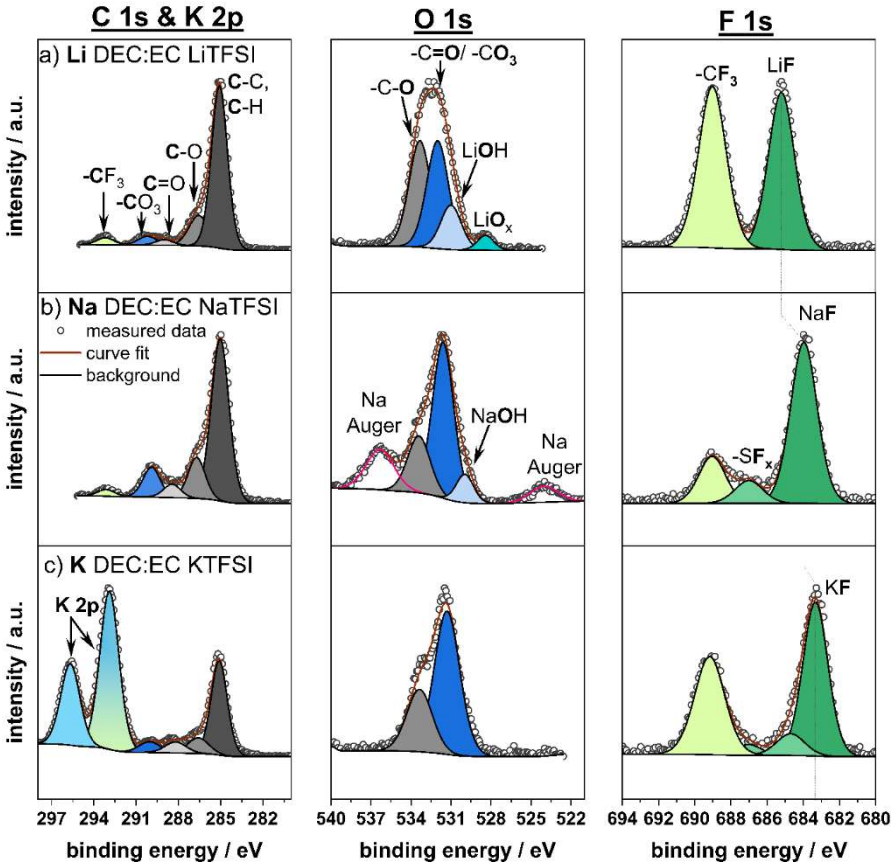


**Figure S14:** Influence of different washing procedures on the composition of the C 1s, O 1s, F 1s and P 2p spectra of pristine Na stored in DEC:EC NaTFSI for 2min. and washed trhough a submersion step afterwards (2min. and 10min.)